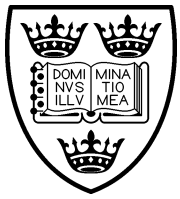
Periodic Pattern Formation In Developmental Biology: A Study Of The Mechanisms Underlying Somitogenesis



Ruth E. Baker

WADHAM COLLEGE

University of Oxford

A thesis submitted for the degree of

Doctor of Philosophy

Hilary Term 2005

Acknowledgements

I am deeply indebted to my supervisors, Professor Philip Maini and Dr. Santiago Schnell for their unwavering support and guidance. To Philip for introducing me to the world of mathematical biology as an undergraduate, for suggestions with the mathematics, and for support in deciding where to go after somites. To Santiago for being my biology mentor and always having time to listen to my ideas.

This study was funded by the Engineering and Physical Sciences Research Council via a doctoral training award and I also acknowledge Wadham College, Oxford for scholarships throughout my academic career in Oxford and St John's College, Oxford for a Stipendiary Lectureship in Applied Mathematics.

I would like to thank Dr. Paul Kulesa, Dr. Olivier Pourquié and Dr. Julien Dubrulle for their kind hospitality at the Stowers Institute, Kansas. In particular to Paul, for helpful comments on the models and for the photographs, to Julien for taking time to patiently explain all the biological detail of his work to a mathematician and to Olivier for embracing mathematical modelling and for taking the time to read manuscripts and reply to my questions. Thanks must also go to Dr. Ruth Diez del Corral for help with the FGF8/RA network model and for the FGF8/RA photographs.

I am grateful to everyone who has worked within the Centre for Mathematical Biology over the last four years and in particular Caroline, Edward, Iain, Ben, Steven and Matthew for providing help and support and for brightening up the days with lots of tea, cakes and crosswords. Thanks also to Rob Hinch for guidance with Chapter 7 and to Edward Flach for help with the NAG routines.

Thank you to those in Oxford that have kept me sane outside of mathematical biology: to Ann for all your support, to Alex and Martin for paving the road ahead and to Charlotte, Kate and the rest of the footballers for dragging me out of the office on many occasions.

Finally, huge thanks go to my family. I am indebted to them for their love and support throughout my education. This work is for you.

Overview

Morphogenesis, the formation of structure in the embryo, is self-evidently of fundamental importance in developmental biology. The processes occurring must be genetically controlled, but genes themselves cannot create the physical pattern; they simply provide a blueprint for the embryo to follow. Much of the research done in developmental biology goes into understanding the mechanisms that convert the blueprint into reality. Hundreds of cell types are generated and laid down in a highly ordered spatio-temporal pattern making it extremely difficult to isolate and separate these mechanisms as they act. In producing a mathematical model for any process, it is important to focus first upon the key mechanisms to produce a framework in which one can make hypotheses and experimentally testable predictions. Whilst testing such predictions, new mechanisms can be found and it is this kind of feedback that is essential in furthering our understanding of the complex interactions that take place during development.

Abstract

Somitogenesis, the sequential formation of a periodic pattern along the antero-posterior axis of vertebrate embryos, is one of the most obvious examples of the segmental patterning processes that take place during embryogenesis and also one of the major unresolved events in developmental biology. The principal aim of this thesis is to develop a series of mathematical models for somite formation.

We begin by reviewing the current models for somitogenesis in the light of new experimental evidence regarding the presence of a segmentation clock and graded expression of FGF8. We conduct a preliminary investigation into the wavefront of FGF8 along the antero-posterior axis and integrate this model into the framework of an existing model for a signalling process. We demonstrate that this new "Clock and Wavefront" model can produce coherent series' of somites in a manner that is tightly regulated in both space and time, and that it can also mimic the effects seen when FGF8 expression is perturbed locally. We then use the model to make some experimentally testable predictions.

The latter part of the thesis concentrates on building more biologically accurate models for the FGF8 gradient. We move to consider a model for the FGF8 gradient which involves a complex network of biochemical interactions with negative feedback between FGF8 and retinoic acid. The resulting system of seven coupled non-linear equations, including both ordinary and partial differential equations, is difficult to analyse. To facilitate our understanding of the non-linear interactions between FGF8 and retinoic acid, we finally consider a reduced model which can display travelling wavefronts of opposing FGF8 and retinoic acid concentrations moving down the antero-posterior axis. The model allowed us to calculate a minimum wave speed for the wavefronts as a function of key model parameters such as the rate of FGF8 and retinoic acid decay; strong dependence on the values of these parameters is a result that is hypothesised to occur *in vivo*.

Contents

1 Introduction **1**

1.1 Biological background 1

1.2 Experimental observations 3

1.2.1 Heat shock 4

1.2.2 Gene perturbation 6

1.2.3 FGF8 signalling 6

1.3 Models for somite formation 7

1.3.1 Clock and wavefront model for somitogenesis 7

1.3.1.1 Consistency with experimental evidence 8

1.3.2 Wave/cell polarisation model for somitogenesis 9

1.3.2.1 Mathematical formulation of the wave/cell polarisation model . . 9

1.3.2.2 Consistency with experimental evidence 12

1.3.3 Reaction-diffusion model for somitogenesis 12

1.3.3.1 Mathematical formulation of the reaction-diffusion model 13

1.3.3.2 Common repressor model 14

1.3.3.3 Direct inhibition model 15

1.3.3.4 Consistency with experimental evidence 15

1.3.4 Cell cycle model for somitogenesis 16

1.3.4.1 Mathematical formulation of the cell cycle model 17

1.3.4.2 Consistency with experimental evidence 18

1.4 Aims of this work 18

2 Analysis of the Cell Cycle Model **21**

2.1 Mathematical formulation of the model 21

2.1.1 Non-dimensionalisation 21

2.1.2 Boundary conditions . . . 22
2.1.3 Modelling assumptions . . . 22
2.1.4 Spatio-temporal analysis . . . 23
2.2 Phase plane study of the model equations . . . 25
2.2.1 The behaviour of the model in Region I . . . 25
2.2.2 The behaviour of the model in Region II . . . 25
2.2.2.1 Stability of the steady states . . . 26
2.2.3 The behaviour of the model in Region III . . . 29
2.3 Numerical solution . . . 31
2.3.1 Approximations . . . 31
2.3.2 Computational domain . . . 31
2.3.3 Initial conditions . . . 32
2.3.4 Parameter values . . . 33
2.3.5 Numerical results . . . 33
2.3.6 Accuracy . . . 33
2.3.6.1 Mesh spacing . . . 34
2.3.6.2 Error parameter . . . 35
2.3.6.3 Zero flux boundary conditions . . . 36
2.4 Explanation of heat shock effects . . . 37
2.4.1 Heat shock algorithm: explanation using the signalling model . . . 38
2.4.2 Spatio-temporal analysis . . . 39
2.4.3 Numerical simulation . . . 40
2.5 Discussion . . . 41

3 Approximations for the Somitogenic Process 44

3.1 Analysis of the signalling equation . . . 46
3.1.1 Approximating v in the initial stages . . . 46
3.1.1.1 Spatial behaviour of a pulse in signalling molecule . . . 46
3.1.2 Analytical expression for the rise in v . . . 47
3.1.2.1 Solving for a general equation . . . 49
3.1.3 Approximating v in the fourth stage . . . 51
3.2 Analysis of the somitic factor equation . . . 53
3.2.1 Approximating u in the first stage . . . 55

3.2.2 Approximating u in the middle stages . . . 56
3.2.3 Approximating u in the fourth stage . . . 60
3.2.4 Domains of validity . . . 62
3.2.5 Comparison with the numerical solution . . . 63
3.3 The posterior boundary of the somite . . . 64
3.4 Discussion . . . 68
3.4.1 Validity of the cell cycle model . . . 69

4 FGF8 expression in the embryo 70
4.1 Experimental evidence . . . 70
4.1.1 Segmental determination . . . 70
4.1.2 fgf8 expression within the PSM . . . 71
4.1.2.1 Specific FGF8 perturbation . . . 71
4.1.3 Maintenance of the FGF8 gradient . . . 73
4.2 A new clock and wavefront model for somitogenesis . . . 74
4.2.1 Local application of FGF8 . . . 78
4.3 A revised model for normal somite formation . . . 79
4.3.1 Initial conditions . . . 80
4.3.2 Boundary conditions . . . 81
4.3.3 The mRNA profile . . . 82
4.3.4 The protein profile . . . 82
4.3.5 Comparison of the analytical and numerical solutions . . . 84
4.3.6 Numerical solution of the fgf8 model for somite formation . . . 84
4.4 Important factors to consider . . . 85
4.4.1 The effects of transcriptional delay . . . 86
4.4.2 Approximations for FGF8 . . . 91
4.5 Discussion . . . 93

5 Perturbation of endogenous FGF8 95
5.1 Normal segmentation . . . 96
5.1.1 Numerical solution . . . 98
5.2 Local application of FGF8 . . . 99
5.2.1 Analytical solution with application of FGF8 . . . 100

5.2.1.1 Solution of the w_b equation using Green's functions 100
5.2.1.2 Parameter dependence of the bead 102
5.2.1.3 Solution of the w equation using Green's functions 102
5.2.2 "Realistic choices" for the parameters 102
5.2.3 Numerical simulation 104
5.3 Approximations 104
5.3.1 Approximations for the endogenous gradient 105
5.3.2 FGF8 perturbation by a bead implant 107
5.4 The model using FGF8 profile approximations 111
5.4.1 Application to model 113
5.5 Numerical solution 114
5.5.1 Numerical results 116
5.6 Discussion 116

6 Experimental Predictions **123**
6.1 Altering the speed of the determination front 123
6.2 Altering the period of the segmentation clock 124
6.3 Inhibiting FGF8 signalling with SU5402 126
6.4 Parameter estimation 130
6.5 Discussion 130

7 Retinoic Acid/FGF8 Feedback Model **131**
7.1 Biological background 131
7.2 RA/FGF8 feedback mechanism 132
7.2.1 Non-dimensionalisation 137
7.2.1.1 Boundary conditions 138
7.2.1.2 Initial conditions 138
7.3 Numerical solution of the '*Original system*' of equations 139
7.4 A singular perturbation problem 140
7.4.1 Inner region 140
7.4.2 Outer region 142
7.4.3 Domains of validity 143
7.5 Solution of the '*Inner system*' 144

7.6 The '*Outer system*' . . . 148
7.6.1 Numerical solution of the '*Outer system* - $\mathcal{O}(1)$' . . . 148
7.6.1.1 Boundary conditions for the '*Outer system* - $\mathcal{O}(1)$' . . . 148
7.6.1.2 Initial conditions for the '*Outer system* - $\mathcal{O}(1)$' . . . 149
7.6.1.3 Results for the '*Outer system* - $\mathcal{O}(1)$' . . . 149
7.6.1.4 Comparison with the '*Original system*' . . . 149
7.6.2 Analytical results for the '*Outer system* - $\mathcal{O}(1)$' . . . 151
7.7 The approximate solutions - a summary . . . 152
7.7.1 Domain of validity . . . 152
7.8 Discussion . . . 152

8 A Coupled FGF8/RA Gradient Model 156
8.1 General model . . . 156
8.1.1 Non-dimensionalisation . . . 157
8.2 Simplification of the model . . . 157
8.3 2-species competition model . . . 158
8.3.1 Phase plane analysis . . . 158
8.3.1.1 Linear stability analysis . . . 159
8.3.1.2 Phase planes . . . 159
8.3.2 Travelling wave analysis . . . 160
8.3.3 Numerical solution . . . 164
8.4 The general model with $n_a = 1$ and $n_f = 1$ . . . 165
8.4.1 Phase plane analysis . . . 165
8.4.1.1 Linear stability analysis . . . 168
8.4.2 Travelling wave analysis . . . 169
8.4.3 Numerical solution . . . 173
8.5 The general model as n_a and n_f vary . . . 174
8.5.1 Cases 1 – 4 . . . 175
8.5.1.1 Numerical solution of the general model with $n_a, n_f \neq 1$ - Cases 1 – 4 . . . 176
8.5.2 Further cases . . . 176
8.6 Discussion . . . 179
8.6.1 Travelling wave speed . . . 180

8.6.2 Conclusions and further work 180

9 Discussion and Conclusions **182**

9.1 Future work 183

9.1.1 Modelling directions 183

9.1.2 Experimental directions 184

9.2 Final words 184

A Numerical Methods **185**

A.1 The NAG library solver D03PCF 185

A.1.1 Method of lines 186

A.1.2 Spatial discretisation 187

A.1.3 Backwards differentiation formula method 188

A.1.3.1 Accuracy and consistency of the LMS formulae 188

A.1.3.2 The s-step backwards differentiation formulae 190

A.2 The MATLAB ODE Solver ode15s 191

A.2.1 odeset 192

A.3 The MATLAB PDE Solver pdepe 192

A.4 The MATLAB BVP Solver bvp4c 193

A.5 The MATLAB numerical integrators quad and quadl 194

A.5.1 Simpson's method 194

A.5.2 Lobatto method 196

A.6 The MATLAB function fzero 196

B Linear stability criteria **197**

C Error function **198**

D Glossary **199**

E Analytical results from Chapter 7 **200**

E.1 Solution of the '*Outer system* - $\mathcal{O}(1)$' with $c_n = 0$ 200

E.1.1 Stability of the '*Outer system* $\mathcal{O}(1)$, *rescaled* x, *zero* c_n' steady states . . . 203

E.2 Solution of the '*Outer system* - $\mathcal{O}(1)$' with $c_n \neq 0$ 206

E.2.1 '*Outer system* - $\mathcal{O}(1)$, *rescaled* x, *non-zero* c_n, *travelling wave* - $\mathcal{O}(1)$' . . 207

E.2.2 '*Outer system - $\mathcal{O}(1)$, rescaled x, non-zero $\tilde{c}_n$, travelling wave - $\mathcal{O}(\tilde{c}_n)$*' . . 208
E.2.2.1 Matching conditions 210
E.2.2.2 Uniqueness of solution to equation (E.58) 210
E.2.3 Numerical Solution for '*Outer system - $\mathcal{O}(1)$, rescaled x, non-zero c_n, travelling wave*' correct to first order in c_n 213
E.2.3.1 Comparison with the NAG numerical solution 214

List of Figures

1.1 A mouse embryo at 9.5 days post fertilisation 2

1.2 A chick embryo with the somites clearly visible 3

1.3 Magnified chick somites 4

1.4 An illustration of the vertebrate embryo during somite formation 5

1.5 An illustration of the periodic somite anomalies that may be caused by application of heat shock 6

1.6 An illustration of the somite anomalies that may be caused by local application of FGF8 7

1.7 An illustration of the way in which cells are recruited into somites in the clock and wavefront model 8

1.8 An illustration of the distribution of polarised PSM cells as envisaged by the wave/cell polarisation model 11

1.9 An illustration of the stages involved in somite formation, as envisaged in Meinhardt's reaction-diffusion model 14

1.10 Schematic representation of the way in which somites are proposed to form in the cell cycle model 19

2.1 An illustration of the manner in which somites are formed in the cell cycle model . 24

2.2 The phase plane for Region II 26

2.3 The phase plane with trajectories for Region II 27

2.4 The phase plane for Region II when $\gamma < \kappa/4$ 28

2.5 The phase plane for Region III 29

2.6 The continuous approximation of the Heaviside function 32

2.7 The numerical solution of the signalling model (1) 34

2.8 The numerical solution of the signalling model (2) 35

2.9 The numerical solution for the signal dynamics 36

2.10 The effect of varying the mesh spacing 37

2.11 The effect of varying the error parameter 38
2.12 The effect of zero flux boundary conditions 39
2.13 The effect of heat shock on the cell cycle 40
2.14 An illustration of somite formation under heat shock 41
2.15 The numerical solution of the signalling model with heat shock 42

3.1 The behaviour of the Heaviside functions during the signalling process 45
3.2 The analytical approximation for the pulse in v 48
3.3 The analytical solution for the rise in v 50
3.4 The behaviour of the signalling molecule between pulses 52
3.5 The numerical solution of the cell cycle model over a range of domains of t 54
3.6 The approximate solution for u in the initial stages of a pulse 57
3.7 The u nullcline 58
3.8 The approximate solution for u in the middle stages of a pulse 59
3.9 The approximate solution for u in the final stages of a pulse 61
3.10 Comparison of the analytical approximations for u with the numerical solution . . 63
3.11 The boundary of the somite 65
3.12 The threshold level of somitic factor 66
3.13 The time taken to reach the somitic factor threshold 67

4.1 An illustration of the vertebrate body plan during somite formation 72
4.2 Implantation of an FGF8 bead reduces the number of cells allocated to somites . . 73
4.3 An illustration of the manner in which a gradient of FGF8 could be maintained along the AP axis 75
4.4 A schematic view of the way in which the level of FGF8 signalling changes over time with local application of FGF8 76
4.5 Diagrammatic representation of the vertebrate body plan during somite formation within the modified model 77
4.6 Plots of the analytical solution for the *fgf8* concentration along the AP axis of embryos 83
4.7 Plot of the analytical solution for the FGF8 concentration 84
4.8 Plots of the analytical and numerical solutions of equations (4.7) and (4.8) 85
4.9 Numerical solution of equations for somitic factor, signal, *fgf8* and FGF8 dynamics 86
4.10 The changes in the FGF8 concentration profile as the delay in protein transcription is varied 87

4.11 An illustration of the possible shapes for the FGF8 profile with a delay in protein transcription 88

4.12 The dependence of τ_c, the critical value for transcriptional delay below which there is no local maximum in the FGF8 profile, on the key parameters 90

4.13 The changes in the protein concentration profile (p) as β, the linear decay rate of *fgf8* is varied 92

5.1 Plots of the travelling wave solution for the FGF8 profile 97

5.2 A plot of the numerical solution of equation (5.3) 99

5.3 The analytic solution (5.30) of equation (5.25) 101

5.4 The FGF8 profile generated by a bead implanted alongside the PSM 103

5.5 Numerical solution for the FGF8 profile along the AP axis 105

5.6 Plots of the individual components of equation (5.33) 106

5.7 Plot of the 5^{th} component of equation (5.33) 108

5.8 Demonstration of the travelling wave nature of the FGF8 profile in the PSM 109

5.9 Comparison between the analytical and approximate solutions for the bead profile . 110

5.10 The progress of the determination front along the AP axis as key parameters are varied 112

5.11 The progress of the positions of the discontinuities of the Heaviside functions for u and v 113

5.12 The progress of the positions of the discontinuities of the Heaviside functions for u and v as ϕ the strength of the bead source is varied 115

5.13 Numerical solution of the FGF8 model for somite formation showing the spatio-temporal dynamics of the somitic factor, the signalling molecule and FGF8 117

5.14 Numerical solution of the FGF8 model with a weak source of FGF8 118

5.15 Numerical solution of the FGF8 model with a medium source of FGF8 119

5.16 Numerical solution of the FGF8 model with a strong source of FGF8 120

5.17 Illustration of the somite anomalies formed with local application of FGF8 121

6.1 Perturbing the FGF8 profile 124

6.2 Numerical solution of the FGF8 model with the rate of axis elongation decreased . 125

6.3 The anomalies formed with application of SU5402 126

6.4 An illustration of the anomalies formed with SU5402 127

6.5 Numerical solution of the FGF8 model with application of SU5402 129

7.1 Expression patterns of RA and FGF8 in the PSM 132

7.2 RA/FGF8 feedback loop 133

7.3 The RA/FGF8 feedback mechanism . . . 134
7.4 The full RA/FGF8 system . . . 139
7.5 The domains of the inner and outer solutions . . . 144
7.6 The inner solution . . . 147
7.7 The '*Outer system* - $\mathcal{O}(1)$ . . . 150
7.8 Comparison between numerical solution of the outer system and the full system . . . 151

8.1 Global stability in Case 4 . . . 160
8.2 Phase planes for the 2-species competition model . . . 161
8.3 Roots and critical points of the polynomial $\bar{p}$ . . . 163
8.4 Travelling wave for 2-species competition model Case 2 . . . 165
8.5 Travelling wave for 2-species competition model Case 4 . . . 166
8.6 Nullclines for the general model with $n_a, n_f = 1$ . . . 167
8.7 Phase planes for the general model with $n_a, n_f = 1$ . . . 170
8.8 Travelling wave for general model with $n_a = n_f = 1$ - Case 2 . . . 174
8.9 Travelling wave for general model with $n_a = n_f = 1$ - Case 4 . . . 175
8.10 The nullclines for the most general case . . . 176
8.11 Phase planes for the general model with $n_a, n_f \neq 1$ . . . 177
8.12 Travelling wave for general model with $n_a, n_f \neq 1$ - Case 2 . . . 178
8.13 Travelling wave for general model with $n_a, n_f \neq 1$ - Case 4 . . . 178
8.14 Case 5 and Case 6 phase planes for the general model with $n_a, n_f \neq 1$ . . . 179
8.15 The minimum wave speed . . . 181

A.1 An illustration of a regular finite difference grid in x and t . . . 186
A.2 The method of lines . . . 187
A.3 Construction of a unique polynomial interpolating the points $v^n, \ldots, v^{n+s}$ . . . 189
A.4 A diagram illustrating Simpson's method . . . 195

E.1 The transcendental equation for B_1 . . . 202
E.2 The steady states of the outer equations with $c_n = 0$ . . . 204
E.3 The steady states of the outer model with $c_n \neq 0$ . . . 209
E.4 The $\mathcal{O}(1)$ and $\mathcal{O}(c_n)$ steady state profiles of the extracellular RA concentrations . . . 212
E.5 Percentage error between the NAG solution and the '*Outer system* - $\mathcal{O}(1)$, *rescaled* x, *non-zero* c_n, *travelling wave* . . . 213

List of Tables

3.1 A summary of the approximate solutions for u 62

7.1 A summary of the inner solution 153

7.2 A summary of the outer solution 154

A.1 A table showing the values of the coefficients for the various BDFs 190

E.1 The solutions for the '*Outer system - $\mathcal{O}(1)$, rescaled x, zero c_n* 203

E.2 The '*Outer system - $\mathcal{O}(1)$, rescaled x, non-zero c_n, travelling wave - $\mathcal{O}(1)$*' 208

E.3 The solutions for the '*Outer system - $\mathcal{O}(1)$, rescaled x, non-zero c_n, travelling wave - $\mathcal{O}(c_n)$*' 211

Chapter 1

Introduction

Somitogenesis is a complex mechanism that results in the sequential production of a periodic pattern along the antero-posterior (AP) axis of vertebrate embryos. Somite formation is one of the most obvious examples of the patterning processes that take place during embryogenesis and is perhaps a leading candidate in developmental biology for a study that aims to couple recent findings at the molecular level with the classical observations at the cell and tissue level. As such, somitogenesis may be thought of as serving as an important model for investigating multi-scale effects in general. Some of the processes involved include the role of biological clocks, gene expression, cell differentiation and cell-cell signalling [50, 51].

1.1 Biological background

In brief, the process of early embryonic development occurs as follows: immediately after fertilisation the process of cleavage begins. A series of rapid mitotic cell divisions takes place so that the zygote becomes transformed into numerous smaller cells which are called blastomeres; the embryo is collectively termed the blastula in this developmental stage. Then the rate of cell division slows, cells begin to become motile and one of the most important processes of early development, gastrulation, takes place. This involves a series of extensive cell rearrangements during which the three germ layers are laid down: the ectoderm, endoderm and mesoderm. The ectoderm forms the outer layer of the embryo and goes on to form cells of the epidermis and the nervous system. The endoderm is the inner layer and later forms the inner lining of the digestive tube and its associated organs, the liver and the pancreas for example. The mesoderm, in which we will be interested in this work, is the middle of the three layers and will become part of several organs (the heart, kidneys etc.), the connective tissues (bones, muscles, tendons etc.) and also the blood cells. Once the germ layers are laid down, the cells interact and the bodily organs are laid down in a process called organogenesis [20, 62]. Figure 1.1 shows a picture of a mouse embryo at 9.5 days post fertilisation. At this stage there are approximately 21-29 somite pairs which can be seen along the tail of the embryo, and condensation of the forelimb bud is becoming apparent just below the head.



Figure 1.1: A mouse embryo at 9.5 days post fertilisation. The scale bar indicates approximately 500 microns. Image courtesy of P. M. Kulesa, Stowers Institute.

In the mesoderm of the chick, events leading to the formation of somites begin when the notochord is laid down as Hensen's node regresses along the AP axis with the primitive streak. The notochord directs the formation of the neural tube, which is the precursor of the brain and the spinal chord. Soon after the notochord is laid down, mesodermal cells migrate laterally to form thick bands of cells which run longitudinally along each side of the embryo. This tissue is known as the paraxial or presomitic mesoderm (PSM), or the segmental plates in the chick. The posterior ends of the PSM move caudally along with the node. More cells are added to the PSM due to cell division within the plate and cells entering from the node.

Soon after the PSM forms, the process of somitogenesis begins; cells in the PSM undergo changes in their adhesive and migratory properties and condense together to form epithelial blocks of cells which are known as somites. The somites bud off from the PSM at regular intervals, the first forming at the anterior-most end and with subsequent somites forming in a strict AP sequence [21, 56, 57]. They are approximately regular in size, occur in pairs and lie on either side of the notochord. Figure 1.2 provides a view along the AP axis of a chick embryo during somite formation. This budding of somites compensates for the addition of cells via cell division and the node, and keeps both segmental plates approximately constant in length, so that they appear to move down the AP

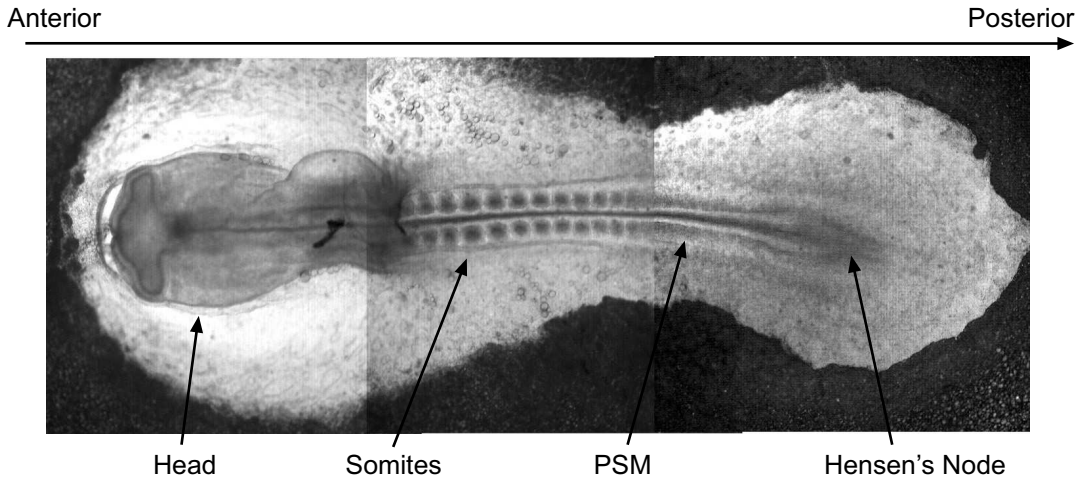


Figure 1.2: A chick embryo with about 10-12 somites clearly visible. The embryo is about 40 hours post fertilisation and approximately 5mm in length. Image courtesy of P. M. Kulesa, Stowers Institute.

axis leaving somites in their wake. The pattern is in fact static in the trunk of the chick during somitogenesis, with cells moving up through it as they develop. The somites are clearly visible in the figure.

Somites are divided by a fissure into anterior and posterior halves and they are approximately regular in size, occur in pairs and lie on either side of the notochord. Somite formation shows capacity for global regulation, the ability to achieve constant proportions despite wide variation among individuals in the amount of tissue available whilst the pattern is forming: the variability of somite number within a species is less than 5% [5]. About 50 somites will form in the chick, 65 in the mouse and as many as 400 in some species of snake [20]. Figure 1.3 shows a picture of chick somites with the notochord running between the pairs. Each chick somite is approximately 100 microns in length.

Shortly after the somites form, they divide up into three components: (i) the sclerotome, which goes on to form the vertebrae and the ribs, (ii) the dermomyotome which forms the dermis of the dorsal (inner layer) skin and (iii) the myotome, which forms the musculature of the back, abdominal organs and limbs. The sclerotomes of the five anterior-most somites contribute to the occipital bone, while the remainder are the precursors of the vertebral arches, bodies and ribs [21]. Figure 1.4 shows a series of cross-sections through the embryo as development proceeds.

1.2 Experimental observations

Genetic or environmental factors can disturb somitogenesis and affect somite size, and there are many recognised clinical conditions that can occur as a result. In humans, disturbance of the somitogenic processes can cause abnormal segmentation of the vertebral column leading to a number of defects as found in Klippel-Feil syndrome, Spondylocostal Dysostosis, Jarcho-Levin syndrome,

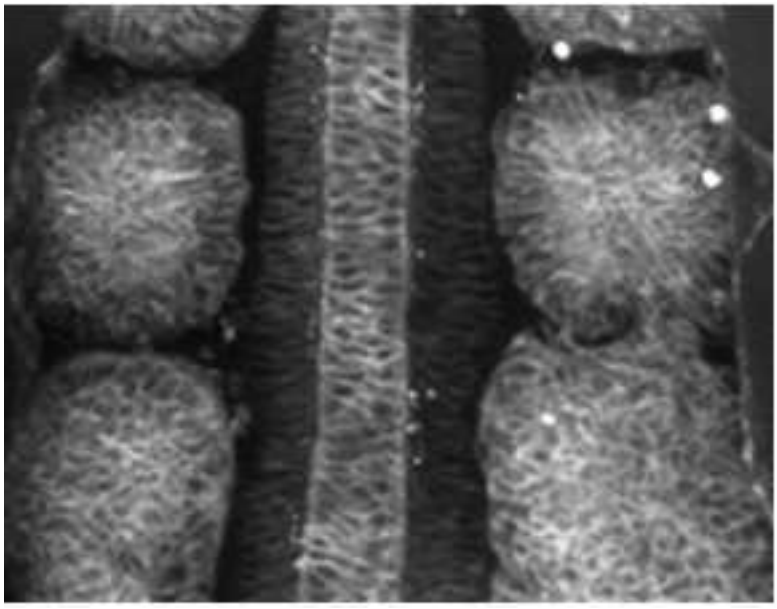


Figure 1.3: A magnified chick embryo. The somites and the notochord are clearly visible. Each somite is approximately 100 microns in length. Image courtesy of P. M. Kulesa, Stowers Institute.

Congenital Scoliosis and Kyphosis, Goldenhar syndrome, among others [43, 57]. The nature and extent of the malformations produced depend on the stage of somitogenesis and include many defects such as vertebral fusion and failure of vertebral formation. Studying the developmental mechanisms in vertebral patterning will aid in the identification of protective or potentially disruptive factors for normal somitogenesis, and could lead towards treatments for the prevention of vertebral patterning disorders.

1.2.1 Heat shock

Heat shock is one such environmental factor that is known to disturb somitogenesis. Initial experiments conducted in the late 1980s reported that transient heat shock application to two day old chick embryos [44, 45] can cause up to 4 discrete, periodic somite anomalies, each restricted to 1 or 2 contiguous segments. Distances between the repeated anomalies were found to be about 6-7 somites, or multiples of this distance, with the first anomaly occurring at a distance of 6-7 somites after the last formed at the time of the heat shock, and the anomalies extending for a maximum distance of 26 somites posterior to this somite. The anomalies caused by heat shock manifest themselves as small, fused or abnormally large somites, and are caused by an alteration in the number of cells that make up each somite. Somite formation in a heat shocked embryo falls back in line with a control case outside the affected region. Figure 1.5 illustrates the periodic character of anomalies formed upon application of heat shock.

Stern and co-workers used their experimental findings to suggest that heat shock affects an oscil-

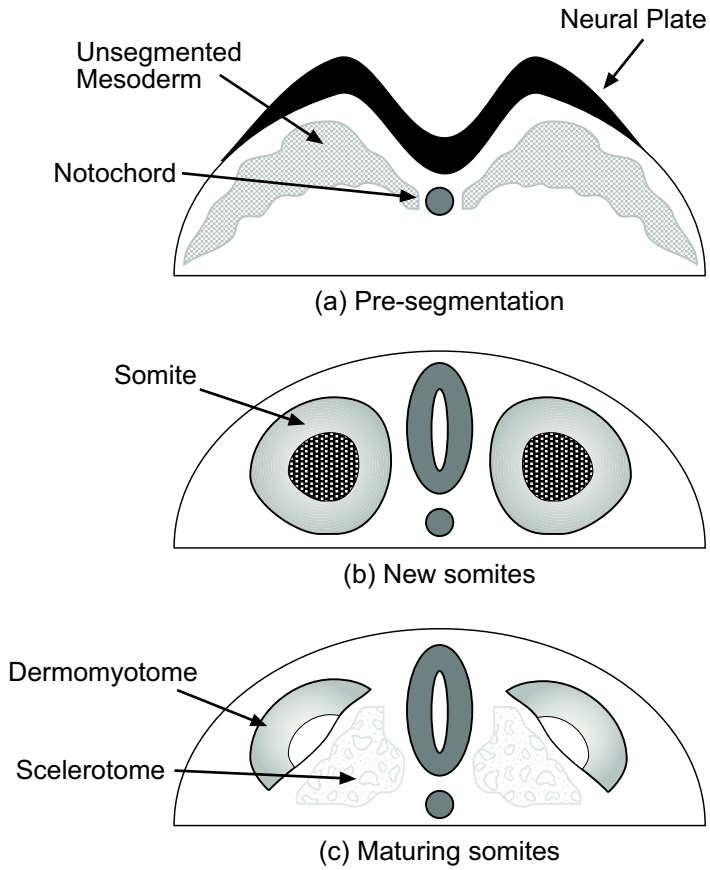


Figure 1.4: An illustration of the vertebrate embryo during somite formation. (a) Cross-section of the embryo before somite formation occurs. The unsegmented mesoderm, or presomitic mesoderm (PSM) lies on either side of the notochord. (b) Somites form in pairs - one each side of the notochord. (c) Somites mature and divide up into 3 components - the dermomyotome and sclerotome are shown here. Reproduced with modifications from [18].

latory process within the somite precursor cells [44, 45, 55] since six to seven somites correspond to one cell cycle worth of PSM cells. Experiments by Primmett and co-workers also suggested that similar periodic anomalies in somite formation could also be caused by drugs inhibiting cell-cycle progression [44].

Stern and co-workers' experiments have been repeated using more modern technology and the results of the heat shock experiments are now less widely recognised [42]: it is not clear whether the cell cycle is the sole factor involved in somitogenesis that is disrupted by heat shock. We also note that recent experiments using BrdU labelling (S-phase) or phosphorylated histone H3 (M-phase) were not able to detect obvious coordination of cell cycles in the PSM [42].

Early in this work, we detail the various models for somitogenesis and their extensions to include the effects of heat shock. Some of these models use the now redundant hypotheses of Stern, Primmett and co-workers as their basis. However, we feel that each model can still provide useful insights into somite formation and should not be discarded in its entirety.

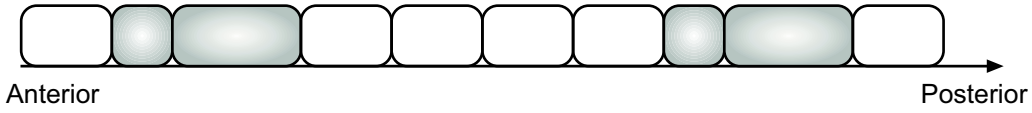


Figure 1.5: An illustration of the periodic somite anomalies that may be caused by application of heat shock.

1.2.2 Gene perturbation

Perturbation of several genes expressed in the PSM has also been shown to affect somite formation. Mutations for *Notch1*, *RBPJK*, *Dll1*, *l-fng* have somites with irregular size and shape and the anterior-posterior (AP) polarity of somites is also affected [9]. During the time taken for one somite to form, expression of *c-hairy-1* and *l-fng* appears to sweep along the PSM in the posterior-anterior direction, narrowing as it moves, until it comes to rest in the posterior half of the forming somite [27, 37]. This wavefront-like expression activates several genes of the Notch/Delta pathway [9, 22].

Taking all the above evidence into account, it seems very likely that somite and somitic boundary formation is controlled by one or more segmentation clocks: it is thought that Lfng establishes a negative feedback loop which implements periodic inhibition of Notch and results in the rhythmic expression expression of these cycling genes [7]. This feedback loop provides a molecular basis for the oscillator underlying the avian segmentation clock. However, it is not yet known whether the major role of *c-hairy-1* and *l-fng* is in the allocation of cells to individual somites or rather in the subdivision of somites into anterior and posterior compartments [4].

1.2.3 FGF8 signalling

Recently, Dubrulle and co-workers [15] have used experimental findings to suggest that in fact it is an interaction between FGF8 signalling and the segmentation clock that controls somite size. The segmental plate is not a homogeneous tissue, but consists of two distinct parts, one in which somite formation has begun; cells have become committed to form part of a somite and are fixed with respect to their AP polarity, and the other in which the cells are not committed or are immature [15, 47]. These two regions are divided by their level of FGF8 signalling: low in the anterior region where segmentation has begun and high in the posterior region where it has not. The border which separates the two regions of the PSM is known as the *determination front*, and this moves in a posterior direction along with the node so that it remains at a constant position within the PSM as it regresses along the AP axis. Local application of FGF8 by implantation of a bead soaked in FGF8 into one side of the PSM results in the formation of a sequence of abnormally sized somites. The sequence consists of several abnormally small somites followed by an abnormally large somite, extending for up to 6-7 somites, and such that the sequence falls back into register with the unaffected side of the embryo. The hypothesis is that this is a direct result of the displacement of the determination front from its constant axial position by a change in FGF8 signalling. Figure 1.6 il-

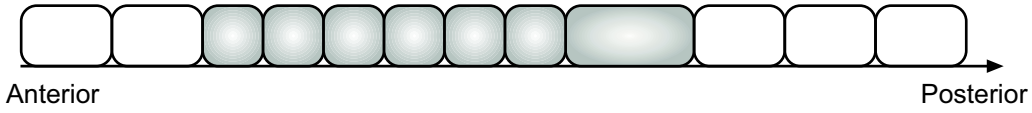


Figure 1.6: An illustration of the somite anomalies that may be caused by local application of FGF8. A bead soaked in FGF8 is implanted next to the PSM between the abnormally large and abnormally small somites.

lustrates the type of anomalies formed upon local application of FGF8. The role of FGF8 in somite formation is discussed in more detail in Chapter 4.

1.3 Models for somite formation

Over the past three decades there have been a number of models [6, 23, 30, 38, 49] proposed to account for somite formation. The role of modelling is to provide insight as to how complex biological processes may be coupled to produce experimentally observed behaviour. However, a model is a partial representation of reality and therefore cannot account for all experimental observations [49, 51]. Below, we consider four of the more widely used models for somitogenesis.

1.3.1 Clock and wavefront model for somitogenesis

In [6] and [63], Cooke and Zeeman propose a clock and wavefront model to explain somite formation. They postulate the existence of a longitudinal *positional information* gradient down the AP axis of the embryo which determines regional development by setting the time in each cell at which it will undergo a *catastrophe*. By catastrophe, they mean a rapid change of state, which could possibly be the change in adhesive behaviour of cells when they become able to form somites. The "clock" is a smooth cellular oscillator, which interacts with the wavefront, periodically inhibiting or altering its passage down the axis. The integration of the clock and the wavefront would gate the PSM cells into groups to segment together, producing a periodic pattern of somites. Figure 1.7 illustrates the way in which cells are recruited into somites in the clock and wavefront model.

Discovery of the periodic expression of *c-hairy-1* and several other genes related to Notch signalling in the PSM provides molecular evidence for the existence of a clock in the PSM [37]. Dubrulle and co-workers [15] propose that the transit of cells from the posterior (FGF8 expressing) part of the PSM to the anterior (non-expressing) part of the PSM is able to constitute the wavefront of Cooke and Zeeman's model. Since the discovery of the cycling genes in the PSM, the clock and wavefront model has generally been favoured for explaining somitogenesis and with Dubrulle et al.'s discovery of the FGF8 defined determination front, many authors have proposed extensions to the clock and wavefront model for somite formation [15, 43, 46].

In the clock and wavefront model, somite size is a function of the frequency of the segmentation

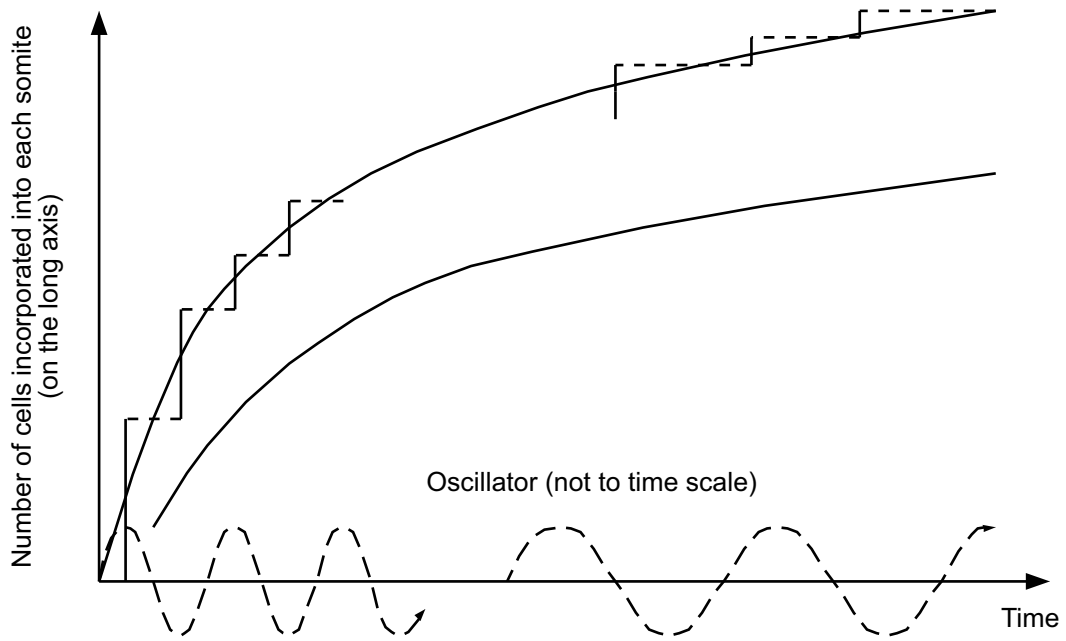


Figure 1.7: An illustration of the way in which cells are recruited into somites in the clock and wavefront model. The hypothetical oscillator advances and retards the recruitment of cells into somites so that the curve is manifest as a step function with the vertical components representing the synchronous adhesion of blocks of cells to make somites. The curve slope (cells per unit time) decreases slightly as time progresses as later somites are smaller and form slightly less often [6]. The lower curve is one that may be expected from a size reduced embryo. Reproduced with modifications from [6].

clock and also of the velocity of the maturation wavefront. An increase in the size of somites could be caused by either a slowing down of the oscillation of the clock, while the speed of the wavefront is kept constant, or by accelerating the progression of the wavefront, while keeping the period of the clock oscillations constant. The former is not a feasible explanation for the observed change in somite size on application of FGF8 since implantation of an FGF8 soaked bead into the PSM causes no asynchrony in the timing of somite boundary formation and the period of the cycling genes is not affected by the bead graft [15]. The latter seems to be a possible explanation that is consistent with experimental evidence; advancing the wavefront through inhibition of FGF8 signalling would cause the determination front to be displaced more caudally, and hence result in the formation of a larger somite. The reverse would apply for the formation of an abnormally small somite.

1.3.1.1 Consistency with experimental evidence

In its original form, Cooke and Zeeman's model has only a very theoretical basis. However, the cyclic and wavefront-like expression of *c-hairy-1* and *l-fng* is considered to be the result of a *segmentation clock* acting within the PSM cells, and it is possible that the gradient of FGF8 signalling mentioned previously could provide a physical basis for the wavefront. We return to the idea of a "clock and wavefront" model later in this work.

We should also note that according to Vasiliauskas and Stern, "the clock and wavefront model predicts that a simple cranial shift of the wavefront should generate a single small somite, followed by a series of normal somites, followed by a larger somite at a position where the wavefront reverted to normal" [60, p. 136]. This prediction is clearly contradicted by the results of Dubrulle et al. [15] showing the formation of "several small somites ahead of the bead, then a larger somite behind the bead and then normal somites" [60, p. 134]. There is no formal mathematical model of Cooke and Zeeman's "word" model and we show later in this work that if a mathematical model (with a clock and wavefront basis) is used to predict somite formation, the results of Dubrulle and co-worker's experiments can be reproduced.

1.3.2 Wave/cell polarisation model for somitogenesis

Polezhaev [38, 39, 40] proposed a model for segmentation in which a wave of cell determination travels down the AP axis of the embryo and interacts with the cell cycle in such a way as to produce a metameric spatial distribution of a few polarised cells, which are known as "centres of determination". Such centres of determination spread the polarised state by the mechanism of contact polarisation.

The model is based on the following assumptions: (i) A mesodermal cell can be polarised only once a wave of somitic determination has passed, and only at a certain stage of its cell cycle. (ii) Polarised PSM cells secrete an inhibitor. Surrounding non-polarised PSM cells can only become polarised themselves [subject to the conditions in (i)], if the level of inhibitor is below a critical threshold. (iii) A cell reacts to changes in the concentration of inhibitor with a certain time lag.

1.3.2.1 Mathematical formulation of the wave/cell polarisation model

The model considers the density of polarised PSM cells, a, and the concentration of an inhibitor, h, in one space dimension, $x \in [0, L]$, with zero flux boundary conditions for the inhibitor:

$$\begin{aligned} \frac{\partial a}{\partial t} &= \frac{M}{T} H(vt - x) H(h_0 - h(t - t_0)), \\ \frac{\partial h}{\partial t} &= ka - dh + D\frac{\partial h^2}{\partial x^2}, \end{aligned}$$

with

$$a(0, x) = 0 = h(0, x) \quad \text{for} \quad x \in [0, L],$$

and

$$\frac{\partial h}{\partial t}(t, 0) = 0 = \frac{\partial h}{\partial t}(t, L).$$

$H(x)$ is the Heaviside function;

$$H(x) = \begin{cases} 1 & \text{if } x \geq 0, \\ 0 & \text{if } x < 0, \end{cases}$$

and M, T, v, h_0, t_0, k and d are positive constants. The transition of PSM cells into a polarised state takes place at a constant rate. M is the initial density of mesodermal cells, T is the period of their cycle and h_0 is the critical threshold of inhibitor. The transition into the polarised state ceases, with time delay equal to t_0, after the moment at which the inhibitor level reaches the threshold level h_0. The inhibitor is produced by polarised cells at a constant rate k, decays and/or dissipates at a constant rate d and diffuses longitudinally with rate D. The length of a somite is taken to be of magnitude $l \ll L$.

The system can be non-dimensionalised using the following substitutions:

$$\alpha = \frac{a}{A}, \quad \chi = \frac{h}{H}, \quad \tau = \frac{t}{t_0}, \quad \rho = \frac{x}{l},$$

where

$$A = \frac{Mt_0}{T} \quad \text{and} \quad H = \frac{kmt_0}{dT}.$$

Assuming that d is mostly determined by dissipation of the inhibitor through transverse diffusion, then it can be evaluated as $d \approx D/l^2$, where l is the cross-sectional size of the PSM. The resulting non-dimensional equations are

$$\begin{aligned} \frac{\partial \alpha}{\partial \tau} &= H(\nu\tau - \rho)H(\chi_0 - \chi(\tau - 1)), \\ \frac{\partial \chi}{\partial \tau} &= \beta\left(\alpha - \chi + \frac{\partial \chi^2}{\partial \rho^2}\right), \end{aligned}$$

where ν, χ_0 and β are positive parameters with $\beta \gg 1$.

After a fast initial transient stage, χ will reach a quasi-equilibrium where

$$\frac{\partial \chi^2}{\partial \rho^2} - \chi \approx -\alpha.$$

Solving the above using Green's functions and the assumption that $l \ll L$,

$$\chi(\rho) \approx \frac{1}{2}\int_{-\infty}^{\infty} \alpha(\rho')e^{-|\rho-\rho'|}\, d\rho',$$

for ρ away from the boundaries $\rho = 0, L/l$. This gives a final equation for α of the form

$$\frac{\partial \alpha}{\partial \tau} = H(\nu\tau - \rho)H\left(\chi_0 - \frac{1}{2}\int_{-\infty}^{\infty} \alpha(\tau - 1, \rho')e^{-|\rho-\rho'|}\, d\rho'\right).$$

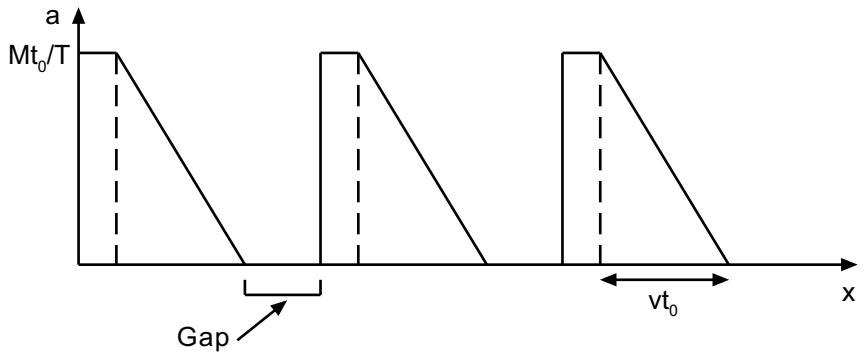


Figure 1.8: An illustration of the distribution of polarised PSM cells as envisaged by the wave/cell polarisation model. Notice that cells in the region marked 'Gap' never polarise as the threshold level of inhibitor is exceeded at time $t \geq t_0$ before the wave of cell determination passes. The x axis corresponds to the AP axis of the embryo, with cells located more posteriorly being situated further along the axis.

Polezhaev has analysed the above equation both analytically and numerically [38, 39, 40]. When both χ_0 and v are reasonably small, the equation generates a periodic pattern of PSM cells along the AP axis.

We can see how the model works by considering the progress of the wave of somitogenic cell determination down the AP axis of the embryo. Cells which have a level of inhibitor below the threshold h_0 will start to polarise as the wave of determination passes. This will in turn cause the level of inhibitor to rise sharply in these cells, and almost immediately it will exceed the threshold level. Cells will continue to polarise until time $t = t_0$ after the threshold level has been reached. The inhibitor will diffuse along the AP axis of the embryo and at some point, P, say, it will overtake the wave of determination. For cells a distance $x = vt_0$ below P, the inhibition threshold will have already been exceeded for time t_0 when the wave of determination reaches them and so they will never polarise. Consequently, the next group of polarised cells will only be able to appear outside this region, i.e. at a distance x^* from the previous one (where $x^* > vt_0$). This distance x^* corresponds to the size of the future somite, and in the non-dimensional model given above we should have $x^* = 1$. Qualitatively, the distribution of polarised PSM cells will appear as in Figure 1.8.

Important points that should be noted from the model are:

(i) The inhibitor must diffuse fast enough so that it is able to overtake the wave of somitogenic determination, otherwise we would not get formation of distinct centres of polarisation as illustrated in Figure 1.8.

(ii) The time lag t_0 must be less than the time taken to form one somite.

(iii) The model predicts that the maximum density of polarised cells is only about Mt_0/T. Using the parameters estimated in [38] we can see that approximately only 5% of cells become polarised initially: it is proposed that these *centres of polarity* grow by contact cell polarisation to form somites.

1.3.2.2 Consistency with experimental evidence

Explanation of Heat Shock Effects Polezhaev's model assumes that PSM cells are not synchronised with respect to their cell cycle. Therefore, cells at any level are uniformly distributed throughout their cycle. In normal circumstances cells become polarised at a constant rate M/T, but if partial synchronisation occurs, for example when heat shock holds up the passage of cells throughout their cycle, then the rate of transition to the polarised state will cease to be constant. In [39], Polezhaev suggests the following revised equations to account for heat shock:

$$\begin{aligned} \frac{\partial \alpha}{\partial \tau} &= H(\nu\tau - \rho)H(\chi_0 - \chi(\tau - 1))H(\text{mod}(\tau|T/t_0) - \Delta\tau), \\ \frac{\partial \chi}{\partial \tau} &= \beta\left(\alpha - \chi + \frac{\partial \chi^2}{\partial \rho^2}\right), \end{aligned}$$

where T/t_0 is the dimensionless duration of the cell cycle and $\Delta\tau$ is the duration of the heat shock. Numerical simulations [39] of the above equations show periodic repeated anomalies consisting of abnormally large somites but no abnormally small somites.

FGF8 signalling in the PSM It is possible that the FGF8 determination front could constitute the *wave of somitogenic cell determination* proposed in the wave/cell polarisation model. Consider local application of FGF8 by implantation of a bead next to the PSM: anterior to the bead there would be an increase in the rate at which the wave of cell determination moved down the AP axis, and *vice versa* posterior to the bead. This would produce abnormally small somites anterior to the bead and abnormally large somites posterior to the bead, as observed experimentally. One condition for the formation of distinct somites would be that the increased rate at which the wave of cell determination moves down the AP axis would still be slower than the rate at which the inhibitor diffused along the PSM.

1.3.3 Reaction-diffusion model for somitogenesis

Meinhardt [31] proposed a reaction-diffusion model to account for somite formation. He assumed that cells can be in one of two possible states, denoted by **a** and **p** and that these states correspond, respectively, to the anterior and posterior halves of somites. If a cell is in state **a**, then the genes that are responsible for synthesis of a substance A are turned on and similarly for a cell in state **p** and a corresponding substance P. The states **a** and **p** are such that they locally exclude each other, but stimulate each other over a long range. Cells will switch from one state to another until they reach a stable state. In this way a pattern of stable **apap...** stripes is formed in the AP direction. The transition from A expressing cells to P expressing cells, say, would constitute a change of segmental specification: it may be that the anterior and posterior halves of the somites could be represented by the expression of A and P. Each **ap** pair or segment would be specified more posteriorly than its predecessor, resulting in the specification of somites with different regional characteristics.

Meinhardt [31] proposes two mechanisms for controlling the switch between states. The first in-

volves the presence of a morphogen gradient which would increase from anterior to posterior along the axis of the embryo. Under the influence of the morphogen gradient, cells would begin to oscillate between the states **a** and **p**, the number of oscillations achieved being controlled by the local morphogen concentration. Cells would count the number of oscillations between **a** and **p** states, and more oscillations would lead to a more posterior specification. This is illustrated in Figure 1.9.

The second involves domain outgrowth. Growth is assumed to take place posteriorly and new cells are assumed to be in the same state as their neighbours when they are incorporated into the PSM. Whenever the distance to a boundary becomes too large, a switch to the alternate state takes place. With each A $\rightarrow$ P transition, activation of a subsequent gene takes place.

1.3.3.1 Mathematical formulation of the reaction-diffusion model

Meinhardt has suggested several possible mathematical models which can describe the generation of periodic patterns such as somites [30, 31]. The embryonic axis extends during somite formation, so here we present a mathematical formulation of the outgrowth model rather than the morphogen gradient model.

Domain and independent variables Meinhardt considers the problem in one spatial dimension, with x representing distance down the AP axis and t representing time. The x domain is taken to be the interval $[0, d(t)]$, and assuming that Hensen's node (and therefore the pattern) moves down the AP axis with constant speed c, $d(t) = d(0) + ct$.

Switch between a and p states and the dependent variables Cells must be in one of the mutually exclusive states **a** or **p**. The model must display the following observed properties of somites:

(i) The **apap...** pattern must be stable, since once they are formed, somites retain their polarity.

(ii) The **a** - **p** borders must be very sharp as there are no intermediate cells,

(iii) Somites are roughly of the same size within an embryo.

Let $a(x,t)$ and $p(x,t)$ represent the concentrations of the substances A and P, which cause the cells to be in the states **a** and **p** respectively. The equations in a and p must be symmetric as the states **a** and **p** each make up half a somite. To ensure that the pattern is maintained once it is set up [(i) above] each substance must be autocatalytic. The stripe-like pattern is possible if each substance stimulates the other over long range. This is achieved in the model by assuming the existence of diffusive chemicals S_a and S_p with concentrations $s_a(x,t)$ and $s_p(x,t)$ respectively. S_a is produced by cells in state **a** and catalyses the production of P and *vice versa*. S_a and S_p are assumed to diffuse, degrade linearly and have a constant background rate of production.

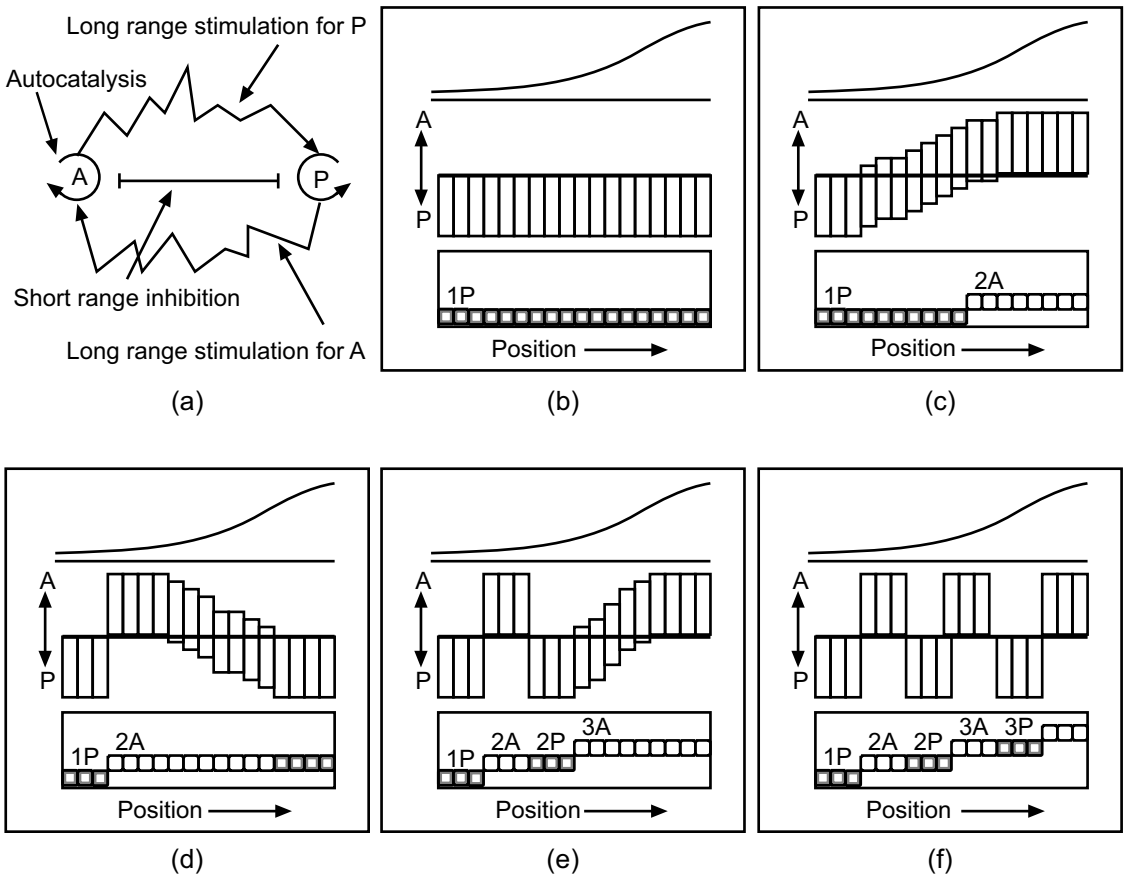


Figure 1.9: An illustration of the stages involved in somite formation, as envisaged in Meinhardt's model. (a) The short range inhibition, long range stimulation feedback loop necessary for such pattern formation to take place. (b) – (f) The stages involved in pattern formation: in each subfigure, the top diagram illustrates the level of morphogen gradient present, the middle diagram illustrates the state of cells with respect to synthesis of the mutually exclusive substances A and P and the bottom diagram illustrates the subsequent gene expression along the AP axis. (b) Initial conditions: all cells are in the state P and gene 1 is turned on. (c) All cells exposed to a certain morphogen gradient switch to the A state and from gene 1 to gene 2 expression. (d) P - A border is formed as cells switch back to the P state. (e) The gene switch occurs as a second A - P border is formed. (f) The final steady state - a periodic pattern of APAP... expression, with corresponding sequential pattern of gene activation 1234..... Reproduced with modifications from [31].

1.3.3.2 Common repressor model

The first model that Meinhardt proposes involves the presence of a common repressor R which has concentration $r(x,t)$. High concentrations $a(x,t)$ and $p(x,t)$ of A and P, respectively, activate production of the repressor, which in turn inhibits both A and P production. The equations for this

model are

$$\begin{aligned}
\frac{\partial s_a}{\partial t} &= \mu a - \lambda s_a + D_s \frac{\partial^2 s_a}{\partial x^2} + \sigma_s, \\
\frac{\partial s_p}{\partial t} &= \mu p - \lambda s_p + D_s \frac{\partial^2 s_p}{\partial x^2} + \sigma_s, \\
\frac{\partial a}{\partial t} &= \frac{k_a s_a a^2}{r} - \kappa a + D \frac{\partial^2 a}{\partial x^2} + \sigma, \\
\frac{\partial p}{\partial t} &= \frac{k_p s_p p^2}{r} - \kappa p + D \frac{\partial^2 p}{\partial x^2} + \sigma, \\
\frac{\partial r}{\partial t} &= k_a s_a a^2 + k_p s_p p^2 - \nu r,
\end{aligned}$$

where μ, λ, σ_s, σ, k_a, k_p, κ, ν, D_s and D are positive constants. In the above equations, the term $k_a s_a a^2/r$ ($k_p s_p p^2/r$) represents autocatalysis of A (P), with inhibition by R. Both substances A and P are linearly degraded with a constant rate λ, diffuse and are produced at constant rate σ_s. Production of the common repressor R is catalysed by production of A and P and it undergoes linear degradation with constant rate ν. R is not allowed to diffuse so that stable stripes of A and P expressing cells can co-exist.

1.3.3.3 Direct inhibition model

The second model assumes that A and P inhibit each other directly. The equations for this model are

$$\begin{aligned}
\frac{\partial s_a}{\partial t} &= \mu a - \lambda s_a + D_s \frac{\partial^2 s_a}{\partial x^2} + \sigma_s, \\
\frac{\partial s_p}{\partial t} &= \mu p - \lambda s_p + D_s \frac{\partial^2 s_p}{\partial x^2} + \sigma_s, \\
\frac{\partial a}{\partial t} &= \frac{k_a s_a}{\epsilon + p^2} - \kappa a + D \frac{\partial^2 a}{\partial x^2} + \sigma, \\
\frac{\partial p}{\partial t} &= \frac{k_p s_p}{\epsilon + a^2} - \kappa p + D \frac{\partial^2 p}{\partial x^2} + \sigma,
\end{aligned}$$

where μ, λ, σ_s, σ, k_a, k_p, κ, ϵ, D_s and D are positive constants. In the above equations $k_a s_a/(\epsilon + p^2)$ ($k_p s_p/(\epsilon + a^2)$) represents long range activation of A (P) by the diffusive chemical S_a (S_p) with inhibition by P (A). This leads to mutual exclusion of the two states. Notice that the autocatalysis of A and P is indirect in this model.

1.3.3.4 Consistency with experimental evidence

Evidence supporting Meinhardt's model comes from the expression of *c-hairy-1* in the PSM [8]. As a newly formed somite buds off from the PSM, its anterior half is devoid of *c-hairy-1* expression, whilst the posterior half continues to maintain *c-hairy-1* expression. Cells may "oscillate between

anterior (*c-hairy-1* off) and posterior (*c-hairy-1* on) states, which become stabilised in the anterior PSM" [8]. Meinhardt's model is currently the only one that addresses anterior/posterior somite subdivision. We should also note that the FGF8 gradient shown to be present in the PSM could constitute the positional information gradient required by the cells in order for the pattern to start forming. However, the model would need to be extended to include the effects of perturbation of FGF8.

1.3.4 Cell cycle model for somitogenesis

The cell cycle model of Stern and co-workers [44, 45, 55] links the cell cycle with somite segmentation. The main observations on which the hypotheses of this model are based include the following: (i) The time interval between specification of successive presumptive somites is approximately 90 – 100 minutes, equivalent to one seventh of the cell cycle (9 – 10 hours). (ii) There exist discrete regions of cell synchrony in the PSM. (iii) Application of single transient heat shock to chick embryos blocks the cell cycle. This causes several somitic anomalies, each separated by distances of 6-7 normal somites.

It is important to note that the cell cycle model does not assume that cells are in perfect synchrony in the PSM, but that there is some degree of cell synchrony between cells in the PSM. This implies that a small *seeding* subpopulation of cells in each region could establish the somite pattern and that the remaining cells are induced by these to give the remaining pattern.

The model proposes that cells destined to form somites leave Hensen's node in the strict order in which they are derived from stem cells in the node. This ensures that there is a certain amount of cell cycle synchrony among cells in the PSM, with cells lying more anteriorly in the PSM being more mature than those lying in the posterior parts. Cells remain in this strict order, so that there is some degree of cell cycle synchrony observed in cells destined to form a potential somite together.

Stern and co-workers conjecture the existence of two points, P_1 and P_2, in the cell cycle of mesodermal cells destined to form somites, which lie 90 minutes apart and between which cells become competent to segment. The synchrony assumption ensures that a small fraction of the cells destined to form a somite together will reach the point P_2 in their cell cycle before the others of that potential somite. Upon reaching P_2 this fraction of cells, termed *pioneer cells*, produce and emit a signal along the PSM. Any cell at a point in its cycle between P_1 and P_2 would respond to such a signal by increasing adhesion to neighbouring cells which are responding in a similar manner, forming a potential somite. At this point a cell has been specified as somitic, and it will become refractory to the signal. Specified cells go on to segment and form somites one cell cycle later (see Fig. 1.10). It should be noted that the PSM is made up of two cell cycles worth of PSM cells, and that the cell cycle mechanism acts on the most anterior cell cycle. The physical distance between the two points P_1 and P_2, caused by the cell cycle synchrony along the PSM, corresponds to the actual size of the somites formed.

1.3.4.1 Mathematical formulation of the cell cycle model

In [4, 29], Collier and co-workers propose a mathematical formulation of the cell cycle model presented above, using a coupled system of non-linear partial differential equations. They make the following further assumptions:

(i) Although segmentation starts anteriorly and moves posteriorly, they take an axis fixed with respect to the PSM cells, which means that the pattern can be considered as moving down the AP axis. The length of the PSM is constant and the pattern moves with constant speed c. The consequence of these assumptions is that given points of the cell cycle (for example mitosis) occur at fixed points within the pattern.

(ii) The signal emitted at P_2 takes the form of a pulse: it is short-lived and diffuses rapidly throughout the domain. This ensures that only cells in the P_1–P_2 time window can respond to the signal, and that all such cells do respond.

(iii) Somites are being formed continually; that is, we are not considering the beginning or the end of the process.

They develop the model in one spatial dimension (the AP axis) and focus upon one side of the embryo (evidence supporting the independence of the different axial sides of the PSM comes from [24, 61]). The two state variables which the system describes are a *somitic factor* (u) which is integral in determining the fate of the cell (only cells with a high level of the factor will be specified as somitic), and a *diffusive signalling molecule* (v) produced by the pioneer cells when they reach the point P_2 in their cell cycle. The somitic factor could be a transcription factor or a precursor to an adhesion molecule. x is taken to be distance down the AP axis, with the origin fixed in a given somite, and t measures time.

Collier and co-workers [4] propose the following dimensional model for somite formation:

$$\frac{\partial u}{\partial t} = \frac{(u+\mu v)^2}{\gamma+\rho u^2}\chi_u(x,t) - \nu u, \tag{1.1}$$

$$\frac{\partial v}{\partial t} = \frac{\kappa}{\epsilon+u}\chi_v(x,t) - \lambda v + D_v\frac{\partial^2 v}{\partial x^2}, \tag{1.2}$$

where

$$\chi_u(x,t) = H(ct - x + x_1), \tag{1.3}$$

$$\chi_v(x,t) = H(ct - x + x_2), \tag{1.4}$$

and $\mu, \gamma, \rho, \nu, \kappa, \epsilon, \lambda, D_v, x_1, x_2$, and c are positive constants, with $x_2 < x_1$ and $x_2 - x_1$ = 1. Note that $P_1 \leftrightarrow x_1 + ct$ and $P_2 \leftrightarrow x_2 + ct$. The Heaviside function H is defined to be

$$H(y) = \begin{cases} 1 & \text{if } y \geq 0, \\ 0 & \text{if } y < 0. \end{cases}$$

Taking the embryonic axis to be fixed with respect to the cells, and letting Hensen's node and the PSM move down the axis at constant speed c, we consider the domain

$$0 \leq x \leq d(t), \quad t \geq 0,$$

where $d(t)$ is the position of a point that moves down the embryonic axis with constant velocity c. Figure 1.10 shows a schematic representation of the way in which somites are formed in the mathematical formulation of the cell cycle model. Cells in stage I of development are unable to form somites. Upon reaching stage II they become capable of responding to the signal produced by *pioneer cells* at P_2. Eventually they will reach stage III and become capable of forming somites. Cells become refractory to the signal when they reach stage III.

1.3.4.2 Consistency with experimental evidence

Criticisms have been made of the cell cycle model. For example, Palmeirim and co-workers [37] have argued against the role of the cell cycle as a segmentation clock based on the cycling times of *c-hairy-1* in the PSM. The expression of this gene occurs with a periodicity similar to the time it takes to form a single somite ($\approx$ 90 min.) rather than the observed cell cycle length ($\approx$ 9 hours). However, we do not yet know whether the major role of this gene is in the allocation of cells to individual somites or rather in the subdivision of somites into anterior and posterior compartments [4]. If the latter is true, then somite and somitic boundary formation may be controlled by one or two segmentation clocks. To date, there is no direct link between the cell cycle and *c-hairy-1* oscillations. Nevertheless, there is evidence suggesting that both are regulated by the same type of post-transcriptional modification and therefore could be part of the same clock [50]. In the next chapter, we detail the algorithm of Schnell and co-workers [50] which shows how the cell cycle model can be modified to include the effects of heat shock.

We also note that some of the major assumptions underlying the model are now disputed among experimentalists. However, the basis of the model is that of a signalling process with control of the signal and its subsequent actions being determined by external factors and with suitable modifications, it can still be applied to study somitogenesis.

1.4 Aims of this work

We began this initial chapter by introducing somites and the background events in the development leading up to their formation. We discussed a number of factors that have been hypothesised to effect somitogenesis; in particular the expression of certain genes in the PSM, both dynamic and static, the presence of an FGF8 signalling gradient and finally the effect on somite formation of transient heat shock. With the development of more sophisticated technology, the specificity of the original heat shock experiments was brought into question and recent experiments have shown that heat shock may not target just the cell cycle and that there is little, if any, cell cycle synchrony along the PSM.

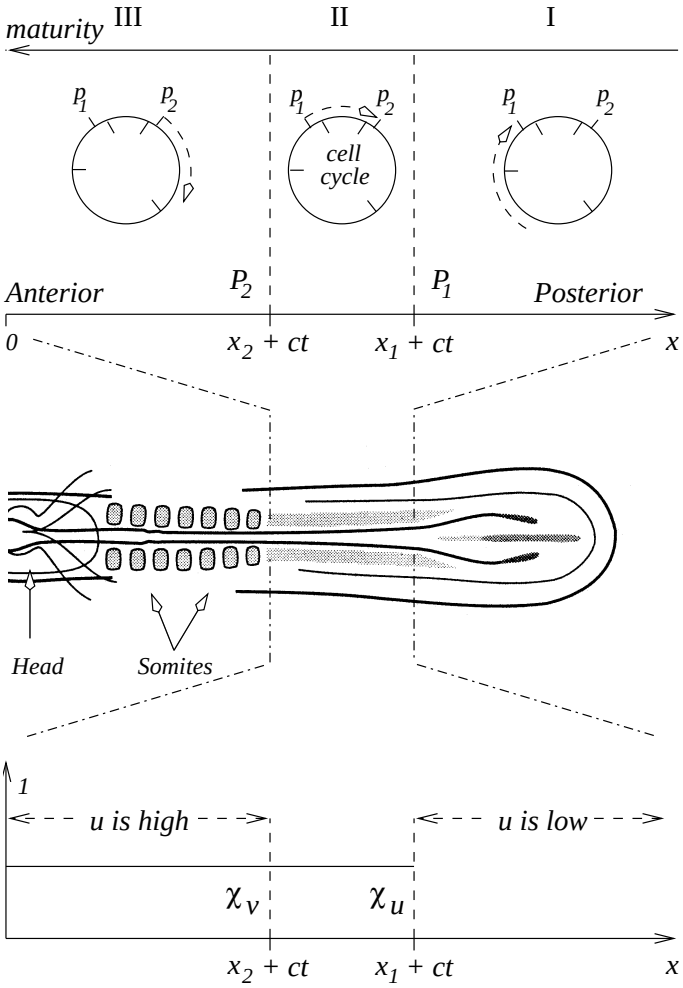


Figure 1.10: Schematic representation of the way in which somites are proposed to form in the cell cycle model. The two points P_1 and P_2 and the three key stages of development are clearly illustrated. Cells in stage I of development are unable to form somites. Upon reaching stage II they become capable of responding to the signal produced by *pioneer cells* at P_2. Eventually they will reach stage III and become capable of forming somites. Cells become refractory to the signal when they reach stage III. Reproduced with permission from [29].

The recent findings on FGF8 and heat shock have shed new light on the validity of the current models for somitogenesis. The FGF8 signalling gradient provides the perfect physical basis for the waves of cell determination hypothesised to exist in the clock and wavefront, reaction-diffusion and wave/cell polarisation models. The repetition of Stern and co-workers heat shock experiments has also weakened the grounds for including the cell cycle model as a valid model for somite formation. However, we can still consider using the mathematical formulation of the cell cycle model as the basis for a signalling model in which the signal and its effects are controlled by external factors. Experimental evidence strongly suggests that somites are formed through the interaction of a segmentation clock and a wavefront - for any cell, specification of the time at which signalling

molecule and somitic factor production could begin, would be controlled by the clock and wavefront. In short, none of the current models for somitogenesis can, in their present form, account for somite formation and the anomalies formed when certain integral factors are perturbed, but each can give useful insight into the somitogenic process and should not be discarded entirely.

The aim of this thesis is to take the "signalling model" and adapt it to become a mathematical basis of the clock and wavefront model. We will use the FGF8 signalling gradient as the basis for the wave of cell determination which controls the ability of cells to become somites, and the segmentation clock (as evidenced by the dynamic expression of *c-hairy-1* and *l-fng*) as the oscillator which interacts with the wavefront. We aim to consider the following questions: (i) can the model exhibit behaviour characteristic of somitogenesis? (ii) can the model mimic the existing experimental data? (iii) can the model be used to make experimental predictions that can be used to test the model?

The following two chapters (2, 3) explore this mathematical model in detail (in its cell cycle format) with the initial chapter concerned with spatio-temporal analysis, phase plane analysis and numerical solution of the system, and the second concerned with making approximations to the model which give further insight into the mechanisms involved. In particular, we find approximations for both the dependent variables and predict the size of somites formed by the model.

We then move to consider the adaptation of the signalling model to a clock and wavefront form (Chapters 4 and 5). We begin by discussing the experimental evidence surrounding FGF8 expression in the PSM and consider the various mechanisms that could be responsible for this gradient formation. We select the most appropriate mechanism, both in terms of its biological footing and the ease of manipulation of its mathematical formulation, and consider the effects of its perturbation. We finally use our adapted model to make some experimentally testable predictions (Chapter 6).

The penultimate chapters (7, 8) consider the most recent experimental findings, which show a gradient of Retinoic acid along the PSM, opposite to that of the FGF8 gradient. It has been shown that FGF8 and Retinoic acid are mutually inhibitory and that there is a complex biochemical network underlying the interaction of the gradients. In Chapter 7 we try to understand this complicated chain of reactions and form a mathematical model which encapsulates the entire system. The mathematical analysis of this model is very tedious and the resulting system too complex to allow much manipulation, so as a result, in Chapter 8 we move to look at a simplified system of FGF8 and Retinoic acid interaction.

Finally, in Chapter 9, we discuss the applicability of our new model, and the redundancy of previous models, for somite formation and discuss further avenues for exploration, both physically and experimentally.

Chapter 2

Analysis of the Cell Cycle Model

In this chapter we explore the cell cycle model for somite formation in more detail. After non-dimensionalising, we carry out a phase plane analysis to find constraints on the model parameters and then solve the equations numerically imposing these constraints. Finally we present an explanation of the effects of heat shock using the algorithm of Schnell and co-workers [50].

2.1 Mathematical formulation of the model

The mathematical formulation of the cell cycle model is

$$\frac{\partial u}{\partial t} = \frac{(u+\mu v)^2}{\gamma+\rho u^2}\chi_u - \nu u, \tag{2.1}$$

$$\frac{\partial v}{\partial t} = \frac{\kappa}{\epsilon+u}\chi_v - \lambda v + D_v\frac{\partial^2 v}{\partial x^2}, \tag{2.2}$$

where

$$\chi_u(x,t) = H(ct - x + x_1) \quad \text{and} \quad \chi_v(x,t) = H(ct - x + x_2). \tag{2.3}$$

$\mu, \gamma, \rho, \nu, \kappa, \epsilon, \lambda, D_v, x_1$, and x_2 are positive constants, with $x_2 < x_1$. Note that $P_1 \leftrightarrow x_1 + ct$ and $P_2 \leftrightarrow x_2 + ct$.

2.1.1 Non-dimensionalisation

The system has eleven parameters: we choose to non-dimensionalise to allow an absolute measure of the quantities involved and to reduce the number of parameters. We take

$$t = \frac{\hat{t}}{\nu}, \quad x = (x_1 - x_2)\hat{x}, \quad u = \frac{\hat{u}}{\nu\rho}, \quad v = \frac{\kappa\nu\rho}{\lambda}\hat{v}. \tag{2.4}$$

Notice that in the new non-dimensional variables, $x_2 - x_1 = 1$ i.e. the distance between the points P_1 and P_2 is equal to 1. We also consider the process on a time scale in which u rises from close to zero to its high equilibrium state. We define the new dimensionless parameters by

$$\hat{\mu} = \frac{\mu\kappa\rho^2\nu^2}{\lambda}, \qquad \hat{\gamma} = \gamma\nu^2\rho, \qquad \hat{\kappa} = \frac{\lambda}{\nu}, \qquad \hat{\epsilon} = \epsilon\nu\rho \tag{2.5}$$

$$\hat{D_v} = \frac{D_v}{\nu(x_1 - x_2)^2}, \quad \hat{c} = \frac{c}{\nu(x_1 - x_2)}, \quad \hat{x_1} = \frac{x_1}{x_2 - x_1}, \quad \hat{x_2} = \frac{x_2}{x_2 - x_1}. \tag{2.6}$$

Dropping the hats for notational convenience yields the non-dimensionalised form of the model:

$$\frac{\partial u}{\partial t} = \frac{(u + \mu v)^2}{\gamma + u^2}\chi_u - u, \tag{2.7}$$

$$\frac{\partial v}{\partial t} = \kappa\left(\frac{1}{\epsilon + u}\chi_v - v\right) + D_v\frac{\partial^2 v}{\partial x^2}, \tag{2.8}$$

where

$$\chi_u(x,t) = H(ct - x + x_1), \quad \chi_v(x,t) = H(ct - x + x_2) \quad \text{and} \quad x_2 - x_1 = 1. \tag{2.9}$$

Note that this is a slightly different non-dimensionalisation to that used by Collier and co-workers in previous work [3, 4, 28, 29].

2.1.2 Boundary conditions

The boundary conditions are found by requiring that for cells which are a "long way" from reaching P_1 in their clock cycle, that is, $x \gg x_1 + ct$ (and therefore $x \gg x_2 + ct$), both the level of the signalling molecule and somitic factor are close to zero, and that cells which have already passed P_2 in their clock cycle "some time ago", that is, $x \ll x_2 + ct$, have some fixed level of the somitic factor and signalling molecule. This is presented schematically in Figure 1.10 and leads to the boundary conditions

$$\begin{aligned} &u, v \to 0 \quad \text{as} \quad x - \{x_2 + ct\} \to +\infty, \\ &u, v \quad \text{are bounded as} \quad x - \{x_2 + ct\} \to -\infty. \end{aligned} \tag{2.10}$$

2.1.3 Modelling assumptions

The crucial modelling assumptions made by Collier et al. [4] are in the form of the non-linear terms in the model kinetics, which allow u to undergo a sudden switch from a low concentration to a high concentration.

The non-linear terms in the u equation correspond to autocatalysis of u, activation of u by v and saturation of u for large values of u. For each x, the production term in the u equation is not active until $x \leq x_1 + ct$, i.e. until a cell has reached the point P_1 in terms of its maturity. This is consistent

with the assumption that a cell cannot respond to a signal unless it is within the P_1–P_2 time window. In the v equation, the non-linear term corresponds to negative feedback: an increase in u production by v causes a decrease in v production, which in turn causes a decrease in the rate of u production. This term (and the choice of ϵ) also ensures that only cells which have not already been specified as somitic (i.e. have low u) can produce a non-negligible amount of signalling molecule. For each x the nonlinear v production term does not become active until $x \leq x_2 + ct$, i.e. until a cell reaches P_2 in terms of its maturity. Linear degradation of both molecules is present, with only the signalling molecule v able to diffuse.

Essentially, we can divide up the domain into 3 distinct regions:

Region I: ($x > x_1 + ct$) Cells which have not yet reached the point P_1. They are incapable of producing or responding to the signalling molecule and the level of somitic factor is close to zero everywhere.

Region II: ($x_1 + ct < x < x_2 + ct$) Cells which are between P_1 and P_2. They are not capable of producing a signal, but are able to respond to a signal by producing somitic factor.

Region III: ($x_2 + ct < x$) Cells which have already reached the point P_2. Cells can respond to, and emit a signal. Pioneer cells at P_2 emit a signal, but cells which have passed P_2 are no longer capable of emitting a signal since the level of somitic factor is high everywhere.

This is shown clearly in Figure 1.10. In general and without loss of generality, in the rest of this work we will let x_1 and x_2 assume the values 1 and 0 respectively.

Figure 2.1 contains a graphical representation of the way in which somites are proposed to form in the cell cycle model. The lower line can be thought of as representing the point P_1 as it moves down the embryonic axis, from anterior to posterior, and is the site of the discontinuity in the somitic factor Heaviside function (χ_u) in the mathematical model. Similarly, the upper line can be thought of as representing the point P_2 as it moves down the embryonic axis, from anterior to posterior, and is the site of the discontinuity in the signalling molecule Heaviside function (χ_v). Region I lies below the line P_1, Region II between the lines P_1 and P_2 and Region III above the line P_2. The positions of the presumptive somites are found by tracing the lines as shown in the diagram, and relative somite sizes are illustrated underneath. Since the horizontal axis measures distance, and the vertical axis measures time, we can think of the slope of the lines representing P_1 and P_2 as measuring the speed with which PSM cells become competent to form somites.

2.1.4 Spatio-temporal analysis

The process of signalling takes places as follows (see previous work by McInerney and co-workers [29]): At time $t = 0$, we have $u \approx 0$ for all points caudal to the point $x_2 \leftrightarrow P_2$, $u \approx 1$ for all points cranial to the point $x_1 \leftrightarrow P_1$ and $v \sim O(1)$ throughout the domain. The Heaviside functions χ_u and χ_v, which control a cell's ability to produce u, v respectively, move caudally with constant speed c. Points (cells) which are initially just caudal to the point x_2 ($x > x_2$) quickly become part of the region where v production is possible (the non-linear production term becomes non-zero) and since

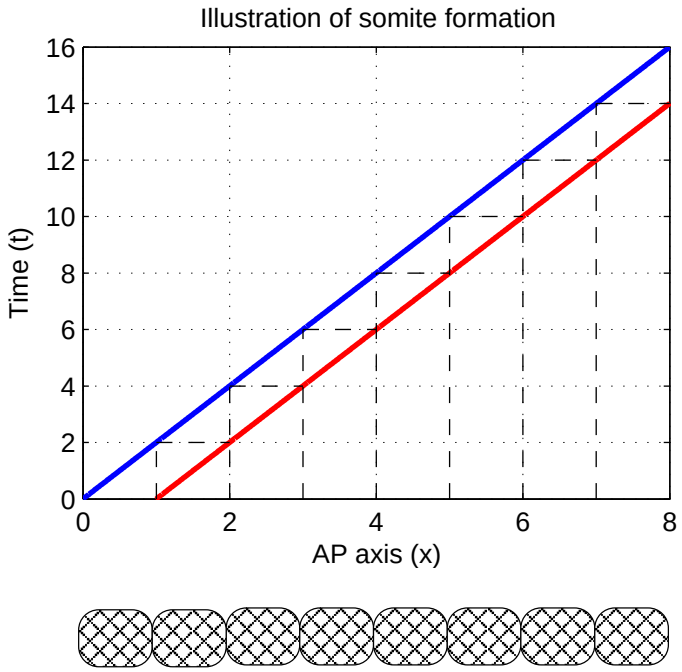


Figure 2.1: Illustration of the manner in which somites are formed in the cell cycle model. In the top diagram, the positions of successive somites are found by tracing the lines as shown. The diagonal lines indicate the positions of the points P_1 (red) and P_2 (blue). The bottom diagram illustrates the relative somite sizes. The gradient of the lines representing P_1 and P_2 is a measure of the speed at which somites are formed.

$u \approx 0$ at these points, it activates v production. The increased v production leads to a pulse in v centered at $x_2 + ct$. At time $t = \tilde{t}$ (which occurs shortly after $t = 0$) the increase in v is sufficient to activate u production in all points between x_2 and $x_1 + c\tilde{t}$ (the position of P_1 at time $\tilde{t}$). As u rises it inhibits v production, and the pulse-like form of v quickly falls such that $v \sim O(1)$ everywhere. The rise in u slows accordingly. A short time later, $u \approx 1$ for all points between x_2 and $x_1 + c\tilde{t}$, and this region has therefore been specified as somitic. The process will begin again when the discontinuity in χ_v reaches the point $x_1 + c\tilde{t}$, and points where $u \approx 0$ become part of the region where v production becomes possible.

Here we see that there is a delay between signalling and specification. Cells in the PSM gain the potential to form a somite a short time after the signal has been emitted, since there is a delay between emission of the signal by pioneer cells at P_2 and the time at which the level of signal is sufficient to activate u production. This delay causes production of somites which are slightly longer than the unit interval; the mathematical model predicts somites of length $1 + c\tilde{t}$. We will look at somite length in more detail in Chapter 3.

2.2 Phase plane study of the model equations

The following sections contain phase plane analysis of the model equations in each of the three regions, neglecting diffusion. In choosing parameter constraints we keep in mind the analysis outlined in Section 2.1.4. The work in this section has been carried out previously by Collier and McInerney and co-workers [3, 4, 28, 29], but we restate the results here as there are slight differences due to the non-dimensionalisation chosen.

2.2.1 The behaviour of the model in Region I

In Region I, the model equations simplify to

$$\frac{\partial u}{\partial t} = -u, \tag{2.11}$$
$$\frac{\partial v}{\partial t} = -\kappa v. \tag{2.12}$$

There is a spatially uniform steady state at $(u, v) = (0, 0)$. We choose $\kappa \gg 1$ to ensure that v decays rapidly compared to u.

2.2.2 The behaviour of the model in Region II

In Region II the system of equations becomes

$$\frac{\partial u}{\partial t} = \frac{(u + \mu v)^2}{\gamma + u^2} - u, \tag{2.13}$$
$$\frac{\partial v}{\partial t} = -\kappa v. \tag{2.14}$$

The spatially uniform steady states are given by $(u, v) = (u^*, 0)$ where u^* is a solution of

$$\Psi(u) = \frac{1}{\mu}\left(-u \pm \sqrt{u(\gamma + u^2)}\right) = 0. \tag{2.15}$$

Notice that we can only have a feasible, non-zero steady state if $\gamma < 1/4$ (see Figure 2.2). In this case, the steady states are given by $(0, 0)$, $(u_+, 0)$ and $(u_-, 0)$ where

$$\begin{aligned} u_+ &= \tfrac{1}{2}\left(1 + \sqrt{1 - 4\gamma}\right) &&\approx 1 - \gamma - \gamma^2 + \mathcal{O}(\gamma^3), \\ u_- &= \tfrac{1}{2}\left(1 - \sqrt{1 - 4\gamma}\right) &&\approx \gamma + \gamma^2 + \mathcal{O}(\gamma^3). \end{aligned}$$

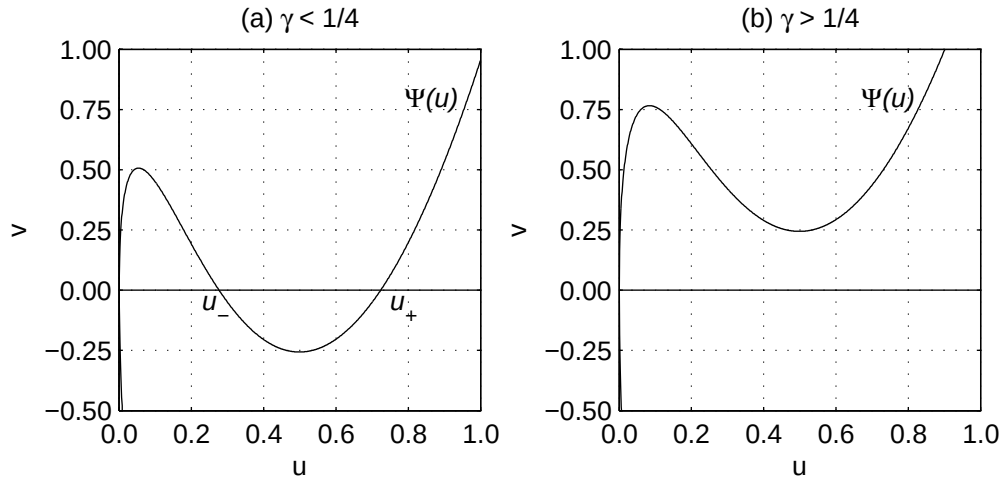


Figure 2.2: Phase plane for Region II. (a) For $\gamma < 1/4$, there are 3 positive steady states: $(u^*, v^*) = (0,0), (u_-, 0)$ and $(u_+, 0)$. (b) For $\gamma > 1/4$, the only positive steady state is $(u^*, v^*) = (0,0)$. Parameters are as follows: $\mu = 0.1$, and (a) $\gamma = 0.2$, (b) $\gamma = 0.3$.

2.2.2.1 Stability of the steady states

We consider small perturbations about the steady state $(u^*, 0)$ of the form $u = u^* + \tilde{u}$, $v = \tilde{v}$ where $\tilde{u}, \tilde{v} \ll 1$. Neglecting higher order terms in $\tilde{u}$ and $\tilde{v}$ the system reduces to

$$\begin{pmatrix} \tilde{u_t} \\ \tilde{v_t} \end{pmatrix} = \begin{pmatrix} f_u & f_v \\ g_u & g_v \end{pmatrix} \begin{pmatrix} \tilde{u} \\ \tilde{v} \end{pmatrix}, \tag{2.16}$$

where

$$\begin{aligned} f(u,v) &= \frac{(u+\mu v)^2}{\gamma + u^2} - u, \\ g(u,v) &= -\kappa v, \end{aligned}$$

and the partial derivatives are evaluated at the steady state $(u^*, 0)$.

We search for a solution of the form $(u \;\; v)^\top = \mathbf{A}_{1,2} \exp(\lambda_{1,2} t)$, where λ is the eigenvalue. Substitution into equation (2.16) determines the eigenvalues $\lambda_{1,2}$ as the solutions of

$$\begin{vmatrix} f_u - \lambda & f_v \\ g_u & g_v - \lambda \end{vmatrix} = \lambda^2 - (f_u + g_v)\lambda + (f_u g_v - f_v g_u) = 0. \tag{2.17}$$

Using Theorem B.1.1 (see Appendix B) we see that the steady states are linearly stable to small perturbations if

$$f_u + g_v < 0, \qquad f_u g_v - f_v g_u > 0. \tag{2.18}$$

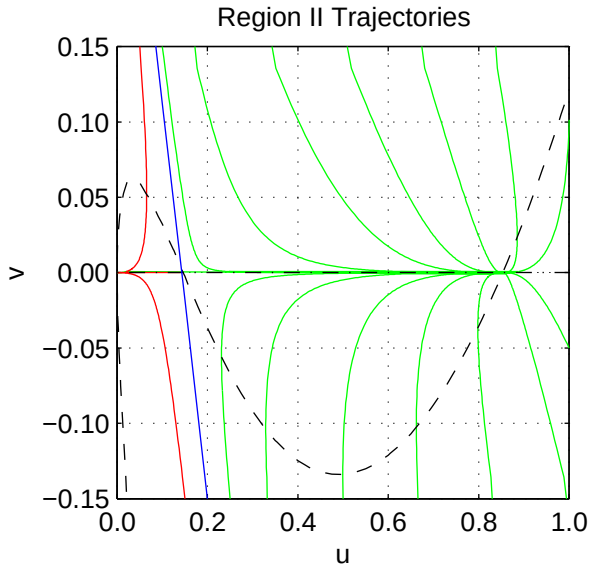


Figure 2.3: Phase plane with trajectories for Region II in the case that $\gamma < 1/4$. The solid red curves indicate trajectories leading to the trivial steady state while the green curves indicate trajectories tending to the non-zero stable steady state. The u null cline is indicated by the dashed curve and the v null cline by the dash-dotted curve (along the line $v = 0$). The phase plane is divided into two regions by the separatrix (solid blue curve). Note that if v is sufficiently high then u will change from approximately zero to a stable steady state of positive value. Parameters are as follows: $\mu = 0.5$, $\kappa = 2$ and $\gamma = 0.125$.

Using Figure 2.2 to calculate the signs of the partial derivatives used above, it is easy to see that $(0, 0)$ and $(u_+, 0)$ are linearly stable, whilst $(u_-, 0)$ is linearly unstable (saddle point).

A key requirement of the model is that u should change from $u \approx 0$ to $u = \mathcal{O}(1)$ in response to a rise in v [3, 28, 29]. From Figure 2.3 we see that this will happen if v is sufficiently high [3, 28, 29]: u will change from approximately zero to the steady state $u = u_+$. There is a separatrix, passing through the unstable steady state $u = u_-$, that divides the phase plane into two parts: trajectories starting to the left of the separatrix converge to the zero steady state, while those on the right converge to the steady state $u = u_+$ [28].

The separatrix must cross the v axis at some point Θ [3] otherwise we would have $v \to \infty$ for $u > 0$ as $t \to -\infty$. But, by equations (2.13) and (2.14), if v is unbounded as $t \to -\infty$, then $\exists\ \tilde{t}$ such that $\partial u/\partial t \geq 1\ \forall\ t \leq \tilde{t}$. This would imply that $u \to -\infty$ as $t \to -\infty$, which contradicts the requirement that $u > 0$ for all $t \in \mathbb{R}$. We note that if $u > 0$ then as $u \to 0$, $u_t = \mu^2 v^2/\gamma > 0$ so the equation does not admit a solution in which u becomes negative. Hence trajectories which start below Θ will converge to the trivial steady state, while those above will converge to $u = u_+$.

The stable manifold of the steady state $(u_-, 0)$ lies on the separatrix [3]. We can use this fact to

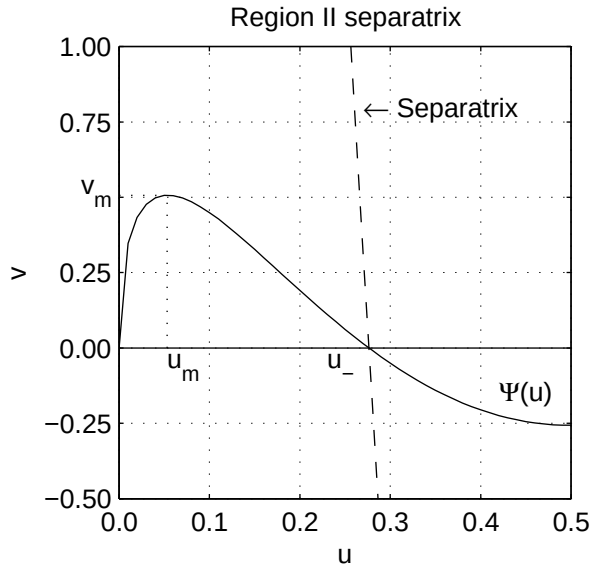


Figure 2.4: Phase plane for Region II when $\gamma < \kappa/4$. The separatrix is depicted by the diagonal line. (u_m, v_m) represents the local maximum of $\Psi(u)$. Parameters are as follows: $\mu = 0.1$, $\kappa = 10$ and $\gamma = 0.2$.

calculate the slope of the separatrix at this point. Solving for $\mathbf{A}_{1,2}$ and $\lambda_{1,2}$ we see that

$$\begin{pmatrix} \tilde{u} \\ \tilde{v} \end{pmatrix} = \begin{pmatrix} 1 \\ 0 \end{pmatrix} e^{f_u t} + \begin{pmatrix} f_v \\ g_v - f_u \end{pmatrix} e^{g_v t}. \tag{2.19}$$

Therefore, the gradient of the separatrix at the saddle point is given by

$$\frac{g_v - f_u}{f_v} = -\frac{\left(\kappa + \sqrt{1-4\gamma} - 1\right)}{2\mu} \approx \frac{\kappa}{2\mu}. \tag{2.20}$$

Assuming that $\kappa \gg 2\mu$ then the separatrix will be almost vertical. This is shown in Figure 2.4. We justify this assumption by noting that in Section 2.2.1 we imposed the condition $\kappa \gg 1$ and that μ must be small enough to ensure that between pulses in v, $u_t < 0$ for $u \ll 1$.

Diffusion also affects Region II. We require u to remain low at points which have not yet responded to a pulse in v, even if $v \approx 1$. That is, we wish u to remain in the interval $0 < u < u_+ \ll 1$. Substituting $v \approx 1$ into equation (2.13) gives

$$\frac{\partial u}{\partial t} \approx \frac{(u+\mu)^2}{\gamma} - u. \tag{2.21}$$

Positive steady states of the above exist only if $\gamma/4\mu > 1$ [3, 28, 29]. Following this result, we define Θ_l, the threshold level of v required in order to stimulate u production, to be $\Theta_l = \gamma/4\mu$.

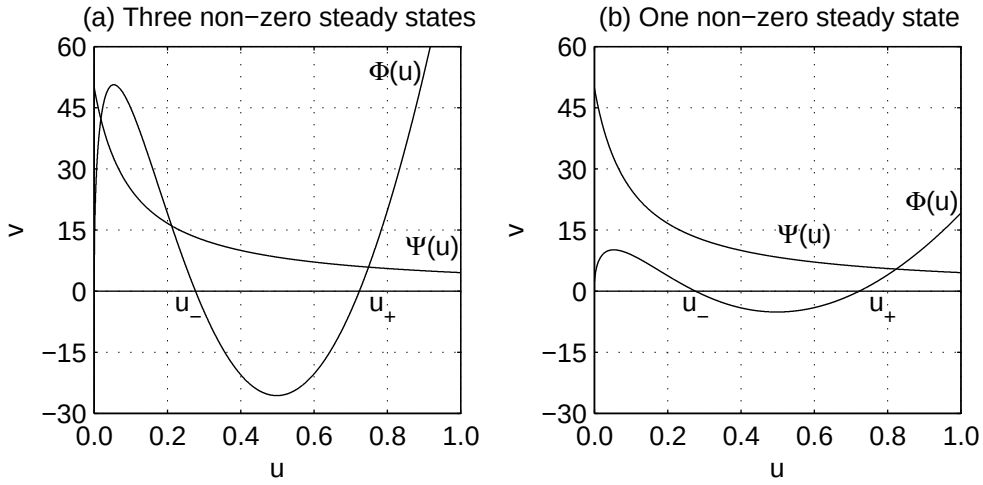


Figure 2.5: Phase plane for Region III. Depending on the parameters, there are one or three steady states. Parameters are as follows: $\gamma = 0.2$, $\epsilon = 0.1$, $\kappa = 0.5$ and (a) $\mu = 0.001$, (b) $\mu = 0.005$.

2.2.3 The behaviour of the model in Region III

The system of equations is now

$$\frac{\partial u}{\partial t} = \frac{(u+\mu v)^2}{\gamma + u^2} - u, \tag{2.22}$$

$$\frac{\partial v}{\partial t} = \kappa\left(\frac{1}{\epsilon + u} - v\right), \tag{2.23}$$

and therefore the nullclines are given by

$$v = \Phi(u) = \frac{1}{\epsilon + u}, \tag{2.24}$$

$$v = \Psi(u) = \frac{1}{\mu}\left(-u \pm \sqrt{u(\gamma + u^2)}\right). \tag{2.25}$$

Depending on the parameters there are one or three steady states, as depicted in Figure 2.5. In the model, it is assumed that cells which have responded to a signal in v have a high level of somitic factor u. Hence the parameters must be chosen so that there is only one positive steady state with the high value of u. To ensure this, we need to ensure that the local maximum of the u null cline lies below the v null cline, that is $v_m < \Phi(u_m)$, where u_m and v_m are as defined in Figure 2.4.

Since $\gamma < 1/4$, we can approximate the unstable steady state by $u_- \approx \gamma + \gamma^2 + \mathcal{O}(\gamma^3)$. At the

local maximum of the u null cline we have that

$$\frac{d\Psi(u)}{du} = \frac{1}{\mu}\left[-1 + \frac{1}{2}\frac{\left(\gamma + 3u^2\right)}{\sqrt{u(\gamma + u^2)}}\right] = 0, \tag{2.26}$$

that is,

$$9u^4 - 4u^3 + 6\gamma u^2 - 4\gamma u + \gamma^2 = 0. \tag{2.27}$$

Expanding u_m in terms of the small parameter γ, i.e.

$$u_m = u_0 + \gamma u_1 + \gamma^2 u_2 + \ldots \tag{2.28}$$

gives for $\mathcal{O}(1)$:

$$9u_0^4 - 4u_0^3 = 0. \tag{2.29}$$

Since $0 < u_m < u_- \ll 1$ we take $u_0 = 0$. On collecting terms that are $\mathcal{O}(\gamma)$, we get $u_1 = 1/4$. Substituting the above to find v, we see that

$$u_m \approx \frac{\gamma}{4} + \frac{5}{4}\left(\frac{\gamma}{4}\right)^2 + \mathcal{O}\left[\left(\frac{\gamma}{4}\right)^3\right], \tag{2.30}$$

$$v_m \approx \frac{1}{\mu}\left\{\frac{\gamma}{4} + \frac{1}{4}\left(\frac{\gamma}{4}\right)^2 + \mathcal{O}\left[\left(\frac{\gamma}{4}\right)^3\right]\right\}. \tag{2.31}$$

Therefore, for the v null cline to lie above the local maximum of the u null cline, we must have, to first order in γ [29],

$$\frac{1}{\epsilon + \frac{\gamma}{4}} > \frac{\gamma}{4\mu}. \tag{2.32}$$

At time $t = \tilde{t}$, just before a signal is emitted, u is approximately zero at $x = x_2 + ct$ and so v increases rapidly since:

$$\frac{\partial v}{\partial t} \approx \kappa\left(\frac{1}{\epsilon} - v\right) \quad \Rightarrow \quad v \approx \frac{1}{\epsilon}(1 - e^{-\kappa t}), \tag{2.33}$$

and we see that v cannot rise above $1/\epsilon$, so the threshold level of v that is required to activate u (Θ_l) must be significantly less than $1/\epsilon$, and lie above the local maximum of the u null cline [29]. This gives the condition

$$\frac{1}{\epsilon} \gg \theta_l > v_m \approx \frac{\gamma}{4\mu} \quad \Rightarrow \quad \frac{\gamma\epsilon}{4\mu} \ll 1. \tag{2.34}$$

For points that have already responded to the signal, we have that $u \approx u_+ \approx 1$. We must ensure that these points cannot trigger another signal when the term with $1/(\epsilon + u)$ becomes active, so we choose $\epsilon \ll u_+ \approx 1$.

One last bound comes from noting that we require the posterior boundary of each somite to be determined by the position of P_1 rather than limited diffusion meaning not all cells between P_1 and P_2 are able to respond to the signal. We therefore take $D_v \gg 1$ [29].

2.3 Numerical solution

We solved the model, equations (2.7) and (2.8), numerically using the NAG (Numerical Algorithm Group) library routine D03PCF, which is designed for nonlinear parabolic (including some elliptic) PDEs in one space variable.

The routine is based on the method of lines, using a finite difference approximation in the spatial variable to reduce the system of PDEs to a system of ODEs in the time variable. The resulting system is solved using an implementation of Gear's method and the Backward Differentiation Formula method. The independent variables form a grid: in general, the mesh consists of either 1001 x 1001 or 2001 x 2001 points, the output of which is plotted using the MATLAB functions imagesc or mesh (on a reduced grid). See Section 2.3.6 for more details on the accuracy of the computed numerical solution and Appendices A.1 and A.2 for more details of the numerical methods used in the NAG library routine D03PCF.

2.3.1 Approximations

We approximated the sharp discontinuities in the model introduced by Heaviside functions of the form $H(x-\alpha)$ by

$$H(x-\alpha) \approx \frac{1}{2}\left[1+\tanh\left(\frac{x-\alpha}{\delta}\right)\right], \tag{2.35}$$

where $\delta > 0$ is a positive constant. As $\delta \to 0$ we recover the Heaviside function. In our simulations we took $\delta = 10^{-3}$ but there was no noticeable difference in results gained with smaller values of δ. Figure 2.6 shows a comparison of the Heaviside function with its continuous $\tanh$ approximation, for $\alpha = 0$.

2.3.2 Computational domain

In our numerical simulations we are forced to consider a closed bounded interval of $\mathbb{R}$. Zero flux boundary conditions are used to simulate the infinite domain boundary conditions. We varied the size of the domain depending on the time over which the simulations were run, to ensure that conditions at the boundary did not affect the patterning process.

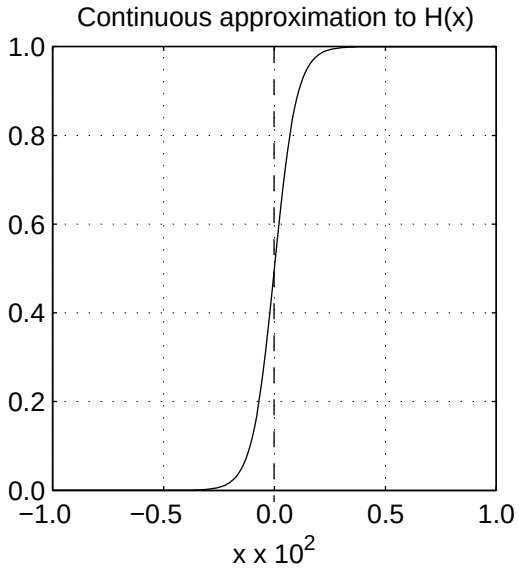


Figure 2.6: Comparison of the discontinuous Heaviside function $H(x)$ (dashed line) with the continuous approximation $\frac{1}{2}\left[1+\tanh(x/0.001)\right]$ (solid line).

2.3.3 Initial conditions

As mentioned earlier, we may, without loss of generality, take $x_2 = 0$, $x_1 = 1$. The implication of this is that at time $t = 0$, cells at the point P_2 are located at the origin. We make the assumption that for cells which have yet to reach P_2 (that is, cells which are in Regions I and II), $u \approx 0$. For cells which have reached P_2 (that is, they are in Region III and have been specified as somitic), we assume that cells have reached the stable steady state value of u, (u_+), which we approximate as one. Hence

$$u(x,0) = \begin{cases} 1 & \text{if } x \leq 0 \\ 0 & \text{if } x > 0. \end{cases} \tag{2.36}$$

The initial condition for v is based on the distribution of v just before the next signal is emitted. For reasons explained later in Chapter 3, we use an approximate analytic solution of the form

$$v(x,0) = AH(-x) + B\cosh(\lambda(l - |x|)), \tag{2.37}$$

where

$$A \equiv \frac{1}{1+\epsilon-\epsilon_1}, \qquad B \equiv \frac{A\text{sign}(x)}{2\cosh(\lambda l)}, \qquad \lambda \equiv \sqrt{\frac{\kappa}{D_v}}, \tag{2.38}$$

and $\epsilon_1 \ll 1$. In general we took $\epsilon_1 = 10^{-3}$ in numerical simulations (unless otherwise stated). l is a parameter measuring the size of the domain and is used in calculating the boundary conditions.

2.3.4 Parameter values

Parameter values used in the simulations were $\mu = 1 \times 10^{-4}$, $\gamma = 1 \times 10^{-3}$, $\kappa = 10$, $\epsilon = 10^{-3}$, $\epsilon_1 = 10^{-3}$, $D_v = 50$, $c = 5 \times 10^{-1}$ and $\delta = 10^{-3}$. The parameter constraints needed to ensure coordinated segmentation takes place are all satisfied:

- $\kappa \gg 1$ is satisfied since $\kappa = 10$.
- $\gamma < 1/4$ is satisfied since $\gamma = 1 \times 10^{-3}$.
- $\gamma/4\mu > 1$ is satisfied since $\gamma/4\mu = (1 \times 10^{-3})/(4 \times 10^{-4}) = 2.5$.
- $\kappa/(\epsilon + \frac{\gamma}{4}) > \gamma/4\mu$ is satisfied since $\kappa/(\epsilon + \frac{\gamma}{4}) = 10/(10^{-3} + 10^{-3}/4) = 8 \times 10^3$ and $\gamma/4\mu = 10^{-3}/(4 \times 10^{-4}) = 2.5$.
- $\gamma\epsilon/4\mu \ll 1$ is satisfied since $\gamma\epsilon/4\mu = (10^{-3}.10^{-3})/(4 \times 10^{-4}) = 2.5 \times 10^{-3}$.
- $\epsilon \ll 1$ is satisfied since $\epsilon = 10^{-3}$.
- $D_v \gg 1$ is satisfied since $D_v = 50$.

2.3.5 Numerical results

As shown in Figures 2.7 and 2.8, the signalling molecule travels down the axis as a series of pulses of v. Figure 2.9 shows each peak occurring approximately 2.5 time units apart, with the first peak occurring at $x = 0$ and with each subsequent peak displaced approximately one spatial unit more caudally than its predecessor. The somitic factor wavefront appears to move down the cranio-caudal axis as a series of jumps as successive groups of cells are triggered to become somitic: the peak at $x = 0$ corresponds to a fairly rapid jump in u occurring in all cells situated between $x = 0$ and $x \approx 1$, etc. Note that the rise in the level of somitic factor occurs at approximately the same time in all cells destined to form a somite together, and also that this coordinated rise slows as the level of u tends towards its maximum, as predicted in earlier analysis. So numerical simulation of the mathematical model can produce results predicted by the 'word' model. Emission of a signal from pioneer cells reaching P_2 results in a synchronous rise in level of the somitic factor in cells situated between P_1 and P_2 and hence in coordinated segmentation of somites.

Note that each somite is approximately 1.2-1.3 units in length. As mentioned previously in Section 2.1.4 this is a consequence of the delay between signalling and somite specification: at time t, all points between x_2 and $x_1 + ct$ are able to respond to the signal provided that levels are high enough. Somite length is discussed in more depth in Chapter 3.

2.3.6 Accuracy

There are a number of issues that must be addressed with regard to the accuracy of the numerical solution obtained using the NAG routine D03PCF.

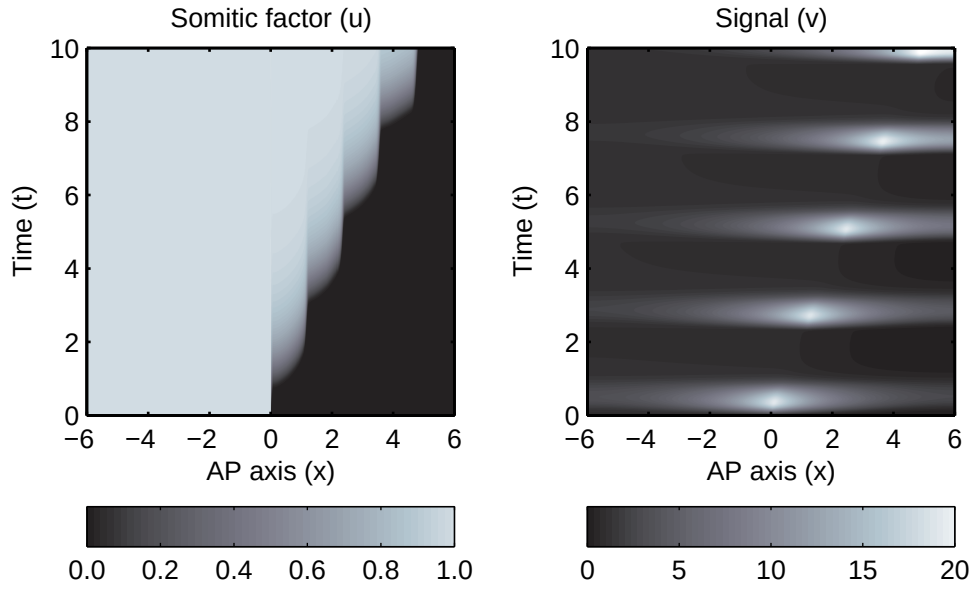


Figure 2.7: Numerical solution for the signalling model of equations (2.7) and (2.8) showing the spatio-temporal dynamics of the somitic factor (left) and the signalling molecule (right). Values were plotted using the MATLAB command imagesc. Each peak in v corresponds to a signal being emitted by a group of pioneer cells reaching P_2 in their cell cycle. The signal diffuses quickly along the embryonic axis, and there is a rapid rise in the somitic factor u which results in somite specification. Parameters are as follows: $\mu = 10^{-4}$, $c = 5 \times 10^{-1}$, $\kappa = 10$, $\epsilon = 10^{-3}$, $D_v = 50$, $\gamma = 10^{-3}$. The simulations were carried out on a square mesh consisting of 1001 x 1001 points.

2.3.6.1 Mesh spacing

The NAG algorithm controls accuracy of the integration in the time direction but not the accuracy of the approximation in space. Spatial accuracy depends both on the mesh spacing and on the distribution of the mesh points in space.

The size of the mesh used in our numerical simulations has a noticeable effect on the results obtained. Use of a coarse mesh with $\mathcal{O}(10^2)$ points results in correct qualitative behaviour but the signal in v is slightly decreased and delayed. It is accompanied by a series of small oscillations. As the spacing is decreased (to $\mathcal{O}(10^3)$ mesh points) the time lag decreases and quantitative differences also decrease. It is important to note that the amplitude of the small oscillations seen during the first signal in v decreases with future signals i.e. these small instabilities in the numerical solution do not propagate. Figure 2.10 demonstrates these results for a range of mesh sizes.

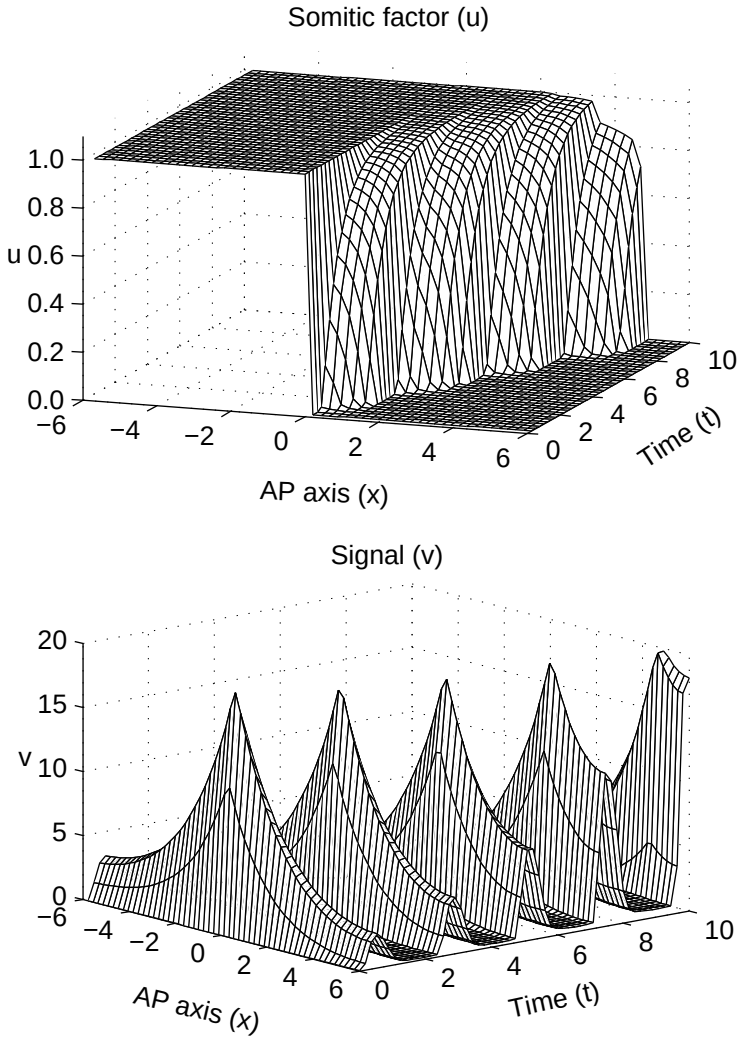


Figure 2.8: Numerical solution for the signalling model of equations (2.7) and (2.8) showing the spatio-temporal dynamics of the somitic factor (above) and the signalling molecule (below). The simulations were carried out on a square mesh consisting of 1001 x 1001 points. Values were plotted using the MATLAB command mesh on a reduced mesh of 60 x 60 points. Parameters are as follows: $\mu = 10^{-4}$, $c = 5 \times 10^{-1}$, $\kappa = 10$, $\epsilon = 10^{-3}$, $D_v = 50$, $\gamma = 10^{-3}$.

2.3.6.2 Error parameter

As mentioned previously, the NAG algorithm controls the accuracy of the integration in the time direction. The error is controlled locally over a single step and so accuracy over a sequence of time steps cannot be guaranteed. It is therefore necessary to test the effect of varying the accuracy parameter in the routine.

Figure 2.11 shows the percentage errors between numerical solutions of the system for a range of mesh sizes and error parameters. For mesh spacing that results in little time lag for the signal (of

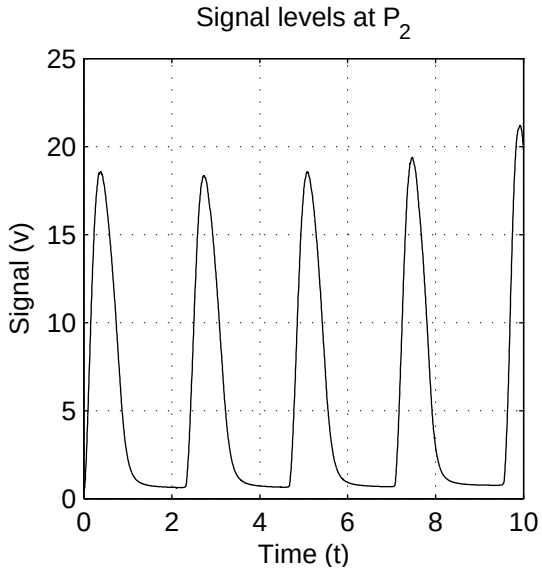


Figure 2.9: Numerical solution for the signalling molecule along a line corresponding to the point P_2. Notice that a signal is emitted approximately every 2.4 - 2.5 time units. The increase in signal intensity over time is due to boundary effects as the peak in the signal moves towards the edge of the domain. Parameters are as follows: $\mu = 10^{-4}$, $c = 5 \times 10^{-1}$, $\kappa = 10$, $\epsilon = 10^{-3}$, $D_v = 50$, $\gamma = 10^{-3}$.

the order of 2000 points), there is little noticeable refinement in results for the signal when the error parameter in the program is below 10^{-5}. Throughout this work we will use an error parameter of 10^{-5} in order to gain a balance between numerical accuracy and computational time.

The percentage error is calculated in Figure 2.11(a) and Figure 2.11(c) for a specific x, to be

$$\text{Percentage error} = 100\left(1 - \frac{v_{-3}(x,t)}{v_{-7}(x,t)}\right), \tag{2.39}$$

where the subscript on the v indicates the size of the error parameter (i.e. $v_{-3}(x,t) \leftrightarrow v(x,t)$ computed using an error of 10^{-3}). Similarly for Figure 2.11(b) and Figure 2.11(d).

2.3.6.3 Zero flux boundary conditions

The boundary conditions of the mathematical model are approximated in the numerical simulations by zero flux boundary conditions. The size of the spatial domain will therefore affect the range over which the signal is able to diffuse and boundary effects may also become significant in the formation of somitic factor if simulations are run over long enough time periods.

We run the NAG library routine on a square mesh (in x, t) so it is hard to accurately gauge the effects of changing the size of the spatial domain. If the size of the domain is doubled, then the mesh size would also need to be doubled to keep the same spatial mesh. Problems then arise with the temporal step since a comparison would require both simulations to be run over the same time

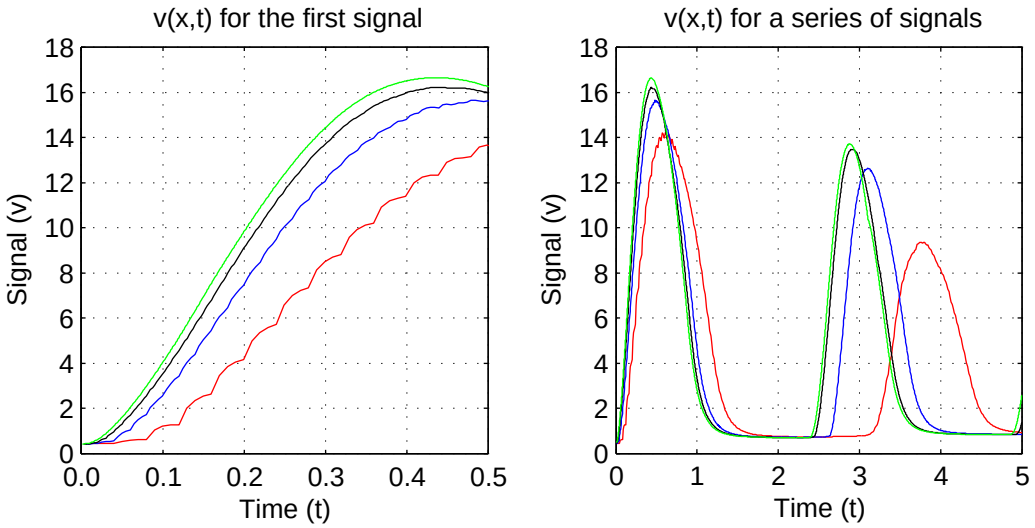


Figure 2.10: Numerical solution of the signal v plotted for a range of mesh sizes. The green line corresponds to 4001 points, the black line to 2001 points, the blue line to 1001 points and the red line to 501 points. Each simulation was carried out on the domain $[-6, 6]$ with an error parameter of 10^{-3}. Parameters are as follows: $\mu = 10^{-4}$, $c = 5 \times 10^{-1}$, $\kappa = 10$, $\epsilon = 10^{-3}$, $D_v = 50$, $\gamma = 10^{-3}$.

period with the same mesh; something that cannot be achieved with a square mesh.

Figure 2.12 compares the numerical solution obtained for the domains $[-5, 5]$ and $[-10, 10]$ during both the first pulse and just before the second pulse of signalling molecule. The results obtained are qualitatively similar with slight deviations appearing between the solutions at the edges of the small domain. Signalling levels on the smaller domain decay to a lesser degree which is to be expected as signalling molecules may not diffuse across the boundaries of the domain due to the zero flux boundary conditions.

2.4 Explanation of heat shock effects

The evidence of Section 1.2.1 suggests that heat shock has the effect of blocking some oscillatory process within the cell cycle. The anomalies caused by heat shocks seem to depend on the following two parameter relations [4, 28, 50]:

(i) The number of somites formed per clock oscillation, ψ. (In the chick embryo this is $6 - 7$ somites [55].)

(ii) The length of the block in the cell cycle caused by the heat shock as a percentage of the time between the points P_1 and P_2, η. (Schnell et al. [50] estimate $\eta \approx 0.6$ which corresponds to the duration of the heat shock divided by the time taken to form a somite.)

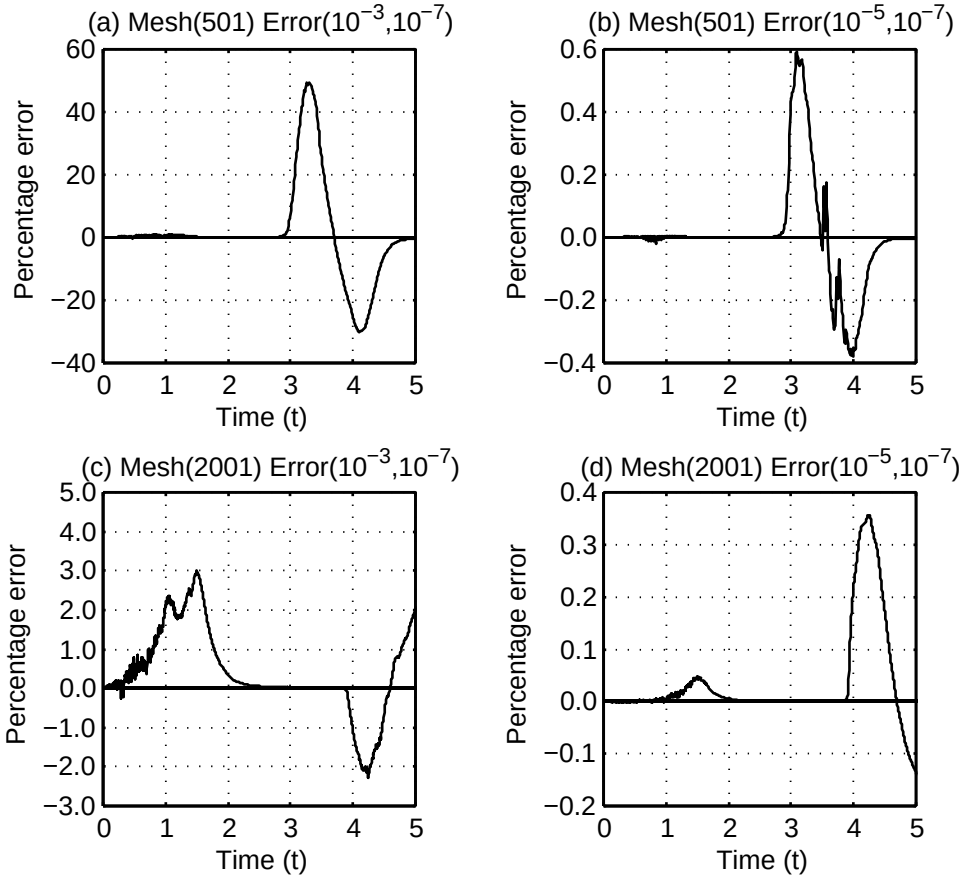


Figure 2.11: Percentage differences in the numerical solution of the signal v for mesh sizes of 501 and 2001 points calculated using the format given by equation (2.39). Plot of the percentage difference between an error parameter of (a) 10^{-3} and 10^{-7} and (b) 10^{-5} and 10^{-7} using mesh size of 501 points and (c) 10^{-3} and 10^{-7} and (d) 10^{-5} and 10^{-7} using mesh size of 2001 points. Parameters are as follows: $\mu = 10^{-4}$, $c = 5 \times 10^{-1}$, $\kappa = 10$, $\epsilon = 10^{-3}$, $D_v = 50$, $\gamma = 10^{-3}$ and the solutions are evaluated at $x = 0.5$.

The effect of heat shock is to vary the time between the points P_1 and P_2 so that different numbers of cells become incorporated into each individual somite. It is achieved by blocking progress of the segmentation clock in cells which have reached a certain point in their clock cycle, for the duration of the heat shock.

2.4.1 Heat shock algorithm: explanation using the signalling model

McInerney and co-workers [28, 50] detail an algorithm which uses the previous model to correctly predict the anomalies produced by heat shock:

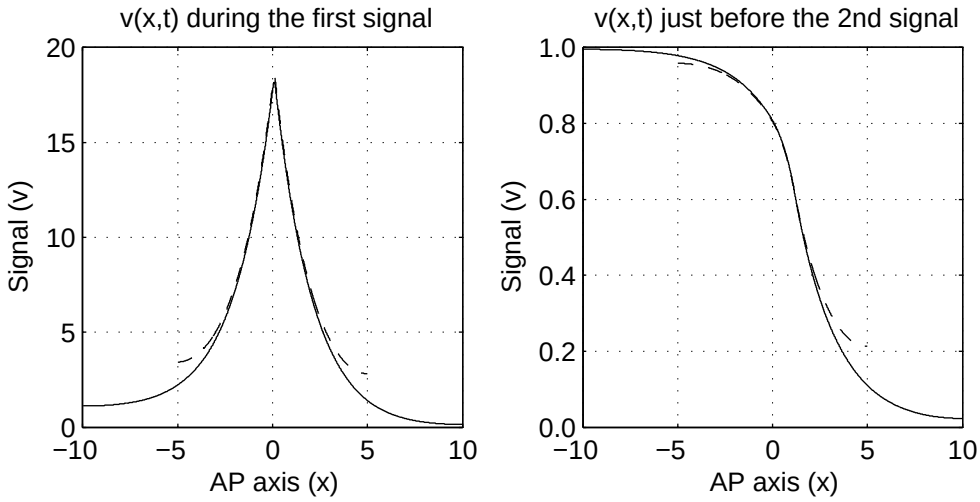


Figure 2.12: Plots comparing the effect of zero flux boundary conditions on the numerical solution. In both subfigures, the dashed line corresponds to a spatial domain of $[-5, 5]$ and the solid line corresponds to a spatial domain of $[-10, 10]$. Parameters are as follows: $\mu = 10^{-4}$, $c = 5 \times 10^{-1}$, $\kappa = 10$, $\epsilon = 10^{-3}$, $D_v = 50$, $\gamma = 10^{-3}$. The simulations are run on 2001 x 2001 and 4001 x 4001 grids for the smaller and larger domains respectively.

(i) Partition the x axis up into intervals

$$I_i = (\alpha_i, \beta_i) \quad \text{for} \quad i = 0, 1, 2, ..., \tag{2.40}$$

where

$$\alpha_i = \delta + i\psi \quad \text{and} \quad \beta_i = \delta + \eta + i\psi, \tag{2.41}$$

with $\delta \geq 0$.

(ii) Once in each clock cycle, impose the condition

$$\{x : x \, \epsilon \, I_i\} \rightarrow \beta_i. \tag{2.42}$$

Figure 2.13 illustrates the areas of the clock cycle that are affected by heat shock. Here, ψ corresponds to the length of the clock cycle, η to the length of the heat shock and δ to the distance between the beginning of the clock cycle and application of heat shock. We note that this δ should not be confused with the δ used in the continuous approximation of the Heaviside function.

2.4.2 Spatio-temporal analysis

Inherent in the construction of the mathematical model presented earlier is the confinement of u and v production to cells which have reached the points P_1 and P_2, respectively, in their clock cycles.

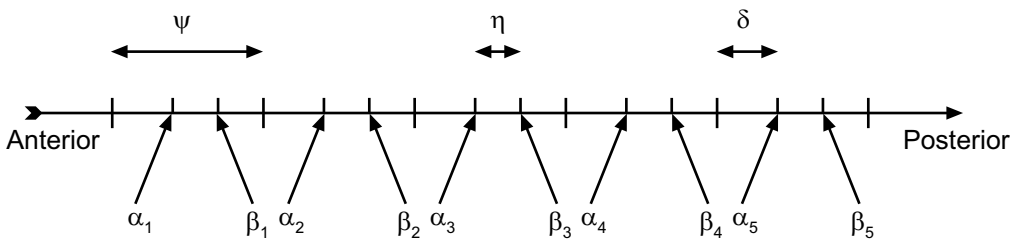


Figure 2.13: An illustration of the areas of the cell cycle on which heat shock is assumed to act in the algorithm of McInerney and co-workers [28, 50]. ψ corresponds to the length of the cell cycle, η to the length of the heat shock and δ to the distance between the beginning of the cell cycle and application of heat shock. For $i = 1, 2, \ldots$, α_i and β_i correspond to the beginning and end of the heat shock, respectively.

In temporal terms, a cell situated at a point x is not able to begin production of u, v, until the times $(x-1)/c$, x/c respectively.

Applying the heat shock algorithm to the mathematical model produces discontinuities in the Heaviside function for u at the point α_i at time $t = \hat{t}_\alpha = (\alpha_i - 1)/c$ and at the point β_i at time $t = \hat{t}_\beta = (\beta_i - 1)/c$: for $t > \hat{t}_\alpha$ the Heaviside function remains fixed at α_i until $t = \hat{t}_\beta$. The implication of these discontinuities is that points which lie inside the interval (α_i, β_i) are unable to respond to changes in the concentration of v until time $\hat{t}_\beta$: if a pulse is emitted by pioneer cells at some time $t \leq \hat{t}_\alpha$ only cells in the range $x \leq \alpha_i$ will be able to respond. By the time $\hat{t}_\beta$, the signal level may be too low to activate u production and hence only cells in the interval up to α_i will be specified as somitic.

Discontinuities are produced in the same manner in the Heaviside function for v: the first occurs at α_i at time $t = \tilde{t}_\alpha = \alpha_i/c$ and the second at β_i at time $t = \tilde{t}_\beta = \beta_i/c$. A pulse in v will be delayed until time $t = \tilde{t}_\beta$, even if u is low in this interval, and when it is finally emitted, it will be much greater in amplitude since all points in (α_i, β_i) will gain the potential to produce v at the same time.

It is easy to visualise the implications of this algorithm with the aid of a diagram similar to that in Figure 2.1. In Figure 2.14, the lines are redrawn to reflect the delayed production of somitic factor and signal in the heat shocked intervals until the times $t = (\beta_i - 1)/c$ and $t = \beta_i/c$ respectively. Figure 2.14 accurately predicts the formation of an abnormally large somite followed by an abnormally small somite. Since the algorithm induces such discontinuities in the Heaviside function once per clock cycle, the model exhibits periodic anomalies (as observed experimentally).

2.4.3 Numerical simulation

Numerical simulations of the algorithm using the same NAG library routine as before show that the algorithm correctly predicts the production of an abnormally small somite followed by an abnormally large somite upon application of transient heat shock. Figure 2.15 illustrates this and also demonstrates the increase in severity of anomalies as the duration of heat shock is increased.

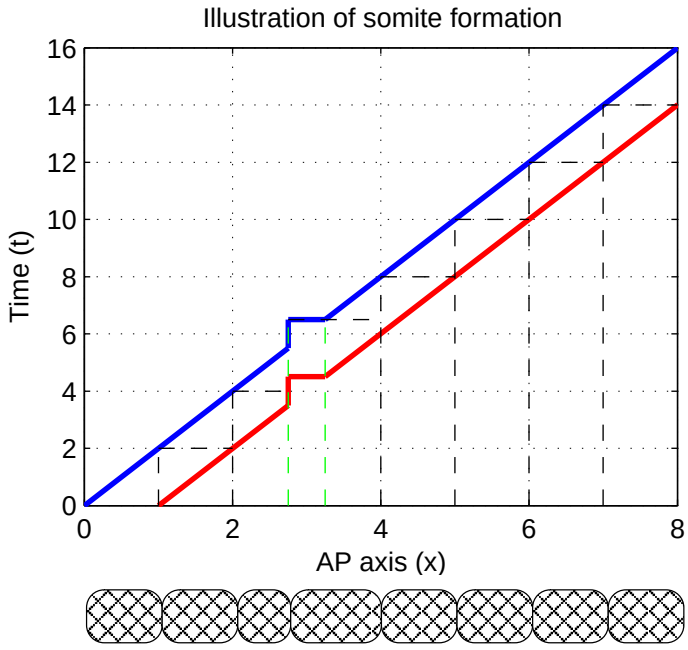
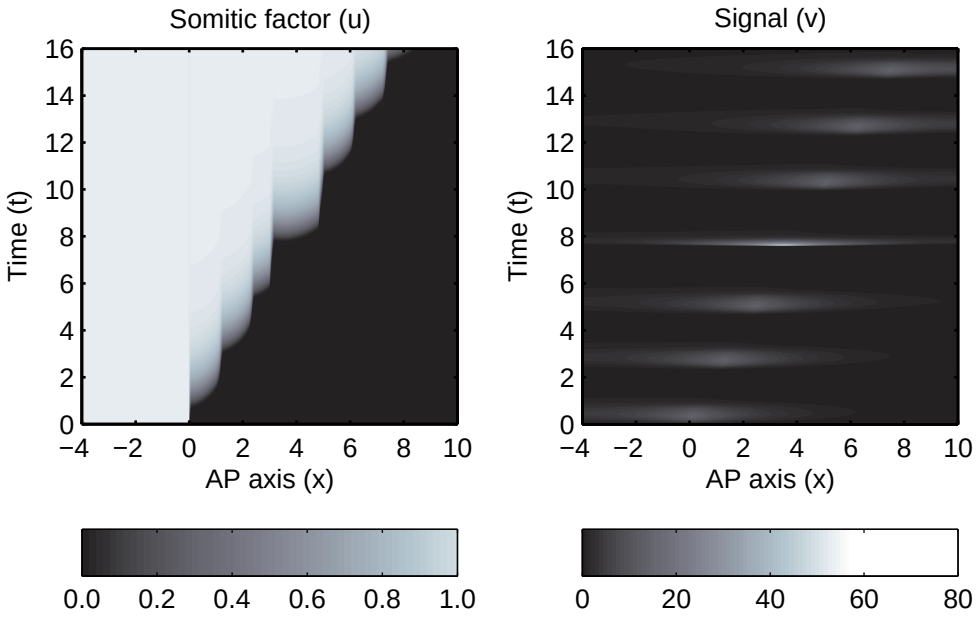


Figure 2.14: An illustration of the manner in which somites are formed when transient heat shock is applied to chick embryos as envisaged by the cell cycle model. Applying the algorithm of McInerney and co-workers [28, 50] we note a delay in the production of the somitic factor and signal, resulting in the formation of an abnormally small somite followed by an abnormally large somite. Heat shock is applied in the region denoted by the dotted green lines, P_1 is denoted by the red line and P_2 is denoted by the blue line.

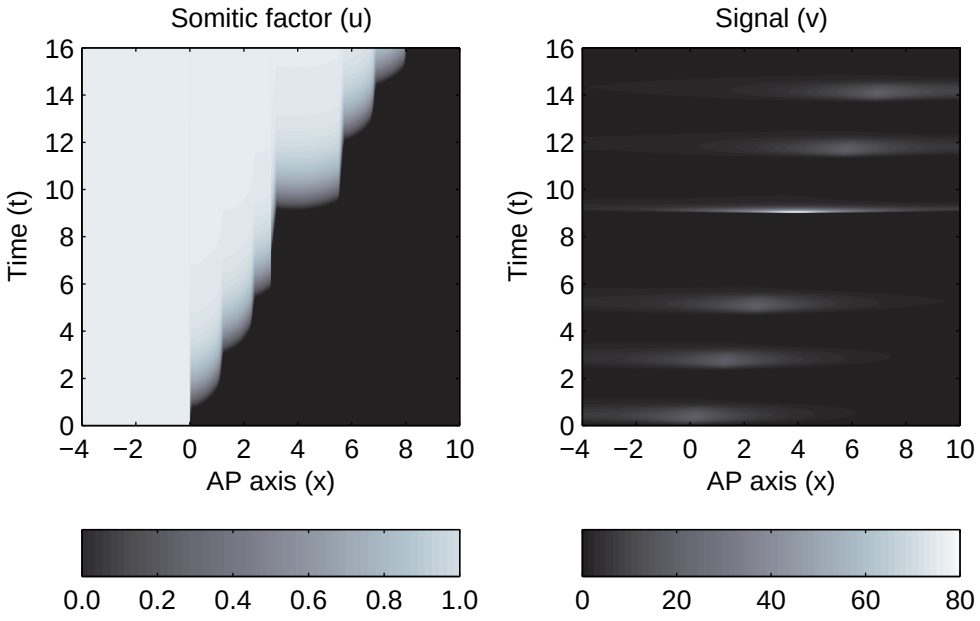
2.5 Discussion

In this chapter, we have analysed the cell cycle model for somitogenesis. Starting from the original mathematical model of Collier and co-workers [4], we non-dimensionalised and carried out a phase plane analysis of the spatially uniform system. Study of the phase plane led to a series of parameter constraints which need to be satisfied in order for the system to be able to generate a series of coherent somites and we summarised these in Section 2.3.4. We also developed a simple method (see Figure 2.1) for tracing the progress of the points P_1 and P_2 which allowed us to estimate the pattern of somites produced by the cell cycle model.

We next used the NAG library software D03PCF to solve equations (2.1) and (2.2) numerically and we presented these results graphically in Section 2.3.5. Following the criticisms made by McInerney [28] on solution of the system using the NAG library software D03PGF, which preceded D03PCF, we looked closely at the accuracy of the numerical results over a range of spatial grids and error parameters. In contrast to the results obtained with D03PGF, we found that with a fine spatial mesh D03PCF could produce solutions free of any minor oscillations. It should be noted however, that the robustness of the numerical simulations as the model parameters were varied was not as concrete as suggested by the earlier phase plane analysis.



(a) Heat shock during the time period $t = 6.0$ and $t = 7.6$.



(b) Heat shock during the time period $t = 6.0$ and $t = 9.0$.

Figure 2.15: Numerical solution of equations (2.7) and (2.8) showing the spatio-temporal dynamics of the somitic factor and the signalling molecule. (a) Simulated heat shock over the time period $t = 6.0$ and $t = 7.6$ causing the third somite to be abnormally small and the fourth somite to be abnormally large as seen experimentally. (b) Simulated heat shock over the time period $t = 6.0$ and $t = 9.0$ causing the third somite to be abnormally small and the fourth somite to be abnormally large as seen experimentally. Notice that there is a larger pulse in the signal corresponding to the formation of the fourth somite. Parameters are as follows: $\mu = 10^{-4}$, $c = 5 \times 10^{-1}$, $\kappa = 10$, $\epsilon = 10^{-3}$, $D_v = 50$, $\gamma = 10^{-3}$.

For example, numerical simulation only produced coherent jumps in somitic factor for a limited range of values of c (typically 0.2-0.8). This may in part be due to the effects of diffusion (very rapid in the case of the signalling molecule) and the limitations of the numerical solver. Collier carries out a sensitivity analysis on the model in [3].

We concluded the chapter by considering the algorithm of McInerney and co-workers [28, 50] to explain the effects of heat shock applied to chick embryos. We used the method described above to predict the anomalies produced as a result of heat shock and incorporated the heat shock algorithm into our numerical simulations in order to further demonstrate the ability of the model to mimic the results seen *in vivo* when heat shock is applied to chick embryos.

Although we have performed phase plane analysis of the model equations to gain some insight into the parameter regimes under which the system can reproduce the pattern of somites seen *in vivo*, there are still many intricacies of the model that need to be explored in more depth. In the following chapter we break the model down into four stages and consider the behaviour of both the signalling molecule and somitic factor concentrations individually in each stage.

Chapter 3

Approximations for the Somitogenic Process

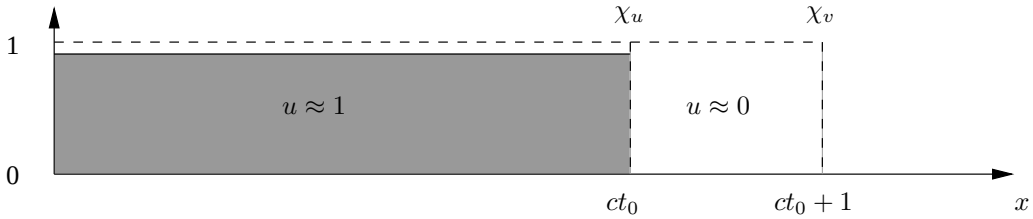
Due to the highly non-linear nature of the equations and the degree of inter-dependence of the dependent variables, it is not possible to gain any further understanding of the model by undertaking a fully rigorous small parameter expansion. There are, however, a number of approximations and simplifications that we can make to the model that will allow us to gain useful insights into the somitogenic process.

The somitogenic process, as described by the model, can be broken down into a number of stages that can be approximated analytically and used to draw useful conclusions about the behaviour of the model. A brief guide to the stages of the somitogenic process is given below and in Figure 3.1.

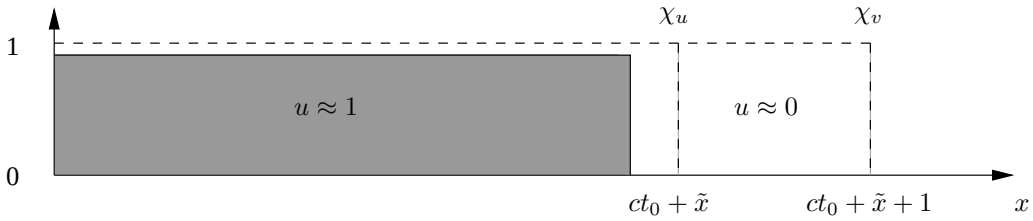
First stage Just before a signal (at $t = t_0$, say), u and v are in an approximate steady state throughout the domain (Figure 3.1(a)). In Figure 3.1(b) we see that at time t_0, the discontinuity in the signalling Heaviside function χ_v begins to move into the region where $u \approx 0$. For $\epsilon \ll 1$ this leads to a rapid rise in v at $x_0 = ct_0$ and for $D_v \gg 1$ the signalling molecule diffuses quickly, leading to a rise in v for all points in the domain.

Second stage At some notional time $t = \tilde{t} > t_0$, the increase in v becomes large enough to activate u production in the region between $x = ct_0$ and $x = c\tilde{t} + 1$. Notice that this region expands as t increases. Signalling levels continue to increase at a rate which is virtually unaffected by changes in the somitic factor levels, until such a time as u becomes significant in size with the parameter ϵ.

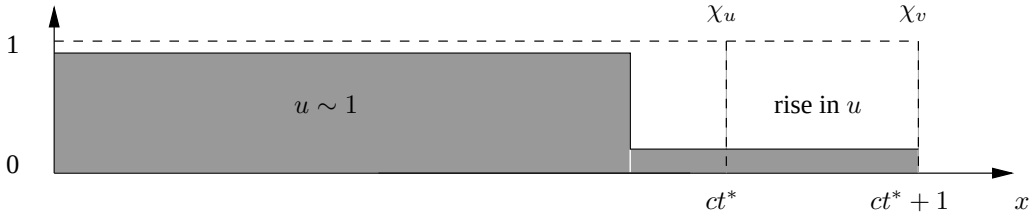
Third stage As u begins to rise it inhibits v production: the rapid rise in u is accompanied by a similarly rapid fall in v. Figure 3.1(c) illustrates the rise in somitic factor. During this stage, the dynamics of the signalling molecule, v, are heavily dependent on the somitic factor u.



(a) The Heaviside functions $\chi_v = H(ct - x)$ and $\chi_u = H(ct - x + 1)$ at time t_0 just before a signal occurs. u and v are both in approximate steady states. The shaded region represents points where $u \approx 1$. At point $x = ct_0$, u drops from a high value, $u \approx 1$, to a low value, $u \approx 0$.



(b) The Heaviside functions $\chi_v = H(ct - x)$ and $\chi_u = H(ct - x + 1)$ at a slightly later time. Notice that the Heaviside function χ_v has moved into the region where $u \approx 0$ leading to a rapid rise in v.



(c) The Heaviside functions $\chi_v = H(ct - x)$ and $\chi_u = H(ct - x + 1)$ at time t^* just after $t = \tilde{t}$. The shaded region represents points where $u \sim 1$. At point $x = ct_0$, u drops from a high value to a low value, $u \approx 0$. The pulse in v has caused a rise in u at all points between ct_0 and $ct^* + 1$.

Figure 3.1: Schematic behaviour of the Heaviside functions along with changes in the value of u during the signalling process.

Fourth stage The fourth and final stage involves both u and v being close to steady state values. The increase in u has forced signalling levels to fall throughout the domain and the coherent rise in somitic factor between the points ct_0 and $ct + 1$ has slowed as levels reach their steady state values.

The posterior boundary of the somite is determined by those cells in the region $x \geq 1 + x^*$ which experience a signal of sufficient strength for a long enough time span to allow them to reach a level of u which ensures $u_t > 0$ for all further time. Further details can be found in Section 3.3. The next pulse occurs when χ_v passes the point $x = 1 + x^*$ at time $t = (x^* + 1)/c$.

3.1 Analysis of the signalling equation

The signalling equation is a reaction-diffusion equation of the following form

$$\frac{\partial v}{\partial t} = \kappa \left(\frac{\chi_v(x,t)}{\epsilon + u} - v \right) + D_v \frac{\partial^2 v}{\partial x^2}, \tag{3.1}$$

where $\chi_v(x,t) = H(ct - x)$. For notational convenience we define the linear differential operator

$$L := \frac{\partial}{\partial t} - D\frac{\partial^2}{\partial x^2}. \tag{3.2}$$

Then equation (3.1) can be written as

$$Lv = \begin{cases} \kappa[(\epsilon + u)^{-1} - v] & \text{if} \quad x \leq ct, \\ -\kappa v & \text{if} \quad x > ct. \end{cases} \tag{3.3}$$

3.1.1 Approximating v in the initial stages

In the initial stages (1^{st} and 2^{nd}) where $u \ll \epsilon$, we can approximate the non-linear source term in equation (3.3) by assuming that for cells posterior to $x_0 = ct_0$, the level of somitic factor is close to its high stable steady state ($u \approx 1 - \epsilon_1$) while for cells anterior to $x_0 = ct_0$, the level of somitic factor is approximately zero ($u \approx \epsilon_2$), where $\epsilon_1, \epsilon_2 \ll 1$. We approximate the equation for the signalling molecule by [29]

$$Lv \approx \begin{cases} \kappa[(1 + \epsilon - \epsilon_1)^{-1} - v] & \text{if} \quad x \leq ct_0, \\ \kappa[(\epsilon + \epsilon_2)^{-1} - v] & \text{if} \quad ct_0 < x \leq ct, \\ -\kappa v & \text{if} \quad x > ct, \end{cases} \tag{3.4}$$

where $\epsilon_1, \epsilon_2 \ll 1$. This approximation is valid for $t \geq t_0$.

3.1.1.1 Spatial behaviour of a pulse in signalling molecule

The spatial behaviour of v in equation (2.38) can be investigated by solving the ordinary differential equation (ODE)

$$\frac{D_v}{\kappa}\frac{d^2 v}{dx^2} - v = \begin{cases} -(1 + \epsilon - \epsilon_1)^{-1} & \text{if} \quad x \leq ct_0, \\ -(\epsilon + \epsilon_2)^{-1} & \text{if} \quad ct_0 < x \leq ct, \\ 0 & \text{if} \quad x > ct, \end{cases} \tag{3.5}$$

subject to zero-flux boundary conditions at $x = \pm l$. For convenience we denote $x_0 = ct_0$ and $ct = x_0 + \tilde{x}$ so that $\tilde{x} = c(t - t_0)$ (see Figure 3.1(b)). The general solution of the problem is found by solving the equation in each subinterval by writing v as a linear combination of the linearly independent functions $\cosh[\lambda(l + x)]$ and $\cosh[\lambda(l - x)]$ where $\lambda = \sqrt{\kappa/D_v}$, plus a particular integral. The solution contains six arbitrary constants, two of which must be zero in order

to satisfy the zero flux boundary conditions and the other four of which can be found by imposing the condition that the solution is continuously differentiable throughout the domain.

For $t \geq t_0$, the equation for v becomes

$$v(x;x_0,\tilde{x}) = \begin{cases} (A-B)\sinh(\lambda(l-x_0))\cosh(\lambda(l+x))/(AB\sinh(2\lambda l)) \\ -A\sinh(\lambda(l-x_0-\tilde{x}))\cosh(\lambda(l+x))/(AB\sinh(2\lambda l)) + 1/A \\ \qquad\qquad\qquad\qquad\qquad\qquad \text{if} \quad -l \leq x \leq x_0, \\ -A\sinh(\lambda(l-x_0-\tilde{x}))\cosh(\lambda(l+x))/(AB\sinh(2\lambda l)) \\ -(A-B)\sinh(\lambda(l+x_0))\cosh(\lambda(l-x))/(AB\sinh(2\lambda l)) + 1/B \\ \qquad\qquad\qquad\qquad\qquad\qquad \text{if} \quad x_0 < x \leq x_0+\tilde{x}, \\ -(A-B)\sinh(\lambda(l+x_0))\cosh(\lambda(l-x))/(AB\sinh(2\lambda l)) \\ -A\sinh(\lambda(l+x_0+\tilde{x}))\cosh(\lambda(l-x))/(AB\sinh(2\lambda l)) \\ \qquad\qquad\qquad\qquad\qquad\qquad \text{if} \quad x_0+\tilde{x} < x \leq l, \end{cases} \tag{3.6}$$

with $\lambda \equiv \sqrt{\kappa/D_v}$, $A = 1+\epsilon-\epsilon_1$ and $B = \epsilon+\epsilon_2$.

The expression (3.6) is plotted for various values of the parameters in Figure 3.2. Notice that the solution is not symmetrical about the origin. Although small in comparison with $1/(\epsilon+\epsilon_2)$, the non-zero source term $(1/(1+\epsilon-\epsilon_1))$ for $x < ct_0$ ensures that the signalling level is slightly higher posterior to the centre of the pulse. It is particularly noticeable in Figure 3.2(c).

Figure 3.2(a) shows the changing profile as $\tilde{x}$ is increased from zero. At $\tilde{x} = 0$ (corresponding to the time just before a signal is emitted) the profile is in an approximate steady state with v low everywhere. As $\tilde{x}$ increases, so does the level of v with the peak being centered in the region $[x_0, x_0+\tilde{x}]$, and moving in a posterior direction as $\tilde{x}$ increases. Figure 3.2(b) shows the profile for various values of the diffusion coefficient D_v. As D_v increases, the signal rapidly becomes less localised. Recall that one of the key requirements in the model equations is that diffusion is large; by increasing the diffusion coefficient D_v, the signal spreads more widely across the domain. Figure 3.2(c) shows a comparison of the NAG numerical solution with the approximation given by equation (3.6). The approximation shows very good agreement with the numerical solution at the beginning of the pulse, while signalling levels are still growing at a rate unaffected by changes in the levels of somitic factor (u). Any error between the two solutions comes from the approximation of the spatial behaviour assumed in equation (3.5).

3.1.2 Analytical expression for the rise in v

We now seek an analytical solution to (2.38). Thereby, we consider

$$\frac{\partial v}{\partial t} - D_v\frac{\partial^2 v}{\partial x^2} + \kappa v \approx \begin{cases} \kappa(1+\epsilon-\epsilon_1)^{-1} & \text{if} \quad x \leq ct_0, \\ \kappa(\epsilon+\epsilon_2)^{-1} & \text{if} \quad ct_0 < x \leq ct, \\ 0 & \text{if} \quad x > ct, \end{cases} \tag{3.7}$$

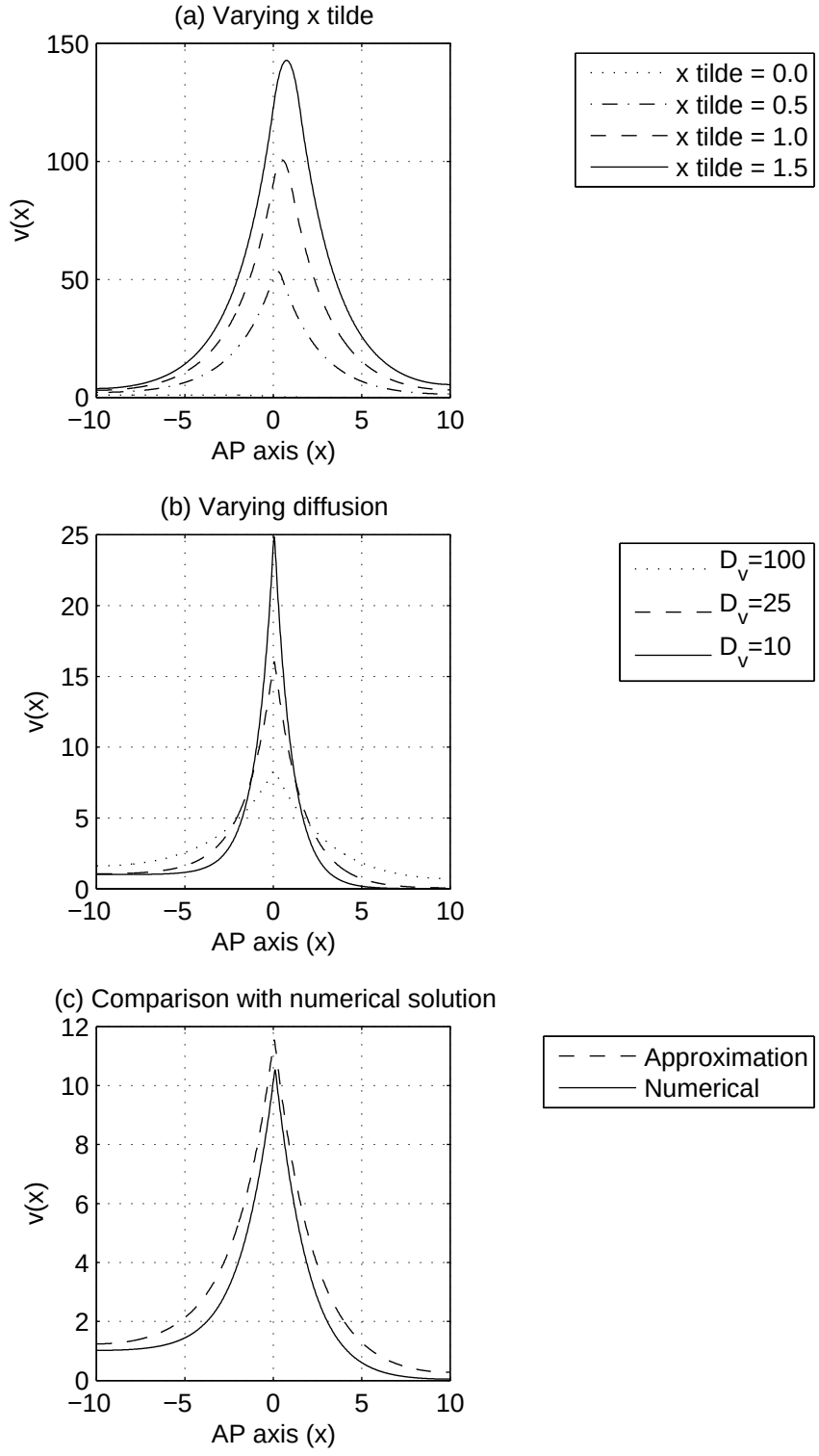


Figure 3.2: Analytic solution (3.6) to the pulse in $v(x,t)$ given by equation (3.5). (a) Varying $\tilde{x}$. (b) Varying diffusion. (c) Comparison with the NAG numerical solution at time $t = 0.2$. The dashed curve is the approximate profile and the solid curve is the profile generated by the NAG numerical solution. Parameters are as follows: $\kappa = 10$, $\gamma = 10^{-2}$, $\mu = 10^{-3}$, $\epsilon = \epsilon_1 = \epsilon_2 = 10^{-3}$, $c = 0.5$ and $x_0 = 0$. $D_v = 50$ and $\tilde{x} = 0.1$ unless otherwise stated.

for $t \geq t_0$. Without loss of generality, we take $t_0 = 0$.

We make a change of variables, so that $y(x,t) = v(x,t)\exp(\kappa t)$ and $y(x,t)$ satisfies

$$\frac{\partial y}{\partial t} - D_v \frac{\partial^2 y}{\partial x^2} \approx \begin{cases} \kappa e^{\kappa t}(1+\epsilon-\epsilon_1)^{-1} & \text{if} \quad x \leq 0, \\ \kappa e^{\kappa t}(\epsilon+\epsilon_2)^{-1} & \text{if} \quad 0 < x \leq ct, \\ 0 & \text{if} \quad x > ct, \end{cases} \tag{3.8}$$

with the same initial and boundary conditions as $v(x,t)$.

3.1.2.1 Solving for a general equation

First we solve for the more general equation

$$\frac{\partial v}{\partial t} = f(x,t) + D\frac{\partial^2 v}{\partial x^2}. \tag{3.9}$$

Taking Fourier Transforms, where

$$\hat{g}(k,t) = \int_{-\infty}^{\infty} g(x,t)e^{ikx}\,dx, \tag{3.10}$$

gives

$$\frac{\partial \hat{y}}{\partial t} + Dk^2\hat{y} = \int_{-\infty}^{\infty} f(x,t)e^{ikx}\,dx. \tag{3.11}$$

Multiplying through by $\exp(Dk^2t)$ and integrating from 0 to t with respect to t gives

$$\int_0^t \frac{\partial}{\partial t'}\left(\hat{y}e^{Dk^2t'}\right)\,dt' = \int_0^t \int_{-\infty}^{\infty} f(x',t')e^{ikx}e^{Dk^2t'}\,dx'\,dt'. \tag{3.12}$$

Therefore

$$\hat{y}(k,t) = \left\{\int_0^t \int_{-\infty}^{\infty} f(x',t')e^{ikx}e^{Dk^2t}\,dx'\,dt'\right\}e^{-Dk^2t} + \hat{y}(k,0)e^{-Dk^2t}. \tag{3.13}$$

Using the Convolution Theorem to invert the Fourier Transforms gives the result

$$\begin{aligned} y(x,t) \quad = \quad & \int_0^t \int_{-\infty}^{\infty} \frac{f(x',t')}{\sqrt{4D\pi(t-t')}} \exp\left[-\frac{(x-x')^2}{4D(t-t')}\right] dx'\,dt' \\ & + \frac{1}{\sqrt{4D\pi t}} \int_{-\infty}^{\infty} y(x',0)\exp\left[-\frac{(x-x')^2}{4Dt}\right] dx'. \end{aligned} \tag{3.14}$$

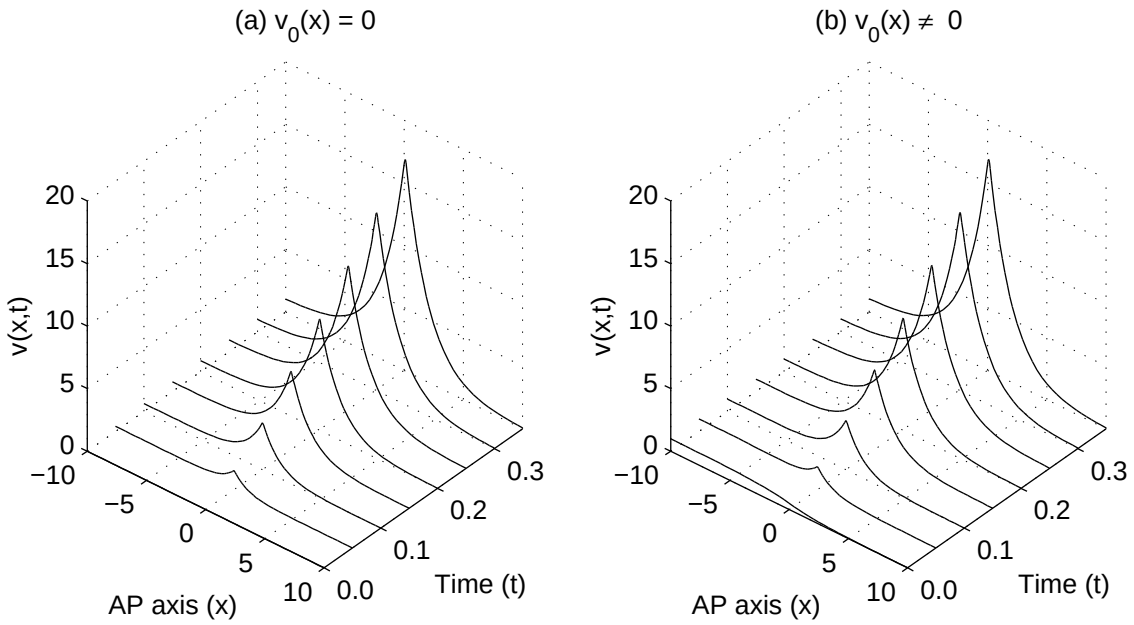


Figure 3.3: Plots of the analytical solution (3.15) for the rise in v. The solution is plotted at time intervals of $\Delta t = 0.05$. (a) $v_0(x) = 0$ and (b) $v_0(x)$ is given by equation (3.22). The initial conditions are quickly absorbed by the pulse in v. Parameters are as follows: $\epsilon = \epsilon_1 = \epsilon_2 = 10^{-3}, D_v = 50$, $c = 0.5$ and $\kappa = 10$.

Using the previous method to solve equation (3.7) we have

$$\begin{aligned} v(x,t) &= \frac{\kappa}{2(1+\epsilon-\epsilon_1)}\int_0^t \left\{1 - \text{erf}\left(\frac{x}{\sqrt{4D_v(t-t')}}\right)\right\} e^{-\kappa(t-t')}\,dt' \\ &+ \frac{\kappa}{2(\epsilon_1+\epsilon_2)}\int_0^t \left\{\text{erf}\left(\frac{x}{\sqrt{4D_v(t-t')}}\right) - \text{erf}\left(\frac{x-ct'}{\sqrt{4D_v(t-t')}}\right)\right\} e^{-\kappa(t-t')}\,dt' \\ &+ \int_{-\infty}^{\infty} \frac{e^{-\kappa t}}{\sqrt{\pi}} v_0(x - \sqrt{4D_v t}z) e^{-z^2}\,dz \end{aligned} \tag{3.15}$$

where $v_0(x)$ is the initial condition for v.

Figure 3.3 shows a plot of the analytical expression for the rise in v given by equation (3.15). Figure 3.3(a) shows the solution with zero initial conditions and Figure 3.3(b) shows the solution with initial conditions given by equation (2.38). Both plots show a rapid rise in v centered about $x = 0$. The initial conditions are rapidly absorbed by the pulse in v and appear to make very little difference to the resulting solution.

We note that McInerney used a δ-function to approximate the pulse in v [28] which whilst giving qualitatively accurate predictions for the pulse in v, could not give quantitatively accurate results without the introduction of a further parameter scaling the effect of the δ-function. The method used

here gives both a quantitatively and qualitatively accurate approximation for the pulse in the signal.

3.1.3 Approximating v in the fourth stage

Our second approximation for the signalling molecule comes from considering Figure 3.1(c): we see that for $t > t^*$, in the region where the non-linear source term is active ($x < ct$), $u \sim 1$. All points in this region have responded to a pulse of v. The parameter constraint $\epsilon \ll 1$, discussed previously, ensures that points which have already responded to a pulse do not trigger another pulse, only points where $u \approx 0$ should signal. Hence for the case when $u \sim 1$ throughout the region where χ_v is active, u can be approximated by $1 - \epsilon_3$ where $\epsilon_3 \ll 1$. Equation (3.3) can then be approximated as [29]

$$Lv \approx \begin{cases} \kappa[(1+\epsilon-\epsilon_3)^{-1} - v] & \text{if} \quad x \leq ct, \\ -\kappa v & \text{if} \quad x > ct, \end{cases} \tag{3.16}$$

where $\epsilon_3 \ll 1$.

The spatial behaviour of v between pulses can be determined from equation (3.16) by solving the ODE

$$\frac{D_v}{\kappa}\frac{d^2v}{dx^2} - v \approx -\frac{H(x_0 - x)}{1+\epsilon-\epsilon_3}, \tag{3.17}$$

where $x_0 = ct$ and the discontinuity in the Heaviside function occurs at x_0. The Heaviside function leads to a discontinuity in the second derivative, that is,

$$\frac{D_v}{\kappa}\frac{d^2v}{dx^2}\Big|_{x_0+\varepsilon}^{x_0-\varepsilon} - v\Big|_{x_0+\varepsilon}^{x_0-\varepsilon} = \frac{1}{1+\epsilon-\epsilon_3}. \tag{3.18}$$

Letting $\varepsilon \to 0$ then for continuous v, we have the following jump condition across $x = x_0$:

$$\left[\frac{d^2v}{dx^2}\right] = \frac{d^2v}{dx^2}\Big|_{x_{0+}} - \frac{\mathrm{d}^2v}{\mathrm{d}x^2}\Big|_{x_{0-}} = -\frac{\kappa}{D_v(1+\epsilon-\epsilon_3)}. \tag{3.19}$$

Using continuity across x_0 along with the jump in the second derivative, equation (3.17) can be solved in a similar manner to equation (3.5), to give

$$v(x,x_0) = \begin{cases} \left[A - \dfrac{1}{1+\epsilon-\epsilon_3}\right]\dfrac{\cosh(\lambda(l+x))}{\cosh(\lambda(l+x_0))} + \dfrac{1}{1+\epsilon-\epsilon_3} & \text{if} \quad -l \leq x \leq x_0, \\ A\dfrac{\cosh(\lambda(l-x))}{\cosh(\lambda(l-x_0))} & \text{if} \quad x_0 < x \leq l, \end{cases} \tag{3.20}$$

with constants A and λ given by

$$A \equiv \frac{(\frac{1}{1+\epsilon-\epsilon_3})\tanh(\lambda(l+x_0))}{\tanh(\lambda(l-x_0)) + \tanh(\lambda(l+x_0))} \quad \text{and} \quad \lambda \equiv \sqrt{\frac{\kappa}{D_v}}. \tag{3.21}$$

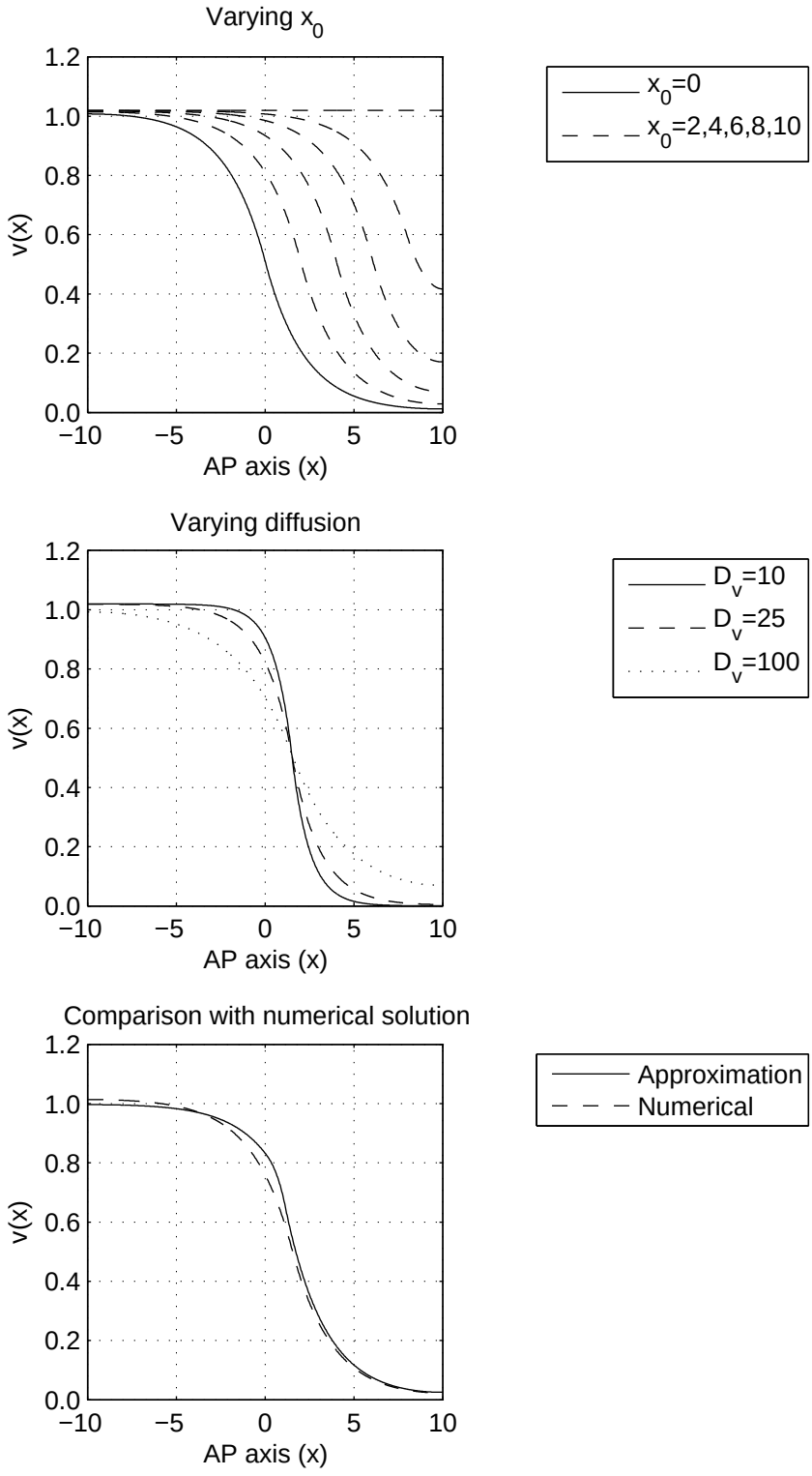


Figure 3.4: Analytic solution (3.20) of equation (3.16) for the behaviour of the signal between pulses. (a) Varying x_0. (b) Varying diffusion. (c) Comparison with the NAG numerical solution at time $t = 2.2$. The dashed curve is the approximate profile and the solid curve is the profile generated by the NAG numerical solution. Parameters are as follows: $\kappa = 10$, $\gamma = 10^{-2}$, $\mu = 10^{-3}$, $\epsilon = \epsilon_1 = \epsilon_2 = 10^{-3}$, $c = 0.5$ and $x_0 = 0$. $D_v = 50$ and $\tilde{x} = 0.1$ unless otherwise stated.

On setting $x_0 = 0$, the solution simplifies to

$$v(x,0) = \frac{H(-x)}{1+\epsilon-\epsilon_3} + A\cosh(\lambda(l-|x|)), \tag{3.22}$$

where

$$A \equiv \frac{\text{sign}(x)}{2(1+\epsilon-\epsilon_3)\cosh(\lambda l)} \quad \text{and} \quad \lambda \equiv \sqrt{\frac{\kappa}{D_v}}. \tag{3.23}$$

Notice that equation (3.22) gives the initial conditions that we used for computing the numerical solutions in Chapter 2.

The spatial behaviour between pulses, given by (3.20), is plotted for various values of x_0 in Figure 3.4(a). As x_0 increases the profile changes and in particular we see that $v(x) \approx 1$ when $x_0 = 10$. This is due to the zero flux boundary conditions. The solution is plotted for various values of the diffusion coefficient D_v in Figure 3.4(b). As D_v is decreased and therefore the distances over which v diffuses becomes limited there is a smooth transition from one to zero around the level $x = 0$ and as D_v increases the transition becomes more blurred. Figure 3.4(c) shows that the approximation given by equation (3.20) is in close agreement with the solution obtained numerically.

3.2 Analysis of the somitic factor equation

The equation describing somitic factor dynamics is

$$\frac{\partial u}{\partial t} = \frac{(u+\mu v)^2}{\gamma+u^2}\chi_u - u. \tag{3.24}$$

Here we will only be interested in cells which have $\chi_u = 1$ and have not already responded to a pulse in the signal v. Cells which have $\chi_u = 0$ have somitic factor dynamics described by the equation

$$\frac{\partial u}{\partial t} = -u \quad \Rightarrow \quad u(x,t) = u(x,0)e^{-t}, \tag{3.25}$$

and cells which have already responded to a signal have gone through the same processes that will be described here, but at an earlier point in time.

Figure 3.5 demonstrates the different domains of t-space within which we need to find approximate solutions for u. Figure 3.5(a) shows the initial stages of somite formation: a rapid rise in v begins at $t \approx 0.0$ (first stage) and activates u production at $t \approx 0.1$. Figure 3.5(b) shows that signalling levels continue to rise unheeded by changes in u concentration until $t \approx 0.2 - 0.3$ (second stage) when u becomes significant in size with ϵ and begins to inhibit v production. At $t \approx 0.4$, v production drops to zero and the continuing rapid rise in u causes v to decrease in a similarly rapid fashion (third stage). Figure 3.5(c) indicates that v remains in an approximate steady state from $t \approx 1.0$ until $t \approx 2.4$ (fourth stage) during which time u continues to grow towards its steady state. Subsequent signals have no noticeable effect on the dynamics of u.

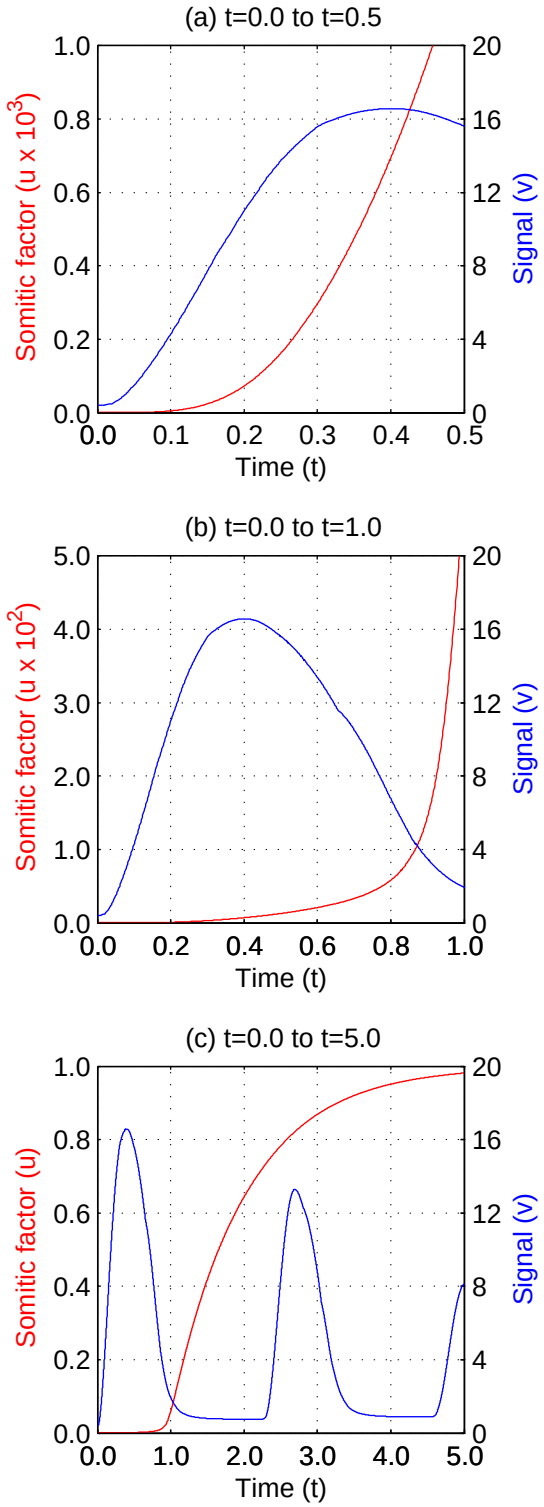


Figure 3.5: The numerical solution of the cell cycle model given by equations (2.7) and (2.8) over a range of different domains in t. Parameters are as follows: $\kappa = 10$, $\gamma = 10^{-2}$, $\mu = 10^{-3}$, $\epsilon = 10^{-3}$, $c = 0.5$ and $D_v = 50$.

We will proceed throughout this section by using the smallness of the parameter γ to make approximations to equation (3.24). Motivation for this comes from the observation that once cells have $u > u_- \approx \gamma$ then u will remain at or above u_- since

$$\frac{\partial u}{\partial t} = \frac{(u_- + \mu v)^2}{\gamma + u_-^2} - u_- \geq \frac{u_-^2}{\gamma + u_-^2} - u_- = 0. \tag{3.26}$$

Hence we need to consider the regimes $u < \mathcal{O}(\gamma)$ and $u > \mathcal{O}(\gamma)$. Note the above is a consequence of the fact that $(u_-, 0)$ is steady state of the system in Region II.

In the first stage we consider the dynamics when both u and v are small with u at most $\mathcal{O}(\gamma)$ and $v = \mathcal{O}(\kappa^{-1})$. In the middle stages, u remains small in comparison with the size of γ but v is now assumed to be large ($\mathcal{O}(\kappa)$). We make assumptions on the form of v to enable analytical approximations to be found for u. In the fourth stage of somite formation and for all subsequent times following this stage (i.e. when other signals propagate) we show that if $u > \mathcal{O}(\gamma)$ then (correct to $\mathcal{O}(1)$) u grows independently of v. Later in Section 3.2 we will find bounds on the validity of the approximations in terms of t and link them back to Figure 3.5. The aim of this section is to understand the exact role of the signal in activating somitic factor production - something that would need to be understood in order to make any significant changes to the model.

3.2.1 Approximating u in the first stage

In the initial stages of a pulse in the signal, levels of both somitic factor and signalling molecule are low. We first make a change of variables by letting

$$u = \gamma \hat{u} \quad \text{and} \quad v = \frac{\hat{v}}{\kappa}, \tag{3.27}$$

which gives a revised equation for the dynamics of u:

$$\frac{\partial \hat{u}}{\partial t} = \frac{(\hat{u} + \gamma \hat{\mu} \hat{v})^2}{1 + \gamma \hat{u}^2} - \hat{u}, \tag{3.28}$$

where $\hat{\mu} = \mu/(\kappa\gamma^2) \sim \mathcal{O}(1)$. We note that with the parameter regime for μ, γ and κ used throughout this work, $\hat{\mu} \approx 10$. In comparison with γ, which has been taken as $\mathcal{O}(10^{-3})$ throughout this work, we will therefore assume that $\hat{\mu} \sim \mathcal{O}(1)$. Given the parameter constraints found in Section 2.2, we require $\hat{\mu} < 1/(4\kappa\gamma)$, where $k \gg 1$ and $\gamma < 1/4$: therefore it seems reasonable to assume that $\hat{\mu}$ will be close to $\mathcal{O}(1)$ in comparison with γ throughout the parameter space.

We approximate $\hat{u}$ and $\hat{v}$ by expanding in terms of γ. Letting

$$\hat{u} = \hat{u}_0 + \gamma \hat{u}_1 + \ldots, \tag{3.29}$$

$$\hat{v} = \hat{v}_0 + \gamma \hat{v}_1 + \ldots, \tag{3.30}$$

where the $\hat{u}_i$ and $\hat{v}_i$ are at most $\mathcal{O}(1)$ for $i = 1, 2, 3, \ldots$, and substituting into equation (3.28) gives

correct to first order in γ:

$$\frac{\partial \hat{u}_0}{\partial t} = \hat{u}_0^2 - \hat{u}_0, \tag{3.31}$$

and correct to second order in γ:

$$\frac{\partial \hat{u}_1}{\partial t} = 2\hat{u}_0(\hat{u}_1 + \hat{\mu}\hat{v}_1)^2 - \hat{u}_0^4 - \hat{u}_1. \tag{3.32}$$

We see that correct to first order in γ, u levels evolve independently of v and therefore we can solve equation (3.31) to obtain

$$\hat{u_0}(t) = \frac{1}{1 - \hat{u}_0^* \exp(t - t_0)}, \quad \text{where} \quad \hat{u}_0^* = \frac{\hat{u}(t_0) - 1}{\hat{u}(t_0)}, \tag{3.33}$$

and t_0 is the time at which the initial stage of the pulse starts.

Taking the initial conditions such that

$$u(t_0) = \gamma\hat{u}(t_0) = \gamma[\hat{u}_0(t_0) + \gamma\hat{u}_1(t_0) + \ldots] \quad \text{and} \quad \hat{u}_i(t_0) = 0 \quad \text{for} \quad i \neq 0, \tag{3.34}$$

gives, correct to $\mathcal{O}(\gamma)$:

$$u(t) = \frac{\gamma}{1 - \hat{u}^* \exp(t - t_0)} \quad \text{where} \quad \hat{u}^* = \frac{u(t_0) - \gamma}{u(t_0)}. \tag{3.35}$$

Figure 3.6 shows a plot of somitic factor levels during the initial stages of a pulse in the signalling molecule. The signal is not strong enough to activate u production and so somitic factor levels decrease monotonically (given that $u(t_0) < \gamma$).

3.2.2 Approximating u in the middle stages

Somitic factor production is activated when signal levels exceed the threshold required to ensure that u_t is positive. Figure 3.7 shows the threshold level of v, above which u_t is positive for all values of u. For the parameters used in Chapter 2, the threshold for the signalling molecule lies around the value $v = 2.5$.

We make similar approximations to those made in the initial stage except that v is now approximately $\mathcal{O}(\kappa)$ and so we take

$$u = \gamma\tilde{u} \quad \text{and} \quad v = \kappa\tilde{v}, \tag{3.36}$$

which gives the revised equation for u:

$$\frac{\partial \tilde{u}}{\partial t} = \frac{(\tilde{u} + \tilde{\mu}\tilde{v})^2}{1 + \gamma\tilde{u}^2} - \tilde{u}, \tag{3.37}$$

where $\tilde{\mu} = \mu\kappa/\gamma \approx \mathcal{O}(1)$. Note that in the parameter regime used in general in this work: $\mu =$

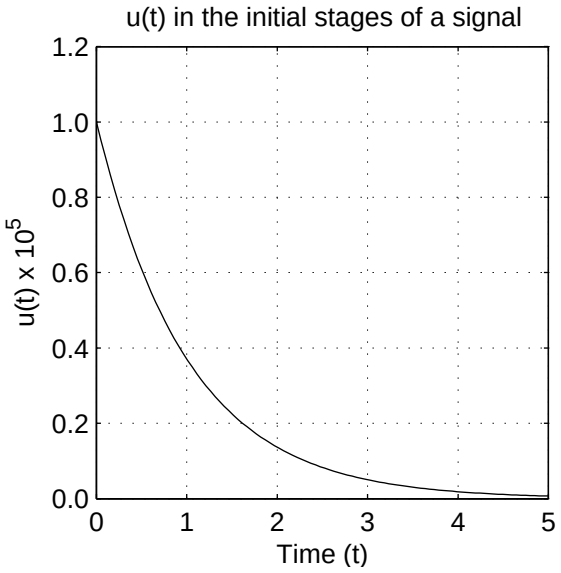


Figure 3.6: Approximate solution given by equation (3.33) for somitic factor levels in the first stage of a pulse in the signalling molecule. Signal levels are still low and not able to activate u production. Parameters are as follows: $\gamma = 10^{-3}$, $t_0 = 0.0$ and $u(0) = 10^{-5}$ (note that this corresponds to $\hat{u}(0) = 10^{-2}$ which is in line with the stipulation that $\hat{u}$ is at most $\mathcal{O}(1)$).

10^{-4}, $\gamma = 10^{-3}$ and $\kappa = 10$, $\tilde{\mu} = 1.0$. Again, we approximate $\tilde{u}$ and $\tilde{v}$ in terms of γ:

$$\tilde{u} = \tilde{u}_0 + \gamma\tilde{u}_1 + \ldots, \tag{3.38}$$

$$\tilde{v} = \tilde{v}_0 + \gamma\tilde{v}_1 + \ldots, \tag{3.39}$$

which, upon substituting into equation (3.37) gives correct to $\mathcal{O}(1)$:

$$\frac{\partial\tilde{u}_0}{\partial t} = (\tilde{u}_0 + \tilde{\mu}\tilde{v}_0)^2 - \tilde{u}_0, \tag{3.40}$$

and correct to $\mathcal{O}(\gamma)$:

$$\frac{\partial\tilde{u}_1}{\partial t} = 2(\tilde{u}_0 + \bar{\mu}\tilde{v}_0)(\tilde{u}_1 + \bar{\mu}\tilde{v}_1) - \tilde{u}_0^2(\tilde{u}_0 + \bar{\mu}\tilde{v}_0)^2 - \tilde{u}_1. \tag{3.41}$$

In order to find an analytical solution to equation (3.40), it is necessary to make some further assumptions on the shape of the signalling pulse. The most obvious choice is to approximate the signal as a series of step functions of the form

$$v = \begin{cases} v_l & \text{if} \quad t \in [s_j, f_j] \\ v_s & \text{if} \quad t \notin [s_j, t_j] \end{cases} = \begin{cases} \kappa\tilde{v}_l & \text{if} \quad t \in [s_j, f_j] \\ \frac{1}{\kappa}\tilde{v}_s & \text{if} \quad t \notin [s_j, t_j] \end{cases} \quad \text{for} \quad j = 1, 2, \ldots . \tag{3.42}$$

$v_l = \mathcal{O}(\kappa)$ approximates the level of v during a pulse in the signal and $v_s = \mathcal{O}\left(\frac{1}{\kappa}\right)$ approximates

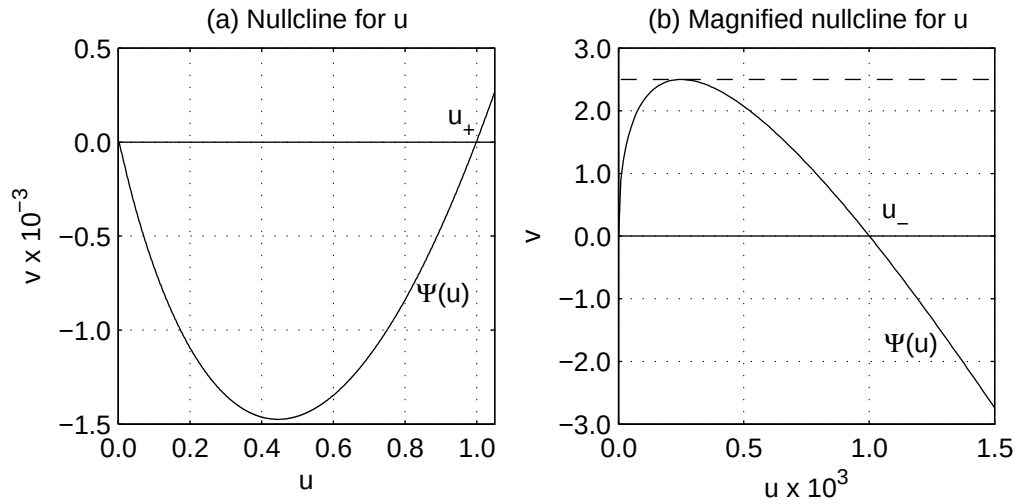


Figure 3.7: (a), (b) The u nullcline, $\Psi(u)$, for the region in which somite formation takes place. (b) demonstrates the existence of a threshold for the signal v, above which u_t is positive for all cells in the PSM. The nullcline is given by $\Psi(u) = \frac{1}{\mu}[-u \pm \sqrt{u(\gamma + u^2)}]$ and the dashed line shows the threshold value for v, above which u_t is positive for all values of u. Parameters are as follows: $\mu = 10^{-4}$ and $\gamma = 10^{-3}$.

the steady state value for the signal. The intervals $[s_j, f_j]$ represent the times at which the pulses in the signal occur. In the middle stages of a signal, $t \in [s_j, f_j]$ for some $j \in \mathbb{N}$ and so equation (3.40) becomes

$$\frac{\partial \tilde{u}_0}{\partial t} = (\tilde{u}_0 + \tilde{\mu}\tilde{v}_l)^2 - \tilde{u}_0, \tag{3.43}$$

which can be solved to obtain

$$\tilde{u}_0(t) = \frac{\lambda_+ - \lambda_- \tilde{u}_0^* \exp{(\lambda_+ - \lambda_-)(t - t_1)}}{1 - \tilde{u}_0^* \exp{(\lambda_+ - \lambda_-)(t - t_1)}}, \tag{3.44}$$

where

$$\tilde{u}_0^* = \frac{(\tilde{u}_0(t_1) - \lambda_+)}{(\tilde{u}_0(t_1) - \lambda_-)}, \qquad \lambda_\pm = \left(\frac{1}{2} - \tilde{\mu}\tilde{v}_l\right) \pm \sqrt{\frac{1}{4} - \tilde{\mu}\tilde{v}_l}, \tag{3.45}$$

and t_1 is the time at which the approximation becomes valid. Since $\tilde{\mu} \approx \mathcal{O}(1)$ and $\tilde{v}_l \approx \mathcal{O}(1)$, it is likely that $\lambda_\pm$ may be complex and we must take the real part of the RHS of equation (3.44).

In a similar fashion to Section 3.2.1 we take

$$u(t_1) = \gamma\tilde{u}(t_1) = \gamma[\tilde{u}_0(t_1) + \gamma\tilde{u}_1(t_1) + \ldots] \quad \text{and} \quad \hat{u}_i(t_1) = 0 \quad \text{for} \quad i \neq 0, \tag{3.46}$$

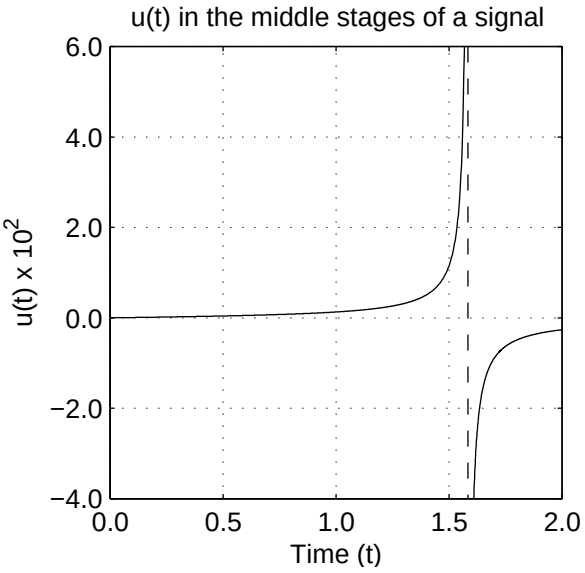


Figure 3.8: Approximate solution for u given by equation (3.47) for somitic factor levels in the middle stages of a pulse in the signalling molecule. Signal levels are high and activate u production. There is an asymptote (dashed line) around $t = 1.6$ as the denominator of the quotient in (3.47) tends to zero. The approximation becomes invalid as u increases much above $\mathcal{O}(\gamma)$ and so the singularity is situated outside the range in which we are interested. Parameters are as follows: $\gamma = 10^{-3}$, $\bar{\mu} = 0.1$, $t_1 = 0.0$, $v_l = 8.0$ and $u(0) = 10^{-5}$.

which gives, correct to first order in γ,

$$u(t) = \frac{\gamma[\lambda_+ - \lambda_- \tilde{u}^* \exp{(\lambda_+ - \lambda_-)(t - t_1)}]}{1 - \tilde{u}^* \exp{(\lambda_+ - \lambda_-)(t - t_1)}}, \tag{3.47}$$

where

$$\tilde{u}^* = \frac{(u(t_1) - \gamma\lambda_+)}{(u(t_1) - \gamma\lambda_-)}, \tag{3.48}$$

and $\lambda_\pm$ are as before.

Figure 3.8 shows a plot of the approximation for u during the intermediate stages of a pulse in the signalling molecule. Signal levels are high throughout the domain and activate u production in the region where $\chi_u = 1$ and somitic factor levels are small. After a slow initial rise, levels increase more and more rapidly as u becomes self-activating. There is a singularity in the solution as $1 - \tilde{u}^* \exp\{(\lambda_+ - \lambda_-)(t - t_1)\} \to 0$; to the LHS of the singularity (i.e. as we approach it from below), $u \to \infty$ and the approximation begins to break down. Looking at the equation for v (2.8 and Figure 3.5), we see that this is because as $u \to \gamma$, v begins to decrease since $\mathcal{O}(\gamma) = \mathcal{O}(\epsilon)$ and u becomes the significant term controlling the rate of production of v: v decreases below $\mathcal{O}(\kappa)$, u increases above $\mathcal{O}(\gamma)$ and the substitutions given by equations (3.36), (3.38) and (3.39) become invalid.

3.2.3 Approximating u in the fourth stage

We show that once u increases past $\mathcal{O}(\gamma)$ signalling levels become irrelevant to the growth of u (correct to $\mathcal{O}(1)$).

While signal (v) levels are still high we can let

$$u = \breve{u} \quad \text{and} \quad v = \kappa\breve{v}, \tag{3.49}$$

which gives the transformed equation for $\breve{u}$:

$$\frac{\partial\breve{u}}{\partial t} = \frac{(\breve{u} + \gamma\breve{\mu}\breve{v})^2}{\gamma + \breve{u}^2} - \breve{u}, \tag{3.50}$$

where $\breve{\mu} = \mu\kappa/\gamma \approx \mathcal{O}(1)$.

Expanding $\breve{u}$ and $\breve{v}$ in terms of γ by writing

$$\breve{u} = \breve{u}_0 + \gamma\breve{u}_1 + \ldots, \tag{3.51}$$
$$\breve{v} = \breve{v}_0 + \gamma\breve{v}_1 + \ldots, \tag{3.52}$$

gives, correct to $\mathcal{O}(1)$ and $\mathcal{O}(\gamma)$:

$$\frac{\partial\breve{u}_0}{\partial t} = 1 - \breve{u}_0, \tag{3.53}$$
$$\frac{\partial\breve{u}_1}{\partial t} = \frac{2(\breve{u}_1 + \breve{\mu}\breve{v}_0)}{\breve{u}_0} - \frac{(1 + 2\breve{u}_0\breve{u}_1)}{\breve{u}_0^2} - \breve{u}_1, \tag{3.54}$$

respectively.

Similarly, supposing that signalling levels have fallen dramatically and are close to the approximate steady state, we let

$$u = \breve{u} \quad \text{and} \quad v = \frac{\breve{v}}{\kappa}, \tag{3.55}$$

which gives the transformed equation for u:

$$\frac{\partial\breve{u}}{\partial t} = \frac{(\breve{u} + \gamma^2\breve{\mu}\breve{v})^2}{\gamma + \breve{u}^2} - \breve{u}, \tag{3.56}$$

where $\breve{\mu} = \mu/(\kappa\gamma^2) \approx \mathcal{O}(1)$.

Expanding $\breve{u}$ and $\breve{v}$ by taking

$$\breve{u} = \breve{u}_0 + \gamma\breve{u}_1 + \ldots, \tag{3.57}$$
$$\breve{v} = \breve{v}_0 + \gamma\breve{v}_1 + \ldots, \tag{3.58}$$

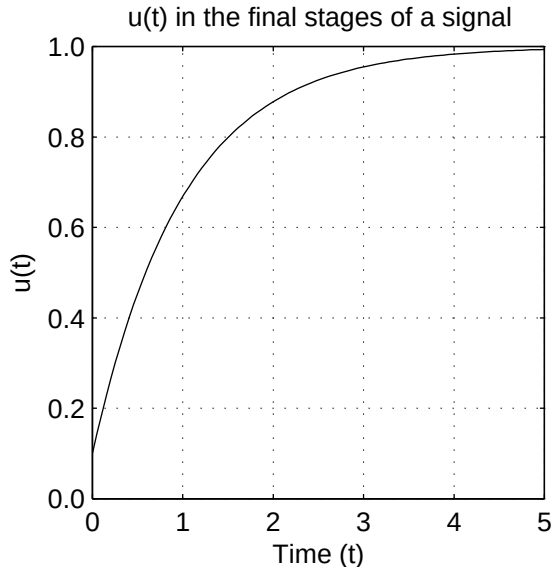


Figure 3.9: Approximate solution given by equation (3.61) for somitic factor levels in the final stages of a pulse in the signalling molecule. Once $u > \mathcal{O}(\gamma)$ then u grows independently of v and as signal levels drop from high to low there is no change in the dynamics of u production (correct to $\mathcal{O}(1)$). Parameters are as follows: $\gamma = 10^{-3}$, $t_2 = 0.0$ and $u(0) = 0.1$.

gives, correct to $\mathcal{O}(1)$ and $\mathcal{O}(\gamma)$:

$$\frac{\partial \breve{u}_0}{\partial t} = 1 - \breve{u}_0, \tag{3.59}$$

$$\frac{\partial \breve{u}_1}{\partial t} = -\frac{1}{\breve{u}_0^2} - \breve{u}_1, \tag{3.60}$$

respectively.

In either case, correct to $\mathcal{O}(1)$, somitic factor levels grow according to the equation

$$u(t) = 1 - [1 - u(t_2)]e^{(t_2 - t)}, \tag{3.61}$$

where t_2 is the time at which the approximation becomes valid and we have assumed

$$u(t_2) = u_0(t_2) + \gamma u_1(t_2) + \ldots \quad \text{and} \quad \hat{u}_i(t_2) = 0 \quad \text{for} \quad i \neq 0. \tag{3.62}$$

Figure 3.9 shows a plot of the dynamics of somitic factor in the final stages of a signal as given by equation (3.61). u continues to increase monotonically towards its high steady state independent of the level of signalling molecule (correct to order one) .

Stage(s)	Order	Approximate solution
First	γ	$u(t) = \dfrac{\gamma}{1-\hat{u}^* e^{(t-t_0)}}$ where $\hat{u}^* = \dfrac{u(t_0)-\gamma}{u(t_0)}$.
Middle	γ	$u(t) = \dfrac{\gamma[\lambda_+ - \lambda_- \tilde{u}^* e^{(\lambda_+-\lambda_-)(t-t_1)}]}{1-\tilde{u}^* e^{(\lambda_+-\lambda_-)(t-t_1)}}$ where $\tilde{u}^* = \dfrac{(u(t_1)-\gamma\lambda_+)}{(u(t_1)-\gamma\lambda_-)}$.
Fourth	1	$u(t) = 1 - [1-u(t_2)]e^{(t_2-t)}$.

Table 3.1: The different approximate solutions for the somitic factor along with the order to which the solution is accurate and the stage(s) of somite formation for which the approximation is valid.

3.2.4 Domains of validity

Thus far we have found approximate solutions for u during three stages of somite formation. Table 3.1 shows a summary of the results which includes the order to which the approximation is valid and the stage within which each approximation is valid. We will consider each stage and its corresponding approximation separately to analyse the domain of t-space over which the assumptions providing the approximation remain valid.

First stage The first stage of somite formation assumes that although a signal in v is just beginning to propagate, signalling levels are not yet high enough to activate u production. Figure 3.7 shows that for the parameters used throughout this model, the threshold level of signal, v_{th}, that ensures $u_t > 0$ wherever $\chi_u = 1$, is approximately $v_{th} = 2.5$. From Figure 3.5 we can conclude that for the parameters used in this model the first stage of somite formation is very short, lasting in the region of $t \approx 0.05 - 0.1$.

Middle stages Figure 3.8 demonstrates the existence of a singularity in the approximation for v in the middle stages. From Table 3.1 we see that as

$$1 - \tilde{u}^* \exp{(\lambda_+ - \lambda_-)(t - t_1)} \to 0, \tag{3.63}$$

or as

$$t \to t_m = t_1 - \frac{1}{\lambda_+ - \lambda_-} \ln \tilde{u}^*, \tag{3.64}$$

then $u \to \infty$. For the parameters used in Figure 3.8, $t_m = 1.58$ (2 d.p.).

The approximations for the middle stages of somite formation are derived under the assumption that

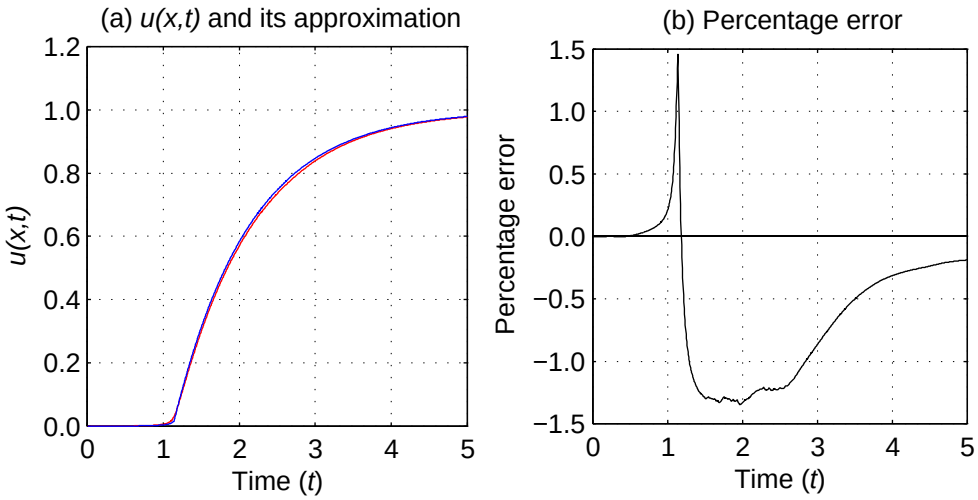


Figure 3.10: (a) Plots of the NAG numerical solution (red) at $x = 0.45$ along with the approximate solution for $u(t)$ (blue) given by joining the approximate solutions of equations (3.33), (3.47) and (3.61). It is hard to differentiate between the 2 plots which indicates a close fitting approximation. (b) A plot of the percentage error between the NAG numerical solution and the approximate solution plotted in (a). Although the error is significant for small t, it quickly decreases at $t \to \infty$. In part the error may be due to bad choices for the parameters t_0, t_1 and t_2, but we must also take into account that this is the region where we switch between approximations. Parameters are as follows: $\kappa = 10$, $\gamma = 10^{-3}$, $\epsilon = 10^{-3}$, $\mu = 10^{-4}$, $D_v = 50$, $c = 0.5$, $t_0 = 0.0$, $t_1 = 0.25$, $t_2 = 1.14$, $v_l = 8.12$ and $u(0) = 10^{-5}$.

u is at most $\mathcal{O}(\gamma)$ and so we see that the approximation for u will become invalid when u increases past $\mathcal{O}(\gamma)$, and hence before t reaches t_m. From Figure 3.8 we estimate that the solution remains valid for approximately $t \approx 0.75 - 1.0$.

Fourth stage From the analysis of Section 3.2.3 we see that once u increases above $\mathcal{O}(\gamma)$, subsequent growth continues according to the relation $u_t = 1 - u$, regardless of the order of v. Therefore, once u enters the fourth stage, the approximation given in Section 3.2.3 holds for all further time.

3.2.5 Comparison with the numerical solution

By joining the three approximations together (at $t = t_1$ and $t = t_2$) we are able to compare the accuracy of our analytical solutions with the computed numerical solution. There will be unavoidable discontinuities in the derivative u_t at these points.

Figure 3.10(a) shows a plot of the NAG numerical solution along with the approximate solution constructed as described. The approximation appears to fit the computed numerical solution very closely. Figure 3.10(b) shows the percentage error between the two solutions and reveals only slight relative errors in the regions where the solution changes from the analytical solution for the middle stages to the analytical solution for the final stages. Although some error may be due to choice of

the parameters t_0, t_1 and t_2 which control the points at which we switch from one approximation for u to another, this error is to be expected as it coincides with a region where u is still relatively small and the dynamics of u and v are heavily interlinked. The percentage error is calculated according to the formula

$$\text{Percentage error} = \frac{u_{num} - u_{approx}}{u_{num}}\text{x}100, \tag{3.65}$$

where u_{num} is the numerical solution evaluated at some point x and u_{approx} is the corresponding approximate solution.

Finally, we comment on the choice of v_l in Figure 3.10: v_l was chosen to provide a good fit with the numerical simulation to demonstrate the accuracy of the approximation. This choice is heavily dependent on the value of x at which we chose to match the simulation since each cell begins making somitic factor at a slightly different point in time, and with a different initial value of somitic factor (see Section 3.3 for more details).

3.3 The posterior boundary of the somite

As we showed in Section 3.2, there is a threshold level of v above which $u_t > 0$ for all cells which have $\chi_u = 1$ and a threshold level for u above which $u_t > 0$ for all subsequent time. We see from this that cells which have responded to a signal by increasing their level of somitic factor above this threshold, u_{th}, cannot be 'switched off' again; they will go on to form part of a somite. For cells which begin making somitic factor but do not make enough to reach u_{th}, somitic factor levels will begin to decrease again once the pulse in v has ended and v is in its approximate steady state. This is demonstrated in Figure 3.11. Cells lying at the levels $x = 0.2$ and $x = 0.9$ are subjected to high signalling levels whilst $\chi_u = 1$ and are incorporated into the first somite. Cells lying in more posterior positions (at $x = 1.2$ and $x = 1.3$ for example) do not have u production switched on until part way through the first signal and are subsequently unable to make enough somitic factor to reach u_{th}. Once the pulse of signal has passed, such cells cannot make somitic factor and levels decrease until a second pulse occurs at about $t = 2.5$, whereupon they become part of the second somite.

The posterior boundary of each somite will therefore be determined by the cells which produce enough somitic factor during a signal to ensure that $u > u_{th}$. In between pulses of the signalling molecule, v is in an approximately steady state with $v \approx \mathcal{O}(10^{-1})$ in the parameter regime considered here. Figure 3.12 shows the u nullcline given by

$$\Psi(u) = \frac{1}{\mu}[-u \pm \sqrt{u(\gamma + u^2)}], \tag{3.66}$$

with the approximate steady state value for v (v_s) and the corresponding u threshold (u_{th}) clearly marked.

If we assume that v reaches its steady state at some notional time t^*, then we know that the posterior boundary of the somite is defined by those cells which have $u(t^*) > u_{th}$. In order to use the

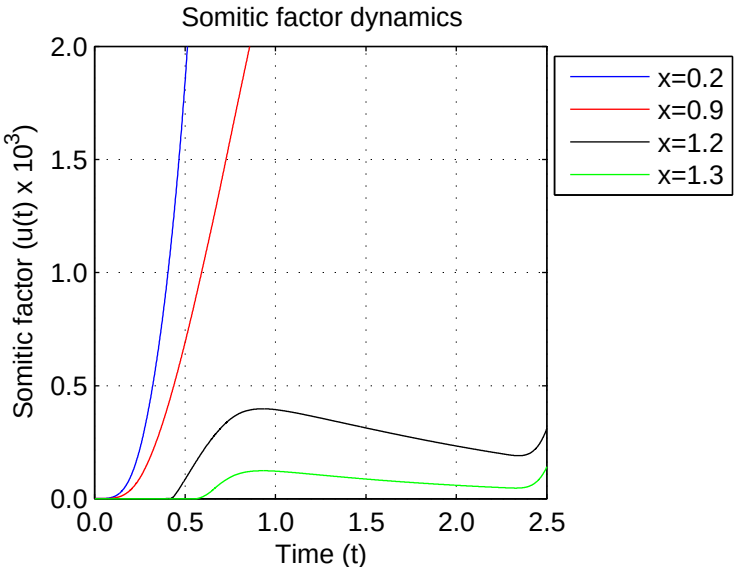


Figure 3.11: Plots of the NAG numerical solution of equations (2.7) and (2.8) at various points x during the first and second signals. Cells situated at $x = 0.2$ and $x = 0.9$ have long enough to make sufficient somitic factor to reach u_{th} and are incorporated into the first somite. Although cells at $x = 1.2$ and $x = 1.3$ begin to make somitic factor, signal levels do not remain high for long enough for them to reach u_{th} and levels begin to decrease after about $t = 1.0$. Following the second signal (just before $t = 2.5$) such cells quickly become part of the second somite. Parameters are as follows: $\mu = 10^{-4}$, $c = 0.5$, $\kappa = 10$, $\epsilon = 10^{-3}$, $D_v = 50$ and $\gamma = 10^{-3}$.

assumptions made above, we need to translate this condition into terms used in the specification of v.

Firstly, we will assume that initial somitic factor levels are $u(0) = 10^{-6}$; this is a reasonable assumption since cells which are situated near the posterior boundary of the somite will not have any previous 'experience' of a pulse in v whilst they have $\chi_u > 0$ and therefore never had an opportunity to produce u. We will also assume that $u_{th} \approx \mathcal{O}(\gamma)$ and hence we are working somewhere in the middle stages of the approximation.

In order to be able to make some analytical approximations to the posterior boundary of the somite we make the same assumption about the form of the signal as in the previous section. That is,

$$v = \begin{cases} v_l & \text{if} \quad t \in [s_j, f_j], \\ v_s & \text{if} \quad t \notin [s_j, f_j], \end{cases} \tag{3.67}$$

which allows us to use the corresponding approximations for the somitic factor levels.

Given that u is initially equal to $u(0)$ we can use equation (3.47) to estimate the time at which u

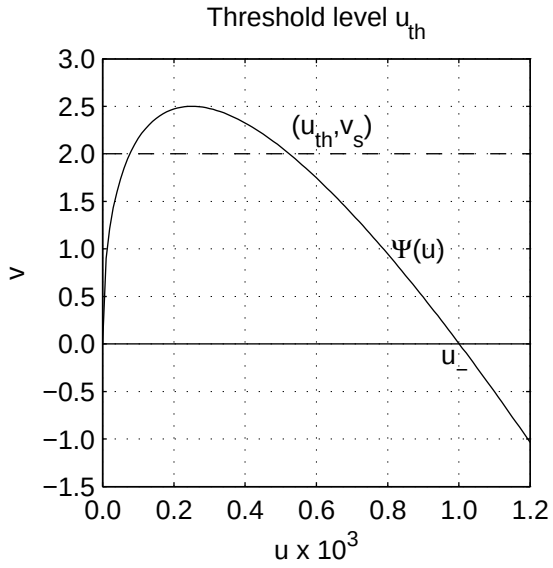


Figure 3.12: Plot of the u nullcline given by equation (2.15) with the threshold level u_{th} marked. Once $u > u_{th}$ then $u_t > 0$ for all subsequent time whatever the level of signal present. Parameters are as follows: $\gamma = 0.2$ and $\mu = 0.1$.

reaches u_{th} as being

$$\tilde{t} = \frac{1}{\lambda_+ - \lambda_-} \log \left[\frac{1}{\tilde{u}^*} \left(\frac{\gamma\lambda_+ - u_{th}}{\gamma\lambda_- - u_{th}} \right) \right] \quad \text{where} \quad \tilde{u}^* = \frac{u(0) - \gamma\lambda_+}{u(0) - \gamma\lambda_-}, \tag{3.68}$$

and $\lambda_\pm$ are as defined in equation (3.45). So for a cell to become incorporated into the j^{th} somite we must have

$$f_j - t > \tilde{t}, \tag{3.69}$$

where t is the time at which the χ_u gets switched on for that cell.

Figure 3.13 shows a plot of the relationship between $v_l = \kappa\tilde{v}_l$ (the approximate pulse level of signal) and the time taken to reach the somitic factor threshold u_{th}. The solution is discontinuous at $\tilde{v}_l = 0.4$ as the argument of the $\log$ term in equation (3.68) goes through one (from below). To ensure that we have a feasible solution for $\tilde{t}$ we must therefore ensure that $\tilde{v}_l > 0.4$ in any calculations.

It should also be noted that in order to ensure that $u_t > 0$ (see equation (3.43)) we must take $\lambda_- > u_{th}$: the nullcline for u_1 is given by the quadratic

$$(\tilde{u}_0 + \tilde{\mu}\tilde{v})^2 - \tilde{u}_0 = 0, \tag{3.70}$$

which has roots given by $\lambda_\pm = (1/2 - \tilde{\mu}\tilde{v}_l) \pm \sqrt{1/4 - \tilde{\mu}\tilde{v}_l}$. If $\tilde{\mu}\tilde{v}_l > 1/4$ then $\lambda_\pm \in \mathbb{C}$ and $u_t > 0$, but if $\tilde{\mu}\tilde{v}_l < 1/4$ then $\lambda_\pm \in \mathbb{R}_+$ and we must have $u_{th} < \lambda_-$ to ensure that $u_t > 0 \; \forall u < u_{th}$.

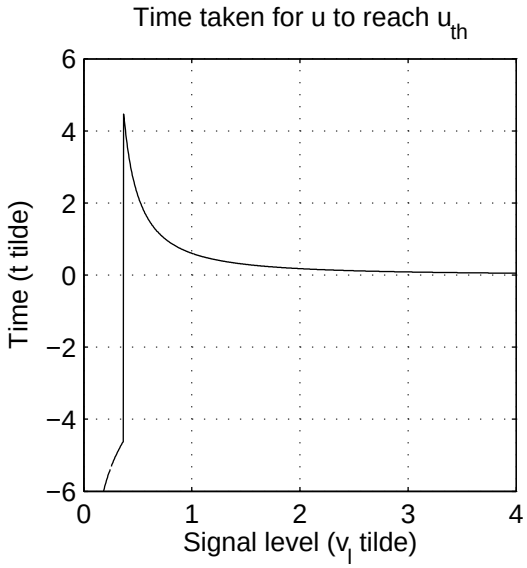


Figure 3.13: Plot of the time taken to reach the threshold value u_{th} of somitic factor as a function of the approximate signal pulse value $\tilde{v}_l$. As $\tilde{t}$ goes through zero there is a discontinuity due to the argument of the $\log$ term going through the value one (from below). Once the time taken to reach the threshold ($\tilde{t}$) becomes positive (i.e. feasible, in the sense that for the parameters chosen here, if $\tilde{v}_l < 0.4$ then u will never reach u_{th}) then $\tilde{t}$ decreases monotonically as $\tilde{v}_l$ is increased. Parameters are as follows: $\tilde{\mu} = 1.0$, $\kappa = 10$, $\gamma = 10^{-3}$, $u(0) = 10^{-5}$ and $u_{th} = 10^{-3}$.

Supposing that $\tilde{v}_l = 0.8$ then the time taken to reach $u_{th} = 10^{-3}$ is approximately $\tilde{t} = 0.8$. Assuming that the first signal starts at $t = 0$ and lasts for one time unit, then the first somite boundary will lie at approximately $x = (1.0 - 0.8).0.5 + 1 = 1.1$. The next pulse should begin when the discontinuity in χ_v reaches $x = 1.1$, which will be at time $t = 1.1/c = 2.2$. The second somite boundary can then be found to lie at $x = (3.2 - \tilde{t})c + 1 = 2.2$ *etc.*

Continuing in this manner we see that given $\tilde{t}$, the time taken to reach u_{th}, and a signal lasting for time $t_s > \tilde{t}$, somites will be approximately of length

$$\tilde{x} = (t_s - \tilde{t})c + 1, \tag{3.71}$$

with successive signals beginning at times

$$s_j = \left[(t_s - \tilde{t}) + \frac{1}{c}\right](j - 1). \tag{3.72}$$

We verify this (very approximately) using previous numerical simulations: From the results of Chapter 2 we see that with the parameters used throughout our numerical computations, somites are of approximate length 1.2-1.4 spatial units and signals are emitted approximately once every 2.3-2.4 time units. Estimating $\tilde{t} \approx 1.0 - 1.2$ and t_s, the time for which the peak in the signal lasts,

to be $t_s \approx 0.6 - 0.8$, we have (noting $c = 0.5$):

$$\tilde{x} = (t_s - \tilde{t})c + 1 \approx 1.1 - 1.3, \tag{3.73}$$

for the size of somites and

$$s_{j+1} - s_j = \left[(t_s - \tilde{t}) + \frac{1}{c}\right] \approx 2.2 - 2.6. \tag{3.74}$$

for the time between successive signals.

3.4 Discussion

We began this chapter by dividing the somitogenic process into four stages: the initiation of a signal, the beginnings of somitic factor production, the decay of the signal and the approach to the steady state, and we proceeded to consider u and v separately in each region.

We began our analysis of the signal dynamics by approximating the dynamics of u (and hence the production terms for v) as a combination of step functions. We solved the resulting approximation to find the spatial behaviour of a pulse in the signal and found very good agreement with our numerical results of Chapter 2. We also solved the same approximation analytically and observed the rapid rise in v as the start of a pulse. The time scale on which these approximations are valid is quite short (of the order $\mathcal{O}(10^{-1})$ time units) as a result of the growth in somitic factor levels generated by the signal itself.

In the final stages of a signal, both u and v are in an approximate steady state and so once again we constructed a spatial approximation for the signal using a series of step functions for u. These results also compared favourably with the numerical results obtained in Chapter 2.

It is very hard to gain any further insight into the signalling process and we justify our approximations for u by arguing that the method described in this chapter is probably one of the only ones that gives a good approximation for v both qualitatively and quantitatively and is solvable analytically. McInerney [28] uses a δ-function approach but this involves the introduction of another parameter controlling the size of the spike and does not give quantitatively accurate results.

In order to gain further understanding of the dynamics of the somitic factor concentration we exploited the presence of the small parameter γ: once cells reach a threshold level of u that is approximately equal to γ, they have $u_t > 0$ and hence cells will continue producing somitic factor for all subsequent time. We found approximate solutions for u in each of three parameter regimes (similarly, by assuming that v took the form of a step function) and we discussed their domains of validity. We note from this investigation that virtually the sole role of the signal is to nudge somitic factor levels over the threshold - this would be important to note when making any changes to the model (and more specifically the signalling equation).

Any failings with this approximation come from the step function approximation used for the signal in the third stage and also from the fact that we were only able to find analytical solutions for u

correct to $\mathcal{O}(1)$. Despite this, patching together the approximations in each region of t-space gave an overall approximation for u that was in very close agreement with the numerical solution of the system in Chapter 2.

The final part of the chapter concentrated on finding the position of the posterior boundary of each somite: this is defined by the number of cells which experience enough of a pulse in the signal, whilst they are competent to produce somitic factor, to enable them to reach a stage where $u_t > 0$ regardless of the value of v. Once more, we approximated the signal by a series of step functions and found an analytical expression for the time taken for cells to reach the threshold level of u such that $u_t > 0$ for all further time. We verified our predictions (very approximately) using the numerical results of Chapter 2.

We should note that the reason for the temporal rounding of the posterior part of somite edges (see Figure 2.7) emerges from the final part of this chapter: cells which lie near the posterior boundary of a somite will gain the ability to produce somitic factor a short period of time later than the remaining cells in that somite. Once cells reach a certain level of u, they become self-activating and their production rate of u increases very rapidly (until they near their steady state). Cells of the posterior edge of the somite will be delayed in reaching this point and so we see a curved edge to the somite in x, t-space.

3.4.1 Validity of the cell cycle model

In light of recent experimental findings, we now question whether the cell cycle model can still be used as a valid mechanism for somite formation. Although there is a wide variety of evidence to suggest that some kind of molecular oscillator does exist in the PSM [7, 16, 27, 37], the results of Stern and co-workers [44, 45, 54, 55] on the existence of discrete regions of cell cycle synchrony along the PSM are now somewhat disputed given the repetition of their experiments with new technology [42].

Equally importantly, it has recently been shown that expression of the fibroblast growth factor FGF8 has important consequences for somite formation. Dubrulle and co-workers have shown the existence of a wavefront of FGF8 expression in the embryo which moves in a posterior direction as development proceeds, and interacts with the segmentation clock to gate cells into somites [15]. Perturbation of FGF8 expression causes somite anomalies in a region local to the disturbance of the wavefront.

The cell cycle model relies heavily on the existence of cell synchrony in the PSM and does not have any mechanism to take into account the effects of FGF8 perturbation in the PSM. In the next chapter, we review the experimental findings of Dubrulle and co-workers and propose a modification to the cell cycle model that uses the interaction of a segmentation clock and the FGF8 wavefront to gate cells into somites.

Chapter 4

FGF8 expression in the embryo

As mentioned in Chapter 1, fgf8 has been found to play an important part in the process of somite formation. Dubrulle and co-workers [15] and Sawada and co-workers [47] have carried out a number of experiments on chick and fish embryos to determine the role of fgf8 in somitogenesis. In this chapter, we present a summary of their main findings and propose a model to explain how fgf8 signalling interacts with the segmentation clock to control somitogenesis.

4.1 Experimental evidence

The experimental findings of Dubrulle and co-workers [15] and Sawada and co-workers [47] can be classified into a number of discrete areas. Firstly, there are results relating to the commitment of cells to a certain developmental pathway, secondly, results relating to fgf8 expression in the PSM and the consequences of perturbation of this expression and thirdly, results relating to the manner in which fgf8 mRNA (*fgf8*) and protein (FGF8) profiles are maintained. We detail the main findings in each area below.

4.1.1 Segmental determination

Dubrulle and co-workers [15] use micro-surgical inversions of the PSM to show that in the chick the PSM is a non-homogeneous tissue divided into two parts: the posterior-most two-thirds where the cells are arranged in a loose mesenchymal manner, and the remaining anterior third where cell arrangement has become more compact and the epithelialisation process underlying somite formation has already begun. The posterior part of the PSM shows normal segmentation when small fragments are removed and replaced in an inverted position, whereas inversion of anterior PSM fragments gives rise to irregular segmentation patterns, indicating some degree of segmental determination [41]. Determination refers to the irreversible commitment of a cell to a particular developmental pathway.

It was using the above experiments that Dubrulle and co-workers were able to demonstrate the existence of a ‘determination front’ around the level of somite -IV: cells lying between somites 0

and -IV are not labile with respect to their segmentation schedule (determined), while cells lying in somites -V to -XII proceed with normal segmentation patterns (undetermined). Sawada and co-workers [47] carried out similar experiments on the zebrafish; they suggest that somites -IV to -V represent a position at which cells become competent to respond to maturation signals.

4.1.2 fgf8 expression within the PSM

fgf8 (mRNA) is expressed in the PSM on a domain which is coincident with the undetermined region of cells. High expression occurs in the posterior-most part of the PSM and levels are found to decrease in a graded fashion up to the level of the determination front [15, 47] (the interface between the determined and undetermined zones). FGF8 (protein) is also expressed in a graded fashion along the PSM together with another molecule AKT which is produced from activation of the PI3 pathway by FGF signalling. Therefore the *fgf8* gradient is translated into a gradient of FGF8 signalling across the PSM [41].

Disruption of the fgf8 signalling gradient by huge over-expression of *fgf8* blocks segmentation completely and maintains the characteristics of cells in the posterior region of the PSM. Dubrulle and co-workers [15, p. 220] suggest that "FGF8 is sufficient to maintain the caudal identity of PSM cells and that down-regulation of FGF signalling in the PSM at the level of the determination front is required for cells to proceed further with their segmentation program."

As development proceeds the body axis lengthens and the determination front moves in a posterior direction at the same rate at which axis extension occurs. Cells which were initially part of the region where FGF signalling prevails begin to experience lower levels of FGF8 as the gradient recedes. Eventually they reach the region where FGF signalling is low and are able to activate their segmentation program. Figure 4.1 illustrates the vertebrate body plan during somite formation, with the determination front, and regions of high and low FGF8 clearly marked.

4.1.2.1 Specific FGF8 perturbation

Dubrulle and co-workers [15] and Sawada and co-workers [47] consider the effect of local application of FGF8 on cells in the PSM. Grafting of FGF8 soaked beads between the PSM and the lateral mesoderm ensures that the bead remains in a fixed location in the PSM while the gradient of endogenous FGF8 is progressively displaced along the PSM axis. The result is formation of abnormally small somites on the grafted side, extending for a distance of up to 6–7 somites rostral to the bead, with one abnormally large somite forming caudal to the bead such that the sequence of affected somites falls back into register with the control side. Figure 4.2 shows the results *in vivo* when an FGF8 bead is implanted alongside the PSM and demonstrates the formation of smaller somites anterior to the bead.

Implantation of the bead within the PSM causes a total absence of somite boundaries in up to 3 somites rostral to the bead and 3 abnormally small somites immediately rostral to this zone. No effect was ever detected rostral to somite -IV at the time of the implant, which can be explained by assuming that response to FGF8 signalling ceases in determined cells.

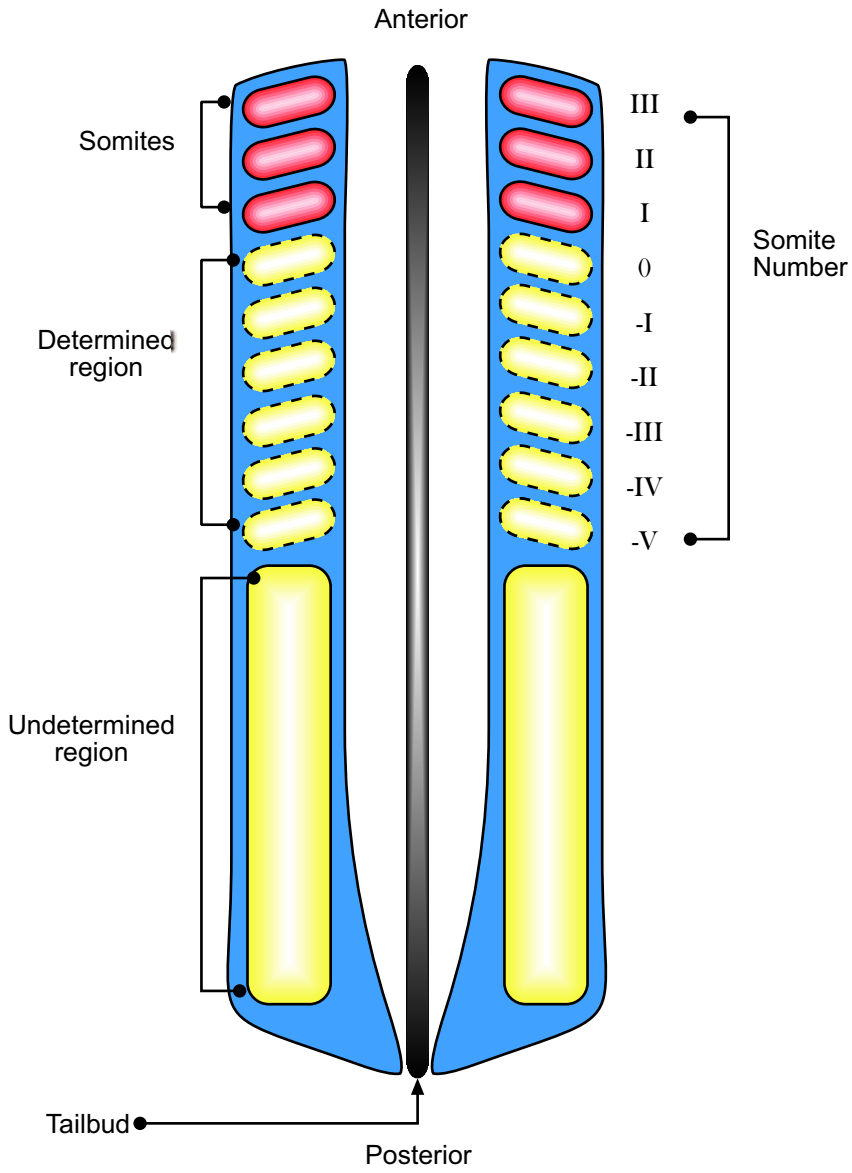


Figure 4.1: An illustration of the vertebrate body plan during somite formation. The red blocks denote individual somites, the yellow blocks denote the determined region of cells with the pre-pattern of somites and the yellow bands represent the undetermined regions of the PSM. There is a determination front at the level of somite $-V$ which divides the PSM into two distinct regions; one where the epithelialisation process has begun (low FGF8) and the other where the cells are still in an immature state (high FGF8).

Experimental evidence suggests that the abnormally small somites formed as a result of FGF8 grafting [15, 47] show a 17-33% decrease in the number of cells recruited into each somite with no significant increase in cell death or compaction, or decrease in cell proliferation. So local application of FGF8 reduces the number of cells incorporated into each somite by changing the positioning of

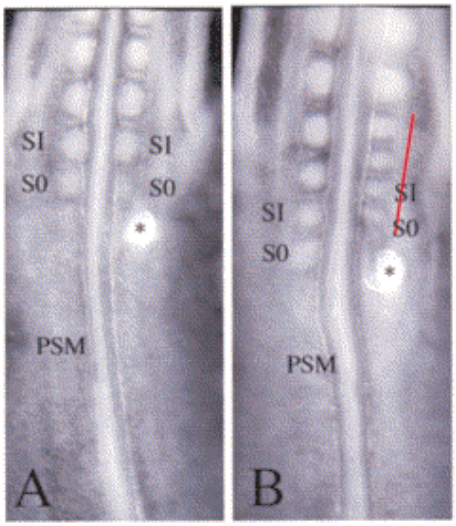


Figure 4.2: Implantation of an FGF8 bead reduces the number of cells allocated to somites: (A) shows an embryo with a control bead and (B) shows an embryo with a bead soaked in FGF8. The position of the bead implant is marked with an asterisk (inside the white circle) and the region over which small somites form is indicated by the red bar. Reprinted from Cell, Vol. 106, J. Dubrulle, M. J. McGrew, O. Pourquié, FGF8 signalling controls somite boundary formation and regulates segmentation clock control of spatiotemporal *Hox* gene activation, pp 219-232, Copyright (2001), with permission from Elsevier and Olivier Pourquié.

somite boundaries but without changing the absolute positions of cells within the PSM.

4.1.3 Maintenance of the FGF8 gradient

Figure 4.3 depicts two possible mechanisms for gradient formation along the AP axis. In both mechanisms, *fgf8* transcription is restricted to the growing posterior tip of the embryo [17]. With the outgrowth mechanism, Figure 4.3(a), as the axis elongates, cells leave the tip and their mRNA levels decrease as *fgf8* is progressively degraded. FGF8 is translated by the remaining *fgf8* and is able to diffuse along the PSM creating a graded FGF8 profile along the embryo. The other mechanism, depicted in Figure 4.3(b), assumes that once cells leave the tailbud they have no *fgf8* and so cannot produce FGF8. The only source of FGF8 comes via diffusion of protein translated by cells still in the tailbud.

Depending on the relative rates of decay of mRNA and protein and the ease with which FGF8 is able to diffuse along the PSM it may be that the gradients produced by the two mechanisms have markedly different shapes and as a result can produce more or less fine grained patterning. Consider the mechanism for gradient formation outlined in Figure 4.3(b): if either (or both) diffusion of FGF8 is very limited or FGF8 is a very unstable protein then it may be that the resulting gradient of FGF8 is very steep and exists over a length scale that is inconsistent with the length of the PSM. This may result in the determination front (region where FGF8 expression drops from high to low) being

misplaced or make fine-grained patterning of the PSM impossible. The outgrowth mechanism for gradient formation would allow a more shallow profile to become established as FGF8 is produced locally by cells outside the tip.

Dubrulle and co-workers [17] believe that the outgrowth mechanism is the one responsible for the FGF8 gradient along the PSM; it seems that the global gradient of FGF8, which is integral for the positioning of somite boundaries, is formed by the "locally restricted expression of a gene encoding a secreted protein signal" (the gene transcribes the mRNA which then is translated into the protein) [48, p. 404]. In the following sections of this chapter we explore both mechanisms for gradient formation and show that under certain parameter conditions, the outgrowth mechanism for gradient formation can be approximated by assuming that FGF8 production is restricted to the tip of the embryo. As yet, there are no estimates for any of the parameters involved in gradient formation.

4.2 A new clock and wavefront model for somitogenesis

Following [15, 58, 60], we hypothesise that there is some interaction between the level of FGF8 in the PSM and the segmentation clock that gates the cells into potential somites.

In a control embryo, a spatially varying FGF8 concentration profile exists along the PSM: a high level of expression is present in the most caudal cells, and this level decreases in a graded fashion down to the level of the determination front. This is illustrated in Figure 4.4(a). Following Dubrulle and co-workers [15], we assume that for a cell at a particular point, competence to segment will only be achieved when FGF8 signalling has decreased below a certain threshold level, this level being that expressed at the position of the determination front. The spatial profile of FGF8 will regress along with the node, ensuring that the relative position of the determination front stays at a constant level in the PSM throughout somitogenesis, as is consistent with experimental data. Hence, at any point in the PSM, the concentration of FGF8 will decrease monotonically over time. Massive over-expression of FGF8 throughout the PSM would cause this spatially-varying profile to be 'wiped out', and the level of FGF8 expression to be too large throughout the PSM to allow somite formation. This is consistent with experimental observations in which ectopic FGF8 expression throughout the PSM causes cells to remain unsegmented, as if they were "forever young" [60], and our model predicts that somite formation would not occur.

Since FGF8 signalling has no effect on the period of oscillation of the cycling genes [15], we propose that it does not alter the timing of the segmentation clock. In this way, we propose a mechanism for segmentation in line with [15, 58] in which the clock controls when the boundaries of the somites will form and FGF8 signalling controls where the boundaries of the somites will form. Once cells have reached the determination front they become able to segment, and then a certain time t_s later cells will become competent to signal. t_s will be equal to the period of the segmentation clock which is coincident with the period of the cycling genes. We will assume that a cell changes its response to FGF8 signalling once it has passed the determination front: essentially we will assume that a cell becomes refractory to FGF8 signalling once it has passed this point. Figure 4.5 illustrates the interaction between the segmentation clock and the determination front as postulated in our model.

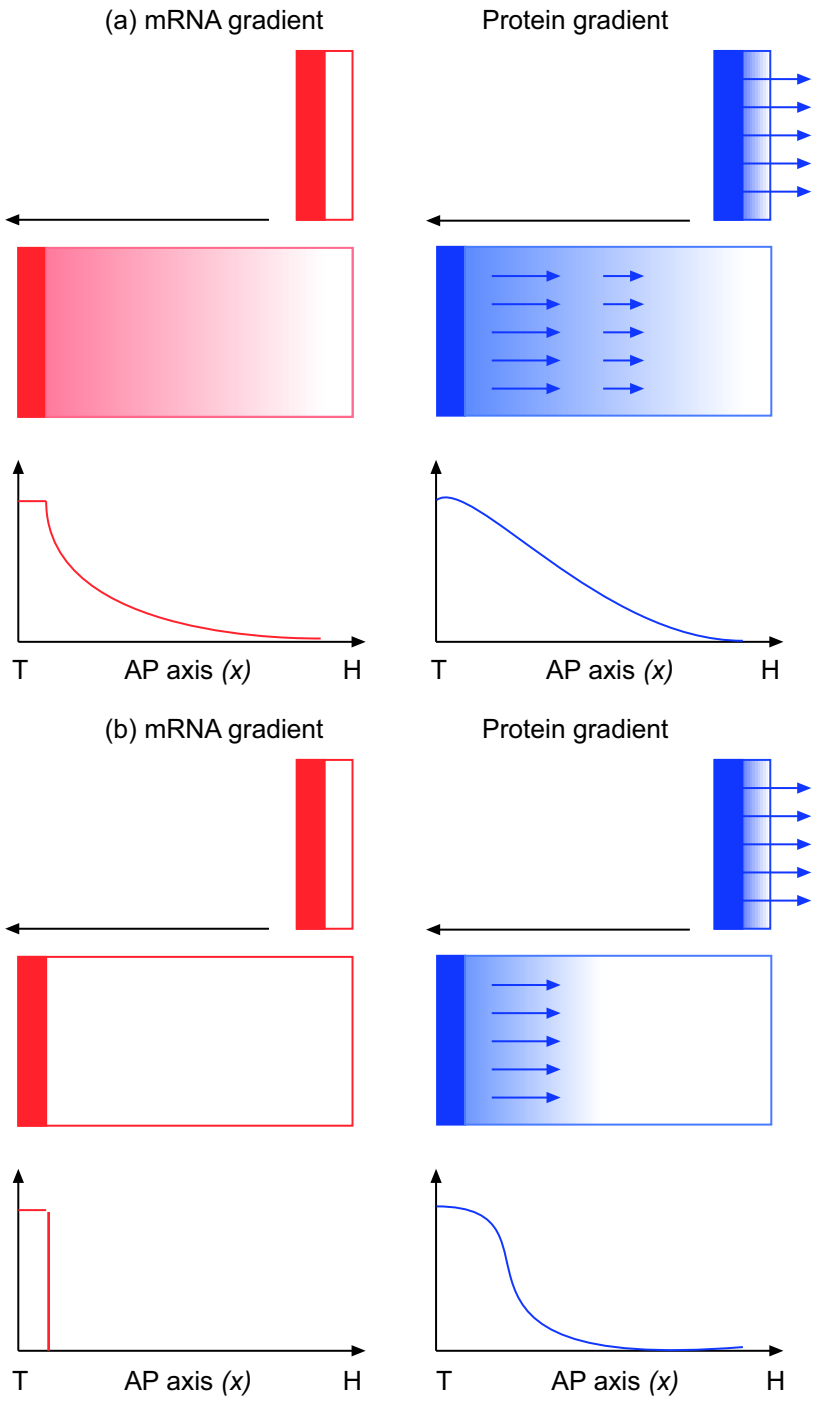


Figure 4.3: An illustration of the manner in which a gradient of FGF8 could be maintained along the AP axis. (a) The outgrowth mechanism: as the tailbud regresses and creates the PSM, cells entering the PSM are endowed with a base level of *fgf8* which degrades over time (see LHS of (a)). Local production of FGF8 by such cells creates a more shallow protein gradient. (b) Once cells leave the tailbud they are no longer able to translate FGF8: FGF8 is produced solely by a localised source of *fgf8* in the tail bud and diffuses along the AP axis. T denotes the tail of the embryo and H the head. Adapted from [17].

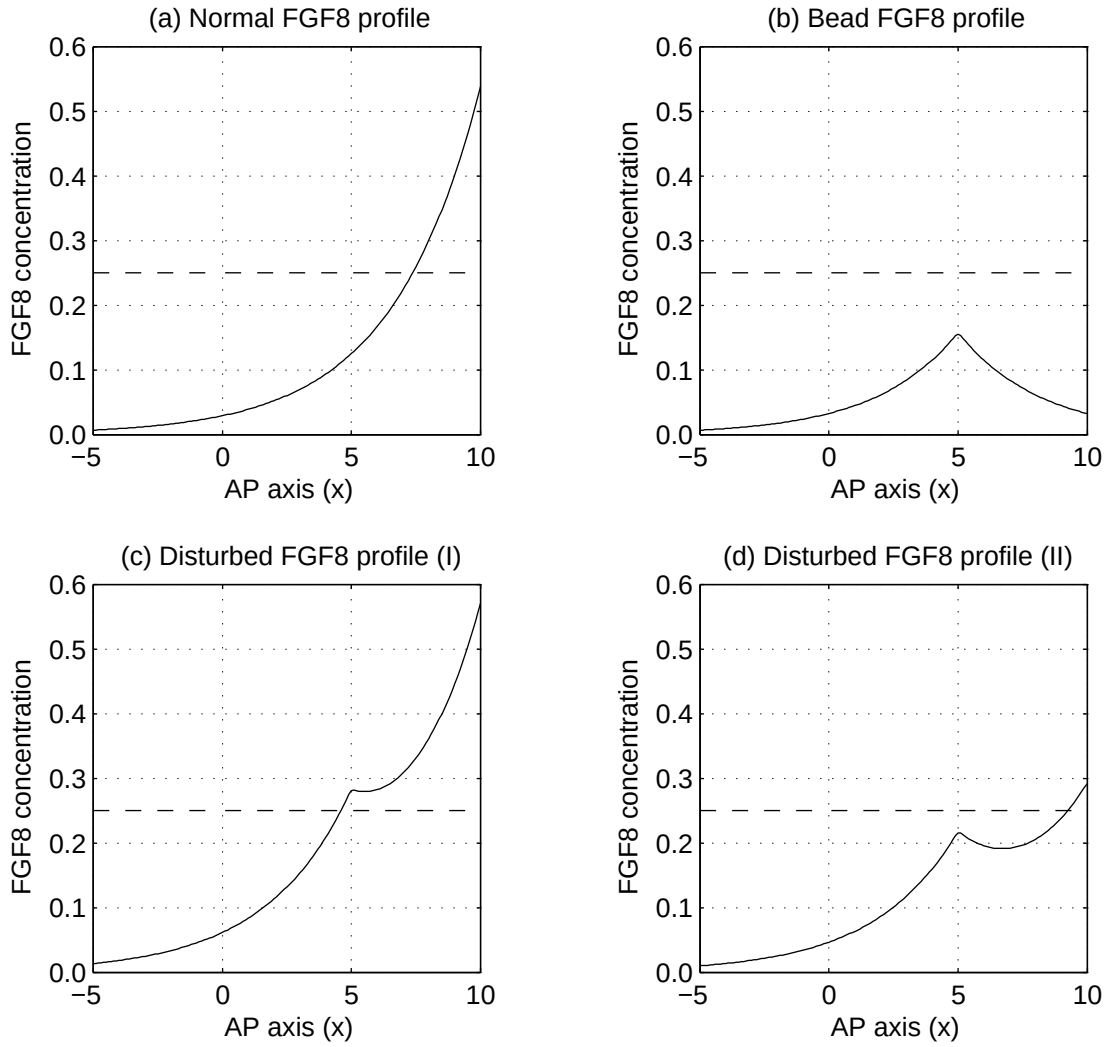


Figure 4.4: A schematic view of the way in which the level of FGF8 signalling changes over time with local application of FGF8 at a constant axial level ($x = 5.0$) and the main source of FGF8 moving caudally. (a) The FGF8 signalling profile in a control embryo with the threshold concentration level of FGF8 clearly marked by the dashed line. It can be seen that the determination front lies at approximately $x = 7.5$. (b) A profile that could be set up by a bead soaked in FGF8. (c) The level of endogenous FGF8 signalling with the presence of a local source of FGF8. Note that in this case the point at which the threshold level of FGF8 signalling is reached is approximately $x = 4.5$, more anterior than in the control case. (d) After some time, the effect of the bead is no longer relevant as the endogenous gradient has moved posteriorly, out of range of the effects of the bead.

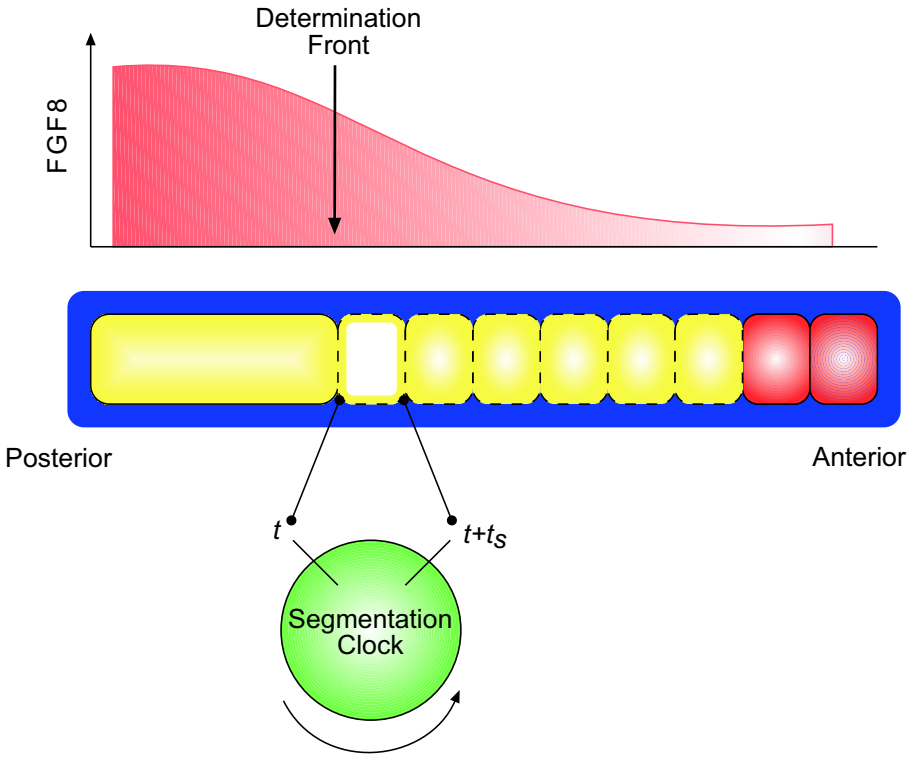


Figure 4.5: Diagrammatic representation of the vertebrate body plan during somite formation within the modified model. In the top part of the diagram the FGF8 wavefront is illustrated together with the position of the determination front. The middle section of the diagram shows the AP axis of the embryo with the somites (red blocks), determined region and its pre-pattern (yellow blocks) and PSM (yellow band) clearly marked. The bottom part of the diagram shows the segmentation clock with the time t at which a cell reaches the determination front and the time t_s later at which it becomes competent to signal. The hollow yellow block marks the position of the next somite to be specified: the posterior boundary is fixed by the position of the determination front at the time at which cells at the anterior boundary become able to produce a signal.

4.2.1 Local application of FGF8

We can 'test' our modified model using the experimental evidence of Dubrulle et al. [15]. Suppose that we have a bead soaked in FGF8 implanted between the lateral mesoderm and the PSM. Then FGF8 molecules will diffuse out from the bead along the PSM with a distribution that depends on the physical properties of the tissue on either side of the bead. Here we will assume that the distribution is symmetric on either side of the bead although this may not be the case as diffusion may become limited on the anterior side of the bead where the epithelialisation processes have begun. We illustrate this in Figure 4.4(b).

As the spatial profile gradient of FGF8 regresses along with the node, the bead will stay at a constant axial level, allowing the local effects to be measured. Superimposing the bead distribution onto the endogenous concentration profile of FGF8 gives a resulting distribution of the form of that in Figure 4.4(c). Diffusion of FGF8 from the bead will affect the level of FGF8 in cells which lie within a certain distance of the bead. Rostral to the bead, the profile will be steeper and caudal to the bead, it will become more shallow. We now consider what effect this has on segmentation, as hypothesised in our model.

Making the FGF8 profile steeper rostral to the bead ensures that within the time frame of the specification of one somite, the determination front will not have regressed as far as it would have done in a control embryo, and hence fewer cells will have become mature enough to segment, resulting in an abnormally small somite. The reverse occurs caudal to the somite: the determination front will regress further than it would have done in a control embryo, and the result will be the formation of an abnormally large somite. See Chapter 5 for more details. Put concisely, local application of FGF8 causes the progression of the determination front to slow rostral to the bead, resulting in the rostral displacement of its position relative to the PSM, and hence the formation of smaller somites and *vice versa*. This was observed experimentally in [15].

It is important to notice that the effects of local application may be slightly different depending on which model we assume for FGF8 gradient formation. In the case where FGF8 production is restricted to the tail of the embryo the resulting FGF8 profile will be steeper and a bead implanted in the PSM will cause perturbation of FGF8 levels over a greater distance relative to the region in which FGF8 levels are changing very quickly. It is therefore possible that the effects of FGF8 perturbation may be more marked than when using the model which assumes that there is local production of FGF8. We propose methods for investigating these effects in Chapter 6.

Notice that a bead soaked in a stronger solution of FGF8 will elicit a stronger response in the embryo. FGF8 molecules will diffuse out and affect the profile more markedly and within a larger distance of the bead. It is possible that while the profile will become steeper rostral to the bead, it may actually become reversed caudal to the bead. Similar effects may also occur when the bead is actually implanted in the PSM since FGF8 molecules will be able to diffuse more easily along the PSM without interference from the extracellular matrix. Implantation in the PSM has led to a complete absence of somite boundary formation immediately rostral to the bead, with some smaller somites forming rostral to this zone [15]. This may be a result of the fact that the gradient of FGF8 has been destroyed: over the time taken to form one somite, there will be no new cells reaching the determination front.

It is important to notice that our model is consistent with three very important experimental observations:

Firstly, we consider the experimental evidence of Dubrulle and co-workers [15, p 221-222] on the effect of positioning of the bead in the PSM: "when the bead was placed mid-way between the caudal-most PSM and somite -IV, only the part of the PSM that was located between the bead and somite -IV was affected ... no effect was ever detected in cells which were rostral to somite -IV at the time of surgery". This supports our assumption that a cell's response to signalling changes as it passes the determination front. Cells that are rostral to the determination front at the time of implantation of the bead can never be affected by changes in the FGF8 gradient because they have become refractory to FGF8 signalling. In this way, we see that the link between the pattern of anomalies seen must be dependent on both the strength of the source, and its placement within the PSM.

Secondly, we consider the maximum distance over which bead anomalies could extend rostral to the bead. Whatever the changes to the FGF8 gradient within the PSM due to the bead, those changes can only be manifest up to the level of the determination front, since we assumed that cells become refractory to FGF8 signalling rostral to this point. Since the undetermined zone is approximately equivalent to 6-7 somites worth of PSM cells our model allows for anomalies to extend only over this distance [15] (see Figure 4.1).

Thirdly, our model predicts that with bead implantation subsequent somite formation will fall back into register with the control side of the embryo. This is because the rate at which the node is regressing is constant and there is no effect upon the segmentation clock. Note that the independence of the clock and the gradient ensures that we can also predict anomalies forming at the same pace as those somites on the control side of the embryo [15].

4.3 A revised model for normal somite formation

Letting m and p denote the levels of fgf8 mRNA and protein in the PSM, respectively, we propose the following model for fgf8 gradient formation:

$$\frac{\partial m}{\partial t} = \Lambda\chi_m - \beta m, \tag{4.1}$$

$$\frac{\partial p}{\partial t} = \Gamma m - \eta p + D_p\frac{\partial^2 p}{\partial x^2}, \tag{4.2}$$

where $\chi_m = H(x - x_n - c_n t)$ and Λ, β, Γ, η, D_p, x_n and c_n are positive constants. c_n represents the rate at which the AP axis is elongating. *fgf8* production is confined to the posterior end of the embryo (by the Heaviside function) and transcribes protein locally. FGF8 alone may diffuse along the AP axis and both substances are assumed to decay linearly. We non-dimensionalise with the same parameters used in Chapter 2 in order to be able to incorporate the above model into the

present equations for the somitic factor u and signal v. Taking

$$t = \frac{\hat{t}}{\nu}, \qquad x = (x_1 - x_2)\hat{x}, \qquad m = \frac{\Lambda}{\nu}\hat{m}, \qquad p = \frac{\Lambda\Gamma}{\beta\nu^2}\hat{p}, \qquad \hat{\beta} = \frac{\beta}{\nu}, \tag{4.3}$$

$$\hat{\eta} = \frac{\eta}{\nu}, \qquad \hat{D}_p = \frac{D_p}{\nu(x_1 - x_2)^2}, \qquad \hat{x}_n = \frac{x_n}{x_1 - x_2}, \qquad \hat{c}_n = \frac{c_n}{\nu(x_1 - x_2)}, \tag{4.4}$$

and incorporating the equations for fgf8 mRNA and protein into the system describing the dynamics of somitic factor and signal, we have (droppings the ˆs),

$$\frac{\partial u}{\partial t} = \frac{(u + \mu v)^2}{\gamma + u^2}\chi_u - u, \tag{4.5}$$

$$\frac{\partial v}{\partial t} = \kappa\left(\frac{\chi_v}{\epsilon + u} - v\right) + D_v\frac{\partial^2 v}{\partial x^2}, \tag{4.6}$$

$$\frac{\partial m}{\partial t} = \chi_m - \beta m, \tag{4.7}$$

$$\frac{\partial p}{\partial t} = \beta m - \eta p + D_p\frac{\partial^2 p}{\partial x^2}, \tag{4.8}$$

where χ_m is as above and somitic factor production is controlled by a Heaviside function of the form

$$\chi_u = H(p^* - p), \tag{4.9}$$

where p^* is the level of FGF8 expressed at some point corresponding to the determination front. In this new model the ability to produce a signal is conferred a time t_s after cells reach the determination front, where t_s corresponds to the period of the segmentation clock. Supposing that a cell at a point $\bar{x}$ reaches the determination front at time $\bar{t}$, that is $p(\bar{x}, \bar{t}) = p^*$, then signal production is controlled by a Heaviside function of the form

$$\chi_v = H(t - \bar{t} - t_s). \tag{4.10}$$

4.3.1 Initial conditions

We take the initial conditions for u and v to be as in Chapter 2:

$$u(x, 0) = \begin{cases} 1 & \text{if } x \leq 0, \\ 0 & \text{if } x > 0, \end{cases} \tag{4.11}$$

and

$$v(x, 0) = AH(-x) + B\cosh(\lambda(l - |x|)), \tag{4.12}$$

where

$$A \equiv \frac{1}{1+\epsilon-\epsilon_1}, \qquad B \equiv \frac{A\text{sign}(x)}{2\cosh(\lambda l)}, \qquad \lambda \equiv \sqrt{\frac{\kappa}{D_v}}, \tag{4.13}$$

and $\epsilon_1 \ll 1$.

The initial conditions for m and p are based on the travelling wave solutions of equations (4.7) and (4.8) at $t = 0$ which are given in Section 4.3.3 and Section 4.3.4 and are such that:

$$m(x,0) = \begin{cases} \frac{1}{\beta}\exp\left[\beta\left(\frac{x-x_n}{c_n}\right)\right] & \text{if} \quad x \le x_n, \\ \frac{1}{\beta} & \text{if} \quad x > x_n, \end{cases} \tag{4.14}$$

and

$$p(x,0) = \begin{cases} A_l\exp\{n_+(x-x_n)\} + A\exp\left\{\beta\frac{(x-x_n)}{c_n}\right\} & \text{if} \quad x \le x_n, \\ B_r\exp\{n_-(x-x_n)\} + \frac{1}{\eta} & \text{if} \quad x > x_n, \end{cases} \tag{4.15}$$

where A, $n_\pm$, A_l and B_r are given by equations (4.23) and (4.24).

Note that these conditions assume that the last formed somite occupies a region up to the point $x = 0$ and so we must choose the position of the determination front accordingly to ensure that the next somite forms as a result of a signal produced by cells at $x = 0$. This is discussed in more detail in Chapter 5.

4.3.2 Boundary conditions

We take boundary conditions for u and v along the same lines as those used in Chapter 2. Cells which are a long way from reaching the determination front have both the level of somitic factor and signalling molecule close to zero, while cells which reached the determination front 'some time ago' have some fixed level of the somitic factor and signalling molecule.

For the FGF8 concentration, we assume that cells which reached the determination front 'some time ago' have *fgf8* and FGF8 levels close to zero and that cells which are a long way from the determination front have fixed levels of *fgf8* and FGF8. In Section 5.2.2 we assume that the position of the determination front is close to the midpoint of the FGF8 profile and therefore lies at approximately $x = x_n + c_n t$. Therefore we take our boundary conditions to be

$$\begin{aligned} &u, v \to 0 \quad \text{as} \quad x - \{x_n + ct\} \to +\infty, \\ &u, v \quad \text{are bounded as} \quad x - \{x_n + ct\} \to -\infty, \\ &m, p \quad \text{is bounded as} \quad x - \{x_n + ct\} \to +\infty, \\ &m, p \to 0 \quad \text{as} \quad x - \{x_n + ct\} \to -\infty. \end{aligned} \tag{4.16}$$

4.3.3 The mRNA profile

Equation (4.7) describing the dynamics of *fgf8* levels can be solved to give

$$m(x,t) = \begin{cases} m(x,0)e^{-\beta t} & \text{if} \quad x \leq x_n, \\ m(x,0)e^{-\beta t} + \frac{1}{\beta}[e^{\beta A} - 1]e^{-\beta t} & \text{if} \quad x > x_n, \end{cases} \tag{4.17}$$

where $A = \min\{t, (x - x_n)/c_n\}$.

Given that we are not considering the beginning of the somitogenic process we are only interested in the profile of *fgf8* once levels have reached a steady state profile relative to the PSM. For this it is sufficient to take the initial conditions as

$$m(x,0) = \begin{cases} \frac{1}{\beta}\exp\left[\beta\left(\frac{x-x_n}{c_n}\right)\right] & \text{if} \quad x \leq x_n, \\ \frac{1}{\beta} & \text{if} \quad x > x_n, \end{cases} \tag{4.18}$$

giving the result

$$m(x,t) = \begin{cases} \frac{1}{\beta}\exp\left[\beta\left(\frac{x-x_n}{c_n} - t\right)\right] & \text{if} \quad x \leq x_n + c_n t, \\ \frac{1}{\beta} & \text{if} \quad x > x_n + c_n t. \end{cases} \tag{4.19}$$

The above solution for m is in travelling wave form since if $x - c_n t = X - c_n T$ then for $x > x_n + c_n t$ we have the trivial result $m(x,t) = m(X,T)$ and otherwise

$$m(x,t) = \frac{1}{\beta}\exp\left[\beta\left(\frac{x-x_n}{c_n} - t\right)\right] = \frac{1}{\beta}\exp\left[\beta\left(\frac{x-x_n}{c_n} - \frac{x - X + c_n T}{c_n}\right)\right] = m(X,T). \tag{4.20}$$

Figure 4.6 shows a plot of the *fgf8* concentration at a series of time points. As t increases the profile moves along the AP axis in a posterior direction with constant shape and speed.

Equations (4.7) and (4.8) can also be solved as in Section 3.1.2.1 to give full analytical solutions which are, unfortunately, sufficiently complicated enough to be virtually unusable in any further calculations. In Chapter 5 we take this approach and demonstrate that the analytical solutions quickly evolve to travelling wave form.

4.3.4 The protein profile

Given the travelling wave nature of the mRNA profile in equation (4.19) we can solve equation (4.8) for the protein by transforming to travelling wave coordinates of the form $z = x - x_n - c_n t$; we have

$$D_p p'' + c_n p' - \eta p = \begin{cases} -e^{-\frac{\beta z}{c_n}} & \text{if} \quad z \leq 0, \\ -1 & \text{if} \quad z > 0, \end{cases} \tag{4.21}$$

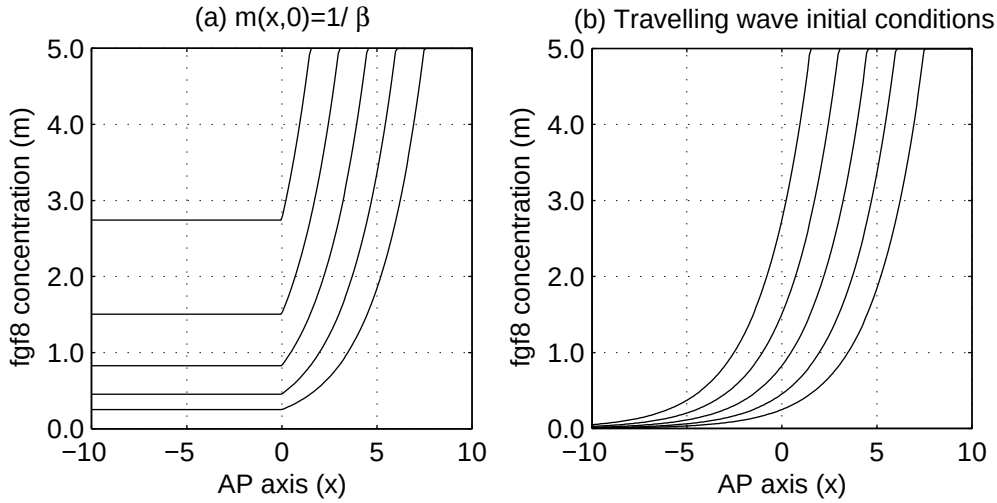


Figure 4.6: Plots of the analytical solution for the *fgf8* concentration along the AP axis of embryos. (a) Solution for $m(x,0) = 1/\beta$ and (b) Solution given by equation (4.19) with travelling wave initial conditions, over the series of time points $t = 0, 3, 6, 9, 12$. The waves move in the posterior direction as time progresses. Parameters are as follows: $\beta = 0.2$, $c_n = 0$ and $x_n = 0.0$.

where $' = d/dz$. The above can be solved in each subinterval to give (assuming bounded solutions as $z \to \pm\infty$ and a differentiably continuous solution at $z = 0$):

$$p(x,t) = \begin{cases} A_l \exp\{n_+(x - x_n - c_n t)\} + A \exp\left\{\beta \frac{(x - x_n - c_n t)}{c_n}\right\} & \text{if} \quad x - x_n - c_n t \leq 0, \\ B_r \exp\{n_-(x - x_n - c_n t)\} + \frac{1}{\eta} & \text{if} \quad x - x_n - c_n t > 0, \end{cases} \tag{4.22}$$

where

$$A = \frac{1}{\left(\eta - \beta - \frac{D_p \beta^2}{c_n^2}\right)}, \qquad n_\pm = \frac{-c_n \pm \sqrt{c_n^2 + 4\eta D_p}}{2D_p}, \tag{4.23}$$

and

$$A_l = \frac{1}{n_+ - n_-}\left(n_- A - \frac{n_-}{\eta} - \frac{\beta A}{c_n}\right), \qquad B_r = \frac{1}{n_+ - n_-}\left(n_+ A - \frac{n_+}{\eta} - \frac{\beta A}{c_n}\right). \tag{4.24}$$

Figure 4.7 shows a plot of the FGF8 concentration profile for a series of time points. As t increases the region of high FGF8 concentration moves down the AP axis with constant profile and speed.

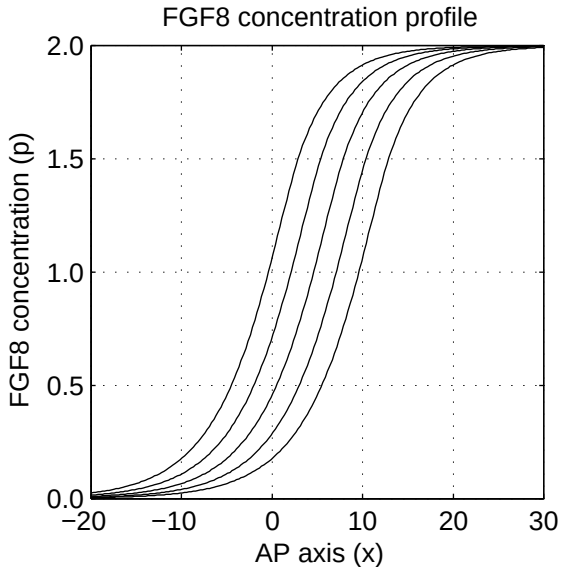


Figure 4.7: Plot of the analytical solution for the FGF8 concentration given by equation (4.22) over the series of time points $t = 0, 5, 10, 15, 20$. The wave moves in a posterior direction as time progresses. Parameters are as follows: $\eta = 0.5$, $D_p = 10$, $\beta = 0.2$, $c_n = 0$ and $x_n = 0.0$.

4.3.5 Comparison of the analytical and numerical solutions

To check the validity of our analytical solutions we solved equations (4.7) and (4.8) numerically using the NAG routine D03PCF and plotted the results against the analytical solutions given by equations (4.19) and (4.22) in Figure 4.8. In Figure 4.8(a) the solutions are indistinguishable for $t = 9.0$ throughout the domain under consideration. In Figure 4.8 (b) the analytical solution matches the computed solution very closely with very a small divergence occurring at the edges of the domain as the zero flux boundary conditions used in the numerical computation to approximate the infinite domain boundary conditions begin to have an effect.

4.3.6 Numerical solution of the fgf8 model for somite formation

We solved the modified equations (4.5)-(4.8) using the NAG routine D03PCF and plotted the results of the numerical computation in Figure 4.9 using the MATLAB function imagesc (as in previous chapters). The profiles of fgf8 recede along the AP axis with time and as levels fall, more cells reach the determination front and become able to produce somitic factor. A series of successive signals produce coherent rises in somitic factor levels thereby generating a pre-pattern of somites.

In order to easily calculate the position of the discontinuity in the Heaviside function for v, we exploit the fact that the speed at which the AP axis elongates is constant to allow us to use two sets of equations for m and p, one which accounts for the determination front and the other which accounts for the time t_s later at which cells become able to signal. As before we approximate the

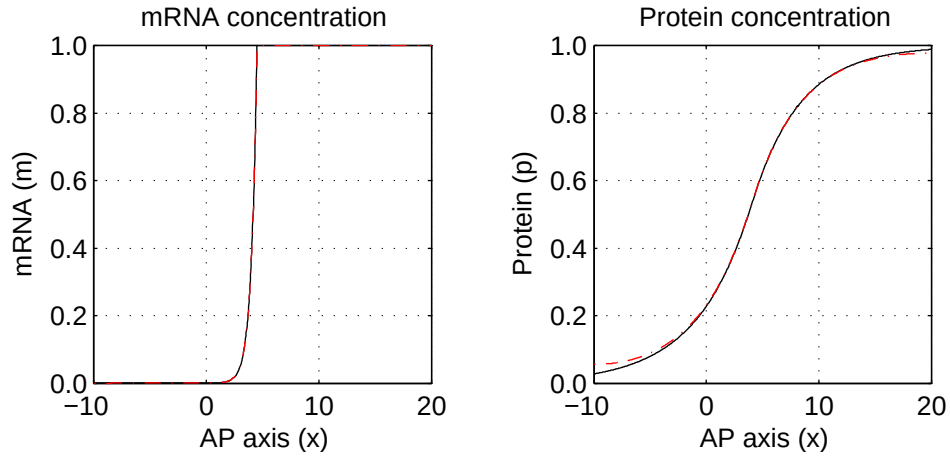


Figure 4.8: Plots of the analytical and numerical solutions of equations (4.7) and (4.8). In both cases the analytical solution is indicated by the solid black line and the numerical solution is indicated by the dash-dotted red line. (a) Comparison between the solutions for *fgf8* concentration given by equation (4.19) and by numerical computation; similarly (b) shows a comparison between the solutions for FGF8 concentration given by equation (4.19) and found by numerical computation. Parameters are as follows: $\beta = 1.0$, $\eta = 1.0$, $D_p = 20$, $x_n = 0.0$, $c_n = 0.5$ and the Heaviside function parameter (as in Chapter 2) $\delta = 10^{-3}$.

infinite domain boundary conditions by using zero flux boundary conditions on a finite domain and the Heaviside functions are approximated using continuous $\tanh$ approximations with $\delta = 10^{-2}$.

4.4 Important factors to consider

There are two important factors to consider with regard to future applications of the model. The first is that we have not, as yet, taken account of the possibility that there may be a delay in FGF8 transcription from *fgf8*; if delays are significant there may be considerable changes to the shape of the FGF8 gradient formed. The second is that the model, as it is, is difficult to solve analytically and the result is impractical, and this may pose problems when we come to consider the effects of local application of FGF8. For certain parameter values the profile produced in the above manner may be similar to that produced with no local production of FGF8 (i.e. if we assume that FGF8 is only produced in the tip of the embryo - see Figure 4.3) and we may be able to use a reduced system of equations to model the effects of FGF8 application.

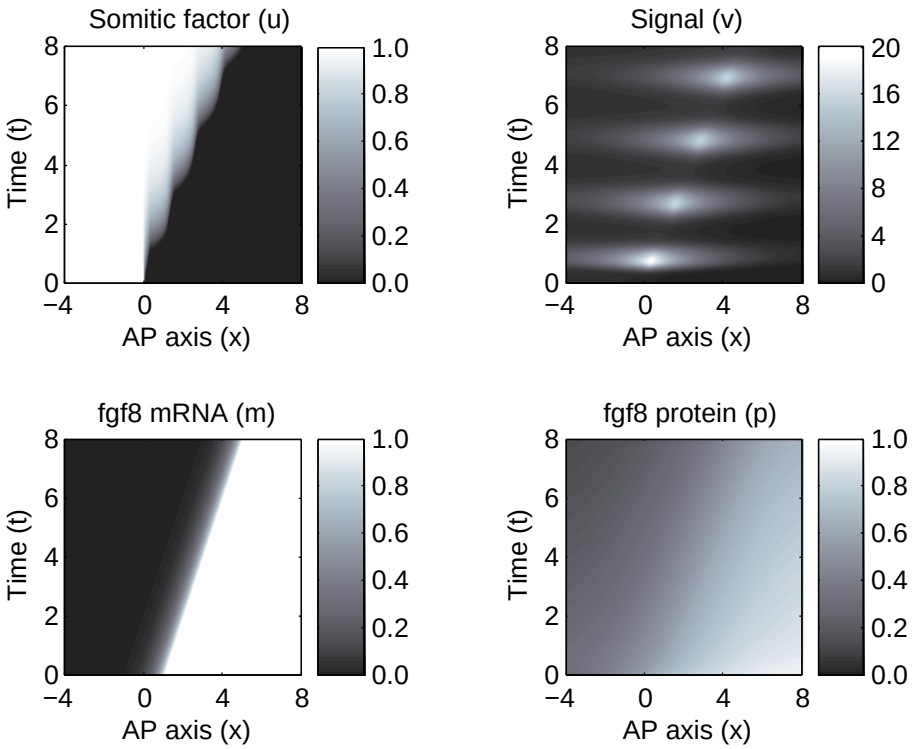


Figure 4.9: Numerical solution of equations (4.5)-(4.8) for somitic factor, signal, *fgf8* and FGF8 dynamics. The profiles of fgf8 recede along the AP axis and as levels fall cells become competent to produce signal and somitic factor. As in the cell cycle model, a series of successive peaks in the signalling molecule produce the coherent jumps in somitic factor that represent blocks of tissue earmarked to form specific somites. Here we consider a fixed domain along the AP axis with the tail moving down the axis at constant speed. Parameters are as follows: $\mu = 10^{-4}$, $\gamma = 10^{-3}$, $\kappa = 10$, $\epsilon = 10^{-3}$, $\eta = 1.0$, $\beta = 1.0$, $D_v = 50$, $D_p = 20$ and $c_n = 0$. The initial position of the discontinuity in the Heaviside function for u is $x_n = 1.0$ and $t_s = 2.0$.

4.4.1 The effects of transcriptional delay

In order to investigate the effects of a delay in FGF8 transcription, we consider the equations

$$\frac{\partial m}{\partial t} = \chi_m - \beta m, \tag{4.25}$$

$$\frac{\partial p}{\partial t} = \beta m(t-\tau) - \eta p + D_p \frac{\partial^2 p}{\partial x^2}, \tag{4.26}$$

where τ is the length of the delay in transcription. The equations can be solved as before to give (with the same initial conditions):

$$m(x,t,\tau) = \begin{cases} \frac{1}{\beta}\exp\left[\beta\left(\frac{x-x_n-c_nt}{c_n}\right)\right] & \text{if} \quad x \le x_n + c_n t, \\ \frac{1}{\beta} & \text{if} \quad x > x_n + c_n t, \end{cases} \tag{4.27}$$

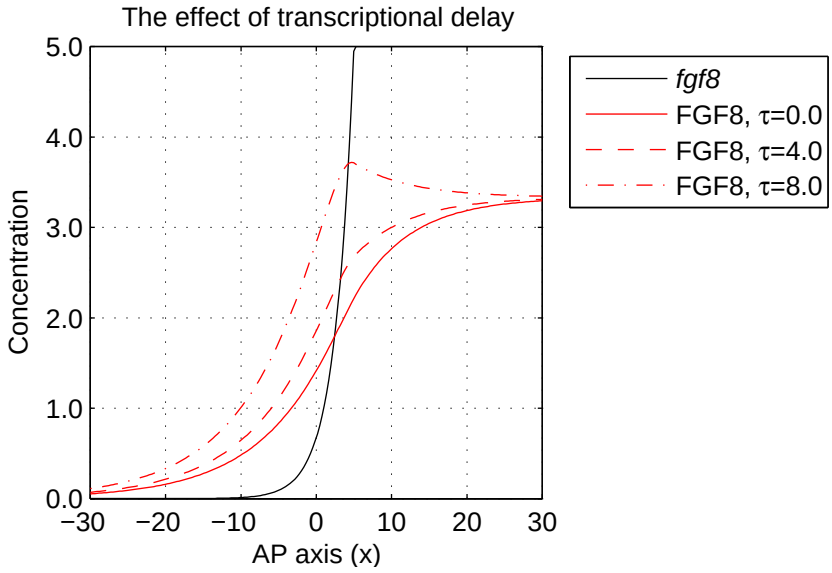


Figure 4.10: The changes in the FGF8 concentration profile as the delay in protein transcription is varied. For small delays the profile remains monotonically increasing as we progress down the AP axis but as the delay is increased the profile has a local maximum around $x = x_n$. Parameters are as follows: $\eta = 0.3$, $\beta = 0.2$, $D_p = 20$, $x_n = 5.0$ and $c_n = 0.5$.

and

$$p(x,t,\tau) = \begin{cases} A_l \exp\{n_+(x - x_n - c_n t)\} + A \exp\left\{\beta \frac{(x - x_n - c_n t)}{c_n}\right\} & \text{if} \quad x - x_n - c_n t \leq 0, \\ B_r \exp\{n_-(x - x_n - c_n t)\} + \frac{1}{\eta} & \text{if} \quad x - x_n - c_n t > 0, \end{cases} \tag{4.28}$$

with

$$A = \frac{e^{\beta\tau}}{\left(\eta - \beta - \frac{D_p \beta^2}{c_n^2}\right)}, \tag{4.29}$$

and the remaining parameters as in equations (4.23) and (4.24).

Figure 4.10 shows a plot of the *fgf8* and FGF8 concentrations for various values of the delay parameter τ. As τ is increased a small disturbance occurs in the FGF8 profile around the level of the determination front, where *fgf8* levels change rapidly from high to low. For large delays the monotonicity of the gradient is destroyed and we see that there may be complications: depending on the chosen level of FGF8 at the determination front and on the duration of the delay of FGF8 transcription, it may be that for some cells, the FGF8 concentration drops below the threshold level for a short period before they have reached the determination front proper.

Figure 4.11 indicates the possible profiles (and therefore complications) for the FGF8 profile along the AP axis. For the case in which there is a local maximum in p (dash-dotted line) there would be

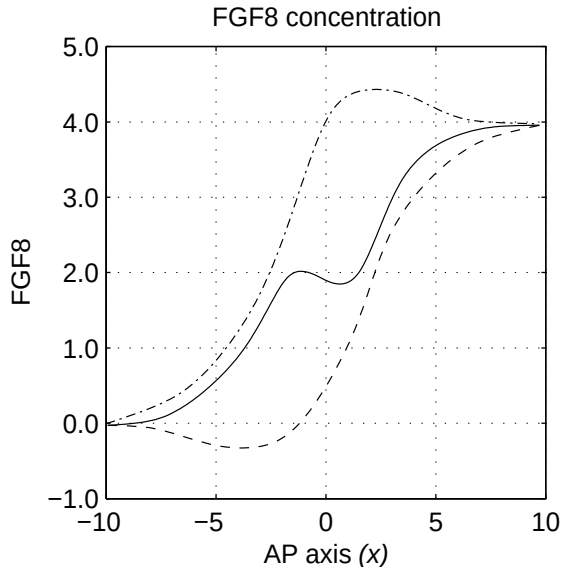


Figure 4.11: An illustration of the possible shapes for the FGF8 profile with a delay in protein transcription. The solid line highlights the possibility of a local maximum and local minimum within the FGF8 profile whereas the dashed and dash-dotted lines reveal the possibilities of a local minimum and maximum (respectively).

no problems associated with segmentation as the level of FGF8 expressed at the determination front must necessarily lie below the level expressed in the tail of the embryo. In the case where there is a local minimum in p (dashed line) there would be problems as this would imply that FGF8 levels had become negative which is infeasible. We show that this cannot be the case subsequently. In the remaining case where there is a local minimum and a local maximum (solid line) it may be the case that for some cells FGF8 levels drop below the threshold level for a brief period before they reach the determination front properly. This may cause problems with segmentation as such cells may respond to a signal and start producing somitic factor too early.

In order to ensure that the latter case does not occur, we consider the stationary points of the FGF8 profile. Differentiating expression (4.28) for p w.r.t. x we see that stationary points must satisfy

$$n_+ A_l \exp\{n_+(x - x_n - c_n t)\} + \frac{\beta A}{c_n} \exp\left\{\frac{\beta(x - x_n - c_n t)}{c_n}\right\} = 0. \tag{4.30}$$

Since e^x is a 1-1 mapping (that is, if x, $\bar{x}$ are such that $e^x = e^{\bar{x}}$ then we must have $x = \bar{x}$) then there can only be one solution of the above equation and we see that we cannot have both a local maximum and local minimum in the p profile.

In order to show that the solution cannot become negative (given non-negative initial conditions) we consider the subsystem describing the fgf8 dynamics given by equations (4.7) and (4.8): we have

that

$$\frac{\partial m}{\partial t} + \beta m = \chi_m \geq 0 \quad \Rightarrow \quad m(x,t) \geq Ke^{-\beta t} \geq 0, \tag{4.31}$$

so m must remain non-negative. Considering the p equation we have

$$\frac{\partial p}{\partial t} + \eta p - D_p \frac{\partial^2 p}{\partial x^2} = \beta m \geq 0. \tag{4.32}$$

From Section 3.1.2.1 we see that the solution of an equation of the form

$$\frac{\partial p}{\partial t} + \eta p - D_p \frac{\partial^2 p}{\partial x^2} = f(x,t), \tag{4.33}$$

with initial conditions given by $p(x,0)$ and boundary conditions of the form p is bounded as $x \to \pm\infty$ is

$$p(x,t) = e^{-\eta t} \int_0^t \int_{-\infty}^{\infty} \frac{f(x',t')}{\sqrt{4\pi D_p (t-t')}} \exp\left[\frac{-(x-x')^2}{4D_P(t-t')}\right] \mathrm{d}x'\mathrm{d}t' \tag{4.34}$$

$$+ \frac{e^{-\eta t}}{\sqrt{4\pi D_p t}} \int_{-\infty}^{\infty} p(x,0) \exp\left[\frac{-(x-x')^2}{4D_p(t-t')}\right] \mathrm{d}t'. \tag{4.35}$$

Since the exponential terms must remain strictly positive and the RHS of equation (4.32) is non-negative, assuming non-negative initial conditions ensures a non-negative solution for p.

Therefore the only possibility is that there will be a local maximum in the FGF8 profile and this will have no effect on somite formation. Although a delay in transcription may cause the determination front to be positioned in a slightly different place in the PSM it will still move posteriorly with speed c_n.

If we do wish to ensure that the FGF8 profile remains monotonically increasing with x then we can find a condition on τ to ensure this. In general $A < 0$ as D_p is reasonably large and c_n reasonably small. $n_+ > 0$ and $n_- < 0$, therefore to ensure that there is no local maximum we must have $A_l < 0$ or:

$$\tau < \frac{1}{\beta} \log\left[\frac{n_-}{\eta}\left(\eta - \beta - \frac{D_p\beta^2}{c_n^2}\right)\left(n_- - \frac{\beta}{c_n}\right)^{-1}\right]. \tag{4.36}$$

For the parameters used in Figure 4.10, $\tau_c = 4.46$ 2.d.p which is consistent with the results shown. It is possible that the delay in protein translation could be another useful tool in gauging parameter sizes for the model.

Figure 4.12 shows how τ_c, the critical value for transcriptional delay below which there is no local maximum in the FGF8 profile, changes as key parameters are varied. Figure 4.12 (a) shows how τ_c varies with β, the linear decay rate of *fgf8*. There is a local maximum just before $\beta = 1.0$ and then τ_c decays as β increases. This can be justified by reasoning that as β increases then $m(t-\tau)$ will be larger relative to $m(t)$ and therefore p production will be increased.

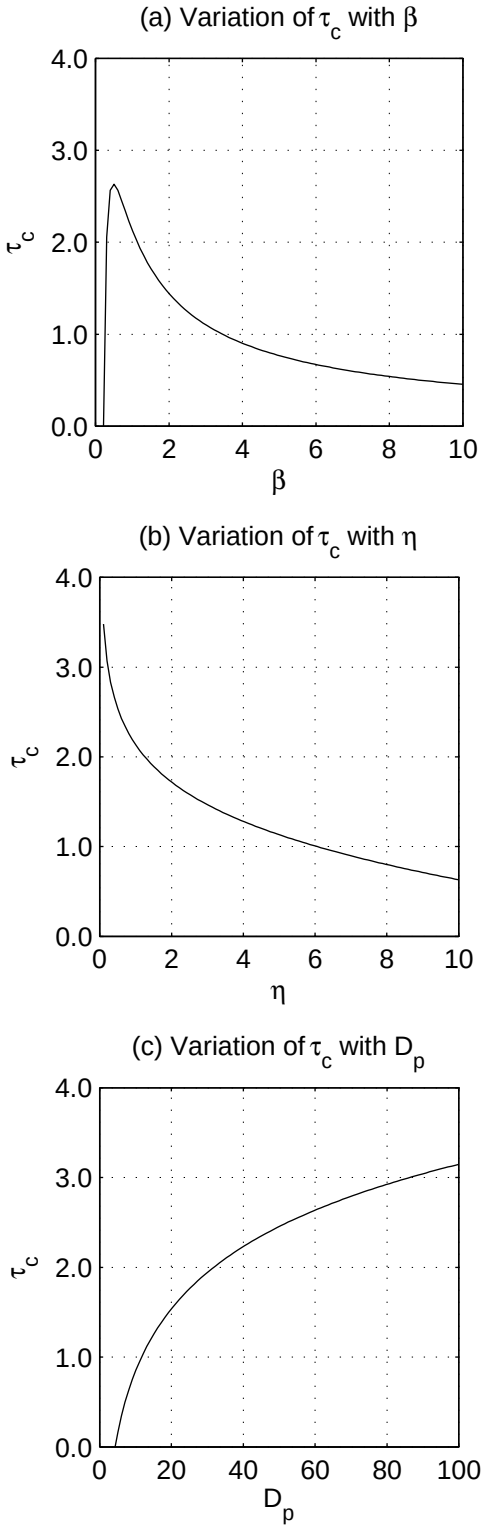


Figure 4.12: Plots of how τ_c, the critical value for transcriptional delay below which there is no local maximum in the FGF8 profile, depends on the key parameters: (a) β, the linear decay rate of *fgf8*, (b) η, the linear decay rate of FGF8, (c) D_p, the diffusion rate of FGF8. Unless otherwise stated parameters are as follows: $\eta = 1.0$, $\beta = 1.0$, $D_p = 20$, $x_n = 0.0$ and $c_n = 0.5$.

Figure 4.12 (b) shows how τ_c varies with η, the linear decay rate of FGF8. As η increases, τ_c decreases. Figure 4.12 (c) shows how τ_c varies with D_p, the diffusion rate of the protein. As the diffusion rate increases, τ_c increases, which can be explained by reasoning that the FGF8 gradient will be less steep and therefore that a higher level of FGF8 production will have less effect on the FGF8 profile. Given that whatever the model parameters and whatever the effects of transcriptional delay on FGF8 production, the FGF8 profile still behaves as a travelling wave and therefore that the determination front progresses down the AP axis with constant speed, it does not seem necessary to include transcriptional delay in our model.

4.4.2 Approximations for FGF8

As mentioned previously, the model incorporating mRNA and protein dynamics (equations (4.7) and (4.8)) results in a system that is hard to solve analytically without resorting to considering only the steady state travelling wave solution. In order to understand the effects of local application of FGF8 we will to consider the effects on the FGF8 profile when there is no local translation of FGF8 (protein) by *fgf8* (mRNA). Biologically this corresponds to the a case in which mRNA decay is very quick and hence there is no local mRNA gradient. To do this we consider two sets of equations: the first system describes the dynamics of fgf8 mRNA and protein, namely;

$$\frac{\partial m}{\partial t} = \chi_m - \beta m, \tag{4.37}$$

$$\frac{\partial p}{\partial t} = \beta m - \eta p + D_p \frac{\partial^2 p}{\partial x^2}, \tag{4.38}$$

and the second describes solely the dynamics of FGF8, with production assumed to be limited to the tail of the embryo:

$$\frac{\partial w}{\partial t} = \chi_w - \eta w + D_w \frac{\partial^2 w}{\partial x^2}, \tag{4.39}$$

where $\chi_w = H(x - x_n - c_n t)$.

Note that the above equation has already been non-dimensionalised in line with Section 4.3. Solving the equation for m as in Section 4.3.3 we are left to compare the following:

$$D_p \frac{\partial^2 p}{\partial x^2} - \frac{\partial p}{\partial t} + \eta p = \begin{cases} -\exp\left\{-\frac{\beta(x-x_n-c_n t)}{c_n}\right\} & \text{if} \quad x - x_n - c_n t \leq 0, \\ -1 & \text{if} \quad x - x_n - c_n t > 0, \end{cases} \tag{4.40}$$

$$D_w \frac{\partial^2 w}{\partial x^2} - \frac{\partial w}{\partial t} + \eta w = \begin{cases} 0 & \text{if} \quad x - x_n - c_n t \leq 0, \\ -1 & \text{if} \quad x - x_n - c_n t > 0. \end{cases} \tag{4.41}$$

As could be predicted, the fit of the approximate model to that of the mRNA/protein model is purely determined by the parameter β which measures the rate of linear decay of the mRNA.

Solving each of the above equations by transforming to travelling wave coordinates, as in Sec-

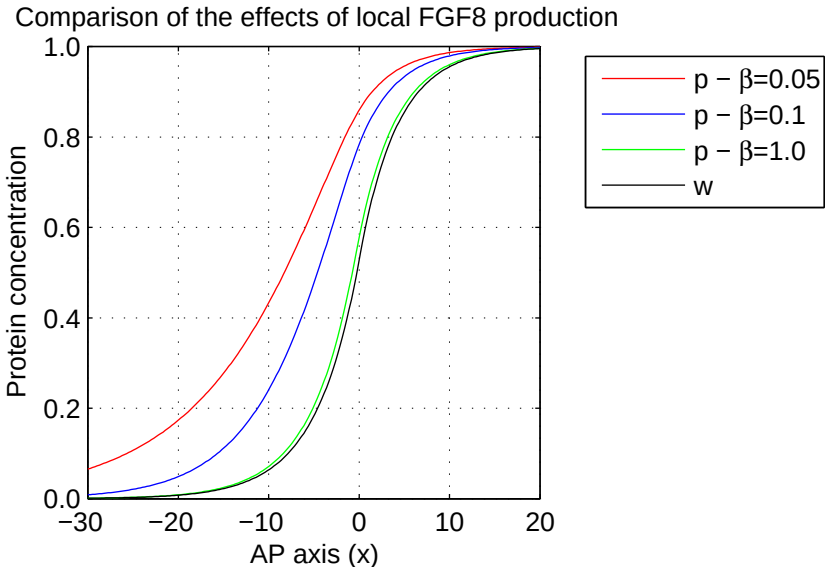


Figure 4.13: The changes in the protein concentration profile (p) as β, the linear decay rate of *fgf8* is varied. The red, blue and green lines show plots of the gradient for $\beta = 0.05, 0.1, 1.0$ respectively and the black profile shows the gradient when protein production is restricted to the tail region. As β is increased towards 1.0 the p gradient becomes more similar to the w gradient, as expected. Parameters are as follows: $\eta = 1.0$, $D_p = D_w = 20$, $x_n = 0.0$, $t = 0.0$ and $c_n = 0$.

tion 4.3.4, we have

$$p(x,t) = \begin{cases} A_l \exp\{n_+(x - x_n - c_n t)\} + A \exp\left\{\beta \frac{(x - x_n - c_n t)}{c_n}\right\} & \text{if} \quad x - x_n - c_n t \leq 0, \\ B_r \exp\{n_-(x - x_n - c_n t)\} + \frac{1}{\eta} & \text{if} \quad x - x_n - c_n t > 0, \end{cases} \tag{4.42}$$

$$w(x,t) = \begin{cases} \frac{n_-}{\eta(n_- - n_+)} \exp\{n_+(x - x_n - c_n t)\} & \text{if} \quad x - x_n - c_n t \leq 0, \\ \frac{n_+}{\eta(n_- - n_+)} \exp\{n_-(x - x_n - c_n t)\} + \frac{1}{\eta} & \text{if} \quad x - x_n - c_n t > 0, \end{cases} \tag{4.43}$$

with A_l, B_r, n_-, n_+ and A as defined in equations (4.23) and (4.24).

Figure 4.13 shows a plot of the changes in the concentration profile of p as the linear decay rate of *fgf8* is varied. When β is very small, there is a very noticeable difference in the steepness of the profiles with the p gradient being very much shallower than the w gradient. As β is increased the difference becomes less marked and for $\beta = 1.0$ the profiles are virtually indistinguishable.

In the following chapter we will consider the effects of local FGF8 application. This takes the form of a bead soaked in FGF8 (protein) implanted alongside the PSM. If β (decay rate of mRNA) is small compared to η (decay rate of protein) then the gradient of endogenous FGF8 will be shallow relative to that created by the bead and *vice versa*. The relative sizes of the parameters will have an effect on the region over which the bead effects are felt, and hence over which the anomalies are

formed. At present there is limited experimental data to determine which system to use and as a consequence of the preference for simplicity we choose to investigate further the properties of FGF8 when production is limited to the tail of the embryo.

4.5 Discussion

We began this chapter by summarising the experimental results of Pourquié, Dubrulle and co-workers [15, 17] and Sawada and co-workers [47] on the expression patterns of FGF8 in the PSM. In particular, we detailed the existence of a wavefront of FGF8 which moves in a posterior direction along the AP axis, the formation of somite anomalies when FGF8 expression is disrupted and the manner in which this gradient of FGF8 is maintained.

Subsequently, we proposed a modification of the cell cycle model which employs the FGF8 wavefront and the segmentation clock as controls for the production of the somitic and signalling factors. In short, the wavefront of FGF8 expression moves down the AP axis conferring, as it progresses, the ability upon cells to produce somitic factor, u. A certain time period (equal to the period of the segmentation clock) later, cells gain the ability to produce the signalling molecule, v. In this way, the model is able to partition cells into individual somites. This revised model can be thought of as a mathematical formulation of the re-invented clock and wavefront model proposed by Pourquié and co-workers [15, 48, 58].

The mathematical basis of this modification consisted of a system of four PDEs; one each for u and v as before, and the remaining two describing the dynamics of fgf8 mRNA, m, and protein, p. The latter two equations are decoupled from the rest of the system and were solved analytically. The full model was then solved numerically and shown to produce a series of coherent somites as seen in the cell cycle model.

We restricted production of *fgf8* to the node region of the embryo via the introduction of a Heaviside function multiplying the production term. It is unknown why the production of *fgf8* is restricted to the tail of the embryo but it is likely that it is connected to the expression of retinoic acid (RA) in more anterior regions of the PSM. We investigate a fuller model of FGF8/RA expression along the AP axis in Chapter 7.

We then considered the effect of transcriptional delay (i.e. a delay in the production of protein from mRNA) upon the FGF8 wavefront. Although such a delay was shown to cause a 'blip' in the monotonicity of the wavefront, any point chosen to be the determination front continued to move along the AP axis with constant speed and at no point before reaching the actual determination front could a cell, however briefly, experience a level of FGF8 below that expressed at the determination front proper. It does therefore not seem necessary to include the effects of transcriptional delay as this will only complicate matters mathematically and not lead to any great insights into the effects of FGF8 perturbation.

The final piece of analysis of this chapter brings us around to the main assumptions that will be carried forward into the following chapter: we investigated the effect of representing both fgf8 mRNA and protein by a generic fgf8 molecule. In contrast to FGF8 but in line with *fgf8*, the generic

factor is only produced in the node region of the embryo and it may diffuse along the PSM. Under all parameter regimes, the generic fgf8 factor gave rise to a wavefront which was qualitatively similar to that produced by the mRNA/protein model except that the gradient of the wavefront produced via the latter method was shallower, ensuring a more gradual progression from high expression levels of FGF8 to low expression levels. Under certain parameter regimes, most notably when the rate of mRNA decay was high, the wavefronts generated by the two mechanisms were almost identical.

In either case, the wavefront remained a monotonically increasing function of the spatial variable x which moved down the AP axis at a constant rate. The gradient of either wavefront can be adjusted via parameters controlling the rate of diffusion and linear decay, about which there is no data at present. In the next chapter, we investigate the effect of local perturbation of FGF8 on somite formation, and for simplicity chose to work with only a generic fgf8 molecule.

Chapter 5

Perturbation of endogenous FGF8

In the previous chapter we explored the formulation of different models for the FGF8 gradient present along the AP axis of vertebrate embryos. Due to a lack of knowledge of values of the parameters involved in the model we chose to model the gradient assuming that there is no *fgf8* present outside the tail of the embryo and therefore no local translation of FGF8. As a result of the previous assumption we choose to model somite formation using the following non-dimensional model:

$$\frac{\partial u}{\partial t} = \frac{(u+\mu v)^2}{\gamma+u^2}\chi_u - u, \tag{5.1}$$

$$\frac{\partial v}{\partial t} = \kappa\left(\frac{\chi_v}{\epsilon+u} - v\right) + D_v\frac{\partial^2 v}{\partial x^2}, \tag{5.2}$$

$$\frac{\partial w}{\partial t} = \chi_w - \eta w + D_w\frac{\partial^2 w}{\partial x^2}. \tag{5.3}$$

As in previous chapters, u represents the concentration of somitic factor, v the concentration of signalling molecule and w the concentration of FGF8. Production of u, v and w are controlled by the respective Heaviside functions

$$\chi_u = H(w^* - w), \tag{5.4}$$

$$\chi_v = H(t - t_w(w^*, x) - t_s), \tag{5.5}$$

$$\chi_w = H(x - x_n - c_n t), \tag{5.6}$$

where w^* is the level of FGF8 at the determination front, $t_w(w^*, x)$ is the time at which a cell at x reaches the determination front (ie. $w(x, t_w) = w^*$), t_s is the period of the segmentation clock, x_n represents the initial position of the tail and c_n represents the rate at which the AP axis is extending.

5.1 Normal segmentation

During normal segmentation the FGF8 gradient evolves according to the equation

$$\frac{\partial w}{\partial t} = \chi_w - \eta w + D_w \frac{\partial^2 w}{\partial x^2}, \tag{5.7}$$

with boundary conditions

$$\begin{array}{l} w \quad \text{is bounded as} \quad x - \{x_n + c_n t\} \to +\infty, \\ w \to 0 \quad \text{as} \quad x - \{x_n + c_n t\} \to -\infty, \end{array} \tag{5.8}$$

and initial conditions given by $w(x,0) = w_0(x)$.

In Section 4.4.2 we solved equation (5.3) by transforming to travelling wave coordinates to give:

$$w(x,t) = \begin{cases} \dfrac{n_-}{\eta(n_- - n_+)} \exp\{n_+(x - x_n - c_n t)\} & \text{if} \quad x - x_n - c_n t \leq 0, \\ \dfrac{n_+}{\eta(n_- - n_+)} \exp\{n_-(x - x_n - c_n t)\} + \dfrac{1}{\eta} & \text{if} \quad x - x_n - c_n t > 0, \end{cases} \tag{5.9}$$

where

$$n_\pm = \frac{-c_n \pm \sqrt{c_n^2 + 4\eta D_w}}{2D_w}. \tag{5.10}$$

Figure 5.1 shows a plot of the travelling wave solution for w given by equation (5.9). Figure 5.1(a) shows the profile as the rate of linear decay varies and demonstrates an increase in the level of FGF8 present as η decreases. Figure 5.1(b) shows that the profile progressively steepens as the diffusion coefficient, D_w, decreases.

We can also solve equation (5.3) by taking Fourier Transforms, as in Section 3.1.2. With general initial conditions we have

$$w(x,t) = \frac{e^{-\eta t}}{\sqrt{4\pi t D_w}} \int_{-\infty}^{\infty} w_0(x') \exp\left(\frac{-(x - x_n - x')^2}{\sqrt{4tD_w}}\right) \mathrm{d}x'. \tag{5.11}$$

$$+\frac{1}{2\eta}\left[1 - e^{-\eta t}\right] + \frac{1}{2} e^{-\eta t} \int_0^t \mathrm{erf}\left(\frac{x - x_n - c_n t'}{\sqrt{4D_w(t - t')}}\right) e^{\eta t'} \, \mathrm{d}t'. \tag{5.12}$$

Throughout this work we will be considering the process of somite formation in its 'middle' stages i.e. we will not be considering the establishment of the FGF8 profile along the AP axis but only the progression of the wavefront once it has reached its steady state profile. It therefore seems sensible

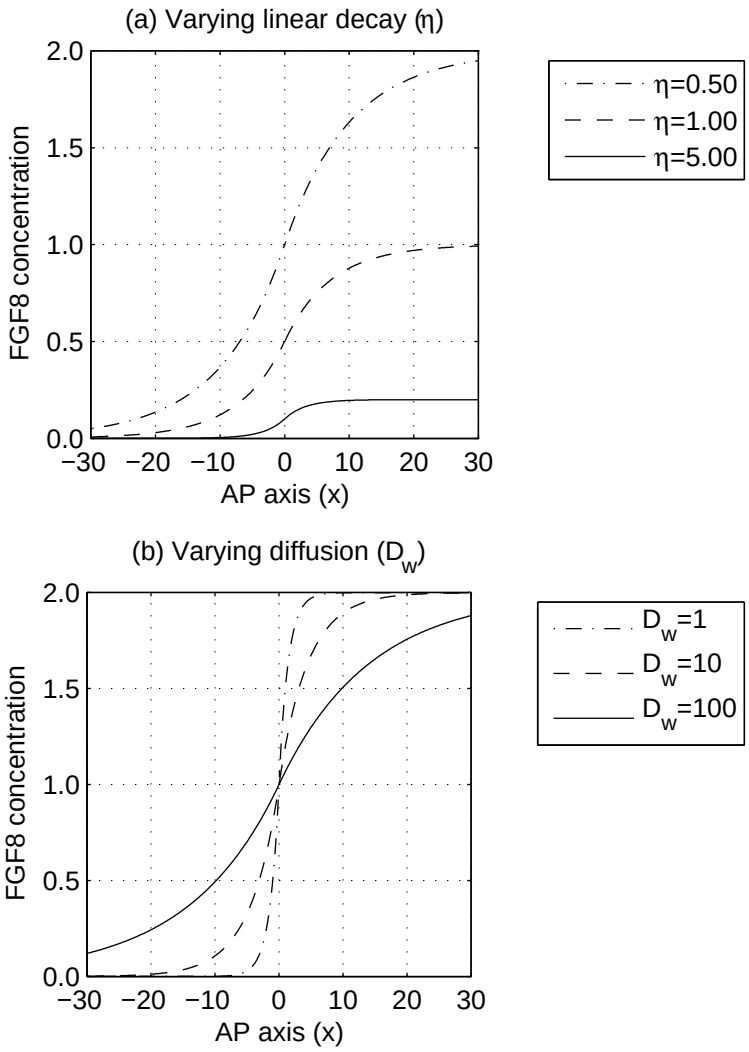


Figure 5.1: Plots of the travelling wave solution given by equation (5.9) for w with varying parameters. (a) Varying the linear decay rate (η). As η is increased the level of FGF8 present in the tail of the embryo decreases. (b) Varying the rate of diffusion (D_w). As D_w is increased the profile becomes more shallow. Unless otherwise stated parameters are as follows: $\eta = 0.5$, $D_w = 50$, $c_n = 0.0$, $x_n = 0.0$ and the Heaviside function parameter, $\delta = 10^{-3}$. All the solutions are plotted at $t = 0.0$.

to use initial conditions given by evaluating equation (5.9) at $t = 0$. In this case we have

$$w_0(x) = \begin{cases} \dfrac{n_-}{\eta(n_- - n_+)} \exp\{n_+(x - x_n)\} & \text{if} \quad x - x_n \leq 0, \\ \dfrac{n_+}{\eta(n_- - n_+)} \exp\{n_-(x - x_n)\} + \dfrac{1}{\eta} & \text{if} \quad x - x_n > 0, \end{cases} \tag{5.13}$$

and as a result:

$$\begin{aligned} w(x,t) &= \frac{1}{2\eta}\left[1+\text{erf}\left(\frac{x-x_n}{\sqrt{4D_w t}}\right)\right]e^{-\eta t} \\ &\quad +\frac{1}{2\eta}\left[1+\text{erf}\left(\frac{x-x_n+2n_-D_w t}{\sqrt{4D_w t}}\right)\right]\frac{n_+}{(n_- - n_+)}e^{n_-(x-x_n-c_n t)-\eta t} \\ &\quad +\frac{1}{2\eta}\left[1-\text{erf}\left(\frac{x-x_n+2n_+D_w t}{\sqrt{4D_w t}}\right)\right]\frac{n_-}{(n_- - n_+)}e^{n_+(x-x_n-c_n t)-\eta t} \\ &\quad +\frac{1}{2\eta}\left[1-e^{-\eta t}\right]+\frac{1}{2}e^{-\eta t}\int_0^t \text{erf}\left(\frac{x-x_n-c_n t'}{\sqrt{4D_w(t-t')}}\right)e^{\eta t'}\,\text{d}t'. \end{aligned} \tag{5.14}$$

We will compare the solutions given by equations (5.9) and (5.14) in Section 5.3.

5.1.1 Numerical solution

We solved equation (5.3) numerically using the MATLAB function pdepe (see Appendix A.3 for more details) which solves initial-boundary value problems for systems of parabolic and elliptic PDEs in one space variable and time. The initial conditions are given by equation (5.13) and the boundary conditions given by (5.8) were approximated by zero flux boundary conditions on a finite domain. As in previous chapters, the Heaviside function is approximated by a continuous $\tanh$ function.

pdepe uses a second order spatial discretisation to reduce the equations to a system of ODEs in time. The resulting system is solved using the MATLAB ODE solver ode15s. (More details can be found in Appendix A.2).

Figure 5.2(a) contains a plot of the numerical solution of equation (5.3) computed using the MATLAB function pdepe and Figure 5.2(b) a plot of the percentage error between the numerical solution and the analytical solutions given by equations (5.9) and (5.14). The integral in the fifth term of equation (5.14) is computed numerically using the MATLAB function quadl which uses an adaptive Lobatto quadrature method (see Appendix A.5 for more details). The percentage error between the solutions is calculated (for a particular x) as

$$\text{Percentage error} = \frac{w_{numerical} - w_{analytical}}{w_{numerical}}\text{x}100. \tag{5.15}$$

In both cases the percentage error between the solutions becomes large as $x \to -\infty$ where both the numerical and analytical solutions tend to zero, but the numerical solution tends to its limit more quickly. Since it is apparent that there is little difference between these solutions and we are not concerned with w levels away from the determination front, we ignore this error. As $x \to \infty$ and both solutions tend to a non-zero constant the percentage error tends to zero.

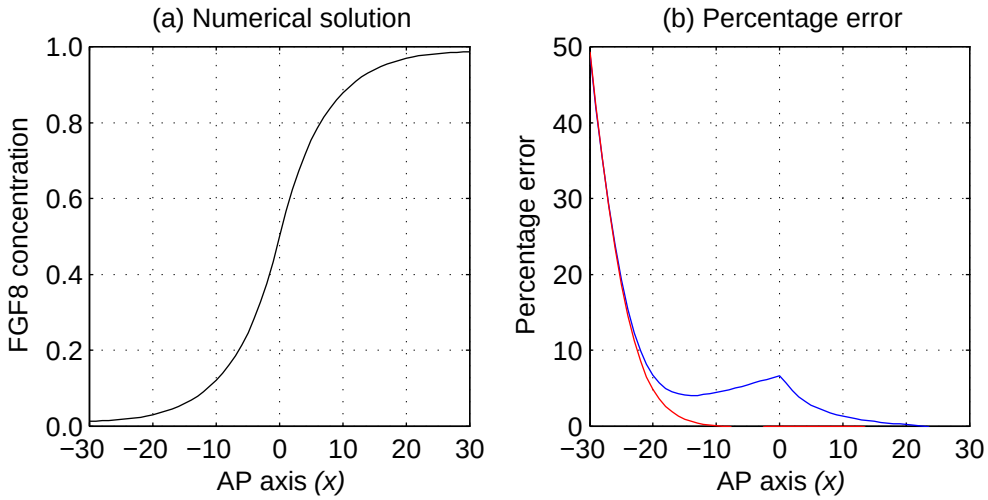


Figure 5.2: (a) A plot of the numerical solution of equation (5.3) computed using the MATLAB function pdepe. (b) A plot of the percentage error between the numerical solution and the analytical solutions given by equations (5.9) and (5.14). The error between the numerical solution and the travelling wave solution is indicated in red and the error between the numerical solution and the solution obtained by taking Fourier Transforms is indicated in blue. Parameters are as follows: $\eta = 1.0$, $D_w = 50$, $c_n = 0.0$, $x_n = 0.0$ and the Heaviside function parameter, $\delta = 10^{-3}$. All the solutions are plotted at $t = 5.0$.

5.2 Local application of FGF8

We now consider the case in which we have local application of FGF8 in the PSM. In experiments carried out by Dubrulle and co-workers [15] heparin beads soaked in FGF8 are implanted next to the PSM. We model this by assuming that there is another source of FGF8 in the PSM which is at a fixed point and which releases FGF8 into the surrounding tissue. The modified non-dimensional equations for somite formation are

$$\frac{\partial u}{\partial t} = \frac{(u+\mu v)^2}{\gamma + u^2}\chi_u - u, \tag{5.16}$$

$$\frac{\partial v}{\partial t} = \kappa\left(\frac{\chi_v}{\epsilon + u} - v\right) + D_v\frac{\partial^2 v}{\partial x^2}, \tag{5.17}$$

$$\frac{\partial w}{\partial t} = \chi_w + \phi\chi_b - \eta w + D_w\frac{\partial^2 w}{\partial x^2}, \tag{5.18}$$

where χ_u, χ_v and χ_w are as in Section 5.1 and $\chi_b = H(\xi - x_b + x)H(\xi + x_b - x)$ represents a source of FGF8 from a bead. x_b is the position of the midpoint of the bead implant and ξ is a measure of the width of the bead (χ_b is non-zero over a region of width 2ξ, centered at x_b). We assume the same boundary conditions for u, v and w as before.

5.2.1 Analytical solution with application of FGF8

The non-dimensionalised w equation is

$$\frac{\partial w}{\partial t} = \chi_w + \phi\chi_b - \eta w + D_w \frac{\partial^2 w}{\partial x^2}, \tag{5.19}$$

where

$$\chi_w(x,t) = H\left(x - x_n - c_n t\right), \tag{5.20}$$
$$\chi_b(x,t) = H(\xi - x_b + x)H(\xi + x_b - x). \tag{5.21}$$

As before, the boundary conditions are given by

$$\begin{array}{l} w \quad \text{is bounded as} \quad x - \{x_n + c_n t\} \to +\infty, \\ w \to 0 \quad \text{as} \quad x - \{x_n + c_n t\} \to -\infty, \end{array} \tag{5.22}$$

and the initial conditions are given by equation (5.13).

Suppose that we may find w_h and w_b, such that w_h solves

$$\frac{\partial w}{\partial t} = \chi_w - \eta w + D_w \frac{\partial^2 w}{\partial x^2}, \tag{5.23}$$

with boundary conditions

$$\begin{array}{l} w \quad \text{is bounded as} \quad x_n - c_n t \to +\infty, \\ w \to 0 \quad \text{as} \quad x_n - c_n t \to -\infty, \end{array} \tag{5.24}$$

and initial conditions given by $w(x,0) = w_0(x)$, and such that w_b solves

$$\frac{\partial w}{\partial t} = \phi\chi_b - \eta w + D_w \frac{\partial^2 w}{\partial x^2}, \tag{5.25}$$

with boundary conditions

$$w \to 0 \quad \text{as} \quad x_n - c_n t \to \pm\infty, \tag{5.26}$$

and initial conditions given by $w(x,0) = 0$. Then $w = w_h + w_b$ solves (5.19).

5.2.1.1 Solution of the w_b equation using Green's functions

We wish to solve

$$\frac{\partial w}{\partial t} = \phi H(\xi - x_b + x)H(\xi + x_b - x) - \eta w + D_w \frac{\partial^2 w}{\partial x^2}, \tag{5.27}$$

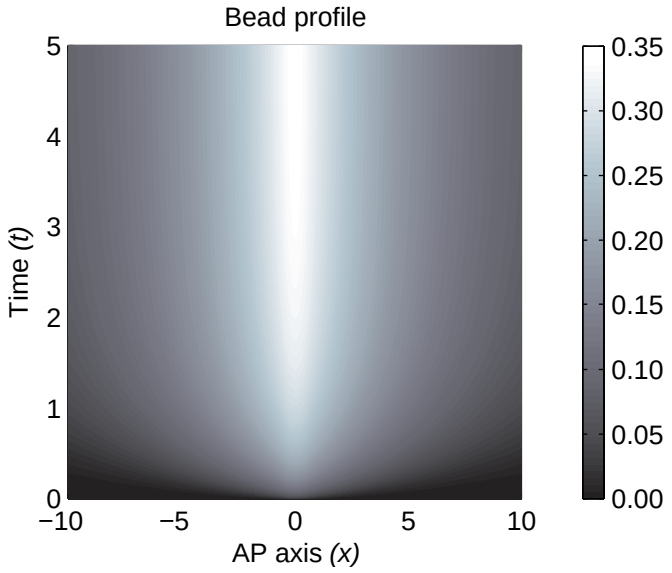


Figure 5.3: The analytic solution (5.30) of equation (5.25). The initial level of FGF8 increases very rapidly and then tails off as the steady state is approached. Parameters are as follows: $\eta = 1.0$, $D_w = 50$, $\xi = 0.5$, $x_b = 0$ and $\phi = 5.0$.

with initial conditions $w(x, 0) = 0$ and boundary conditions $w \to 0$ as $x \to \pm\infty$. Using the method introduced in Section 3.1.2 we have, letting $y(x, t) = w(x, t) \exp(\eta t)$,

$$y(x,t) = \int_0^t \int_{-\infty}^{\infty} \frac{\phi H(\xi - x_b + x) H(\xi + x_b - x)}{\sqrt{4D_w \pi (t - t')}} \exp\left[\eta t' - \frac{(x - x')^2}{4D_w(t - t')}\right] \mathrm{d}x' \, \mathrm{d}t'. \quad (5.28)$$

Therefore

$$w_b(x,t) = \frac{\phi}{2} \int_0^t \left[\mathrm{erf}\left(\frac{x - x_b + \xi}{\sqrt{4D_w(t - t')}}\right) - \mathrm{erf}\left(\frac{x - x_b - \xi}{\sqrt{4D_w(t - t')}}\right)\right] \exp\left[-\eta(t - t')\right] \, \mathrm{d}t'. \quad (5.29)$$

Making the change of variables $s = \eta(t - t')$ gives

$$w_b(x,t) = \frac{\phi}{2\eta} \int_0^{\eta t} \left[\mathrm{erf}\left(\frac{x - x_b + \xi}{\sqrt{4D_w s/\eta}}\right) - \mathrm{erf}\left(\frac{x - x_b - \xi}{\sqrt{4D_w s/\eta}}\right)\right] e^{-s} \, \mathrm{d}s. \quad (5.30)$$

Figure 5.3 shows the analytic solution (5.30) of equation (5.25). Starting with zero initial conditions, the profile quickly grows, with a peak centered around the point x_b, and reaches a steady state within the time taken to form one or two somites.

5.2.1.2 Parameter dependence of the bead

Figure 5.4 shows a plot of the steady state FGF8 profile created by a bead implant for different values of the key parameters η, D_w and ξ. As in Figure 5.2, the integrals of equation (5.30) were evaluated using the MATLAB function quadl.

5.2.1.3 Solution of the w equation using Green's functions

The solution of equation (5.19) with boundary conditions given by equation (5.8) and initial conditions given by equation (5.13) is

$$\begin{aligned} w(x,t) &= \frac{1}{2\eta}\left[1+\text{erf}\left(\frac{x-x_n}{\sqrt{4D_w t}}\right)\right]e^{-\eta t} \\ &+\frac{1}{2\eta}\left[1+\text{erf}\left(\frac{x-x_n+2n_-D_w t}{\sqrt{4D_w t}}\right)\right]\frac{n_+}{(n_- - n_+)}e^{n_-(x-x_n-c_n t)-\eta t} \\ &+\frac{1}{2\eta}\left[1-\text{erf}\left(\frac{x-x_n+2n_+D_w t}{\sqrt{4D_w t}}\right)\right]\frac{n_-}{(n_- - n_+)}e^{n_+(x-x_n-c_n t)-\eta t} \\ &+\frac{1}{2\eta}\left[1-e^{-\eta t}\right]+\frac{1}{2}e^{-\eta t}\int_0^t \text{erf}\left(\frac{x-x_n-c_n t'}{\sqrt{4D_w(t-t')}}\right)e^{\eta t'}\,\text{d}t' \\ &+\frac{\phi}{2}e^{-\eta t}\int_0^t\left[\text{erf}\left(\frac{x-x_b+\xi}{\sqrt{4D_w(t-t')}}\right)-\text{erf}\left(\frac{x-x_b-\xi}{\sqrt{4D_w(t-t')}}\right)\right]e^{\eta t'}\,\text{d}t'. \end{aligned} \tag{5.31}$$

5.2.2 "Realistic choices" for the parameters

As mentioned earlier, there is no experimental evidence available to indicate what parameter choices we might select. Consider the non-dimensional equation for FGF8:

$$\frac{\partial w}{\partial t} = H(x-x_n-c_n t)+\phi H(\xi-x_b+x)H(\xi+x_b-x)-\eta w+D_w\frac{\partial^2 w}{\partial x^2}. \tag{5.32}$$

The parameter ϕ is simply a measure of the relative strengths of the sources of FGF8 coming from the tail of the embryo and the bead implant. Although there is data indicating the relative strengths of the two sources it is very hard to translate this into parameters for the model. In experiments where FGF8 is perturbed locally, the sources of FGF8 are created by soaking Heparin beads overnight in certain concentrations of FGF8 solution and then implanting them alongside the PSM [15]. It is difficult to assess the amount of FGF8 absorbed by the bead whilst it is soaking in solution and also the rate at which it is released once implanted *in vivo*. Other factors which make it hard to assess the effects of the bead are that there is little data to indicate how much FGF8 is able to pass into the PSM itself and the rate at which it will diffuse once inside. It is likely that only a small fraction of the FGF8 diffusing out from the bead is able to enter the PSM and such measurements are not available at this time. In Chapter 6 we propose a method by which the anomalies produced by our model can be used to estimate the amount of FGF8 entering the PSM and its rate of diffusion.

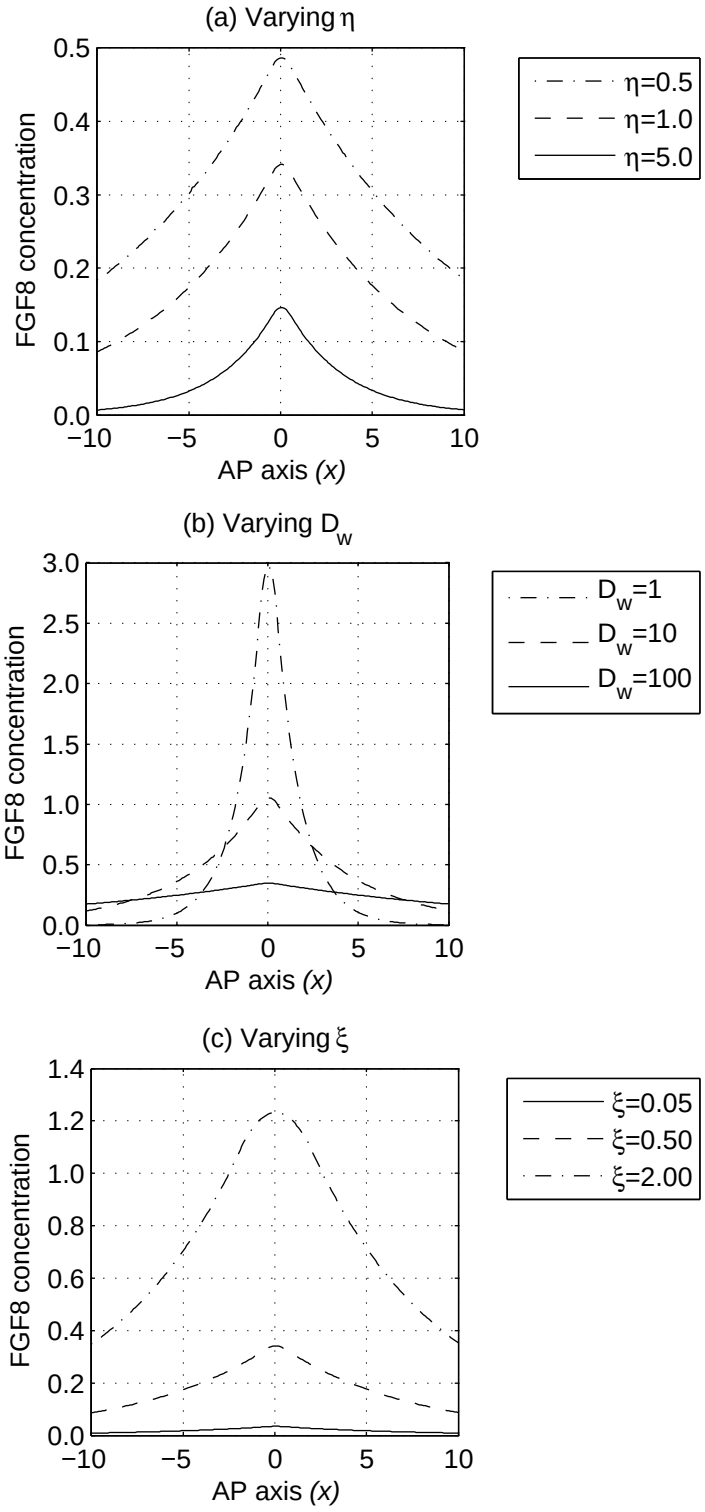


Figure 5.4: The FGF8 profile generated by a bead implanted alongside the PSM. (a) Variation of the profile as the linear decay rate of FGF8 is varied: as η is increased the level of FGF8 decreases. (b) Variation of the profile as the diffusion parameter is varied: as D_w is increased, the effects of the bead extend over a wider range either side of the bead. (c) Variation of the profile as the width of the bead is varied: as the bead width is increased the height of the profile increases. Unless otherwise stated, parameters are as follows: $\eta = 1.0$, $D_w = 50$, $\xi = 0.5$, $x_b = 0$ and $\phi = 5.0$.

The linear decay rate, η, and diffusion coefficient, D_w, control the gradient and level of FGF8 along the PSM. Since we wish to have a stable gradient of FGF8 established along the PSM it seems reasonable to chose a decay rate for w that is much slower than that for the signal v.

Although we wish to ensure that the FGF8 profile is not too sharp (so that we can see the effects of small FGF8 perturbations) we will chose $D_v > D_w \gg 1$ in order that the profile does not have too steep a gradient but to ensure that w diffuses less quickly than the signal, v.

Assuming that $c_n \ll 1$ seems realistic since chick somites are approximately of length 100μm and one somite forms every 90 minutes, giving a (dimensional) rate of extension of the embryo of order 10^{-8} ms^{-1}. Unless the rate of linear decay of the somitic factor is very slow ($\nu < 10^{-4}$ - see Chapter 2), the non-dimensionalised rate of axis extension will also be such that $c_n \ll 1$. The position of the node is represented by the parameter x_n. Given the assumption that c_n is small compared with ηD_w, then $n_+ \approx -n_-$ in equation (5.10) and the midpoint of the profile lies at approximately $x = x_n$. The PSM is made up of about 12-14 cells worth of somites [15] with the determination front lying around the middle of the PSM. Therefore assuming that the determination front corresponds to the midpoint of the FGF8 profile (reasonable since it coincides with the point at which FGF8 signalling drops from high to low), we can assume that $2(x_n + c_n t)$ will estimate the position of the tail of the embryo and that $x_n \approx 0$ if the determination front initially lies at $x = 0$.

5.2.3 Numerical simulation

As previously, the numerical solution is computed using the NAG library software D03PCF. We use zero flux boundary conditions on the domain $[-10, 30]$ to approximate the infinite domain used in the model and continuous $\tanh$ approximations for the Heaviside functions controlling the production of w. Initial conditions were taken to be the state of the travelling wave given by equation (5.9) at $t = 0$. Figure 5.5 shows plots of the numerical solution for the FGF8 profile along the AP axis over a series of time steps. In Figure 5.5(a) a control embryo is shown with the determination front moving a constant distance during each time step. In Figure 5.5(b) a bead is implanted at $x = 10.0$ and we see that the constant progression of the determination front is disturbed. In a region ahead of the bead the front moves more slowly whilst behind the bead it moves more quickly.

5.3 Approximations

In order to be able to manipulate the results for $w(x, t)$ more easily, it is useful to make some approximations to the FGF8 concentration profiles originating from endogenous *fgf8* in the tail of the embryo and the bead implant.

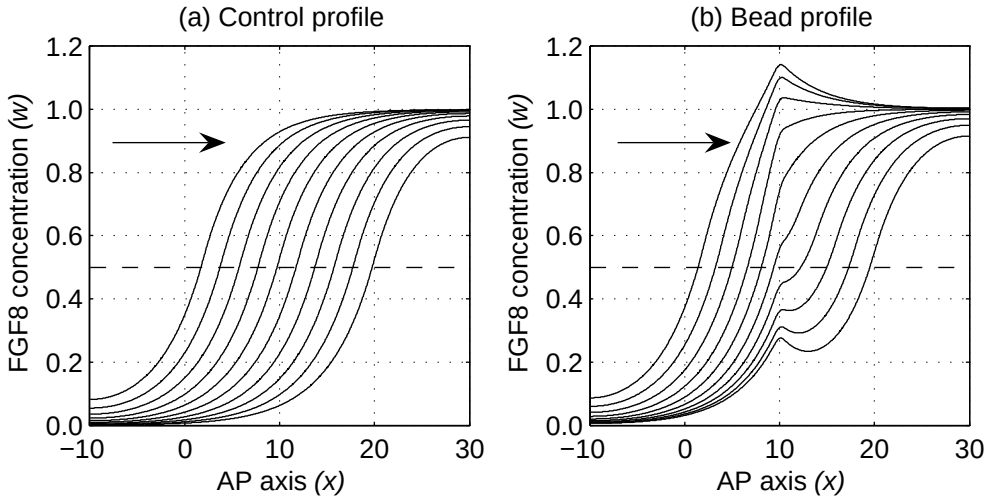


Figure 5.5: Numerical solution for the FGF8 profile along the AP axis. In each graph the solution is plotted for $t = 4, 8, 12, 16, 20, 24, 28, 32, 36, 40$ and the hypothetical level of FGF8 marking the determination front is indicated by the dashed line. (a) In a control embryo the position of the determination front moves with constant speed down the AP axis. (b) A bead soaked in FGF8 is implanted at $x = 10.0$ resulting in perturbation of the determination front: in a region ahead of the bead progression of the determination front slows, whilst behind the bead the rate of progression of the determination front increases. Parameters are as follows: $\eta = 1.0$, $D_w = 50$, $\xi = 0.5$, $x_b = 0$ and $\phi = 5.0$.

5.3.1 Approximations for the endogenous gradient

We have the following solution for the FGF8 profile with an endogenous source of FGF8 in the PSM:

$$\begin{aligned} w(x,t) &= \frac{1}{2\eta}\left[1+\text{erf}\left(\frac{x-x_n}{\sqrt{4D_w t}}\right)\right]e^{-\eta t} \\ &\quad +\frac{1}{2\eta}\left[1+\text{erf}\left(\frac{x-x_n+2n_-D_w t}{\sqrt{4D_w t}}\right)\right]\frac{n_+}{(n_- - n_+)}e^{n_-(x-x_n-c_n t)-\eta t} \\ &\quad +\frac{1}{2\eta}\left[1-\text{erf}\left(\frac{x-x_n+2n_+D_w t}{\sqrt{4D_w t}}\right)\right]\frac{n_-}{(n_- - n_+)}e^{n_+(x-x_n-c_n t)-\eta t} \\ &\quad +\frac{1}{2\eta}\left[1-e^{-\eta t}\right]+\frac{1}{2}e^{-\eta t}\int_0^t \text{erf}\left(\frac{x-x_n-c_n t'}{\sqrt{4D_w(t-t')}}\right)e^{\eta t'}\,\text{d}t'. \end{aligned} \tag{5.33}$$

The first three terms arise from the initial conditions on w given by equation (5.13) and we have for the first term:

$$\frac{1}{2\eta}\left[1+\text{erf}\left(\frac{x-x_n}{\sqrt{4D_w t}}\right)\right]e^{-\eta t} \to 0 \quad \text{as} \quad t \to \infty, \tag{5.34}$$

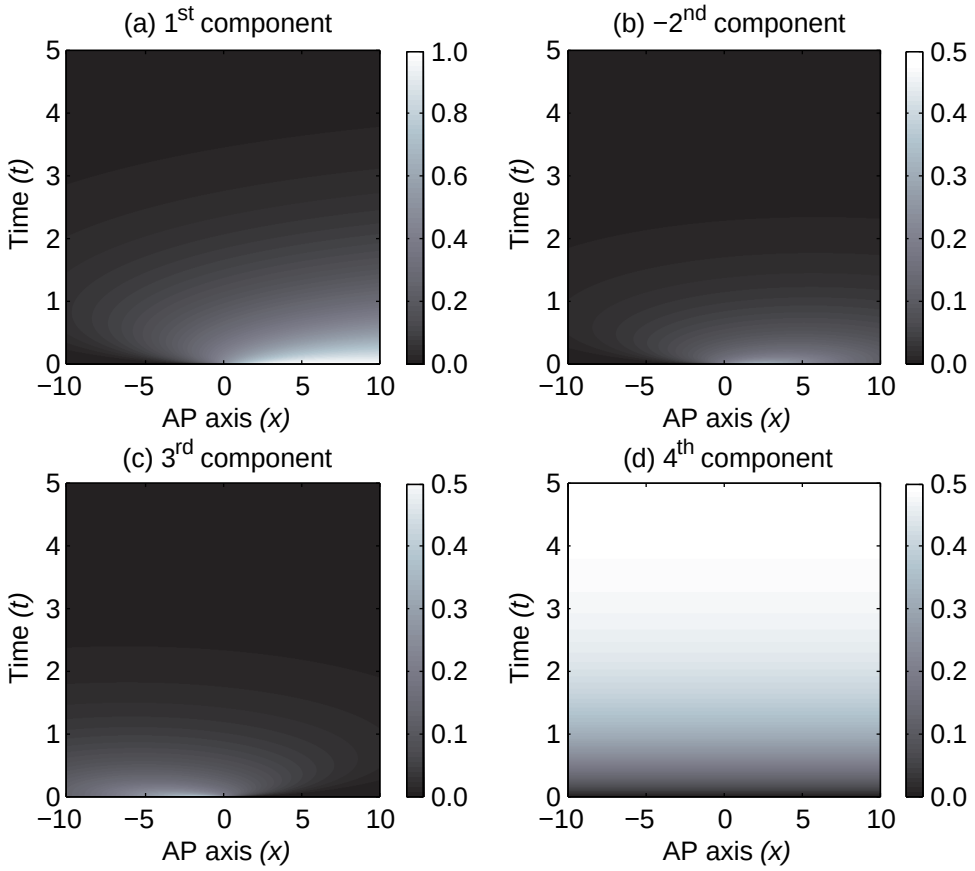


Figure 5.6: Plots of the individual components of equation (5.33) which gives the analytical solution for the FGF8 profile established by an endogenous source of FGF8. (a) – (c) show plots of the first three terms of the solution which arise through the initial conditions given by equation (5.13) and they tend to zero everywhere very quickly. In (d) we see that the 4th term tends to $1/2\eta$. Parameters are as follows: $\eta = 1.0$, $D_w = 50$, $x_n = 0.0$, and $c_n = 0.5$.

and similarly for the third term:

$$\frac{1}{2\eta}\left[1 - \text{erf}\left(\frac{x - x_n + 2n_+ D_w t}{\sqrt{4D_w t}}\right)\right]\frac{n_-}{(n_- - n_+)}e^{n_+(x - x_n - c_n t) - \eta t} \to 0 \quad \text{as} \quad t \to \infty, \tag{5.35}$$

since $n_+ > 0$, $\eta > 0$, $c_n > 0$ and $|\text{erf}(x)| \leq 1, \ \forall x \in \mathbb{R}$. The second term behaves like $[1 + \text{erf}(\sqrt{t})]e^t$ as $t \to \infty$ and using Theorem C.1.1 (see Appendix C) we see that it also tends to zero as $t \to \infty$.

It is easy to see that the fourth term tends to $1/2\eta$. Figure 5.6 contains plots of the first four terms of equation (5.33) and demonstrates that each component quickly tends to a steady state value.

The fifth term represents the travelling wave part of the solution since if $x - c_n t = X - c_n T$ then

$$e^{-\eta t} \int_0^t \text{erf}\left(\frac{x - x_n - c_n t'}{\sqrt{4D_w(t-t')}}\right) e^{\eta t'} \, \mathrm{d}t' \tag{5.36}$$

$$= \int_0^{\frac{x-X}{c_n}+T} \text{erf}\left(\frac{x - x_n - (x-X) - c_n T}{\sqrt{4D_w(\frac{x-X}{c_n} + T - t')}}\right) \exp\left(t' - \frac{(x-X)}{c_n} - T\right) \mathrm{d}t'. \tag{5.37}$$

Letting $t'' = t' - (x-X)/c_n$:

$$= \int_{-\frac{x-X}{c_n}}^{T} \text{erf}\left(\frac{X - x_n - c_n T}{\sqrt{4D_w(T-t'')}}\right) \exp\left(t'' - T\right) \mathrm{d}t'. \tag{5.38}$$

$$= \int_0^T \text{erf}\left(\frac{X - x_n - c_n T}{\sqrt{4D_w(T-t'')}}\right) \exp\left(t'' - T\right) \mathrm{d}t'$$

$$+ \int_{-\frac{x-X}{c_n}}^{0} \text{erf}\left(\frac{X - x_n - c_n T}{\sqrt{4D_w(T-t'')}}\right) \exp\left(t'' - T\right) \mathrm{d}t'. \tag{5.39}$$

Since $\text{erf}(z)$ is bounded the second term of equation (5.39) tends to zero as $T \to \infty$ and we see that the solution (5.33) for the FGF8 profile along the AP axis approaches travelling wave form as $t \to \infty$. Figure 5.7 shows a plot of the 5^{th} component of equation (5.33) and demonstrates the travelling wave nature of the solution.

Figure 5.8 shows a plot of the analytical solution for w, given by equation (5.33), in a moving frame of the form $x = c_n t + A$ for an arbitrary choice of $A = 1.0$. That each of the dashed and dash-dotted lines tends to a constant (and therefore that the solid line does also) is consistent with the notion that the solution can be represented with a travelling wave (although not proof of that fact).

5.3.2 FGF8 perturbation by a bead implant

From Figure 5.3 we see that an FGF8 profile set up by a bead of FGF8 very quickly reaches a steady state: within the time taken to form one to two somites, the bead source has reached a steady profile. Consider equation (5.30):

$$w_b(x,t) = \frac{\phi}{2\eta} \int_0^{\eta t} \left[\text{erf}\left(\frac{x - x_b + \xi}{\sqrt{4D_w s/\eta}}\right) - \text{erf}\left(\frac{x - x_b - \xi}{\sqrt{4D_w s/\eta}}\right)\right] e^{-s} \, \mathrm{d}s.$$

Letting $A_\pm = (x - x_b \pm \xi)/\sqrt{4D_w/\eta}$ we have

$$\begin{aligned} w_b(x,t) &= \frac{\phi}{\eta\sqrt{\pi}} \int_0^{\eta t} \left\{ \int_0^{A_+/\sqrt{y}} e^{-v^2} \, \mathrm{d}v - \int_0^{A_-/\sqrt{y}} e^{-v^2} \, \mathrm{d}v \right\} e^{-y} \, \mathrm{d}y, \\ &= \frac{\phi}{\eta\sqrt{\pi}} \int_0^{\eta t} \left\{ \text{sign}(A_+) \int_0^{|A_+|/\sqrt{y}} e^{-v^2} \, \mathrm{d}v - \text{sign}(A_-) \int_0^{|A_-|/\sqrt{y}} e^{-v^2} \, \mathrm{d}v \right\} e^{-y} \, \mathrm{d}y. \end{aligned} \tag{5.40}$$

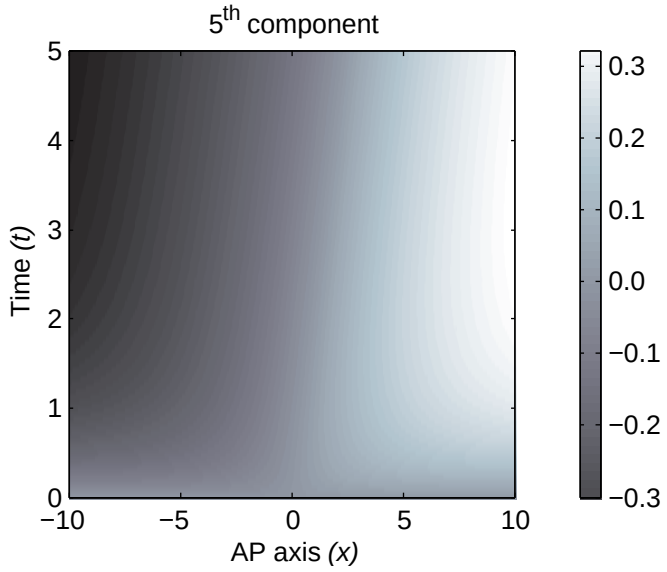


Figure 5.7: Plot of the 5^{th} component of equation (5.33) demonstrating the travelling wave nature of the solution: as t increases the region of high FGF8 moves down the AP axis with constant speed. Parameters are as follows: $\eta = 1.0$, $D_w = 50$, $x_n = 0.0$ and $c_n = 0.5$.

Interchanging the order of integration gives

$$\begin{aligned}
w_b(x,t) &= \frac{\phi}{\eta\sqrt{\pi}}\text{sign}(A_+)\int_{|A_+|/\sqrt{\eta t}}^{\infty}\int_0^{{A_+}^2/v^2} e^{-(y+v^2)}\,\mathrm{d}y\,\mathrm{d}v \\
&\quad -\frac{\phi}{\eta\sqrt{\pi}}\text{sign}(A_-)\int_{|A_-|/\sqrt{\eta t}}^{\infty}\int_0^{{A_-}^2/v^2} e^{-(y+v^2)}\,\mathrm{d}y\,\mathrm{d}v, \\
&= \frac{\phi}{\eta\sqrt{\pi}}\text{sign}(A_+)\int_{|A_+|/\sqrt{\eta t}}^{\infty} e^{-v^2}\left[1-e^{-A_+^2/v^2}\right]\,\mathrm{d}v \\
&\quad -\frac{\phi}{\eta\sqrt{\pi}}\text{sign}(A_-)\int_{|A_-|/\sqrt{\eta t}}^{\infty} e^{-v^2}\left[1-e^{-A_-^2/v^2}\right]\,\mathrm{d}v, \\
&= \frac{\phi}{2\eta}\text{sign}(A_+)\text{erfc}\left(\frac{|A_+|}{\sqrt{\eta t}}\right) - \frac{\phi}{2\eta}\text{sign}(A_-)\text{erfc}\left(\frac{|A_-|}{\sqrt{\eta t}}\right) \\
&\quad -\frac{\phi}{\eta\sqrt{\pi}}\text{sign}(A_+)\int_{|A_+|/\sqrt{\eta t}}^{\infty} e^{-v^2-A_+^2/v^2}\,\mathrm{d}v \\
&\quad +\frac{\phi}{\eta\sqrt{\pi}}\text{sign}(A_-)\int_{|A_-|/\sqrt{\eta t}}^{\infty} e^{-v^2-A_-^2/v^2}\,\mathrm{d}v. \qquad (5.41)
\end{aligned}$$

Consider

$$\int_a^b e^{-v^2-\frac{M^2}{v^2}}\,\mathrm{d}v = \frac{1}{2}\int_a^b\left(1+\frac{M}{v^2}\right)e^{-v^2-\frac{M^2}{v^2}}\,\mathrm{d}v + \frac{1}{2}\int_a^b\left(1-\frac{M}{v^2}\right)e^{-v^2-\frac{M^2}{v^2}}\,\mathrm{d}v. \qquad (5.42)$$

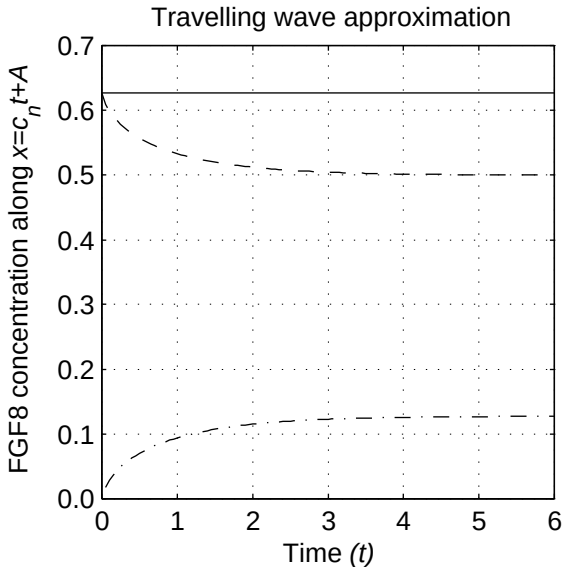


Figure 5.8: Demonstration of the travelling wave nature of the FGF8 profile in the PSM: the sum of the first four components of equation (5.33) is indicated by the dashed line, the fifth by the dash-dotted line and the sum of all the components by the solid line. In all of the plots $x = c_n t + A$ where A is some constant. Plotting such a profile is equivalent to viewing the solution through a travelling frame moving with speed c_n. The solid line, indicating the level of endogenous FGF8, is constant which is in agreement with the suggestion that the profile can be approximated by a travelling wave solution. Parameters are as follows $\eta = 1.0$, $D_w = 20$, $x_n = 0.0$, $c_n = 0.5$ and $A = 1.0$.

This can be evaluated by making a change of variables: in the first integral let $u = v - M/v$ and in the second integral let $u = v + M/v$.

Applying this to the previous equation,

$$\begin{aligned} w_b(x,t) &= \frac{\phi}{2\eta}\text{sign}(A_+)\text{erfc}\left(\frac{|A_+|}{\sqrt{\eta t}}\right) - \frac{\phi}{2\eta}\text{sign}(A_-)\text{erfc}\left(\frac{|A_-|}{\sqrt{\eta t}}\right) \\ &\quad -\frac{\phi}{4\eta}\text{sign}(A_+)\left[1-\text{erf}\left(\frac{|A_+|-\eta t}{\sqrt{\eta t}}\right)\right]\exp(-2|A_+|) \\ &\quad -\frac{\phi}{4\eta}\text{sign}(A_+)\left[1-\text{erf}\left(\frac{|A_+|+\eta t}{\sqrt{\eta t}}\right)\right]\exp(2|A_+|) \\ &\quad +\frac{\phi}{4\eta}\text{sign}(A_-)\left[1-\text{erf}\left(\frac{|A_-|-\eta t}{\sqrt{\eta t}}\right)\right]\exp(-2|A_-|) \\ &\quad +\frac{\phi}{4\eta}\text{sign}(A_-)\left[1-\text{erf}\left(\frac{|A_-||+\eta t}{\sqrt{\eta t}}\right)\right]\exp(2|A_-|). \end{aligned} \tag{5.43}$$

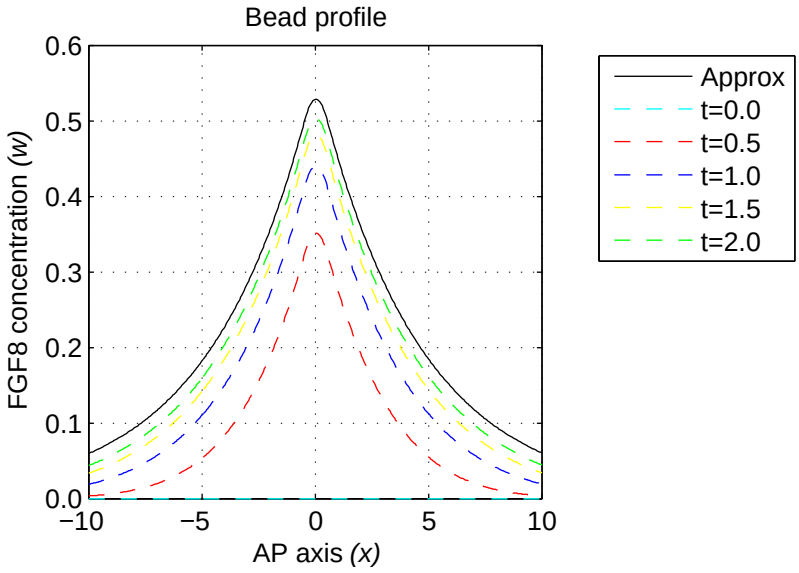


Figure 5.9: Comparison between the analytical solution for the bead profile given by equation (5.30) and its approximation (5.44) as t increases. The analytical solutions for $t = 0.0, 0.5, 1.0, 1.5, 2.0$ are indicated by the dashed lines (see key for more details) and the approximate solution by the solid black line. We see that the analytical profile quickly tends to the steady state profile. Parameters are as follows: $\eta = 1.0$, $D_w = 20$, $x_b = 0.0$, $\phi = 5.0$ and $\xi = 0.5$.

Letting $t \to \infty$ gives the steady state solution

$$w_{bs}(x) = \begin{cases} \dfrac{\phi}{2\eta}\left[\exp\left(\dfrac{x - x_b + \xi}{\sqrt{D_w/\eta}}\right) - \exp\left(\dfrac{x - x_b - \xi}{\sqrt{D_w/\eta}}\right)\right] & \text{if} \quad x \leq x_b - \xi, \\ \dfrac{\phi}{\eta} - \dfrac{\phi}{2\eta}\left[\exp\left(\dfrac{x - x_b - \xi}{\sqrt{D_w/\eta}}\right) + \exp\left(-\dfrac{x - x_b + \xi}{\sqrt{D_w/\eta}}\right)\right] & \text{if} \quad x_b - \xi < x \leq x_b + \xi, \\ \dfrac{\phi}{2\eta}\left[\exp\left(-\dfrac{x - x_b - \xi}{\sqrt{D_w/\eta}}\right) - \exp\left(-\dfrac{x - x_b + \xi}{\sqrt{D_w/\eta}}\right)\right] & \text{if} \quad x > x_b + \xi. \end{cases} \tag{5.44}$$

Figure 5.9 shows a comparison between the analytical solution for the bead profile given by equation (5.30) and its steady state approximation given by equation (5.44). The analytical solution is plotted for a succession of increasing times and shows the solution quickly tending towards the steady state.

5.4 The model using FGF8 profile approximations

Using the above approximations the (x,t) plane can be divided up into 6 regions to give

$$w(x,t)=\begin{cases}\frac{n_-}{\eta(n_--n_+)}e^{n_+X}+\frac{\phi}{2\eta}\left[e^{A_+}-e^{A_-}\right] & \text{if} \quad x\le x_b-\xi \quad \text{and} \quad x\le x_n+c_nt,\\ \frac{n_+}{\eta(n_--n_+)}e^{n_-X}+\frac{1}{\eta}+\frac{\phi}{2\eta}\left[e^{A_+}-e^{A_-}\right] & \text{if} \quad x\le x_b-\xi \quad \text{and} \quad x> x_n+c_nt,\\ \frac{n_-}{\eta(n_--n_+)}e^{n_+X}+\frac{\phi}{\eta}-\frac{\phi}{2\eta}\left[e^{A_-}+e^{-A_+}\right] & \text{if} \quad x_b-\xi< x\le x_b+\xi \quad \text{and} \quad x\le x_n+c_nt,\\ \frac{n_+}{\eta(n_--n_+)}e^{n_-X}+\frac{1}{\eta}+\frac{\phi}{\eta}-\frac{\phi}{2\eta}\left[e^{A_-}+e^{-A_+}\right] & \text{if} \quad x_b-\xi< x\le x_b+\xi \quad \text{and} \quad x> x_n+c_nt,\\ \frac{n_-}{\eta(n_--n_+)}e^{n_+X}+\frac{\phi}{2\eta}\left[e^{-A_-}-e^{-A_+}\right] & \text{if} \quad x> x_b+\xi \quad \text{and} \quad x\le x_n+c_nt,\\ \frac{n_+}{\eta(n_--n_+)}e^{n_-X}+\frac{1}{\eta}+\frac{\phi}{2\eta}\left[e^{-A_-}-e^{-A_+}\right] & \text{if} \quad x> x_b+\xi \quad \text{and} \quad x> x_n+c_nt,\end{cases} \tag{5.45}$$

where

$$A_\pm=\frac{x-x_b\pm\xi}{\sqrt{D_w\eta}} \quad \text{and} \quad X=x-x_n-c_nt. \tag{5.46}$$

To find the path of the determination front, we need to solve $w(x,t)=w^*$ for some constant w^*, representing the level of FGF8 at the determination front. First we must test to find which branch of the travelling wave solution is valid: we do this by imposing the test condition

$$\text{If} \quad w_e(x,(x-x_n)/c_n)\begin{cases}\ge w^* & \text{then use the} \quad t\ge\frac{x-x_n}{c_n} \quad w_e \text{ solution},\\ < w^* & \text{then use the} \quad t<\frac{x-x_n}{c_n} \quad w_e \text{ solution}.\end{cases} \tag{5.47}$$

The position of the determination front is therefore given by

$$t=\begin{cases}-\frac{1}{n_+c_n}\ln\left\{\frac{\eta(n_--n_+)}{n_-}e^{n_+(x_n-x)}\left(w^*-\frac{\phi}{2\eta}\left[e^{A_+}-e^{A_-}\right]\right)\right\} & \\ \qquad \text{if} \quad x\le x_b-\xi \quad \text{and} \quad w_e(x,(x-x_n)/c_n)\ge w^*,\\ -\frac{1}{n_-c_n}\ln\left\{\frac{\eta(n_--n_+)}{n_+}e^{n_-(x_n-x)}\left(w^*-\frac{1}{\eta}-\frac{\phi}{2\eta}\left[e^{A_+}-e^{A_-}\right]\right)\right\} & \\ \qquad \text{if} \quad x\le x_b-\xi \quad \text{and} \quad w_e(x,(x-x_n)/c_n)< w^*,\\ -\frac{1}{n_+c_n}\ln\left\{\frac{\eta(n_--n_+)}{n_-}e^{n_+(x_n-x)}\left(w^*-\frac{\phi}{\eta}+\frac{\phi}{2\eta}\left[e^{A_-}+e^{-A_+}\right]\right)\right\} & \\ \qquad \text{if} \quad x_b-\xi< x\le x_b+\xi \quad \text{and} \quad w_e(x,(x-x_n)/c_n)\ge w^*,\\ -\frac{1}{n_-c_n}\ln\left\{\frac{\eta(n_--n_+)}{n_+}e^{n_-(x_n-x)}\left(w^*-\frac{1}{\eta}-\frac{\phi}{\eta}+\frac{\phi}{2\eta}\left[e^{A_-}+e^{-A_+}\right]\right)\right\} & \\ \qquad \text{if} \quad x_b-\xi< x\le x_b+\xi \quad \text{and} \quad w_e(x,(x-x_n)/c_n)< w^*,\\ -\frac{1}{n_+c_n}\ln\left\{\frac{\eta(n_--n_+)}{n_-}e^{n_+(x_n-x)}\left(w^*-\frac{\phi}{2\eta}\left[e^{-A_-}-e^{-A_+}\right]\right)\right\} & \\ \qquad \text{if} \quad x> x_b+\xi \quad \text{and} \quad w_e(x,(x-x_n)/c_n)\ge w^*,\\ -\frac{1}{n_-c_n}\ln\left\{\frac{\eta(n_--n_+)}{n_+}e^{n_-(x_n-x)}\left(w^*-\frac{1}{\eta}-\frac{\phi}{2\eta}\left[e^{-A_-}-e^{-A_+}\right]\right)\right\} & \\ \qquad \text{if} \quad x> x_b+\xi \quad \text{and} \quad w_e(x,(x-x_n)/c_n)< w^*.\end{cases} \tag{5.48}$$

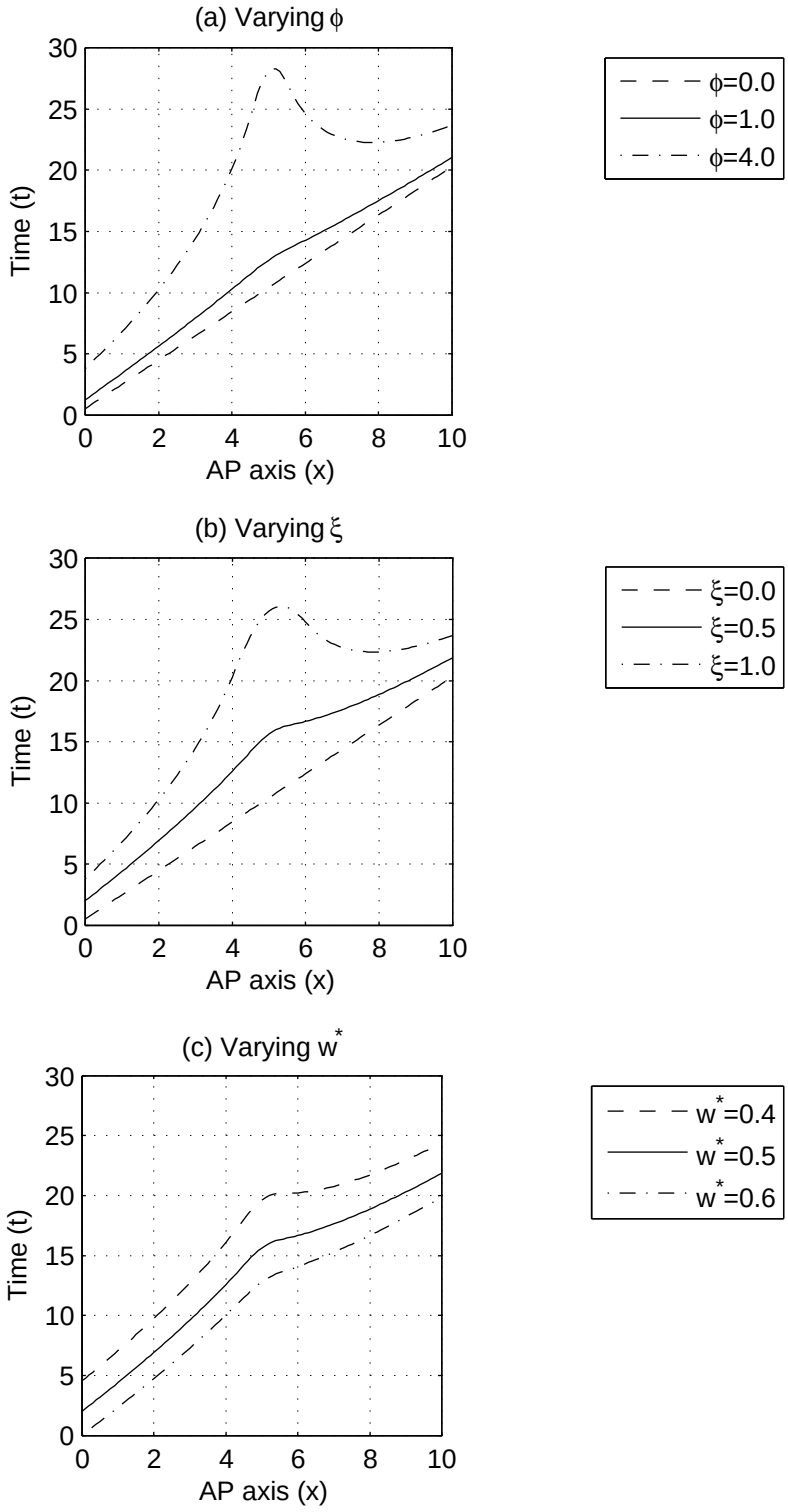


Figure 5.10: The progress of the determination front along the AP axis as key parameters are varied. (a) Varying ϕ, the relative strength of the bead source. (b) Varying ξ, the size of the bead implant. (c) Varying w^*, the level of FGF8 at the determination front. As ϕ and ξ are increased and w^* decreased the determination front is perturbed further from its usual path. Unless otherwise stated parameters are as follows: $\eta = 1.0$, $D_w = 20$, $x_n = 0.0$, $c_n = 0.5$, $x_b = 5.0$, $\phi = 1.0$, $\xi = 0.5$ and $w^* = 0.5$.

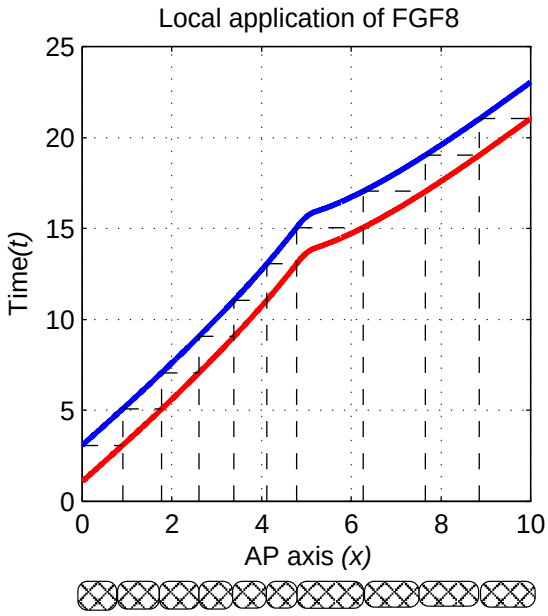


Figure 5.11: The progress of the positions of the discontinuities of the Heaviside functions for u and v. The red line depicts the Heaviside function for u and therefore the time at which cells reach the determination front and become able to produce somitic factor. The blue line depicts the Heaviside function for v and shows the time at which cells become able to send out a signal. The boundaries of the presumptive somites are marked by the dashed lines. As in Chapter 2 the positions of the somite boundaries are found by tracing between the two lines. A schematic diagram below the main graph shows the relative somite sizes. Parameters are as follows: $\eta = 1.0$, $D_w = 10$, $x_n = 0.0$, $c_n = 0.5$, $x_b = 5.0$, $\phi = 3.0$, $\xi = 0.2$ and $w^* = 0.5$.

Figure 5.10 shows how the position of the determination front changes as key parameters are varied. Figure 5.10(a) shows how the position of the determination front varies as ϕ, the strength of the bead source relative to the endogenous source, is varied. As expected, increasing the strength of the bead source results in greater deviation of the determination front from its usual position. Figure 5.10(b) shows how the position of the determination front is altered as ξ, the width of the bead implant, is varied. Again, as expected, the level of displacement increases as the width of the bead increases. Figure 5.10(c) looks at the way the progression of the determination front varies as w^*, the threshold level of FGF8 expression, varies. In this case, as w^* increases the degree of displacement of the determination front decreases. This can be explained by reasoning that if the threshold level of FGF8 is low then the additional FGF8 from a bead will be sufficient to push more cells over the threshold level.

5.4.1 Application to model

We can apply the above results to our model to find the positions of the discontinuities in the Heaviside functions of equations (5.1) and (5.2) and therefore predict the pattern of somites produced in

the same manner as in Chapter 2. Figure 5.11 illustrates the pattern of somite anomalies predicted by the approximate model for the FGF8 wavefront. Anterior to the bead implant (at $x = 5.0$) a sequence of small somites is observed and posterior to the bead a large somite is present.

Figure 5.12 demonstrates how the severity of anomalies produced by FGF8 changes as the strength of the bead implant is increased. In Figure 5.12(a) a relatively weak source of FGF8 produces little deviation of the Heaviside functions from their usual paths and the anomalies are not particularly noticeable. In Figure 5.12(b) a stronger source of FGF8 is able to reverse the FGF8 gradient posterior to the bead and the effect on somite size is very marked. In Figure 5.12(c) a further increased source of FGF8 obliterates the endogenous gradient to the extent that some cells never reach the threshold level of FGF8 required for segmentation. A complete absence of somite boundary formation occurs immediately anterior to the bead, with a series of small somites forming rostral to this zone. This has been observed experimentally [15].

5.5 Numerical solution

We have the following equations for the dynamics of the somitic factor, signalling molecule and FGF8:

$$\frac{\partial u}{\partial t} = \frac{(u+\mu v)^2}{\gamma+u^2}\chi_u - u, \tag{5.49}$$

$$\frac{\partial v}{\partial t} = \kappa\left(\frac{\chi_v}{\epsilon+u} - v\right) + D_v\frac{\partial^2 v}{\partial x^2}, \tag{5.50}$$

$$\frac{\partial w}{\partial t} = \chi_w + \phi\chi_b - \eta w + D_w\frac{\partial^2 w}{\partial x^2}, \tag{5.51}$$

with

$$\chi_u = H(w - w^*), \tag{5.52}$$

$$\chi_v = H(t - t_w(w^*, x) - t_s), \tag{5.53}$$

$$\chi_w = H(x - x_n - c_n t), \tag{5.54}$$

$$\chi_b = H(\xi - x_b + x)H(\xi + x_b - x). \tag{5.55}$$

As in previous chapters we solve the above system of equations numerically using the NAG library routine D03PCF. We use zero flux boundary conditions on a closed bounded interval of $\mathbb{R}$ to approximate the infinite domain boundary conditions and continuous $\tanh$ approximations for the Heaviside functions. As previously, the initial conditions for w are taken to be the state of the travelling wave at $t = 0$ given by equation (5.13) and the initial conditions for u and v are as in Chapter 2. The level of FGF8 at the determination front is taken so that cells at the anterior edge of the next somite (i.e. cells at $x = 0$) are able to signal at $t = 0$. That is, they reached the determination front a time $t = t_s$ previously.

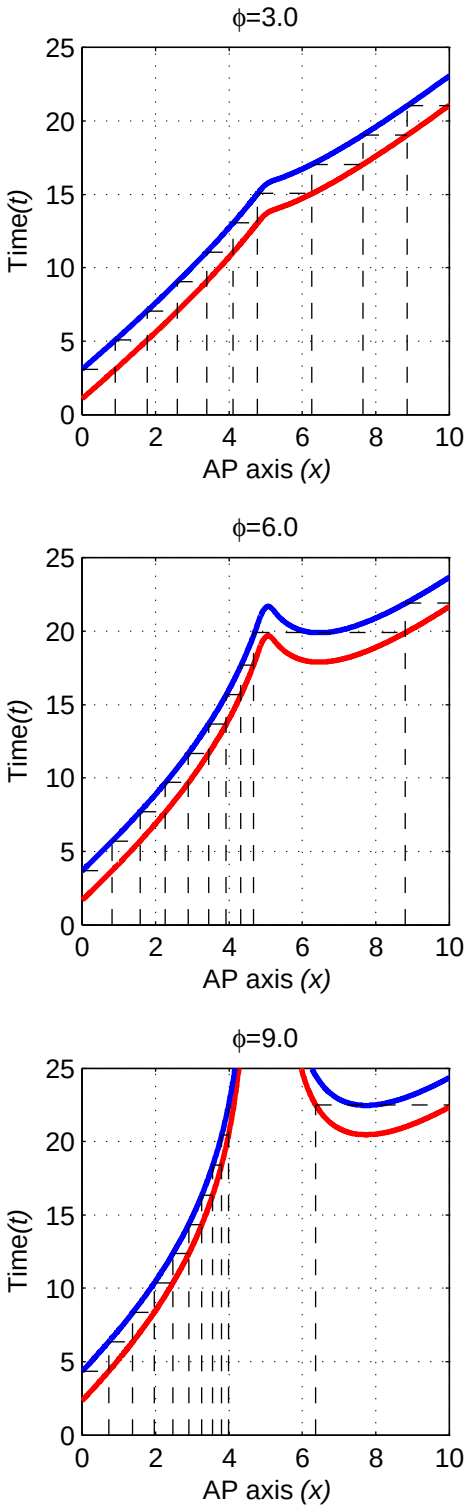


Figure 5.12: The progress of the positions of the discontinuities of the Heaviside functions for u and v as ϕ, the strength of the bead source, is varied. The red line depicts the Heaviside function for u and therefore the time at which cells reach the determination front and become able to produce somitic factor. The blue line depicts the Heaviside function for v and shows the time at which cells become able to send out a signal. The boundaries of the presumptive somites are marked by the dashed lines. As in Chapter 2 the positions of the somite boundaries are found by tracing between the two lines. Parameters are as follows: $\eta = 1.0$, $D_w = 10$, $x_n = 0.0$, $c_n = 0.5$, $x_b = 5.0$, $\xi = 0.2$ and $w^* = 0.5$.

In the cell cycle model we non-dimensionalised in space so that the length of a normal somite was $x = 1.0$. To ensure that somites are of approximately unit length in the revised FGF8 model we take $t_s = 1/c_n$ and therefore

$$w^* = \frac{n_-}{\eta(n_- - n_+)} e^{n_+(-x_n + c_n t_s)} = \frac{n_-}{\eta(n_- - n_+)} e^{n_+(-x_n+1)}. \tag{5.56}$$

5.5.1 Numerical results

Figures 5.13 – 5.16 illustrate the differing degrees of anomalies produced by the model with local perturbation of FGF8. In each of the figures (a) shows the dynamics of the somitic factor, (b) the dynamics of the signalling molecule and (c) the dynamics of FGF8.

Figure 5.13 illustrates a control case: the region of high FGF8 expression recedes along the AP axis at constant speed, generating the succession of pulses in the signalling molecule which lead to the production of coherent somites.

In the remaining cases a bead of FGF8 (width $x = 1.0$) is implanted at the axial level $x = 5.0$. Figure 5.14 demonstrates the severity of anomalies that form upon local application of a weak source of FGF8: a sequence of 2-3 small somites forms ahead of the bead and a large somite forms behind the bead with normal somites forming outside of this zone. Similarly, Figure 5.15 demonstrates the severity of anomalies produced upon application of a slightly stronger source of FGF8: about 4-5 small somites are produced anterior to the bead and a very large somite forms posterior to the bead. Figure 5.16 shows the anomalies produced upon application of a very strong source of FGF8: in a region immediately surrounding the bead somite formation is completely destroyed and about 3-4 smaller somites form anterior to this zone. Posterior to the annihilated section we see formation of a larger somite. All of these cases have been seen *in vivo* [15, 58, 60].

Each of Figures 5.13 – 5.16 can be compared with an illustration in Figure 5.17 for comparison of the differing effects of local application of FGF8. It is interesting to note that in each of Figures 5.13 – 5.15, 9 somites form in the domain over which the figures are plotted. Eventually it can be seen that in the perturbed cases somite formation has fallen back into line with the control embryo, as seen experimentally [15].

5.6 Discussion

In this chapter we analysed the mathematical formulation of Pourquié's revised clock and wavefront model for somite formation proposed in Chapter 4. We began by restating the model and solving, both analytically and numerically, the decoupled equation describing the dynamics of FGF8. We next considered extending the model to include the effects of local perturbation of FGF8. We represented a heparin-soaked bead implanted in the PSM by a constant production term for FGF8, which is confined to a small region of the AP axis by using a combination of Heaviside functions. In a similar manner, we were able to solve the revised equation for FGF8 expression both analytically and numerically and demonstrate the displacement of the determination front from its conventional path.

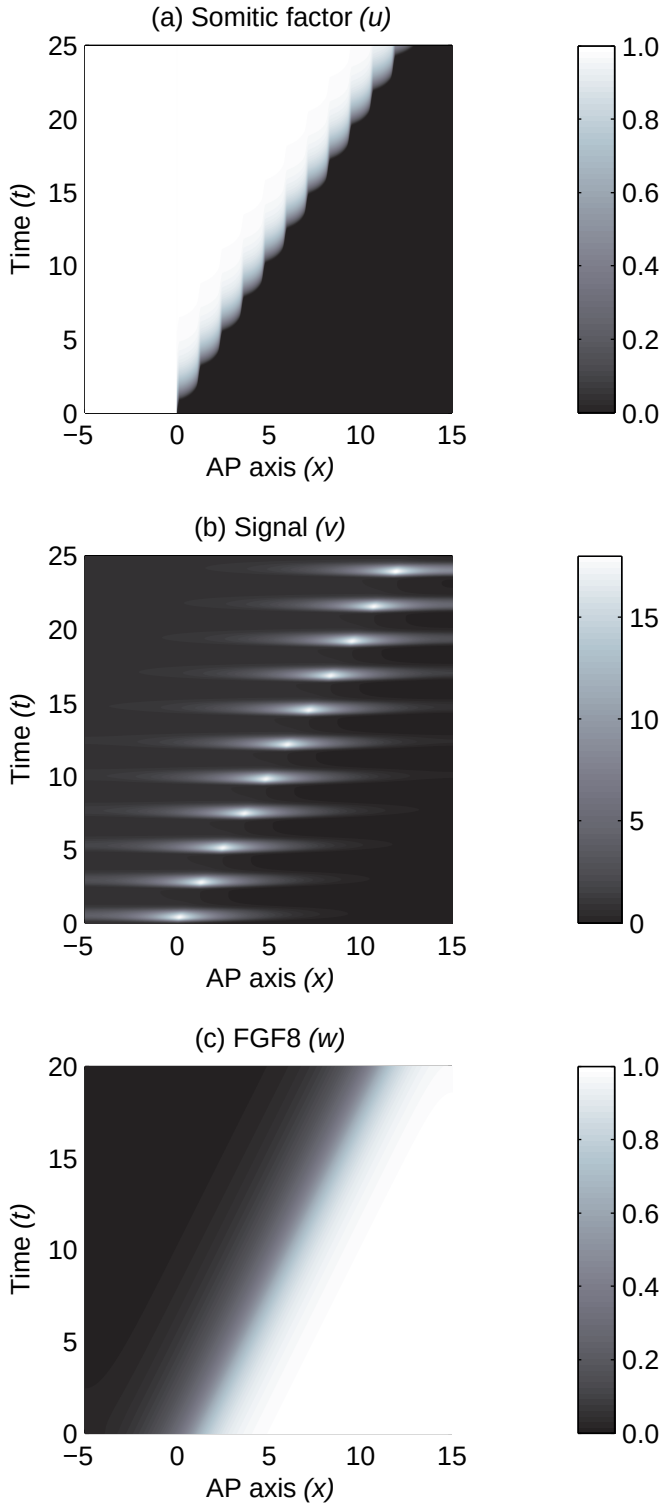


Figure 5.13: Numerical solution of the FGF8 model for somite formation showing the spatio-temporal dynamics of the somitic factor (a), the signalling molecule, (b), and FGF8, (c). The dynamics were plotted using the MATLAB function imagesc. Parameters are as follows: $\mu = 10^{-4}$, $\gamma = 10^{-3}$, $\kappa = 10$, $\epsilon = 10^{-3}$, $\eta = 1.0$, $\phi = 0.0$, $D_v = 50$ $D_w = 20$, $x_n = 0.0$, $c_n = 0.5$, $x_b = 7.5$, $\xi = 0.5$ and the Heaviside function parameter $\delta = 10^{-3}$.

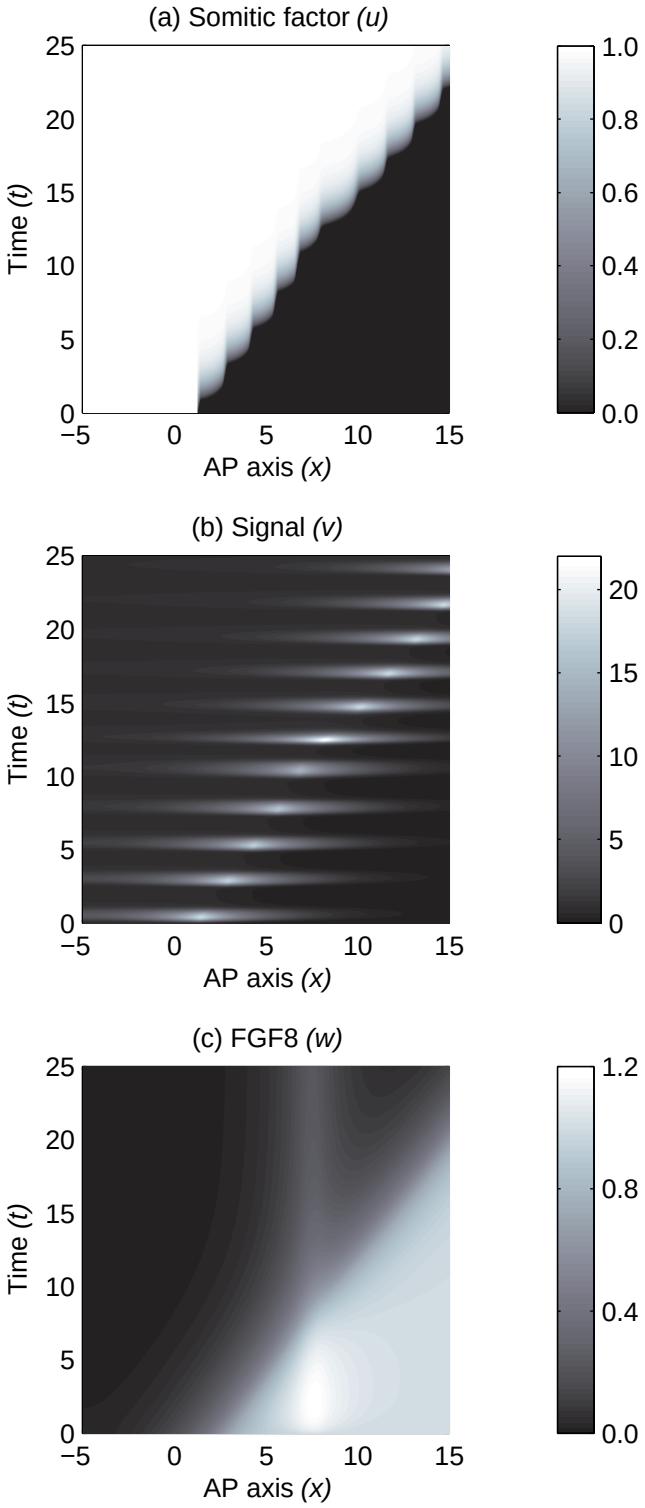


Figure 5.14: Numerical solution of the FGF8 model for somite formation showing the spatio-temporal dynamics of the somitic factor (a), the signalling molecule, (b), and FGF8, (c). With a weak source of FGF8 implanted at $x = 5.0$ we see a series of mildly abnormal somites. The dynamics were plotted using the MATLAB function imagesc. Parameters are as follows: $\mu = 10^{-4}$, $\gamma = 10^{-3}$, $\kappa = 10$, $\epsilon = 10^{-3}$, $\eta = 1.0$, $\phi = 0.75$, $D_v = 50$ $D_w = 20$, $x_n = 0.0$, $c_n = 0.5$, $x_b = 7.5$, $\xi = 0.5$ and the Heaviside function parameter $\delta = 10^{-3}$.

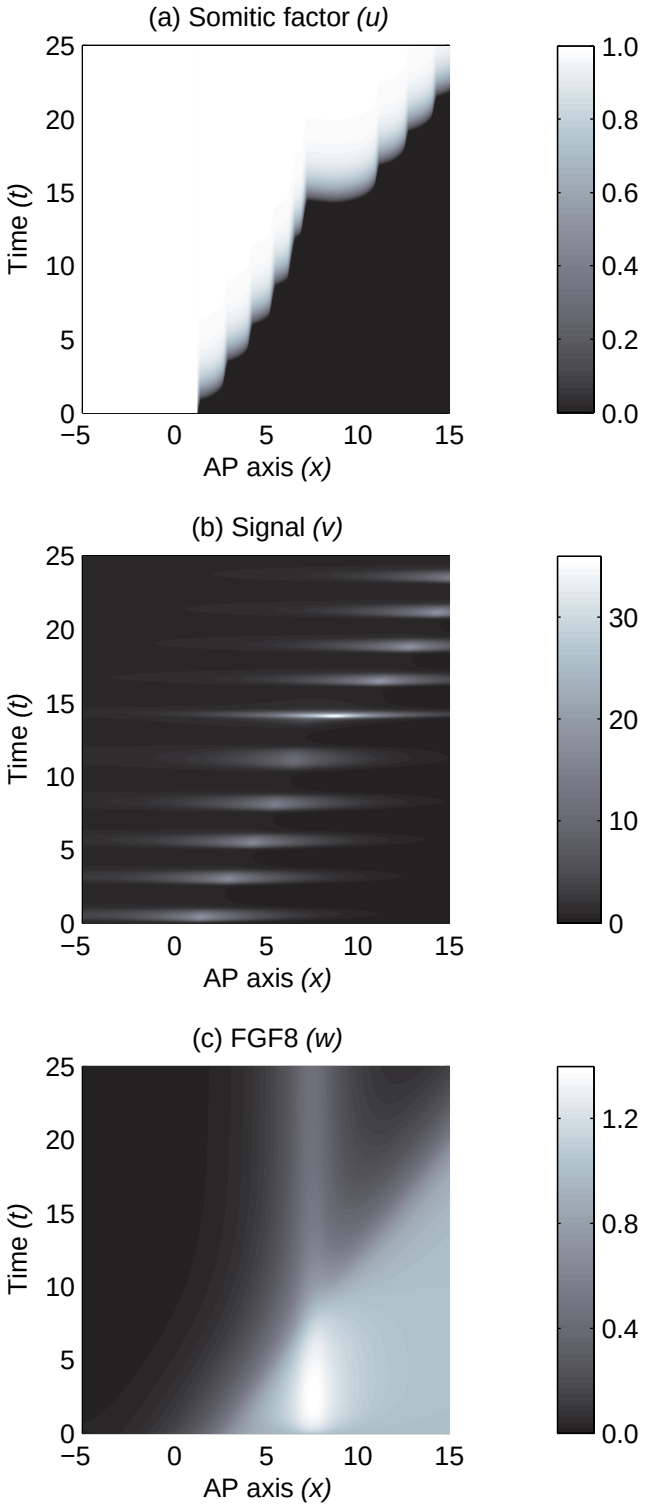


Figure 5.15: Numerical solution of the FGF8 model for somite formation showing the spatio-temporal dynamics of the somitic factor (a), the signalling molecule, (b), and FGF8, (c). With a stronger source of FGF8 implanted in the PSM the somite anomalies are more obvious. The dynamics were plotted using the MATLAB function imagesc. Parameters are as follows: $\mu = 10^{-4}$, $\gamma = 10^{-3}$, $\kappa = 10$, $\epsilon = 10^{-3}$, $\eta = 1.0$, $\phi = 1.5$, $D_v = 50$ $D_w = 20$, $x_n = 0.0$, $c_n = 0.5$, $x_b = 7.5$, $\xi = 0.5$ and the Heaviside function parameter $\delta = 10^{-3}$.

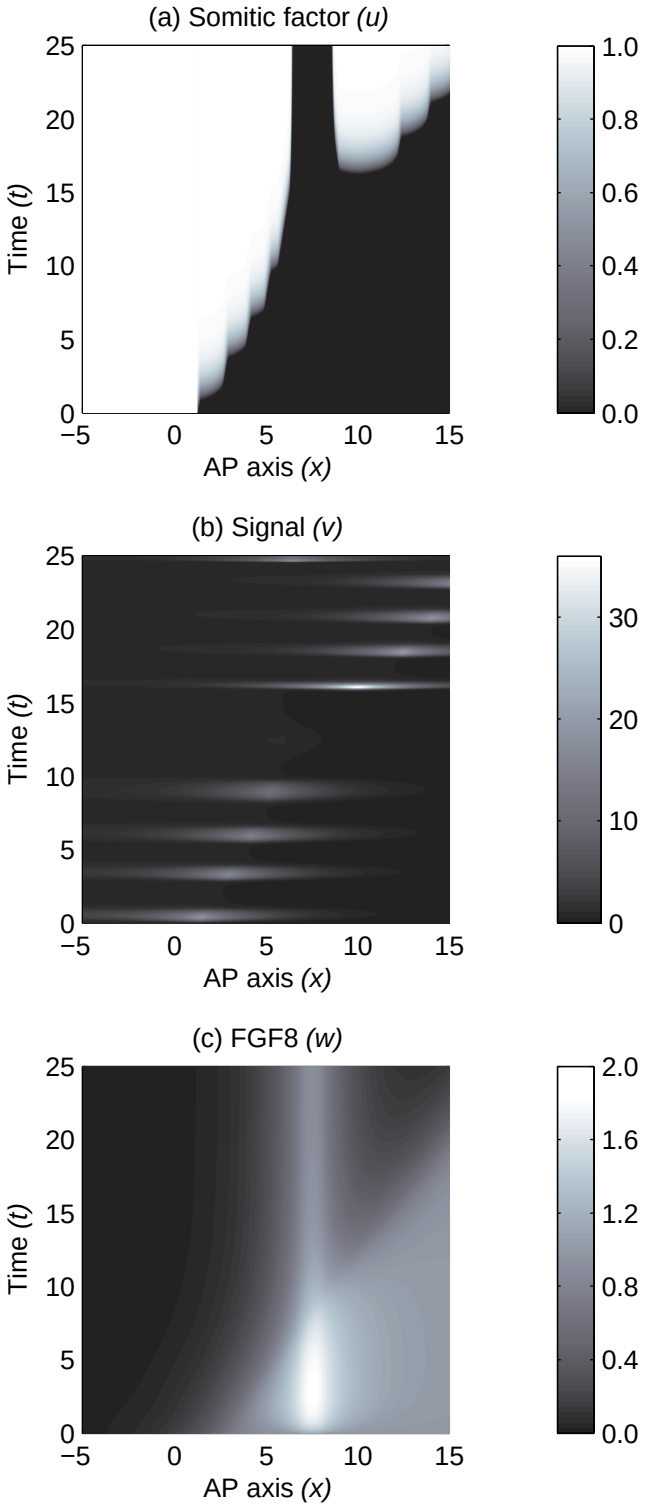


Figure 5.16: Numerical solution of the FGF8 model for somite formation showing the spatio-temporal dynamics of the somitic factor (a), the signalling molecule, (b), and FGF8, (c). With a very strong source of FGF8 implanted we see complete absence of somite formation in a region surrounding the bead. The dynamics were plotted using the MATLAB function imagesc. Parameters are as follows: $\mu = 10^{-4}$, $\gamma = 10^{-3}$, $\kappa = 10$, $\epsilon = 10^{-3}$, $\eta = 1.0$, $\phi = 3.0$, $D_v = 50$ $D_w = 20$, $x_n = 0.0$, $c_n = 0.5$, $x_b = 7.5$, $\xi = 0.5$ and the Heaviside function parameter $\delta = 10^{-3}$.

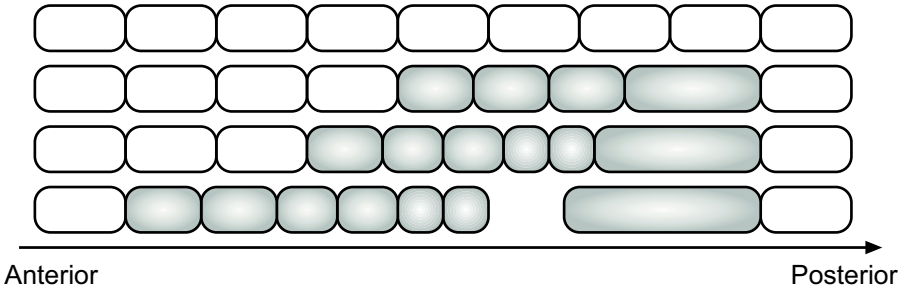


Figure 5.17: Illustration of the somite anomalies formed with local application of FGF8. The top diagram represents a control case (see Figure 2.1) while the next two diagrams represent cases in which a bead soaked in FGF8 is implanted alongside the PSM: the strength of the FGF8 source increases in successive diagrams (see Figures 5.14, 5.15). The bottom diagram represents the case in which a bead is implanted within the PSM (see Figures 5.16). In each of the cases the bead has been implanted on the right hand side of the most posterior small somite.

We then made some approximations for both the endogenous wavefront of FGF8 and the profile created by a bead implanted in the PSM. Since we are not concerned with the initiation of the wavefront, it seems wise to consider only a steady state travelling wave solution for the progression of the wavefront - this provides a result that is much more tractable analytically.

The second approximation we made was to assume that the bead implant in the PSM creates an FGF8 profile that reaches a steady state very quickly. This will in part be dependent on the diffusion rate of FGF8 and on the rate at which the bead is able to release FGF8. Once again, there is little data on the magnitude of these parameters but we expect the steady state approximation to give qualitatively similar anomalistic results to the temporally changing profile.

We also note at this stage that it is likely that the effects of local application of FGF8 via a heparin-soaked bead will wear off before all the PSM that would otherwise be affected by this perturbation has been gated into somites [42]. Decaying effects of local application of FGF8 could result in pronounced ‘large’ somite anomalies as the decay of the source would confer the potential to become somitic to many cells at the same time. A temporally varying local source of FGF8 is something that remains to be investigated.

We used the approximations for FGF8 to derive an expression for the position of the determination front along the AP axis. As in Chapter 2, we used knowledge of the positions of the discontinuities of the Heaviside functions controlling u and v production to predict the pattern of somites formed both in the control case and with local application of FGF8.

We concluded the chapter by solving the system of equations numerically. In the control case, the computed numerical solution showed a sequence of somites uniformly separated in space and time. Solution of the equations with weak and intermediate sources of local FGF8 gave rise to a pattern of anomalies that looked qualitatively similar to those depicted in the middle rows of Figure 5.17: a sequence of smaller somites, followed by an abnormally large somite. As expected, the effects were more pronounced for the stronger source. The final numerical experiment consisted of applying a strong source of FGF8 locally and resulted in a pattern of small somites, followed by a region

devoid of any somite patterning whatsoever and then an abnormally large somite (compare with the bottom line of Figure 5.17). It is very encouraging to note that all these results have been found to occur when experiments are carried out *in vivo* [15].

It has been shown that anomalies cannot extend past the position of the determination front at the time of the implant. This could be as a result of a change in response to FGF8 signalling once cells have reached the determination front but it is a fact that needs to be specified as a further condition in our model. Once a cell reaches the determination front and experiences a pulse in the signalling molecule sufficient for it to reach a level of u such that $u_t > 0$ for all further t, it cannot be switched off again. Therefore, we need to stipulate that once a cell reaches the determination front and χ_u switches from zero to one, it remains at one for all further time. A similar requirement is needed for χ_v, the Heaviside function controlling the production of the signalling molecule.

Lastly, we note that the results of this chapter clearly show the incorporation of certain cells into differently numbered somites than their control counterparts. It can be seen that such cells will go on to segment within a different time step and will therefore experience a different number of clock oscillations before segmenting. Dubrulle and co-workers [p. 220] [15] demonstrate that "FGF8 treatment can increase the number of clock oscillations experienced by PSM cells without altering their absolute axial position in tissue. Cells which experience an extra oscillation become incorporated into a differently numbered somite and exhibit *Hox* expression indicative of a more posterior fate when compared with contralateral control cells." Our model clearly accounts for this result.

It is very encouraging to see that our model can account for normal somite formation and mimic the results seen with local application of FGF8 but there are other experimental perturbations that need to be tested to further validate the model. In the following chapter we investigate the effects of inhibition of FGF8 and also pose some experimentally testable hypotheses.

Chapter 6

Experimental Predictions

In the previous chapter we explored the effect on somite formation of local application of FGF8. We now move on to investigate other ways in which somite formation could be perturbed. We begin by considering two of the most obvious ways in which to disturb somite formation; altering the rate of progression of the determination front and altering the period of the segmentation clock. We then move to consider the effect of blocking FGF8 signalling using the drug SU5402. There have been some preliminary investigations of the effects of this *in vivo* [15] but it is something that remains to be investigated in more detail.

6.1 Altering the speed of the determination front

Changing the rate at which the AP axis of the embryo is elongating would result in a corresponding change in the rate at which the determination front is regressing. The parameter c_n controls the rate at which the Heaviside function specifying P_u (the time at which cells become able to produce u) becomes non-zero. As a result, it also is a controlling factor in the Heaviside function specifying P_v. Increasing c_n corresponds to increasing the rate at which the node of the embryo is regressing (since FGF8 is only produced in the node) and therefore increasing the rate at which the AP axis is elongating (since the node lies in the tail of the embryo).

Decreasing the rate at which the axis is extending (whilst keeping the period of the segmentation clock constant) would result in the determination front moving a shorter distance during one oscillation of the segmentation clock than it would otherwise in a control case. The result of this would be less cells competent to form a new somite and therefore reduced somite size.

Figure 6.1(a) shows an illustration of the expected pattern of somites when the rate of axis elongation is decreased. We see a pattern of regularly sized, smaller somites forming with same temporal regularity as the control case. Figure 6.2 shows the results of numerically solving the system of PDEs given by equations (5.1)-(5.3) and shows similar results to those illustrated in Figure 6.1(a).

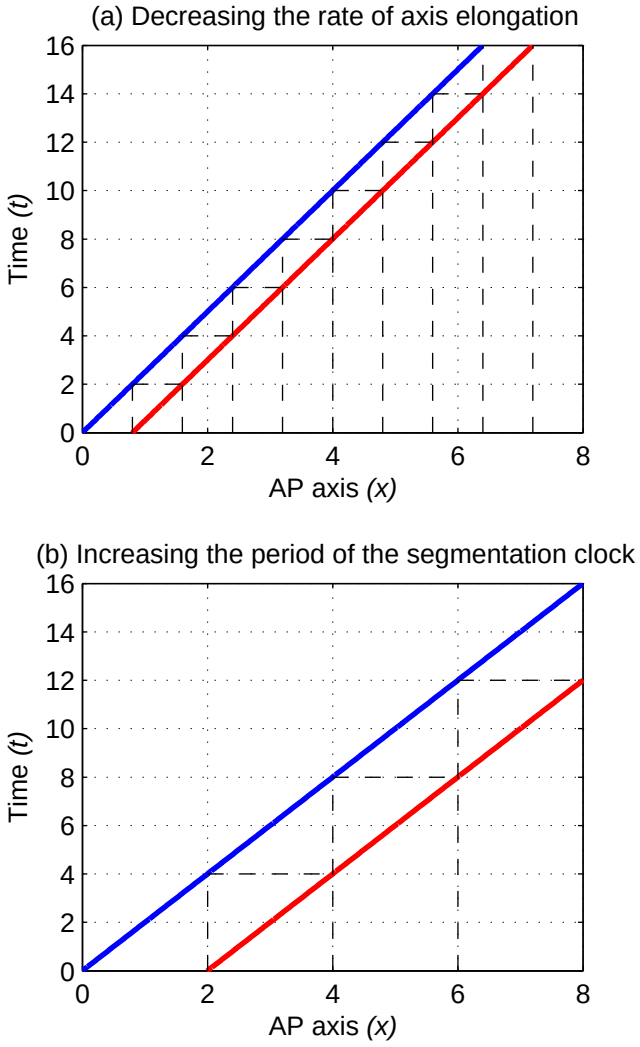


Figure 6.1: An illustration of the manner in which the pattern of somites can be perturbed. (a) Decreasing the rate of axis elongation results in fewer cells being specified as somitic during an oscillation of the segmentation clock and hence smaller somites. (b) Increasing the period of the segmentation clock results in more cells reaching the determination front during one cycle of the segmentation clock and hence larger somites.

6.2 Altering the period of the segmentation clock

Altering the period of the segmentation clock in our model would result in changing the time between the points P_u and P_v i.e. between cells becoming able to segment and produce the signalling molecule v. Increasing the period of the segmentation clock would mean that when the pioneer cells at the anterior end of the PSM send out a signal, more cells will have reached the determination front and become competent to form somites than in a control case. We illustrate the pattern of somites formed when the period of the segmentation clock is increased in Figure 6.1(b).

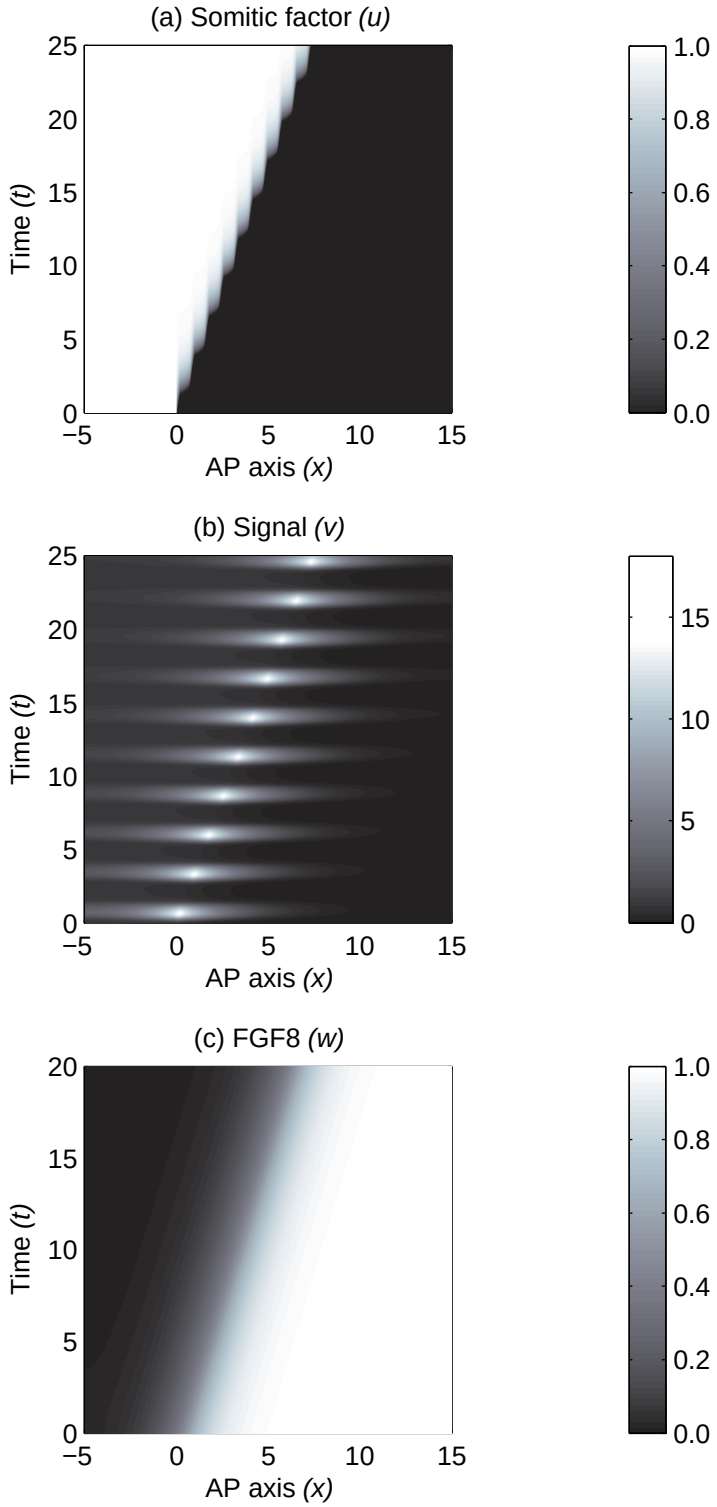


Figure 6.2: Numerical solution of the FGF8 model for somite formation showing the spatio-temporal dynamics of the somitic factor (a), the signalling molecule, (b), and FGF8, (c) when the rate of axis elongation is decreased. The dynamics were plotted using the MATLAB function imagesc. Parameters are as follows: $\mu = 10^{-4}$, $\gamma = 10^{-3}$, $\kappa = 10$, $\epsilon = 10^{-3}$, $\eta = 1.0$, $D_v = 50$ $D_w = 20$, $x_n = 0.0$, $c_n = 0.3$, $\xi = 0.5$ and the Heaviside function parameter $\delta = 10^{-3}$.

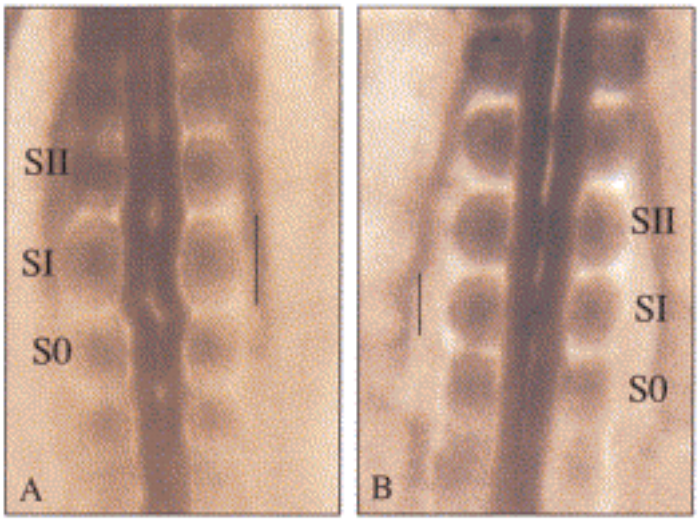


Figure 6.3: (A) shows an embryo injected with SU5402 while (B) shows a control embryo. The SI pair of somites (somites 21) is enlarged in the treated case and is marked by a black bar. The corresponding somite is marked in the control case. Reprinted from Cell, Vol. 106, J. Dubrulle, M. J. McGrew, O. Pourquié, FGF8 signalling controls somite boundary formation and regulates segmentation clock control of spatiotemporal *Hox* gene activation, pp 219-232, Copyright (2001), with permission from Elsevier and Olivier Pourquié.

6.3 Inhibiting FGF8 signalling with SU5402

SU5402 is a drug that can be used to inhibit FGF8 signalling and it works by blocking the kinase activity of FGF receptors. There have been some preliminary experiments to investigate the results of inhibiting FGF8 signalling in the PSM using SU5402 [15] and in general the pattern of somites produced contained an abnormally large pair of somites at the level of somite $-V$ at the time of injection of the drug. Figure 6.3 shows the results of somite formation upon application of SU5402.

We can explain the formation of this anomalous somite by reasoning that upon injection, SU5402 blocks the kinase activity of the FGF receptors [15] and therefore decreases the level of FGF8 signalling throughout the PSM (as opposed to locally as is the case for a bead soaked in FGF8), thereby resulting in a posterior shift of the determination front. SU5402 is rapidly degraded and it is expected that FGF8 signalling is only affected during a time frame of the order of the period of the segmentation clock [42]. Degradation of SU5402 would result in an increase in FGF8 signalling throughout the embryo, back to the original undisturbed level. We note that the determination front will reassume the position it would otherwise have occupied at the time the effects of SU5402 wear off as the node is still regressing at a constant rate.

We can estimate the anomalies that will form using the same method as for Figure 6.1: application of SU5402 would decrease the level of FGF8 signalling globally, thereby conferring the ability to segment upon a very large number of cells at one time. Hence the formation of a very large somite. Whilst SU5402 is acting, the determination front would continue to move, from its new position, at

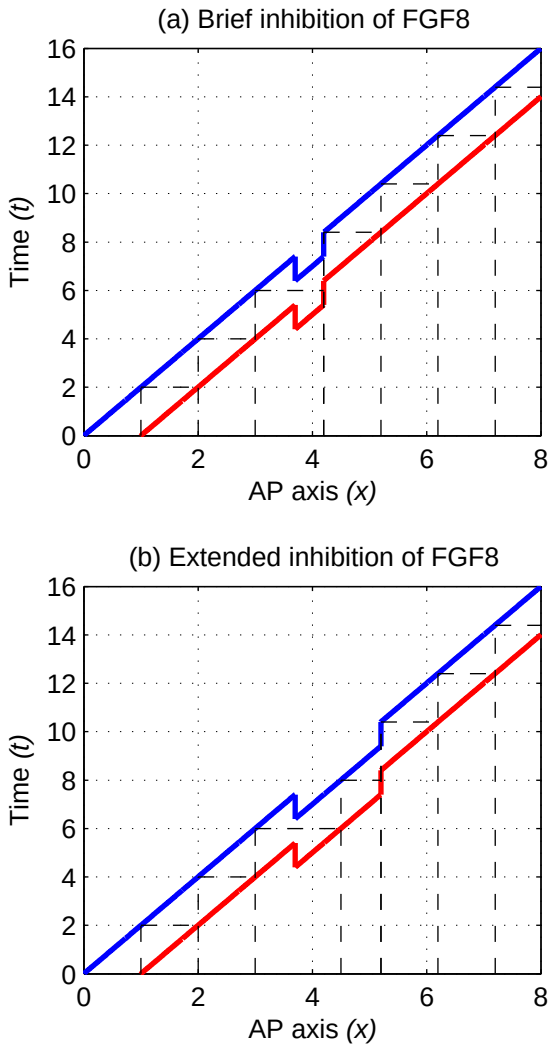


Figure 6.4: Inhibition of FGF8 signalling results in somite anomalies. (a) Case in which SU5402 is assumed to act for a brief period (less than the period of the segmentation clock). (b) Case in which FGF8 is assumed to be inhibited for a longer period. The blue line depicts the progress of P_v and shows the time at which cells become able to send out a signal. The boundaries of the presumptive somites are marked by the dashed lines.

a constant speed and so normal somites will form. When SU5402 degrades, the determination front will return to its original position, possibly in the process forming a smaller somite, and normal segmentation will resume. Assuming that all the above changes happen instantaneously we can trace the lines representing P_u and P_v as in Figure 6.4.

Figure 6.4(a) shows the possible sequence of somites formed with injection of SU5402 lasting only for a short time period. A large somite forms at the position of the determination front (approximately somite $-V$) at the time of the injection and thereafter normal segmentation is observed. Figure 6.4(b) shows the possible sequence of somite anomalies formed with a slightly longer last-

ing period of inhibition of FGF8 signalling. A large somite forms at the position of the determination front at the initial time of injection, followed by a smaller somite as the determination front reverts back to its usual position. It is easy to see that if FGF8 signalling were to be inhibited for an increased period of time, there could be a sequence of normal somites between the large and the small somite.

We model this mathematically by introducing a sink term into our equation for FGF8 which is active for a certain time period and proportional to the amount of FGF8 present in the PSM:

$$\frac{\partial u}{\partial t} = \frac{(u+\mu v)^2}{\gamma+u^2}\chi_u - u, \tag{6.1}$$

$$\frac{\partial v}{\partial t} = \kappa\left(\frac{\chi_v}{\epsilon+u} - v\right) + D_v\frac{\partial^2 v}{\partial x^2}, \tag{6.2}$$

$$\frac{\partial w}{\partial t} = \chi_w - \rho w\chi_s - \eta w + D_w\frac{\partial^2 w}{\partial x^2}. \tag{6.3}$$

As in previous chapters, u represents the concentration of somitic factor, v the concentration of signalling molecule and w the concentration of FGF8. Production of u, v and w are controlled by the respective Heaviside functions

$$\chi_u = H(w-w^*), \tag{6.4}$$

$$\chi_v = H(t-t_w(w^*,x)-t_s), \tag{6.5}$$

$$\chi_w = H(x-x_n-c_nt), \tag{6.6}$$

$$\chi_s = H(t-t_i)H(t_f-t), \tag{6.7}$$

where (as before) w^* is the level of FGF8 at the determination front, $t_w(w^*,x)$ is the time at which a cell at x reaches the determination front (ie. $w(x,t_w)=w^*$), t_s is the period of the segmentation clock, x_n represents the initial position of the tail and c_n represents the rate at which the AP axis is extending. t_i and t_f represent the times at which the SU5402 is injected and wears off, respectively.

In the above mathematical model, we are assuming that SU5402 acts instantly, that its effects are constant throughout the time $[t_i,t_f]$ and also that they wear off instantly. The effect on the points P_u and P_v will not be as abrupt as pictured in Figure 6.4 but of a similar nature.

We can solve the above PDE system numerically as in previous chapters using the NAG solver D03PCF. The results are shown in Figure 6.5: SU5402 is applied between $t=8.5$ until $t=9.5$ and we see a corresponding decrease in FGF8 signalling throughout the PSM in Figure 6.5(c). The posterior shift of the determination front as a result of SU5402 causes the fifth somite to be generated whilst the determination front is repressed posteriorly from its usual position and therefore the fifth somite is abnormally large. Normal segmentation resumes after this point.

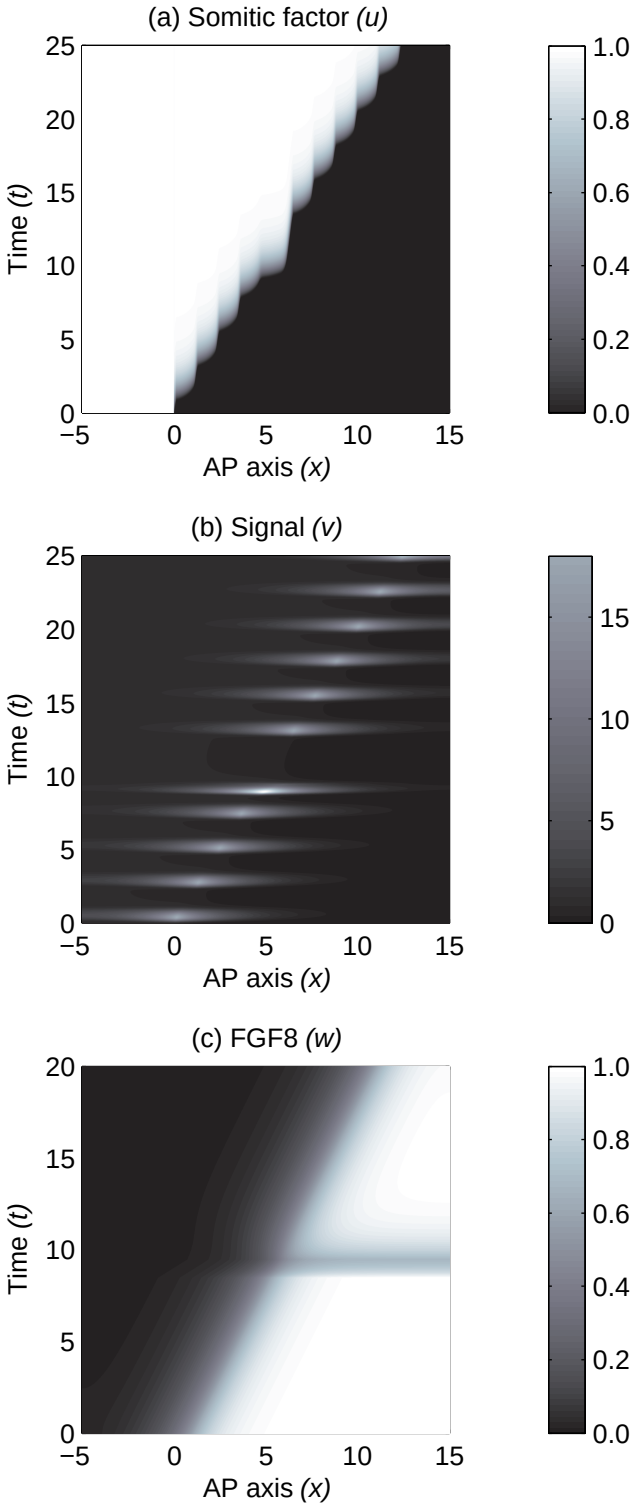


Figure 6.5: Numerical solution of the FGF8 model for somite formation showing the spatio-temporal dynamics of the somitic factor (a), the signalling molecule, (b), and FGF8, (c). With inhibition of FGF8 signalling using SU5402 we see the formation of a large somite at the level of the determination front at the time the drug is applied ($t = 8.5$ until $t = 9.5$). Parameters are as follows: $\mu = 10^{-4}$, $\gamma = 10^{-3}$, $\kappa = 10$, $\epsilon = 10^{-3}$, $\eta = 1.0$, $\rho = 0.65$, $D_v = 50$, $D_w = 20$, $x_n = 0.0$, $c_n = 0.5$, $\xi = 0.5$.

6.4 Parameter estimation

In order to make quantitative predictions for the somite anomalies produced when FGF8 expression is perturbed it will be necessary to have accurate estimates of the parameters involved. More specifically, the rate at which FGF8 is able to diffuse along the PSM and its rate of decay in relation to the speed of axis elongation and correspondingly, somite formation.

In experiments in which FGF8 is perturbed locally by implantation of a bead alongside the PSM, it is uncertain how much of the diffusing FGF8 is actually able to enter the PSM and affect somite formation. Our model does not take this into account, but it may be possible to match the anomalies seen experimentally under different concentrations of bead source with the anomalies produced by the mathematical model. In this way it may be possible to estimate the amount of FGF8 entering the PSM from the severity of the anomalies produced. Before this can happen however, we need accurate estimation of the rate at which FGF8 is able to diffuse along the PSM and its rate of decay.

6.5 Discussion

In this chapter we have considered some of the ways, besides local application of FGF8, in which somite formation can be perturbed. Firstly, we considered the rate of axis elongation of the embryo and showed that somite size should increase as the rate of axis elongation increases and *vice versa*. Secondly, we considered perturbing the period of the segmentation clock and showed that somite size should also increase as the period of the segmentation clock is increased and *vice versa*.

Lastly we considered perturbing FGF8 signalling via application of SU5402, a drug which inhibits FGF8 signalling. We showed that there are a variety of somite anomalies that could arise as a result of injection of SU5402 and showed that with brief suppression of FGF8 signalling, our model could replicate the results seen during the initial experiments *in vivo*. The effects of SU5402 application could be investigated in more detail using time varying functions for the inhibition parameter ρ. It may also be of interest to model the effect of suppressing FGF8 signalling in confined regions of the PSM.

It is hoped that all the above effects can be investigated experimentally in the near future and that the predictions of this chapter can be used along with the experimental results to verify and/or modify the model used here.

Although there is plenty of evidence to suggest that down-regulation of FGF8 signalling in the PSM is required for cells to become competent to form somites, retinoic acid (RA) has also been shown to be expressed in the PSM with a spatial concentration gradient opposite to that of the FGF8 gradient [13] and perturbation of the RA gradient has been shown to produce somite anomalies. FGF8 and RA are mutually inhibitory and each acts on the other via a complicated network of interactions. In the following chapter, we explore the experimental evidence for RA expression in more detail and consider modelling the FGF8/RA network in detail.

Chapter 7

Retinoic Acid/FGF8 Feedback Model

7.1 Biological background

As discussed previously, fgf8 persists in the caudal PSM and promotes the expression of markers of the undifferentiated PSM whilst repressing the onset of expression of somitic genes. FGF signalling is required to maintain the caudal progenitors of the PSM and for the positioning of somitic boundaries [15].

Recently it has been shown that there is another morphogen expressed in a graded fashion along the AP axis during somite formation [25]. Retinoic acid (RA) is expressed in a distinct spatio-temporal pattern and in an opposing fashion to FGF8, with high expression levels found in the somites and low expression levels seen in the posterior PSM [1], see Figure 7.1. It acts in a concentration dependent manner and has been shown to influence several aspects of differentiation including the regulation of *Hox* gene expression [25].

Although it is not yet clear whether the presence of RA is required for the differentiation of somites, it seems likely that perturbation of RA levels will give rise to somite anomalies [33]. Hence it is important to investigate the effects of RA signalling in the PSM to understand how such anomalies may form and also how RA may alter the shape of the FGF8 profile along the PSM: suppression of FGF8 levels by RA could influence the position of the determination front, thereby affecting somite production.

In this chapter, we investigate a possible model for an RA/FGF8 feedback mechanism which can establish and maintain the patterns of gene expression which are observed experimentally. We begin by using experimental evidence to build up a mathematical model of 7 coupled PDEs describing the system and then exploit properties of the system (including different time scales and the presence of a small parameter) to reduce the system to a model for which it is possible to find some analytical approximations. We finish by comparing our results to those for FGF8 gradients established in previous chapters and recommending some avenues for future exploration.

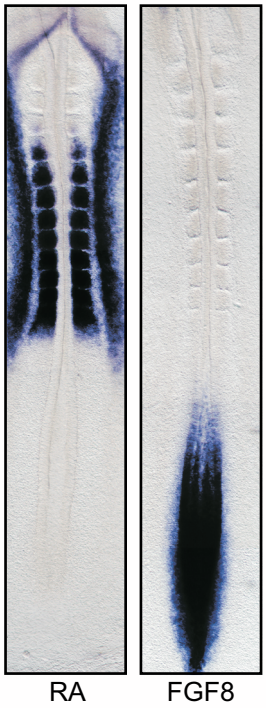


Figure 7.1: Expression patterns of RA (LHS) and FGF8 (RHS) in stage 10-13 chick embryos. Permission for use of this figure kindly given by R. Diez del Corral [13].

7.2 RA/FGF8 feedback mechanism

RA is synthesised in the differentiating PSM and somites, and its presence is indicated by the RA synthesising enzyme RALDH2 [2, 12] whose expression pattern coincides with that of RA [14]. RA diffuses over relatively large distances within the PSM [25] and promotes differentiation by down-regulating *fgf8*. FGF8, in turn, controls RA synthesis by inhibiting *raldh2* production and it is this mutually inhibitory relationship between RA and FGF8 that suggests a global mechanism for controlling axis elongation [12]. In the context of somite formation and the models considered here, it seems likely that the effect of RA on FGF8 expression levels will be to sharpen the wavefront of FGF8 expression in the PSM and help regulate any disturbances to this concentration profile.

It is proposed to model the RA/FGF8 feedback loop as shown in Figure 7.2 [11, 13]. (i) Production of *raldh2* is inhibited by the presence of extracellular FGF8 and *raldh2* transcribes RALDH2. (ii) RALDH2 synthesizes the production of intracellular RA from Retinal. (iii) Intracellular RA is transported across the cell membrane and extracellular RA inhibits the production of *fgf8* (which is limited to the node region). (iv) *fgf8* transcribes intracellular FGF8 which is transported across the cell membrane and extracellular FGF8 inhibits *raldh2* production.

There are some simplifying assumptions made in the above model: we assume that *fgf8* production

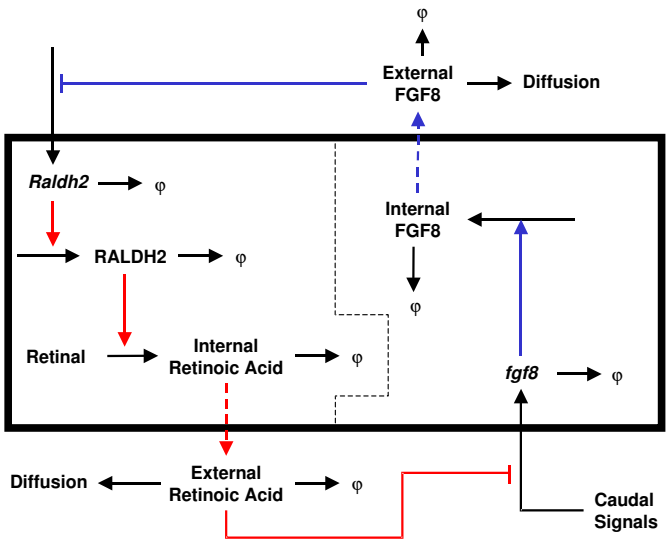


Figure 7.2: A diagram of the proposed interaction between FGF8 and RA along the AP axis of vertebrate embryos. *raldh2* transcribes RALDH2 which in turn synthesizes the production of RA from Retinal. *fgf8* transcribes FGF8. RA and FGF8 are both transported across the cell membrane where they diffuse and inhibit *fgf8* and *raldh2* production respectively. φ represents decay of the substances and is assumed to be linear in this model. The solid black line indicates the cell membrane.

is limited to the node region by some external factor, but it may be that high expression of extracellular RA is the sole regulating factor governing the restriction of *fgf8* production. We also make the assumption that extracellular FGF8 inhibits *raldh2* production but it is likely that extracellular FGF8 would need to re-enter the cell in order to become inhibitory to the production of *raldh2*. The remaining factor that we do not consider is the possibility that fgf8 may be self-activating, in that presence of high FGF8 concentrations may increase the rate of *fgf8* production in the node region. There is also no experimental evidence for the exact forms any of the above interactions take.

The system of PDEs describing the system can be found by considering Figure 7.3 and using the Law of Mass Action:

***raldh2* (r):** production is inhibited by extracellular FGF8 (F_e) and it is assumed to decay linearly (φ term). The resulting equation governing *raldh2* dynamics is

$$\frac{\partial r}{\partial t} = \frac{k_1}{k_2 + {F_e}^{N_1}} - k_3 r. \tag{7.1}$$

RALDH2 (R): *raldh2* (r) translates RALDH2 (R), which then facilitates the production of RA (A_i) by forming a complex (C_R) with Retinal (HR). RALDH2 acts in an enzymatic manner as it is released back into the cell upon production of RA and it is assumed to decay linearly. The resulting

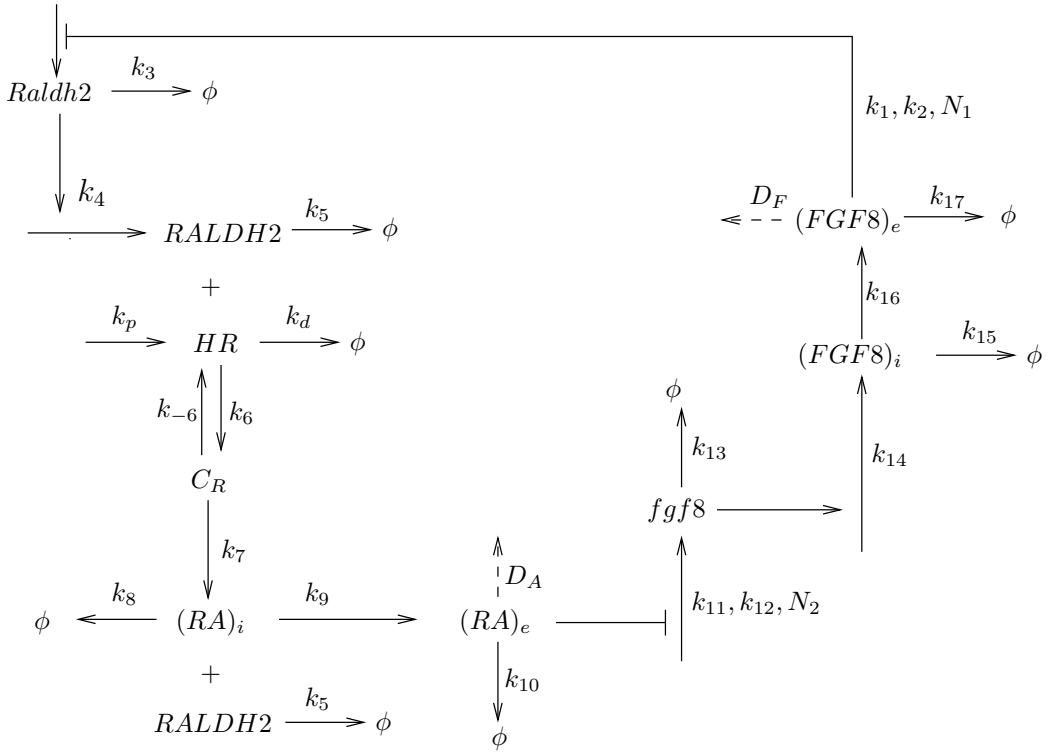


Figure 7.3: An illustration of the RA/FGF8 feedback mechanism as hypothesised in our model: The k_i's are non-negative rate constants, the N_i's represent possible allosteric effects, HR represents Retinal, C_R represents the RALDH2-Retinal complex, and the subscripts i and e indicate intracellular and extracellular concentrations of the respective reactants. The dashed lines and corresponding parameters D_A and D_F indicate the diffusive reactants and their rate of diffusion. ϕ represents the linear decay of each substance.

equation governing RALDH2 dynamics is

$$\frac{\partial R}{\partial t} = k_4 r - k_5 R - k_6 R(HR) + k_{-6}(C_R) + k_7(C_R). \tag{7.2}$$

Retinal (HR): acts as a substrate in the reaction: it binds to the enzyme RALDH2 to form a complex C_R. The rate of (HR) production depends on the amount of (HR) present and it is assumed to decay linearly. The resulting equation describing Retinal dynamics is

$$\frac{\partial (HR)}{\partial t} = k_p(HR) - k_6 R(HR) + k_{-6}(C_R) - k_d(HR). \tag{7.3}$$

RALDH2-Retinal complex (C_R): can either dissociate to give RALDH2 and Retinal or form the product, intracellular RA (A_i). We assume that C_R cannot decay, except into its constituent

components. The resulting equation describing the dynamics of the complex is

$$\frac{\partial(C_R)}{\partial t} = k_6 R(HR) - k_{-6}(C_R) - k_7(C_R). \tag{7.4}$$

Intracellular RA (A_i): is formed as the product of the enzymatic reaction involving RALDH2 and Retinal. It decays linearly and it is assumed to be transported out of the cell to become extracellular RA (A_e).

$$\frac{\partial A_i}{\partial t} = k_7(C_R) - (k_8 + k_9)A_i. \tag{7.5}$$

Extracellular RA (A_e): Intracellular RA (A_i) is transported across the cell membrane where it is able to diffuse within the surrounding tissue and it decays linearly. The equation describing the extracellular RA dynamics can be written:

$$\frac{\partial A_e}{\partial t} = k_9 A_i - k_{10} A_e + D_A \frac{\partial^2 A_e}{\partial x^2}. \tag{7.6}$$

***fgf8* (f):** Production of *fgf8* is inhibited by extracellular RA (A_e) and *fgf8* decays linearly. We also restrict *fgf8* production to the tail of the embryo (as is consistent with experimental results [17]). The equation describing the *fgf8* dynamics can be written

$$\frac{\partial f}{\partial t} = \frac{k_{11}}{k_{12} + A_e^{N_2}} \chi_f(x,t) - k_{13} f, \tag{7.7}$$

where the term $\chi_f = H(x - x_n - c_n t)$ limits *fgf8* (f) production to the node region. x_n represents the position of the tail at time $t = 0$ and c_n represents the rate of axis extension of the embryo.

Intracellular FGF8 (F_i): FGF8 is translated by *fgf8* (f) and it decays linearly. Intracellular FGF8 (F_i) is transported across the cell membrane to become extracellular FGF8 (F_e). The equation describing intracellular FGF8 dynamics can be written

$$\frac{\partial F_i}{\partial t} = k_{14} f - (k_{15} + k_{16}) F_i. \tag{7.8}$$

Extracellular FGF8 (F_e): Intracellular FGF8 (F_i) is transported across the cell membrane to become extracellular FGF8 (F_e) where it is able to diffuse throughout the surrounding tissue. Extracellular FGF8 also decays linearly. The equation describing the dynamics of FGF8 is therefore

$$\frac{\partial F_e}{\partial t} = k_{16} F_i - k_{17} F_e + D_F \frac{\partial^2 F_e}{\partial x^2}. \tag{7.9}$$

We now make some simplifying assumptions: firstly, we assume that Retinal is present in abundance so that $(HR) \approx$ constant [11]. We also assume that the rate constants involved in the formation and

dissociation of the complex C_R are very large [11], so that

$$k_6 = \frac{k_6'}{\delta}, \quad k_{-6} = \frac{k_{-6}'}{\delta}, \tag{7.10}$$

where $\delta \ll 1$. We can then rewrite equation (7.3) as

$$\delta \frac{\partial (HR)}{\partial t} - \delta \left[k_p (HR) - k_d (HR) \right] = -k_6' R(HR) + k_{-6}'(C_R). \tag{7.11}$$

Since $\delta \ll 1$ we assume that the LHS is approximately zero and hence

$$-k_6' R(HR) + k_{-6}'(C_R) = 0 \quad \Rightarrow \quad (C_R) = \frac{k_6 (HR)}{k_{-6}} R = k_6'' R. \tag{7.12}$$

Our second approximation comes from assuming that the intracellular reactions are in equilibrium [11] so that

$$k_i = \mathcal{O}(1) \quad \text{for} \quad i = 1, 2, 3, 7, 10, 11, 12, 13, 17$$

and

$$k_i = \frac{\tilde{k}_i}{\epsilon} \quad \text{for} \quad i = 4, 5, 8, 9, 14, 15, 16 \quad \text{where} \quad \epsilon \ll 1.$$

Note that $k_6'' \gg 1$ as Retinal is assumed to be present in abundance and so we take $k_6'' = k_6'''/\epsilon$.

Rewriting the above system of equations, with the inclusion of the ϵ's and dropping the $\tilde{}$'s, we have

$$\begin{aligned}
\frac{\partial r}{\partial t} &= \frac{k_1}{k_2 + {F_e}^{N_1}} - k_3 r, && (7.13)\\
\epsilon \frac{\partial R}{\partial t} &= k_4 r - k_5' R, && (7.14)\\
\epsilon \frac{\partial A_i}{\partial t} &= k_7' R - (k_8 + k_9) A_i, && (7.15)\\
\frac{\partial A_e}{\partial t} &= k_9 A_i - k_{10} A_e + D_A \frac{\partial^2 A_e}{\partial x^2}, && (7.16)\\
\frac{\partial f}{\partial t} &= \frac{k_{11}}{k_{12} + A_e^{N_2}} \chi_f(x,t) - k_{13} f, && (7.17)\\
\epsilon \frac{\partial F_i}{\partial t} &= k_{14} f - (k_{15} + k_{16}) F_i, && (7.18)\\
\frac{\partial F_e}{\partial t} &= k_{16} F_i - k_{17} F_e + D_F \frac{\partial^2 F_e}{\partial x^2}, && (7.19)
\end{aligned}$$

where $k_5' = k_5 - k_6''' k_7$ and $k_7' = k_6''' k_7$. In subsequent sections, we will drop the $'$'s on the parameters.

7.2.1 Non-dimensionalisation

The system has 24 parameters: we non-dimensionalise to minimise the number of parameters involved. For simplicity we take $N_1 = N_2 = 1$ [11] and

$$t = \frac{\hat{t}}{k_{17}}, \quad x = \hat{x}\sqrt{\frac{D_F}{k_{17}}}, \quad F_e = k_2\hat{F}_e, \quad A_e = k_{12}\hat{A}_e, \quad F_i = \frac{k_2 k_{17}}{k_{16}}\hat{F}_i,$$

$$f = \frac{k_2 k_{17}^2}{k_{14}k_{16}}\hat{f}, \quad A_i = \frac{k_{12}k_{17}}{k_9}\hat{A}_i, \quad R = \frac{k_{12}k_{17}^2}{k_7 k_9}\hat{R}, \quad r = \frac{k_{12}k_{17}^3}{k_4 k_7 k_9}\hat{r}.$$

Defining the new non-dimensionless parameters by

$$\hat{k}_3 = \frac{k_3}{k_{17}}, \quad \hat{k}_5 = \frac{k_5}{k_{17}}, \quad \hat{k}_8 = \frac{k_8}{k_{17}}, \quad \hat{k}_9 = \frac{k_9}{k_{17}}, \quad \hat{k}_{10} = \frac{k_{10}}{k_{17}}, \quad \hat{k}_{13} = \frac{k_{13}}{k_{17}},$$

$$\hat{k}_{15} = \frac{k_{15}}{k_{17}}, \quad \hat{k}_{16} = \frac{k_{16}}{k_{17}}, \quad \hat{k}_{11} = \frac{k_{11}k_{14}k_{16}}{k_2 k_{12}k_{17}^3}, \quad \hat{k}_1 = \frac{k_1 k_4 k_7 k_9}{k_2 k_{12}k_{17}^4},$$

$$\hat{x}_n = x_n\sqrt{\frac{k_{17}}{D_F}}, \quad \hat{c}_n = \frac{c_n}{k_{17}}\sqrt{\frac{k_{17}}{D_F}}, \quad \hat{\chi}_f = H(\hat{x} - \hat{x}_n - \hat{c}_n\hat{t}), \quad \hat{D} = \frac{D_A}{D_F},$$

and dropping the hats for notational convenience, the non-dimensional equations are

$$\frac{\partial r}{\partial t} = \frac{k_1}{1+F_e} - k_3 r, \tag{7.20}$$

$$\epsilon\frac{\partial R}{\partial t} = r - k_5 R, \tag{7.21}$$

$$\epsilon\frac{\partial A_i}{\partial t} = R - (k_8 + k_9)A_i, \tag{7.22}$$

$$\frac{\partial A_e}{\partial t} = A_i - k_{10}A_e + D\frac{\partial^2 A_e}{\partial x^2}, \tag{7.23}$$

$$\frac{\partial f}{\partial t} = \frac{k_{11}}{1+A_e}\chi_f(x,t) - k_{13}f, \tag{7.24}$$

$$\epsilon\frac{\partial F_i}{\partial t} = f - (k_{15} + k_{16})F_i, \tag{7.25}$$

$$\frac{\partial F_e}{\partial t} = F_i - F_e + \frac{\partial^2 F_e}{\partial x^2}. \tag{7.26}$$

We denote the above system the '*Original system*'.

7.2.1.1 Boundary conditions

The boundary conditions for the system are taken to be

$$\begin{array}{l} f, F_i, F_e \to 0 \quad \text{as} \quad x - \{x_n + c_n t\} \to -\infty, \\ f, F_i, F_e \quad \text{are bounded as} \quad x - \{x_n + c_n t\} \to +\infty, \\ r, R, A_i, A_e \quad \text{are bounded as} \quad x - \{x_n + c_n t\} \to \pm\infty. \end{array} \tag{7.27}$$

7.2.1.2 Initial conditions

We derive initial conditions by finding the spatially uniform steady states of the model. Hence we take

$$r(x,0) = \begin{cases} \frac{k_1}{k_3} & \text{for} \quad x - x_n \le 0, \\ r_\infty & \text{for} \quad x - x_n > 0. \end{cases} \tag{7.28}$$

$$R(x,0) = \begin{cases} \frac{k_1}{k_3 k_5} & \text{for} \quad x - x_n \le 0, \\ \frac{r_\infty}{k_5} & \text{for} \quad x - x_n > 0. \end{cases} \tag{7.29}$$

$$A_i(x,0) = \begin{cases} \frac{k_1}{k_3 k_5 (k_8+k_9)} & \text{for} \quad x - x_n \le 0, \\ \frac{r_\infty}{k_5 (k_8+k_9)} & \text{for} \quad x - x_n > 0. \end{cases} \tag{7.30}$$

$$A_e^0(x,0) = \begin{cases} \frac{k_1}{k_3 k_5 (k_8+k_9) k_{10}} & \text{for} \quad x - x_n \le 0, \\ \frac{r_\infty}{k_5 (k_8+k_9) k_{10}} & \text{for} \quad x - x_n > 0. \end{cases} \tag{7.31}$$

$$f(x,0) = \begin{cases} 0 & \text{for} \quad x - x_n \le 0, \\ \frac{k_{11}}{k_{13}\left[1+\frac{r_\infty}{k_5(k_8+k_9)}\right]} & \text{for} \quad x - x_n > 0. \end{cases} \tag{7.32}$$

$$F_i(x,0) = \begin{cases} 0 & \text{for} \quad x - x_n \le 0, \\ \frac{k_{11}}{k_{13}(k_{15}+k_{16})\left[1+\frac{r_\infty}{k_5(k_8+k_9)}\right]} & \text{for} \quad x - x_n > 0. \end{cases} \tag{7.33}$$

$$F_e(x,0) = \begin{cases} 0 & \text{for} \quad x - x_n \le 0, \\ \frac{k_{11}}{k_{13}(k_{15}+k_{16})\left[1+\frac{r_\infty}{k_5(k_8+k_9)}\right]} & \text{for} \quad x - x_n > 0. \end{cases} \tag{7.34}$$

r_∞ is the positive solution of

$$k_3 k_t r_\infty^2 + [k_3(1+k_s) - k_1 k_t] r_\infty - k_1 = 0, \tag{7.35}$$

where

$$k_s = \frac{k_{11}}{k_{13}(k_{15}+k_{16})} \quad \text{and} \quad k_t = \frac{1}{k_5(k_8+k_9)k_{10}}. \tag{7.36}$$

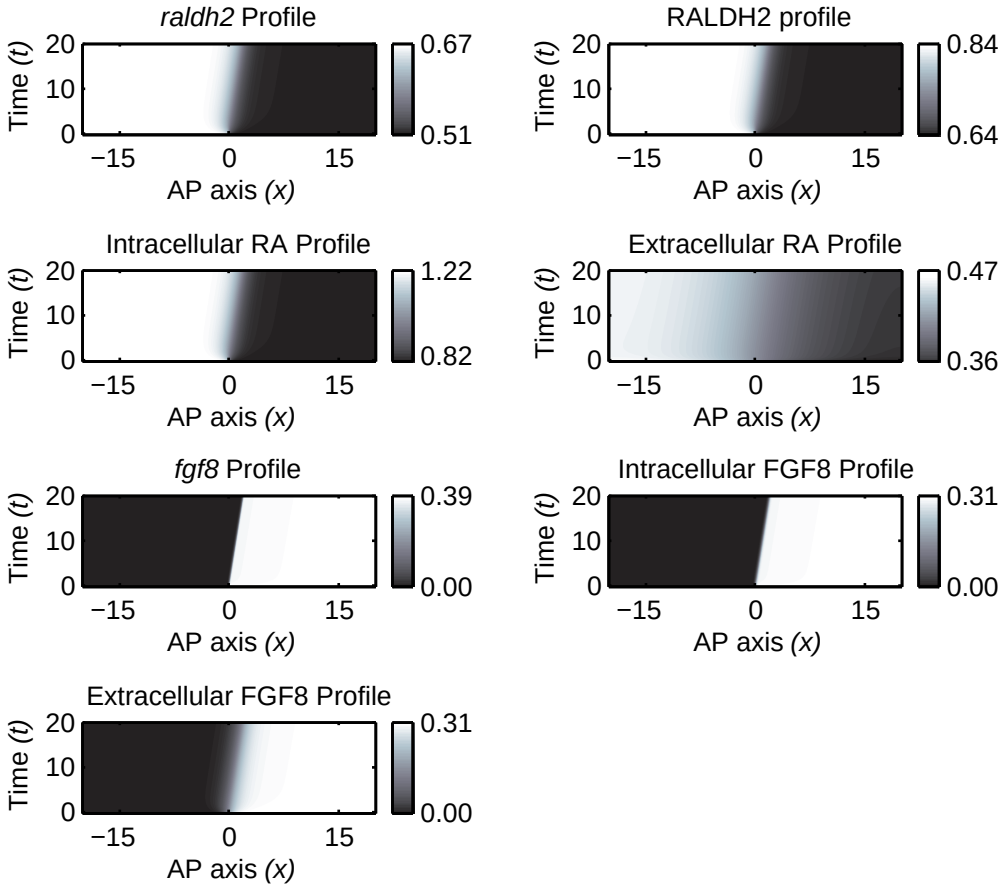


Figure 7.4: Plots of the NAG numerical solution of the full RA/FGF8 feedback model, the '*Original system*', given by equations (7.20)-(7.26). The plots clearly show opposing gradients of RA and FGF8 moving in a posterior direction along the AP axis with constant speed. The initial conditions are given by equations (7.28)-(7.34). Parameters are as follows: $k_3 = 1.0$, $k_3 = 1.5$, $k_5 = 0.8$, $k_8 = 0.4$, $k_9 = 0.5$, $k_{10} = 2.0$, $k_{11} = 1.3$, $k_{13} = 2.5$, $k_{15} = 0.6$, $k_{16} = 0.65$, $D = 100$ and $c_n = 0.1$.

7.3 Numerical solution of the '*Original system*' of equations

The '*Original system*' of equations describing the interactions between RA and FGF8 given by equations (7.20)-(7.26) can be solved as in other chapters using the NAG library routine D03PCF. The infinite domain boundary conditions given by equation (7.27) are approximated using zero flux boundary conditions on a finite domain, and the Heaviside function is approximated using a continuous $\tanh$ approximation, as discussed previously. The system is solved on a mesh consisting of 1001 x 1001 points and the output is plotted using the MATLAB function imagesc.

Figure 7.4 shows plots of the numerical solution of the '*Original system*' of equations describing the RA/FGF8 feedback model given by (7.20)-(7.26). *raldh2*, RALDH2 and RA levels are highest in

the anterior region and decrease monotonically along the AP axis. *fgf8* and FGF8 levels behave in a contrasting manner with low expression levels seen in the anterior region and high expression levels found in the posterior region. The position of the determination front, the axial level at which FGF8 signalling changes from high to low, moves with constant speed in a posterior direction. Figure 7.4 shows that with the given parameters and initial conditions, the model for FGF8/RA feedback given by equations (7.20)-(7.26) can produce the results seen *in vivo* (see Figure 7.1).

7.4 A singular perturbation problem

The presence of the small parameter ϵ multiplying the time derivative of three equations in the '*Original system*' given by equations (7.20)-(7.26), indicates a singular perturbation problem. More specifically, after a short initial stage where concentrations of RALDH2, intracellular RA and intracellular FGF8 concentrations change very rapidly, their concentrations will become approximately constant - over the longer time scale in which *raldh2*, extracellular RA, *fgf8* and extracellular FGF8 vary. We proceed by expanding the variables in terms of ϵ to approximate the solutions on a long time scale and also transform t to look more closely at the solution close to $t = 0$.

7.4.1 Inner region

Expanding time around $t = 0$ by making the transformation $\sigma = t/\epsilon$, expanding the variables in terms of ϵ by letting

$$\begin{aligned} r &= r^0 + \epsilon r^1 + \ldots, \\ R &= R^0 + \epsilon R^1 + \ldots, \\ A_i &= A_i^0 + \epsilon A_i^1 + \ldots, \\ A_e &= A_e^0 + \epsilon A_e^1 + \ldots, \\ f &= f^0 + \epsilon f^1 + \ldots, \\ F_i &= F_i^0 + \epsilon F_i^1 + \ldots, \\ F_e &= F_e^0 + \epsilon F_i^1 + \ldots, \end{aligned}$$

and substituting into equations (7.20)-(7.26) gives the '*Inner system*' of equations describing the initial dynamics:

raldh2

$$\frac{\partial r^0}{\partial \sigma} = 0, \tag{7.37}$$

$$\frac{\partial r^1}{\partial \sigma} = \frac{k_1}{1 + F_e^0} - k_3 r^0. \tag{7.38}$$

RALDH2

$$\frac{\partial R^0}{\partial \sigma} = r^0 - k_5 R^0, \tag{7.39}$$
$$\frac{\partial R^1}{\partial \sigma} = r^1 - k_5 R^1. \tag{7.40}$$

Intracellular RA

$$\frac{\partial A_i^0}{\partial \sigma} = R^0 - (k_8 + k_9) A_i^0, \tag{7.41}$$
$$\frac{\partial A_i^1}{\partial \sigma} = R^1 - (k_8 + k_9) A_i^1. \tag{7.42}$$

Extracellular RA

$$\frac{\partial A_e^0}{\partial \sigma} = 0, \tag{7.43}$$
$$\frac{\partial A_e^1}{\partial \sigma} = A_i^0 - k_{10} A_e^0 + D \frac{\partial^2 A_e^0}{\partial x^2}. \tag{7.44}$$

fgf8

$$\frac{\partial f^0}{\partial \sigma} = 0, \tag{7.45}$$
$$\frac{\partial f^1}{\partial \sigma} = \frac{k_{11}}{1 + A_e^0} \chi_f - k_{13} f^0. \tag{7.46}$$

Intracellular FGF8

$$\frac{\partial F_i^0}{\partial \sigma} = f^0 - (k_{15} + k_{16}) F_i^0, \tag{7.47}$$
$$\frac{\partial F_i^1}{\partial \sigma} = f^1 - (k_{15} + k_{16}) F_i^1. \tag{7.48}$$

Extracellular FGF8

$$\frac{\partial F_e^0}{\partial \sigma} = 0, \tag{7.49}$$
$$\frac{\partial F_e^1}{\partial \sigma} = F_i^0 - F_e^0 + \frac{\partial^2 F_e^0}{\partial x^2}. \tag{7.50}$$

We explore the '*Inner system*' in more detail in Section 7.5.

7.4.2 Outer region

Expanding each variable in terms of the small parameter ϵ yields

$$\begin{aligned} r &= r_0 + \epsilon r_1 + \ldots, \\ R &= R_0 + \epsilon R_1 + \ldots, \\ A_i &= A_{i0} + \epsilon A_{i1} + \ldots, \\ A_e &= A_{e0} + \epsilon A_{e1} + \ldots, \\ f &= f_0 + \epsilon f_1 + \ldots, \\ F_i &= F_{i0} + \epsilon F_{i1} + \ldots, \\ F_e &= F_{e0} + \epsilon F_{e1} + \ldots, \end{aligned}$$

and upon substituting into equations (7.20)-(7.26) gives, correct to first order in ϵ, the '*Outer system*' of equations describing the long term dynamics:

raldh2

$$\frac{\partial r_0}{\partial t} = \frac{k_1}{1+F_{e0}} - k_3 r_0, \tag{7.51}$$

$$\frac{\partial r_1}{\partial t} = -\frac{k_1 F_{e1}}{(1+F_{e0})^2} - k_3 r_1. \tag{7.52}$$

RALDH2

$$0 = r_0 - k_5 R_0, \tag{7.53}$$

$$\frac{\partial R_0}{\partial t} = r_1 - k_5 R_1. \tag{7.54}$$

Intracellular RA

$$0 = R_0 - (k_8 + k_9) A_{i0}, \tag{7.55}$$

$$\frac{\partial A_{i0}}{\partial t} = R_1 - (k_8 + k_9) A_{i1}. \tag{7.56}$$

Extracellular RA

$$\frac{\partial A_{e0}}{\partial t} = A_{i0} - k_{10}A_{e0} + D\frac{\partial^2 A_{e_0}}{\partial x^2}, \tag{7.57}$$

$$\frac{\partial A_{e1}}{\partial t} = A_{i1} - k_{10}A_{e1} + D\frac{\partial^2 A_{e_1}}{\partial x^2}. \tag{7.58}$$

fgf8

$$\frac{\partial f_0}{\partial t} = \frac{k_{11}}{1 + A_{e0}}\chi_f - k_{13}f_0, \tag{7.59}$$

$$\frac{\partial f_1}{\partial t} = -\frac{k_{11}A_{e1}}{(1 + A_{e0})^2}\chi_f - k_{13}f_1. \tag{7.60}$$

Intracellular FGF8

$$0 = f_0 - (k_{15} + k_{16})F_{i0}, \tag{7.61}$$

$$\frac{\partial F_{i0}}{\partial t} = f_1 - (k_{15} + k_{16})F_{i1}. \tag{7.62}$$

Extracellular FGF8

$$\frac{\partial F_{e0}}{\partial t} = F_{i0} - F_{e0} + \frac{\partial^2 F_{e_0}}{\partial x^2}, \tag{7.63}$$

$$\frac{\partial F_{e1}}{\partial t} = F_{i1} - F_{e1} + \frac{\partial^2 F_{e_1}}{\partial x^2}. \tag{7.64}$$

We explore the '*Outer system*' in more detail in Section 7.6.

7.4.3 Domains of validity

We will need impose matching conditions in order to guarantee continuity of the solutions. In the limit $\epsilon \to 0$, we see that $\sigma = t/\epsilon \to \infty$ regardless of the value of t (for $t > 0$). Hence, in the limit $\epsilon \to 0$, we expect the solutions of the '*Outer system*' as $t \to 0$ to be equal to the solutions of the '*Inner system*' as $\sigma \to \infty$.

Figure 7.5 illustrates the different domains of t space in a singular perturbation problem of the kind present in the '*Original system*'. In a region of $t = 0$ where the '*Inner system*' of equations is valid, we see from equations (7.37)-(7.50) that, correct to $\mathcal{O}(1)$, *raldh2*, extracellular RA, *fgf8* and extracellular FGF8 concentrations are approximately constant (compare with the slow variable in Figure 7.5) and the remaining concentrations are changing more rapidly (compare with the fast variable in Figure 7.5). The reverse is true in the outer region. We will discuss the domains of

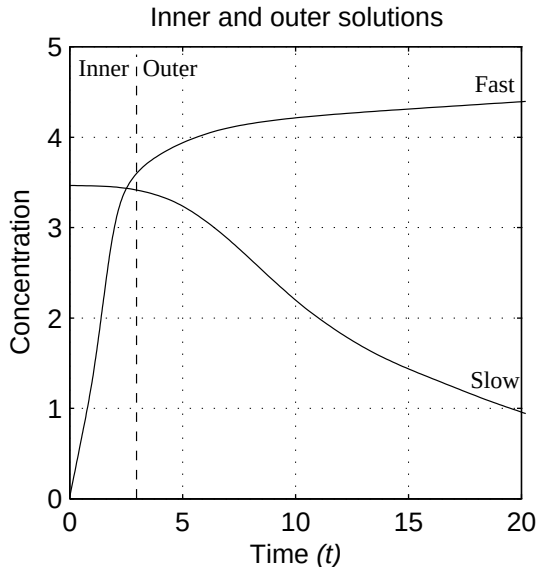


Figure 7.5: A schematic illustration of the domains of t space expected with a singular perturbation problem. The dashed line indicates the transition between the fast and slow time scales. To the LHS of the dashed line while the inner time scale is valid, variables which vary on the slow time scale (marked slow) are approximately constant while variables which vary on the fast time scale (marked fast) change very rapidly. The reverse is true to the RHS of the dashed line where the outer time scale is valid.

validity of the solutions later in this chapter.

7.5 Solution of the '*Inner system*'

Correct to $\mathcal{O}(1)$, the dynamics of the system on the fast time scale are governed by the equations:

$$\frac{\partial r^0}{\partial \sigma} = 0, \tag{7.65}$$

$$\frac{\partial R^0}{\partial \sigma} = r^0 - k_5 R^0, \tag{7.66}$$

$$\frac{\partial A_i^0}{\partial \sigma} = R^0 - (k_8 + k_9) A_i^0, \tag{7.67}$$

$$\frac{\partial A_e^0}{\partial \sigma} = 0, \tag{7.68}$$

$$\frac{\partial f^0}{\partial \sigma} = 0, \tag{7.69}$$

$$\frac{\partial F_i^0}{\partial \sigma} = f^0 - (k_{15} + k_{16}) F_i^0, \tag{7.70}$$

$$\frac{\partial F_e^0}{\partial \sigma} = 0, \tag{7.71}$$

which can be solved directly to give the '*Inner solution* - $\mathcal{O}(1)$':

$$
\begin{aligned}
r^0 &= r^0(x,0), && (7.72)\\
R^0 &= \frac{1}{k_5} r^0(x,0) + \alpha e^{-k_5\sigma}, && (7.73)\\
A_i^0 &= \frac{1}{k_5(k_8+k_9)} r^0(x,0) + \frac{1}{k_8+k_9-k_5}\alpha e^{-k_5\sigma} + \beta e^{-(k_8+k_9)\sigma}, && (7.74)\\
A_e^0 &= A_e^0(x,0), && (7.75)\\
f^0 &= f^0(x,0), && (7.76)\\
F_i^0 &= \frac{1}{k_{15}+k_{16}} f^0(x,0) + \gamma e^{-(k_{15}+k_{16})\sigma}, && (7.77)\\
F_e^0 &= F_e^0(x,0), && (7.78)
\end{aligned}
$$

where

$$
\begin{aligned}
\alpha &= R^0(x,0) - \frac{r^0(x,0)}{k_5}, && (7.79)\\
\beta &= A_i^0(x,0) - \frac{r^0(x,0)}{k_5(k_8+k_9)} - \frac{\alpha}{k_8+k_9-k_5}, && (7.80)\\
\gamma &= F_i^0(x,0) - \frac{1}{k_{15}+k_{16}} f^0(x,0). && (7.81)
\end{aligned}
$$

Correct to $\mathcal{O}(\epsilon)$, the dynamics of the system on the fast time scale are governed by the equations:

$$
\begin{aligned}
\frac{\partial r^1}{\partial \sigma} &= \frac{k_1}{1+F_e^0} - k_3 r^0, && (7.82)\\
\frac{\partial R^1}{\partial \sigma} &= r^1 - k_5 R^1, && (7.83)\\
\frac{\partial A_i^1}{\partial \sigma} &= R^1 - (k_8+k_9) A_i^1, && (7.84)\\
\frac{\partial A_e^1}{\partial \sigma} &= A_i^0 - k_{10} A_e^0 + D\frac{\partial^2 A_e^0}{\partial x^2}, && (7.85)\\
\frac{\partial f^1}{\partial \sigma} &= \frac{k_{11}}{1+A_e^0}\chi_f - k_{13} f^0, && (7.86)\\
\frac{\partial F_i^1}{\partial \sigma} &= f^1 - (k_{15}+k_{16}) F_i^1, && (7.87)\\
\frac{\partial F_e^1}{\partial \sigma} &= F_i^0 - F_e^0 + \frac{\partial^2 F_e^0}{\partial x^2}. && (7.88)
\end{aligned}
$$

These can also be solved directly, but the solutions are algebraically very messy. The '*Inner solution*

- $\mathcal{O}(\epsilon)$' is given by:

$$
\begin{aligned}
r^1(x,\sigma) &= A\sigma + r^1(x,0), && (7.89)\\
R^1(x,\sigma) &= \frac{A}{k_5}\sigma + B + Ce^{-k_5\sigma}, && (7.90)\\
A_i^1(x,\sigma) &= \frac{A\sigma}{k_5(k_8+k_9)} - \tilde{D} + \frac{C}{k_8+k_9-k_5}e^{-k_5\sigma} + Ee^{-(k_8+k_9)\sigma}, && (7.91)\\
A_e^1(x,\sigma) &= F + G\sigma - \frac{\beta}{k_8+k_9}e^{-(k_8+k_9)\sigma} - \frac{\alpha}{k_5(k_8+k_9-k_5)}e^{-k_5\sigma}, && (7.92)\\
f^1(x,\sigma) &= H\sigma + f^1(x,0), && (7.93)\\
F_i^1(x,\sigma) &= \frac{H\sigma + f^1(x,0)}{k_{15}+k_{16}} - \frac{H}{(k_{15}+k_{16})^2} + Ie^{-(k_{15}+k_{16})\sigma}, && (7.94)\\
F_e^1(x,\sigma) &= J + K\sigma - \frac{\gamma}{k_{15}+k_{16}}e^{-(k_{15}+k_{16})\sigma}, && (7.95)
\end{aligned}
$$

where

$$
\begin{aligned}
A &= \frac{k_1}{1+F_e^0(x,0)} - k_3 r^0(x,0), && (7.96)\\
B &= \frac{r^1(x,0)}{k_5} - \frac{A}{k_5^2}, && (7.97)\\
C &= R^1(x,0) + \frac{A}{k_5^2} - \frac{r^1(x,0)}{k_5}, && (7.98)\\
\tilde{D} &= \frac{B}{k_8+k_9} + \frac{A}{k_5(k_8+k_9)^2}, && (7.99)\\
E &= A_i^1(x,0) + \frac{A}{k_5(k_8+k_9)^2} - \frac{B}{k_8+k_9} - \frac{C}{k_8+k_9-k_5}, && (7.100)\\
F &= A_e^1(x,0) + \frac{\beta}{k_8+k_9} + \frac{\alpha}{k_5(k_8+k_9-k_5)}, && (7.101)\\
G &= \frac{r^0(x,0)}{k_5(k_8+k_9)} - k_{10}A_e^0(x,0) + D[A_e^0(x,0)]_{xx}, && (7.102)\\
H &= \frac{k_{11}}{1+A_e^0(x,0)}\chi_f - k_{13}f^0(x,0), && (7.103)\\
I &= F_i^0(x,0) + \frac{H}{(k_{15}+k_{16})^2} - \frac{f^1(x,0)}{k_{15}+k_{16}}, && (7.104)\\
J &= F_e^1(x,0) + \frac{\gamma}{k_{15}+k_{16}}, && (7.105)\\
K &= \frac{f^0(x,0)}{k_{15}+k_{16}} - F_e^0(x,0) + [F_e^0(x,0)]_{xx}. && (7.106)
\end{aligned}
$$

Figure 7.6(a) shows a plot of the inner solutions, correct to $\mathcal{O}(\epsilon)$ (i.e. $r^0 + \epsilon r^1$ etc.), at a particular spatial point x. As expected, *raldh2*, extracellular RA, *fgf8* and extracellular FGF8 concentrations vary only slightly while RALDH2, intracellular RA and intracellular FGF8 quickly tend to steady state values. We have assumed all the initial conditions are independent of x and plotted the solu-

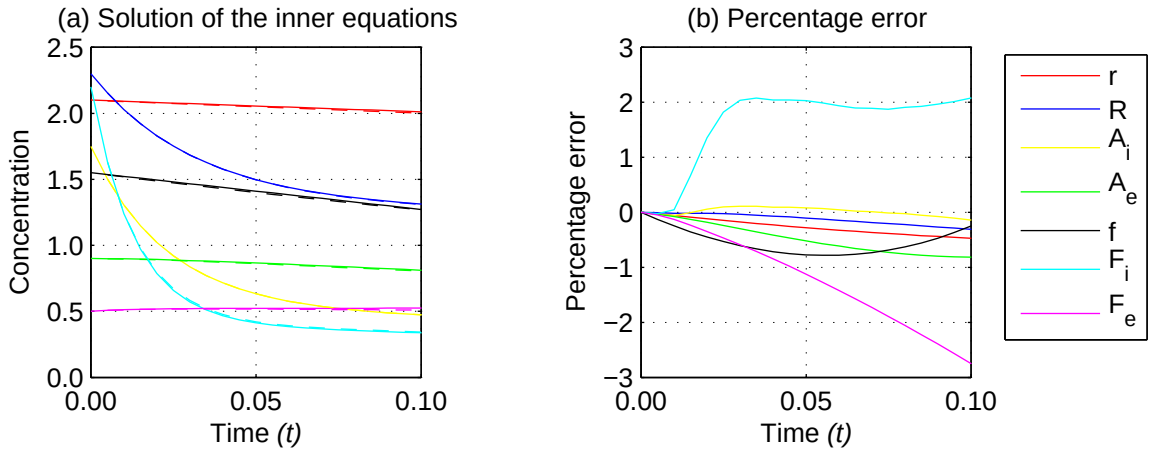


Figure 7.6: (a) Plot of the $\mathcal{O}(\epsilon)$ approximation for the inner solution at the point $x = 2.0$ on the AP axis (solid lines) and the numerical solution of the '*Original System*' (dashed lines). *raldh2*, extracellular RA, *fgf8* and extracellular FGF8 remain approximately constant and RALDH2, intracellular RA and intracellular FGF8 quickly tend to steady state values. (b) Plots of the percentage error between the $\mathcal{O}(\epsilon)$ analytical solution and the NAG numerical solution of the '*Full System*'. Parameters are as follows: $D = 100$, $c_n = 0.0$, $x_n = 0.0$, $\epsilon = 0.05$, $k_1 = 1.0$, $k_5 = 1.1$, $k_8 = 1.3$, $k_9 = 1.5$, $k_{15} = 2.1$, $k_{16} = 1.7$, $r^0(x,0) = 2.0$, $R^0(x,0) = 2.1$, $A_i^0(x,0) = 1.6$, $A_e^0(x,0) = 0.8$, $f^0(x,0) = 1.4$, $F_i^0(x,0) = 2.1$, $F_e^0(x,0) = 0.4$, $r^1(x,0) = 2.0$, $R^1(x,0) = 4.0$, $A_i^1(x,0) = 3.0$, $A_e^1(x,0) = 2.0$, $f^1(x,0) = 3.0$, $F_i^1(x,0) = 2.0$ and $F_e^1(x,0) = 2.0$.

tions for $\chi_f > 0$.

Figure 7.6(b) shows a plot of the percentage error between the $\mathcal{O}(\epsilon)$ analytical solution and the NAG numerical solution of the '*Original System*'. The percentage error is given (for a specific x) by, for example,

$$\text{Percentage error} = \frac{r_{num} - (r^0 + \epsilon r^1)}{r_{num}} \text{x} 100, \tag{7.107}$$

where A_{num} is the numerical solution evaluated at x. We see that whilst t is small the errors for each dependent variable remain small indicating a close fitting approximation.

7.6 The '*Outer system*'

Equations (7.53), (7.55) and (7.61) can be used to reduce the number of $\mathcal{O}(1)$ equations of the '*Outer system*' to give

$$\frac{\partial r_0}{\partial t} = \frac{k_1}{1+F_{e0}} - k_3 r_0, \tag{7.108}$$

$$\frac{\partial A_{e0}}{\partial t} = k_{18} r_0 - k_{10} A_{e0} + D\frac{\partial^2 A_{e_0}}{\partial x^2}, \tag{7.109}$$

$$\frac{\partial f_0}{\partial t} = \frac{k_{11}}{1+A_{e0}}\chi_f - k_{13} f_0, \tag{7.110}$$

$$\frac{\partial F_{e0}}{\partial t} = k_{19} f_0 - F_{e0} + \frac{\partial^2 F_{e_0}}{\partial x^2}, \tag{7.111}$$

where

$$k_{18} = \frac{1}{k_5(k_8+k_9)} \quad \text{and} \quad k_{19} = \frac{1}{k_{15}+k_{16}}.$$

We denote this system the '*Outer system* - $\mathcal{O}(1)$'

7.6.1 Numerical solution of the '*Outer system* - $\mathcal{O}(1)$'

In this section, we compare the results of numerical solution of the '*Original system*' with numerical solution of '*Outer system* - $\mathcal{O}(1)$'. In Appendix E we will derive approximate solutions for the '*Outer system* - $\mathcal{O}(1)$' but it is important before we do this to check that the numerical solution of the '*Outer system* - $\mathcal{O}(1)$' gives similar results to the numerical solution of the '*Original system*'.

As previously, we solve the '*Outer system* - $\mathcal{O}(1)$' using the NAG library routine D03PCF. We solve the system on a mesh consisting of 1001 x 1001 points and plot the results using the MATLAB function imagesc. We approximate the Heaviside function by a continuous $\tanh$ function and solve the equations on a domain that is large enough to ensure that conditions at the boundaries do not have an effect.

7.6.1.1 Boundary conditions for the '*Outer system* - $\mathcal{O}(1)$'

The boundary conditions for the system, given earlier in this chapter, are

$$\begin{array}{ll} f, F_e \to 0 \quad \text{as} & x - \{x_n + c_n t\} \to -\infty, \\ f, F_e \quad \text{are bounded as} & x - \{x_n + c_n t\} \to +\infty, \\ r, A_e \quad \text{are bounded as} & x - \{x_n + c_n t\} \to \pm\infty. \end{array} \tag{7.112}$$

As in previous numerical computations we approximate the infinite domain boundary conditions by zero flux boundary conditions on a finite domain.

7.6.1.2 Initial conditions for the '*Outer system* - $\mathcal{O}(1)$'

The initial conditions are given by finding the spatially uniform steady states of the model. As before, we take

$$r(x,0) = \begin{cases} \frac{k_1}{k_3} & \text{for} \quad x - x_n \leq 0, \\ r_\infty & \text{for} \quad x - x_n > 0. \end{cases} \tag{7.113}$$

$$A_e(x,0) = \begin{cases} \frac{k_1}{k_3 k_5 (k_8+k_9) k_{10}} & \text{for} \quad x - x_n \leq 0, \\ \frac{r_\infty}{k_5 (k_8+k_9) k_{10}} & \text{for} \quad x - x_n > 0. \end{cases} \tag{7.114}$$

$$f(x,0) = \begin{cases} 0 & \text{for} \quad x - x_n \leq 0, \\ \frac{k_{11}}{k_{13}\left[1+\frac{r_\infty}{k_5(k_8+k_9)}\right]} & \text{for} \quad x - x_n > 0. \end{cases} \tag{7.115}$$

$$F_e(x,0) = \begin{cases} 0 & \text{for} \quad x - x_n \leq 0, \\ \frac{k_{11}}{k_{13}(k_{15}+k_{16})\left[1+\frac{r_\infty}{k_5(k_8+k_9)}\right]} & \text{for} \quad x - x_n > 0. \end{cases} \tag{7.116}$$

r_∞ is the positive solution of

$$k_3 k_t r^2 + [k_3(1+k_s) - k_1 k_t] r - k_1 = 0, \tag{7.117}$$

where

$$k_s = \frac{k_{11}}{k_{13}(k_{15}+k_{16})} \quad \text{and} \quad k_t = \frac{1}{k_5(k_8+k_9)k_{10}}. \tag{7.118}$$

7.6.1.3 Results for the '*Outer system* - $\mathcal{O}(1)$'

Figure 7.7 shows the results of the numerical solution of the '*Outer system* - $\mathcal{O}(1)$'. We see that the results look qualitatively similar to those for the '*Original system*' shown in Figure 7.4: *raldh2* and extracellular RA concentrations are highest in the anterior PSM with the region at which the concentrations drop from high to low moving posteriorly with constant speed and *vice versa* for the *fgf8* and extracellular FGF8 concentrations.

7.6.1.4 Comparison with the '*Original system*'

Figure 7.8 shows plots of the NAG numerical solutions generated by the '*Original system*' of equations and the '*Outer system* - $\mathcal{O}(1)$' of equations, along with the percentage error between them. We define the percentage error for each x to be, for example,

$$\text{Percentage error} = \frac{r_{Original} - r_{Outer}}{r_{Original}} \text{x} 100, \tag{7.119}$$

where $r_{Original}$ is the numerical solution of the '*Original system*' evaluated at x etc. For *raldh2*, RALDH2 and *fgf8* the errors remain small throughout the domain with the only significant error

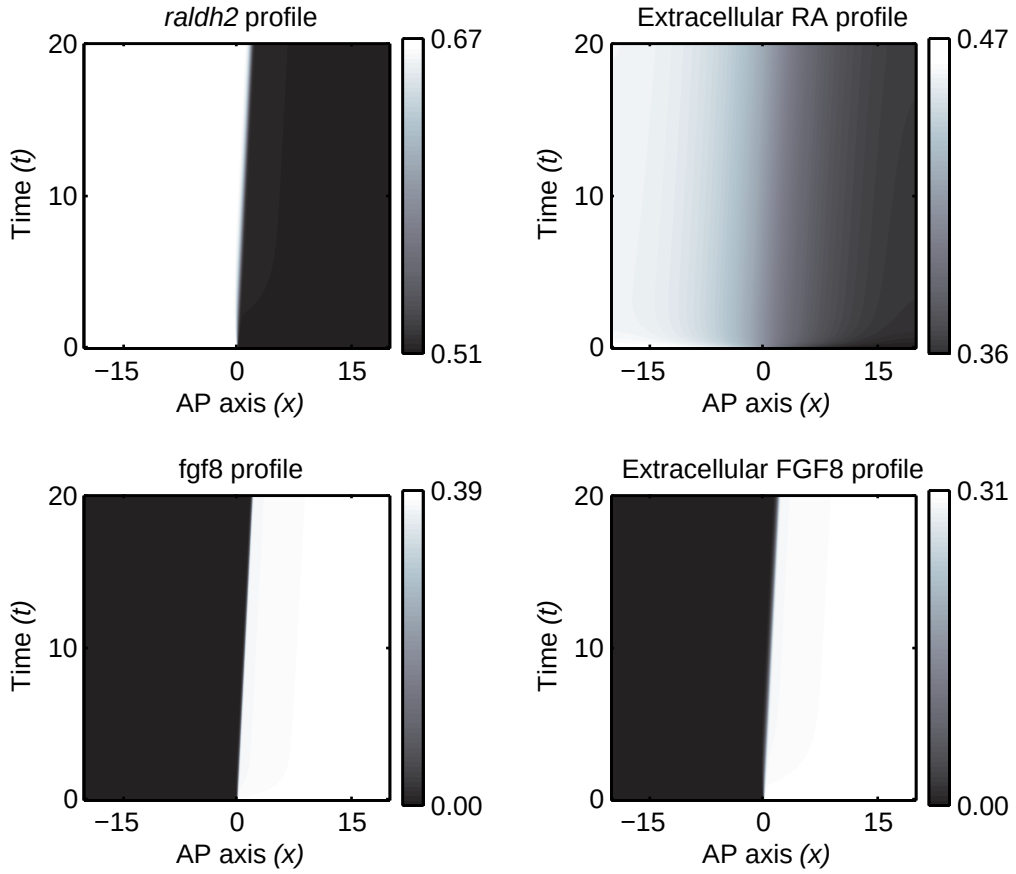


Figure 7.7: Plots of the NAG numerical solutions generated by the '*Outer system* - $\mathcal{O}(1)$'. Qualitatively the numerical solution of the '*Outer system* - $\mathcal{O}(1)$' seems to agree with the numerical solution of the '*Original system*' shown in Figure 7.4. In Figure 7.8 we show that the '*Outer system* $\mathcal{O}(1)$' gives a very close approximation to the '*Original system*' for $t = 20$. The figures were plotted using the MATLAB function imagesc. Parameters are as follows: $k_1 = 1.0$, $k_3 = 1.5$, $k_5 = 0.8$, $k_8 = 0.4$, $k_9 = 0.5$, $k_{10} = 2.0$, $k_{11} = 1.3$, $k_{13} = 2.5$, $k_{15} = 0.6$, $k_{16} = 0.65$, $D = 100$, $x_n = 0.0$, $c_n = 0.1$ and $\epsilon = 0.01$.

in the FGF8 profile seen at the position of the Heaviside function discontinuity. We now have the necessary information to progress further with finding an approximate solution for the '*Outer system* - $\mathcal{O}(1)$'.

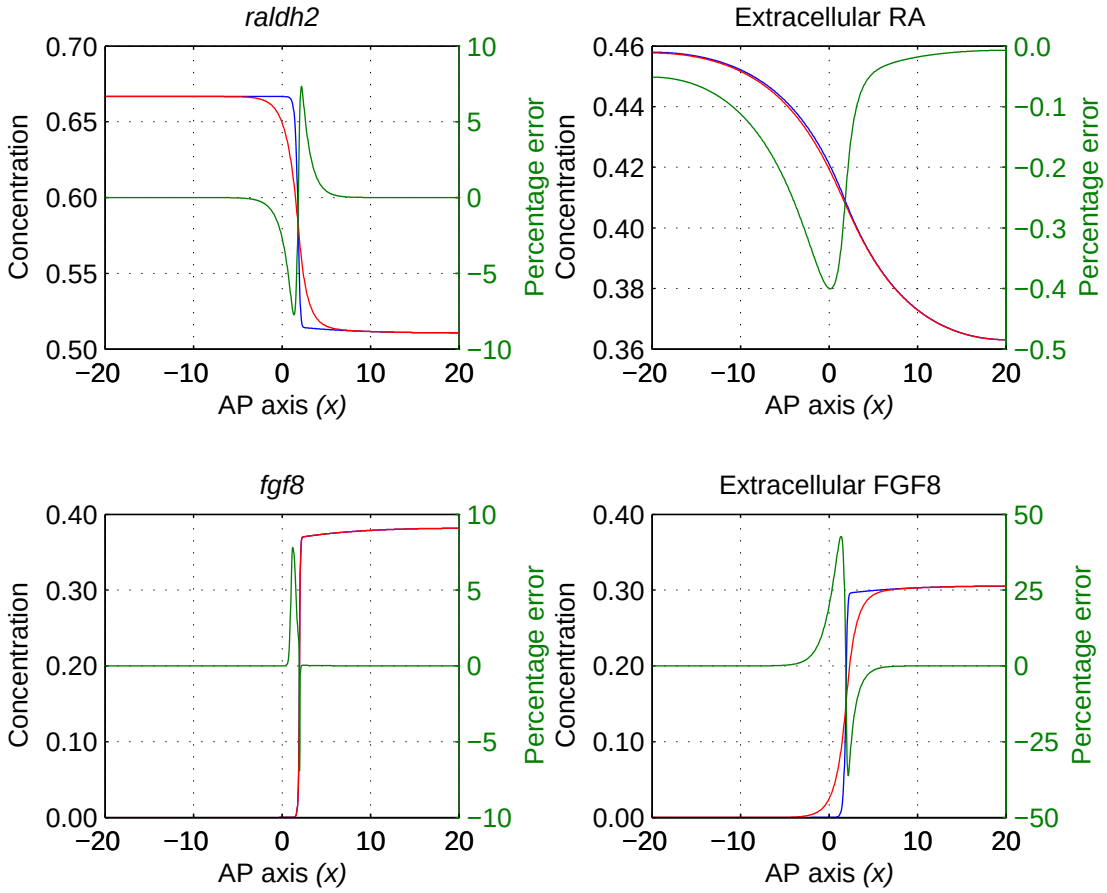


Figure 7.8: Plots of the NAG numerical solutions generated by the '*Original system*' of equations (7.20)-(7.26) (blue) and the '*Outer system* - $\mathcal{O}(1)$' of equations (E.5)-(E.8) (red). The percentage error between the two solutions is plotted on the right-hand axes (green). The profiles are plotted for $t = 20$. For *raldh2*, RALDH2 and *fgf8* the errors remain small throughout the domain with the only significant error in the FGF8 profile seen at the position of the Heaviside function discontinuity at $x = 2$. Parameters are as follows: $k_1 = 1.0$, $k_3 = 1.5$, $k_5 = 0.8$, $k_8 = 0.4$, $k_9 = 0.5$, $k_{10} = 2.0$, $k_{11} = 1.3$, $k_{13} = 2.5$, $k_{15} = 0.6$, $k_{16} = 0.65$, $D = 100$, $x_n = 0.0$, $c_n = 0.1$ and $\epsilon = 0.01$.

7.6.2 Analytical results for the '*Outer system* - $\mathcal{O}(1)$'

In Appendix E we make some analytical approximations for the '*Outer system* - $\mathcal{O}(1)$' by expanding the equations in terms of the small parameter c_n. The resulting approximate solutions are summarised in the following section.

7.7 The approximate solutions - a summary

We have summarised the analytical results generated so far in this chapter (and in Appendix E) in Table 7.1 and Table 7.2. Table 7.1 shows (correct to $\mathcal{O}(\epsilon)$) the solutions of the '*Inner system*' in terms of the rescaled time variable σ. Table 7.2 shows the results detailed in the Appendix of the (correct to $\mathcal{O}(1)$) steady state solutions of the '*Outer system*'. A_{c0} and A_{c1} are specified by equations (E.68) and (E.69).

The solutions were found by first transforming the spatial variable x such that $y = \sqrt{D}x$ and then ignoring terms of $\mathcal{O}\left(D^{-1}\right)$ where it was assumed that $D \gg 1$ ('*Outer system, rescaled x*'). Once the spatial transformation was made, we made another transformation of variables, this time to travelling wave coordinates of the form $\xi = x - c_n t$ and $\tau = t$. The resulting system ('*Outer system, rescaled x, non-zero c_n, travelling wave*') was solved to find the steady state solutions ($\partial/\partial\tau = 0$) by using the small parameter c_n to expand the solutions in terms of powers of c_n. We solved this final system correct to first order in c_n.

Since we have only found the steady state solutions in the outer regime, we cannot use matching techniques on the solution to get a result that is valid for all time, but we can estimate the domains over which we expect our approximations to be valid.

7.7.1 Domain of validity

In terms of the domain of validity of each of the solutions, we expect the solution of the '*Inner system*' to be valid over a time scale of approximately $\mathcal{O}(\epsilon)$ and we see (from Figure 7.6) that this is certainly the case: the percentage error between the approximate solution of the '*Inner system*' and the numerical solution of the '*Original system*' remains low throughout the region $t \in [0, 0.2]$ for $\epsilon = 0.05$.

7.8 Discussion

We began this chapter by reviewing the experimental evidence regarding the mechanism by which a gradient of FGF8 is established along the AP axis of vertebrate embryos. We then considered the RA/FGF8 feedback loop suggested by Diez and co-workers [11, 13] to construct a system of PDEs describing the evolution of RA and FGF8 concentrations along the AP axis. We made some simplifying approximations that allowed us to reduce this system of 9 PDEs to a system of 7 PDEs, 3 of which had their time derivative multiplied by a small parameter. The presence of this small parameter enabled us to make some asymptotic expansions and consider the system on an initial fast time scale and a subsequent longer time scale. We were able to solve the inner solution analytically, correct to first order in ϵ, but the equations describing the outer regime were intractable. We present some approximate results for the outer solution in Appendix E. We showed that the reduced system of equations describing the outer system was able to produce results that compared very favourably with the full system when solved numerically.

Variable	Solution correct to $\mathcal{O}(\epsilon)$
raldh2	$r(x,\sigma) = r^0(x,0) + \epsilon\left[A\sigma + r^1(x,0)\right]$
RALDH2	$R(x,\sigma) = \frac{1}{k_5} r^0(x,0) + \alpha e^{-k_5\sigma} + \epsilon\left[\frac{A}{k_5}\sigma + B + Ce^{-k_5\sigma}\right]$
Intracellular RA	$A_i(x,\sigma) = \frac{1}{k_5(k_8+k_9)} r^0(x,0) + \frac{1}{k_8+k_9-k_5}\alpha e^{-k_5\sigma} + \beta e^{-(k_8+k_9)\sigma}$ $+\epsilon\left[\frac{A\sigma}{k_5(k_8+k_9)} - D + \frac{C}{k_8+k_9-k_5}e^{-k_5\sigma} + Ee^{-(k_8+k_9)\sigma}\right]$
Extracellular RA	$A_e(x,\sigma) = A_e^0(x,0) + \epsilon\left[F + G\sigma - \frac{\beta}{k_8+k_9}e^{-(k_8+k_9)\sigma} - \frac{\alpha}{k_5(k_8+k_9-k_5)}e^{-k_5\sigma}\right]$
fgf8	$f(x,\sigma) = f^0(x,0) + \epsilon\left[H\sigma + f^1(x,0)\right]$
Intracellular FGF8	$F_i(x,\sigma) = \frac{1}{k_{15}+k_{16}} f^0(x,0) + \gamma e^{-(k_{15}+k_{16})\sigma} + \epsilon\left[\frac{H\sigma+f^1(x,0)}{k_{15}+k_{16}} - \frac{H}{(k_{15}+k_{16})^2} + Ie^{-(k_{15}+k_{16})\sigma}\right]$
Extracellular FGF8	$F_e(x,\sigma) = F_e^0(x,0) + \epsilon\left[J + K\sigma - \frac{\gamma}{k_{15}+k_{16}}e^{-(k_{15}+k_{16})\sigma}\right]$

Table 7.1: A summary of the inner solution for the '*Original system*' correct to $\mathcal{O}(\epsilon)$. Parameters α–γ are given by equations (7.79)–(7.81) and A–G are given by equations (7.96)–(7.106).

Variable	Steady state solution correct to $\mathcal{O}(1)$ in ϵ and $\mathcal{O}(c_n)$ in travelling wave coordinates.
raldh2	$r(\xi) = \begin{cases} \dfrac{k_1(1+A_{c0-}(\xi))}{k_3\left[1+\frac{k_{11}k_{19}}{k_{13}}+A_{c0-}(\xi)\right]} + c_n \left[\dfrac{k_1k_s\left[1+\frac{1}{k_3}+\frac{1}{k_{13}}\right]}{k_3[1+A_{c0-}(\xi)+k_s]^2}\dfrac{\partial A_{c0}}{\partial\xi} + \dfrac{k_1k_s}{k_3[1+A_{c0-}(\xi)+k_s]^2}A_{c1-}(\xi)\right] & \text{if} \quad \xi < 0 \\ \dfrac{k_1}{k_3} & \text{if} \quad \xi \geq 0 \end{cases}$
RALDH2	$R(\xi) = \begin{cases} \dfrac{k_1(1+A_{c0-}(\xi))}{k_3k_5\left[1+\frac{k_{11}k_{19}}{k_{13}}+A_{c0-}(\xi)\right]} + \dfrac{c_n}{k_5}\left[\dfrac{k_1k_s\left[1+\frac{1}{k_3}+\frac{1}{k_{13}}\right]}{k_3[1+A_{c0-}(\xi)+k_s]^2}\dfrac{\partial A_{c0}}{\partial\xi} + \dfrac{k_1k_s}{k_3[1+A_{c0-}(\xi)+k_s]^2}A_{c1-}(\xi)\right] & \text{if} \quad \xi < 0 \\ \dfrac{k_1}{k_3k_5} & \text{if} \quad \xi \geq 0 \end{cases}$
Intracellular RA	$A_i(\xi) = \begin{cases} \dfrac{k_1(1+A_{c0-}(\xi))}{k_3k_5(k_8+k_9)\left[1+\frac{k_{11}k_{19}}{k_{13}}+A_{c0-}(\xi)\right]} + \dfrac{c_n}{k_5(k_8+k_9)}\left[\dfrac{k_1k_s\left[1+\frac{1}{k_3}+\frac{1}{k_{13}}\right]}{k_3[1+A_{c0-}(\xi)+k_s]^2}\dfrac{\partial A_{c0}}{\partial\xi} + \dfrac{k_1k_s}{k_3[1+A_{c0-}(\xi)+k_s]^2}A_{c1-}(\xi)\right] & \text{if} \quad \xi < 0 \\ \dfrac{k_1}{k_3k_5(k_8+k_9)} & \text{if} \quad \xi \geq 0 \end{cases}$
Extracellular RA	$A_e(\xi) = \begin{cases} A_{c0-}(\xi) + c_nA_{c1-}(\xi) & \text{if} \quad \xi < 0 \\ \alpha_1e^{\sqrt{-k_{10}}\xi} + \dfrac{k_1k_{18}}{k_3k_{10}} + c_n\left[\alpha_3e^{-\sqrt{k_{10}}\xi} + \frac{1}{2}\alpha_1\xi e^{-\sqrt{k_{10}}\xi}\right] & \text{if} \quad \xi \geq 0 \end{cases}$
fgf8	$f(\xi) = \begin{cases} \dfrac{k_{11}}{k_{13}[1+A_{c0-}(\xi)]} + c_n\left[\dfrac{k_{11}}{k_{13}^2[1+A_{c0}(\xi)]^2}\dfrac{\partial A_{c0}}{\partial\xi} - \dfrac{k_{11}}{k_{13}[1+A_{c0}(\xi)]^2}A_{c1-}(\xi)\right] & \text{if} \quad \xi < 0 \\ & \text{if} \quad \xi < 0 \\ 0 & \text{if} \quad \xi \geq 0 \end{cases}$
Intracellular FGF8	$F_i(\xi) = \begin{cases} \dfrac{k_{11}}{k_{13}(k_{15}+k_{16})[1+A_{c0-}(\xi)]} + \dfrac{c_n}{k_{15}+k_{16}}\left[\dfrac{k_s\left[1+\frac{1}{k_{13}}\right]}{[1+A_{c0}(\xi)]^2}\dfrac{\partial A_{c0}}{\partial\xi} - \dfrac{k_s}{[1+A_{c0}(\xi)]^2}A_{c1-}(\xi)\right] & \text{if} \quad \xi < 0 \\ 0 & \text{if} \quad \xi \geq 0 \end{cases}$
Extracellular FGF8	$F_e(\xi) = \begin{cases} \dfrac{k_{11}k_{19}}{k_{13}[1+A_{c0-}(\xi)]} + c_n\left[\dfrac{k_s\left[1+\frac{1}{k_{13}}\right]}{[1+A_{c0}(\xi)]^2}\dfrac{\partial A_{c0}}{\partial\xi} - \dfrac{k_s}{[1+A_{c0}(\xi)]^2}A_{c1-}(\xi)\right] 0 & \text{if} \quad \xi \geq 0 \end{cases}$

Table 7.2: A summary of the steady state outer solution for the '*Original system*' correct to $\mathcal{O}(1)$ in ϵ and $\mathcal{O}(c_n)$ in travelling wave coordinates.

Our model was able to mimic the results seen *in vivo*; opposing gradients of FGF8 and RA travelled down the AP axis with constant speed. We expect the model to be reasonably accurate biologically and it would be interesting to have experimental estimates of the parameters involved in order to test the model further. Throughout this chapter, we have only been able to make crude estimations of the magnitude of the parameters involved.

The effects of down-regulation of RA on somite formation have been studied via the creation of Vitamin A deficient quail embryos [26] and have resulted in embryos with (i) somites of approximately half their normal size (although the total number of somites remains constant), (ii) increased apoptosis in the lateral halves, (iii) disrupted gene expression (although the period of cycling genes such as *c-hairy-1* and *l-fng* are not affected).

Our model could account for this in one of two ways: if the rate of axis extension was decreased in Vitamin A deficient embryos (which is feasible since the total length of the axis is decreased) then the wavefront of FGF8 would move more slowly down the AP axis. If the segmentation clock remains unaffected, which seems to be the case given that cycling times of *c-hairy-1* and *l-fng* remain unchanged, then the result predicted by our model would be smaller somites. The other manner in which our model could account for this is if the rate of axis extension remains the same as in a control case, but increased apoptosis of cells leads to smaller somites. It could, of course, be a combination of the two effects.

Apart from accurate estimation of the parameters involved, there are many other intricacies of the model that need to be explored experimentally: is fgf8 self-promoting? How do the rates of diffusion of RA and FGF8 differ? Why is transcription of *fgf8* limited to the node region of the embryo? Experimental investigation of these factors would allow us to modify further the model presented in this chapter and produce a more accurate overview of the RA/FGF8 feedback mechanism along the PSM.

There is however, little further insight that can be gained from this model. The sheer number of equations, along with their coupling and non-linearities, are not conducive to analytical solution and it is very hard to compare the results produced by this model with those produced by the model in Chapter 4 and Chapter 5. Further work could investigate the results gained when perturbing FGF8 expression (as in previous chapters) but this would all have to be conducted numerically. We must therefore ask whether it is prudent to consider such a model when mathematically simpler models allow us to gain much further insight into somite formation.

In the following chapter, we build a much simpler model for the formation of opposing gradients of RA and FGF8 along the AP axis: we consider only concentrations of generic RA and FGF8 substances. Such a model provides much more scope for analytical investigation and we ask whether such a model can provide more insight than the full system: we investigate whether we can find travelling waves along the AP axis (without restricting production of FGF8 to the node), with the speed determined by parameters governing the interaction of RA and FGF8 rather than the rate at which the AP axis is extending.

Chapter 8

A Coupled FGF8/RA Gradient Model

In the previous chapter, we considered a detailed model for the gradient of FGF8 along the AP axis. The model consisted of a system of seven coupled, non-linear PDEs in time and one spatial dimension, and as a result was difficult to analyse. In this chapter we consider a simpler model for the opposing FGF8 and RA gradients: whereas previously we considered *raldh2*, RALDH2, intracellular RA and extracellular RA, which all behaved in a qualitatively similar manner, we now consider only a generic RA substance. Similarly, where we previously considered each of *fgf8*, intracellular FGF8 and extracellular FGF8, we now consider only a generic fgf8 substance. We wish to construct a model that can display the following behaviour: fgf8 and RA must be mutually inhibitory and the feedback mechanism should result in the possibility of opposing gradients of RA and fgf8 travelling along the spatial axis.

8.1 General model

The general model that we begin by considering is of the form:

$$\frac{\partial A}{\partial t} = \frac{r_A A}{(\mu_A + F)(\gamma_A + A^{n_a})} - \lambda_A A + D_A \frac{\partial^2 A}{\partial x^2}, \tag{8.1}$$

$$\frac{\partial F}{\partial t} = \frac{r_F F}{(\mu_F + A)(\gamma_F + F^{n_f})} - \lambda_F F + D_F \frac{\partial^2 F}{\partial x^2}, \tag{8.2}$$

where A represents the concentration of RA, F represents the concentration of fgf8 and r_A, r_F, μ_A, μ_F, λ_A, λ_F, n_a, n_f, D_A and D_F are positive constants. Both A and F are self-regulatory, inhibit production of the other substance and undergo linear decay.

8.1.1 Non-dimensionalisation

We non-dimensionalise by letting

$$A = [A]a, \quad F = [F]f, \quad t = \frac{r_A}{[F]\gamma_A}\tau, \quad x = \sqrt{\frac{D_A r_A}{[F]\gamma_A}}y, \quad \mu_A = \frac{\mu_A}{[F]}, \quad \mu_F = \frac{\mu_F}{[A]},$$

$$\lambda_a = \frac{\lambda_A r_A}{[F]\gamma_A}, \quad \lambda_a = \frac{\lambda_F r_A}{[F]\gamma_A}, \quad r = \frac{r_F r_A}{\gamma_A\gamma_F[A][F]}, \quad D = \frac{D_F}{D_A}, \tag{8.3}$$

where $[A]^{n_a} = \gamma_A$ and $[F]^{n_f} = \gamma_F$. The resulting non-dimensional equations are

$$\frac{\partial a}{\partial \tau} = \frac{a}{(\mu_a + f)(1 + a^{n_a})} - \lambda_a a + \frac{\partial^2 a}{\partial y^2}, \tag{8.4}$$

$$\frac{\partial f}{\partial \tau} = \frac{r}{(\mu_f + a)(1 + f^{n_f})} - \lambda_f f + D\frac{\partial^2 f}{\partial y^2}. \tag{8.5}$$

We take a series of approaches in analysing this model. Firstly we will assume that $n_a = n_f = 1$ and under this assumption we will proceed with two lines of investigation: we will begin with simplifying the reaction kinetics by expanding the quotients and ignoring higher order terms in a and f and then we will use this basis to inform our study of the non-simplified model. Finally we will move to consider the case in which n_a and n_f are not necessarily equal to unity. The results from the previous models will provide us with much useful insight into this more complicated case.

8.2 Simplification of the model

As mentioned above, we begin by making two main simplifying assumptions: firstly that $n_a = n_f = 1$ and secondly that we can expand the quotients of equations (8.4) and (8.5) to give:

$$\frac{\partial a}{\partial \tau} = \frac{a}{\mu_a}\left[1 - \frac{f}{\mu_a} - \ldots\right]\{1 - a - \ldots\} + \frac{\partial^2 a}{\partial y^2}, \tag{8.6}$$

$$\frac{\partial f}{\partial \tau} = \frac{rf}{\mu_f}\left[1 - \frac{a}{\mu_f} - \ldots\right]\{1 - f - \ldots\} + D\frac{\partial^2 f}{\partial y^2}. \tag{8.7}$$

Ignoring terms of cubic order and higher we have a system of two competing species:

$$\frac{\partial a}{\partial \tau} = \hat{r}_a a\left(1 - \frac{a}{\hat{r}_a\mu_a} - \frac{f}{\hat{r}_a\mu_a^2}\right) + \frac{\partial^2 a}{\partial y^2}, \tag{8.8}$$

$$\frac{\partial f}{\partial \tau} = \hat{r}_f f\left(1 - \frac{a}{\hat{r}_f\mu_f/r} - \frac{a}{\hat{r}_f\mu_f^2/r}\right) + D\frac{\partial^2 f}{\partial y^2}. \tag{8.9}$$

where

$$\hat{r}_a = 1/\mu_a = \lambda_a \quad \text{and} \quad \hat{r}_f = r/\mu_f - \lambda_f. \tag{8.10}$$

Note that we shall require $\hat{r}_a, \hat{r}_f > 0$ so that each species grows in a bounded manner (i.e. for large a, f that $\frac{\partial a}{\partial \tau}, \frac{\partial f}{\partial \tau} \to 0$).

Non-dimensionalising once more gives the standard "2-species competition model":

$$\frac{\partial \hat{a}}{\partial T} = \hat{a}\left(1 - \hat{a} - \hat{\lambda}_a \hat{f}\right) + \frac{\partial^2 \hat{a}}{\partial z^2}, \tag{8.11}$$

$$\frac{\partial \hat{f}}{\partial T} = \hat{r}\hat{f}\left(1 - \hat{f} - \hat{\lambda}_f \hat{a}\right) + D\frac{\partial^2 \hat{f}}{\partial z^2}. \tag{8.12}$$

8.3 2-species competition model

In this section we will analyse the standard 2-species competition model in more detail. We drop the ˆ's for notational simplicity so that the system becomes:

$$\frac{\partial a}{\partial T} = a\left(1 - a - \lambda_a f\right) + \frac{\partial^2 a}{\partial z^2}, \tag{8.13}$$

$$\frac{\partial f}{\partial T} = rf\left(1 - f - \lambda_f a\right) + D\frac{\partial^2 f}{\partial z^2}. \tag{8.14}$$

Firstly we will use phase plane analysis to determine the critical points of the system and their stability, and secondly, we will move to a travelling wave coordinate system to see if the system can display travelling wavefront solutions. The analysis is standard (see, for example [34, 35]).

8.3.1 Phase plane analysis

The system given by equations (8.13) and (8.14) has spatially uniform steady states which satisfy

$$g(a, f) = a(1 - a - \lambda_a f) = 0, \tag{8.15}$$

$$h(a, f) = rf(1 - f - \lambda_f a) = 0. \tag{8.16}$$

Depending on the values of λ_a and λ_f there are three or four possible steady states:

$$(a, f) = \quad (0, 0), \quad (1, 0), \quad (0, 1), \quad \text{and} \quad (a^*, f^*) = \left(\frac{1 - \lambda_a}{1 - \lambda_a\lambda_f}, \frac{1 - \lambda_f}{1 - \lambda_a\lambda_f}\right). \tag{8.17}$$

For the final steady state we require that either $\lambda_a, \lambda_f > 1$ or $\lambda_a, \lambda_f < 1$.

8.3.1.1 Linear stability analysis

To analyse the linear stability of the system, we consider the eigenvalues of the matrix A evaluated at each of the steady states, where

$$A = \begin{pmatrix} \frac{\partial g}{\partial a} & \frac{\partial g}{\partial f} \\ \frac{\partial h}{\partial a} & \frac{\partial h}{\partial f} \end{pmatrix} = \begin{pmatrix} 1 - 2a - \lambda_a f & -\lambda_a a \\ -\lambda_f f & r(1 - 2f - \lambda_f a) \end{pmatrix}. \tag{8.18}$$

The steady state $(0, 0)$**:** The eigenvalues of A are given by $\alpha = 1$ and $\alpha = r$ and the steady state is therefore an unstable node.

The steady state $(1, 0)$**:** The eigenvalues of A are given by $\alpha = -1$ and $\alpha = r(1 - \lambda_f)$ and the steady state is therefore a stable node when $\lambda_f > 1$ and a saddle point otherwise.

The steady state $(0, 1)$**:** The eigenvalues of A are given by $\alpha = -r$ and $\alpha = (1 - \lambda_a)$ and the steady state is therefore a stable node when $\lambda_a > 1$ and a saddle point otherwise.

The steady state (a^*, f^*)**:** The eigenvalues of A are given by the equation

$$\alpha^2 + (a^* + rf^*)\alpha + ra^* f^*(1 - \lambda_a \lambda_f) = 0. \tag{8.19}$$

Using Theorem B.1.1 (see appendix for more details) we can therefore see that (a^*, f^*) is a stable node if $1 - \lambda_a \lambda_f > 0$, and a saddle otherwise. Furthermore, we can prove that (a^*, f^*) is a globally stable steady state and we do this by considering the vector of derivatives $(da/dT, df/dT)$ along any closed rectangle containing the steady state.

Figure 8.1 illustrates such a rectangle in the phase plane of Case 4. On the vertical side with smaller a we have $da/dT > 0$ and on the vertical side with larger a we have $da/dT < 0$. Similarly, on the horizontal side with smaller f we have $df/dT > 0$ and on the other horizontal side we have $df/dT < 0$. Hence on any rectangle surrounding the steady state, the vector of derivatives points into the rectangle, or along the boundary of the rectangle and so we can conclude that the steady state must be globally stable.

8.3.1.2 Phase planes

Figure 8.2 shows the phase plane and trajectories for each of the possible cases of the 2-species competition model. In Case 1 there are two non-zero steady states, only one of which, $(0, 1)$, is linearly stable. Similarly, in Case 2 there are two non-zero steady states, but the linearly stable steady state has now switched to $(1, 0)$. In the final two cases there is another non-zero steady state with both a and f non-zero. In Case 3 this is a saddle point; this results in a separatrix through (a^*, f^*) and trajectories will tend to either $(0, 1)$ or $(1, 0)$ depending on the initial conditions. In Case 4, the steady state (a^*, f^*) is globally stable and all trajectories tend to this state.

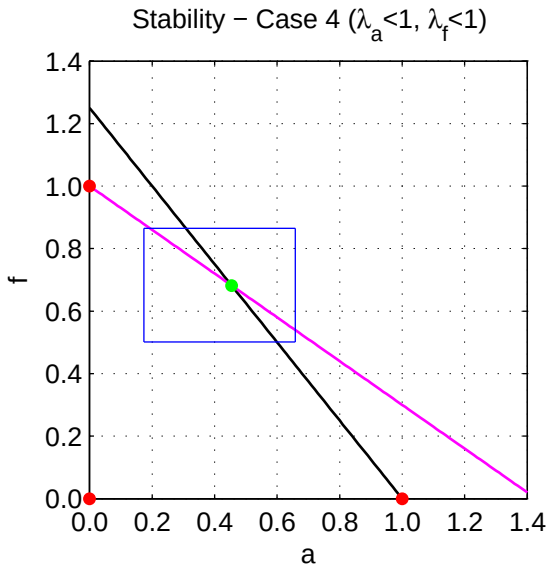


Figure 8.1: The phase planes for Case 4 of the 2-species competition model. Stable steady states are indicated by green dots and unstable steady states by red dots. The black line indicates the non-zero part of the a null cline and the pink line indicates the non-zero part of the f null cline. Parameters are as follows: $\lambda_a = 0.7$, $\lambda_f = 0.8$ and $r = 2.0$.

8.3.2 Travelling wave analysis

In Case 2, there is a stable steady state with high a and low f and an unstable steady state with low a and high f. Similarly in Case 4. From this we see that in either case, there exists the possibility of a trajectory connecting a region of high f/low a concentration to a region of low f/high a concentration and hence that there may be travelling wavefront solutions between the two steady states.

If such a travelling wavefront exists then it can be written in the form

$$\boldsymbol{u}(z,T) = \boldsymbol{U}(\xi), \quad \text{where} \quad \xi = z - cT \quad \text{and} \quad \boldsymbol{u} = \begin{pmatrix} a \\ f \end{pmatrix}, \tag{8.20}$$

where c is the speed of the wavefront. We note that in taking $-cT$ in the definition of ξ we will have reversed the stability of the steady states. This will be an important point to note in future analysis. We wish to find a solution such that either

$$\text{Case 2}: \quad a(-\infty) = 1, \quad a(\infty) = 0, \quad f(-\infty) = 0, \quad f(\infty) = 1, \tag{8.21}$$

or

$$\text{Case 4}: \quad a(-\infty) = a^*, \quad a(\infty) = 0, \quad f(-\infty) = f^*, \quad f(\infty) = 1. \tag{8.22}$$

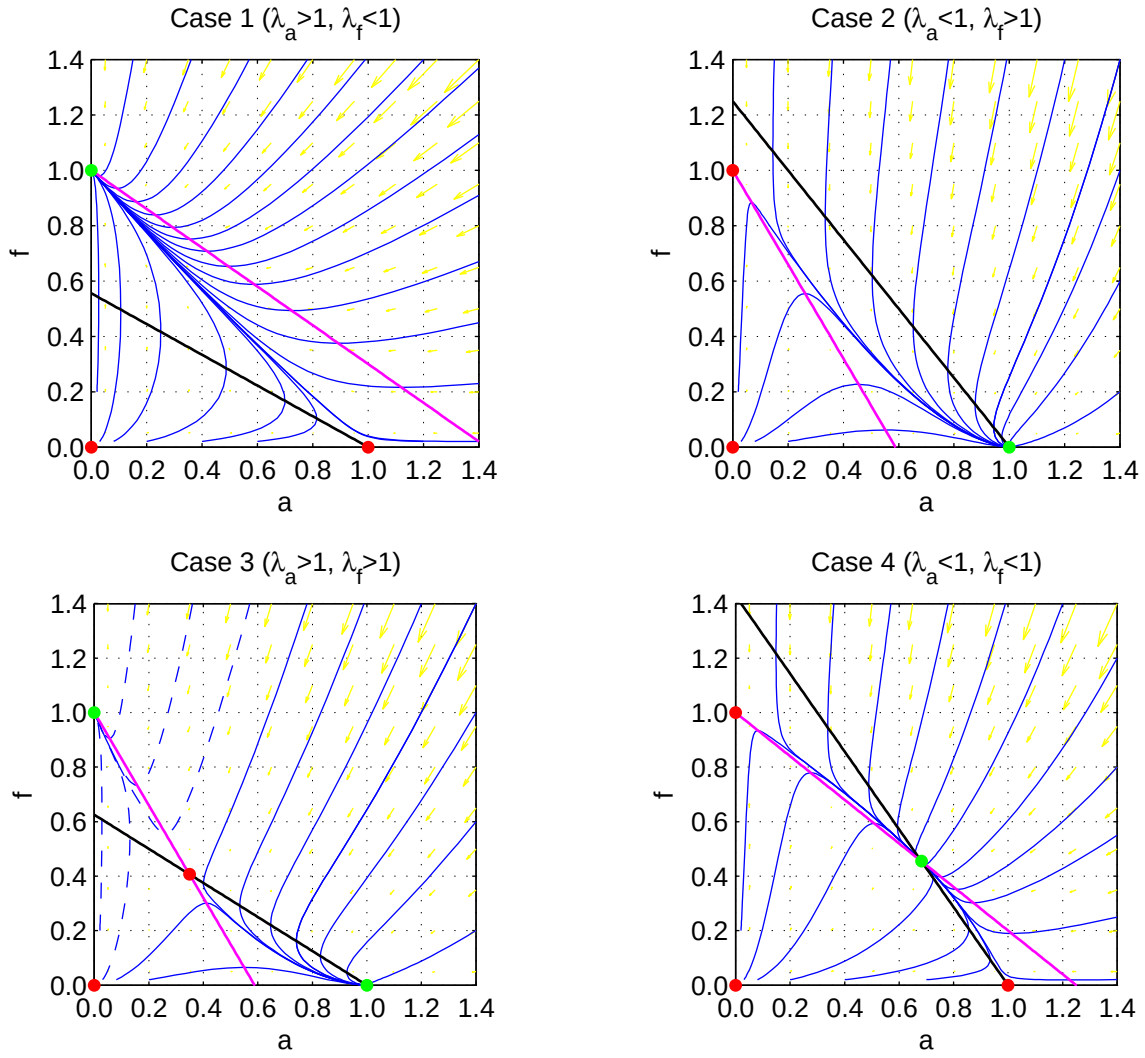


Figure 8.2: The phase planes for the 2-species competition model. Stable steady states are indicated by green dots, unstable steady states by red dots, the trajectories by blue lines and the velocity field by yellow arrows. The black line indicates the non-zero part of the a nullcline and the pink line indicates the non-zero part of the f nullcline. In Case 1 there is a stable node at $(0, 1)$ and a saddle at $(1, 0)$. The reverse is true in Case 2. Cases 3 and 4 have an extra steady state in which both a and f are non-zero. In Case 3 this is a saddle and trajectories tend to one of the stable nodes at $(1, 0)$ and $(0, 1)$. Trajectories tending to the first of these are indicated by dashed lines. In Case 4 the steady state (a^*, f^*) is stable and all trajectories tend to this point. Parameters are as follows: Case 1: $\lambda_a = 1.8$, $\lambda_f = 0.7$, $r = 2.0$; Case 2: $\lambda_a = 0.7$, $\lambda_f = 1.8$, $r = 2.0$; Case 3: $\lambda_a = 1.6$, $\lambda_f = 1.7$, $r = 2.0$; Case 4: $\lambda_a = 0.7$, $\lambda_f = 0.8$, $r = 2.0$.

Letting $'$ denote $d/d\xi$, the system given by equations (8.13) and (8.14) can be written

$$0 = a'' + ca' + a(1 - a - \lambda_a f), \tag{8.23}$$
$$0 = Df'' + cf' + rf(1 - f - \lambda_f a). \tag{8.24}$$

To simplify further analysis, we will assume that $D \ll 1$ (see Chapter 7 for justification) so that the term Df'' can be ignored.

Letting $b = a'$, we can convert the above to a system of three first order ODEs:

$$a' = b, \tag{8.25}$$
$$b' = -cb - a(1 - a - \lambda_a f), \tag{8.26}$$
$$f' = -\frac{rf}{c}(1 - f - \lambda_f a). \tag{8.27}$$

Once more (depending on the parameters), the system has up to four steady states:

$$(a, b, f) = \quad (0,0,0), \quad (1,0,0), \quad (0,0,1), \quad \text{and} \quad (a^*, 0, f^*). \tag{8.28}$$

Linear stability can be investigated by considering the eigenvalues of the matrix A evaluated at the steady states where:

$$A = \begin{pmatrix} 0 & 1 & 0 \\ -1 + 2a + \lambda_a f & -c & \lambda_a a \\ r\lambda_f f/c & 0 & r(-1 + 2f + \lambda_f a)/c \end{pmatrix}. \tag{8.29}$$

The steady state $(0,0,0)$**:** The eigenvalues of A evaluated at $(0,0,0)$ are

$$\alpha = -\frac{r}{c} \quad \text{and} \quad \frac{-c \pm \sqrt{c^2 - 4}}{2}, \tag{8.30}$$

which all have negative real parts.

The steady state $(1,0,0)$**:** The eigenvalues of A evaluated at $(1,0,0)$ are

$$\alpha = \frac{r}{c}(\lambda_f - 1) \quad \text{and} \quad \frac{-c \pm \sqrt{c^2 + 4}}{2}. \tag{8.31}$$

In Case 2 this results in two positive eigenvalues and one negative eigenvalue so (as required for a travelling wavefront) there is an unstable manifold associated with this steady state.

The steady state $(0,0,1)$**:** The eigenvalues of A evaluated at $(0,0,1)$ are

$$\alpha = \frac{r}{c} \quad \text{and} \quad \frac{-c \pm \sqrt{c^2 + 4(\lambda_a - 1)}}{2}. \tag{8.32}$$

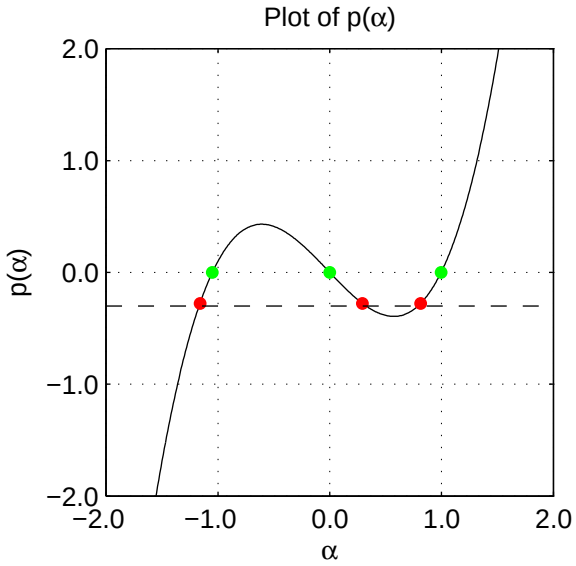


Figure 8.3: A plot of the polynomial $\bar{p}(\alpha)$ showing the roots of $\bar{p}(\alpha) = 0$ (green dots) and the roots of $p(\alpha) = 0$ (red dots). The dashed black line indicates the value of $-p(0)$. Parameters are as follows: $\lambda_a = 0.5$, $\lambda_f = 0.7$, $r = 0.6$ and $c = 0.5$.

In both Case 2 and Case 4 this results in two negative eigenvalues and one positive eigenvalue and so there is a stable manifold associated with this steady state.

The steady state $(a^*, 0, f^*)$**:** The eigenvalues of A evaluated at $(a^*, 0, f^*)$ are given by the equation:

$$p(\alpha) = \alpha^3 + \left(c - \frac{rf^*}{c}\right)\alpha^2 - (rf^* + a^*)\alpha + \frac{ra^*f^*}{c}(1 - \lambda_a\lambda_f). \tag{8.33}$$

We can gain information about the roots of $p(\alpha)$ by considering the roots of $\bar{p}(\alpha) = p(\alpha) - p(0)$: the roots of $\bar{p}(\alpha)$ are given by

$$\alpha = 0 \quad \text{and} \quad \alpha_\pm = \frac{1}{2}\left[\left(c - \frac{rf^*}{c}\right) \pm \sqrt{\left(c - \frac{rf^*}{c}\right)^2 + 4(ra^* + f^*)}\right], \tag{8.34}$$

hence we see that $\alpha_- < 0$ and $\alpha_+ > 0$ (say). The roots of $p(\alpha) = 0$ are the solutions of

$$\bar{p}(\alpha) = -p(0) = -\frac{ra^*f^*}{c}(1 - \lambda_a\lambda_f). \tag{8.35}$$

In Case 4, the RHS of the above equation is negative. Hence using Figure 8.3 we see that p must have one negative root and two roots with positive real parts.

We also note that to ensure non-oscillatory behaviour as we move away from the steady state

(a^*, f^*) (and hence a monotonic gradient in f), we must have purely real roots of equation (8.33), which requires that

$$p(\alpha_{max}) \geq 0 \quad \text{and} \quad p(\alpha_{min}) \leq 0, \tag{8.36}$$

where α_{max} and α_{min} are the points at which the local maximum and local minimum of p occur and are given by

$$\alpha_{max,min} = \frac{1}{3}\left[\left(c - \frac{rf^*}{c}\right) \mp \sqrt{\left(c - \frac{rf^*}{c}\right)^2 + 3(ra^* + f^*)}\right]. \tag{8.37}$$

The first of the conditions given by equation (8.36) always holds in Case 4 by continuity of p, since $p(\alpha) \to -\infty$ as $\alpha \to -\infty$, $p(0) > 0$ and $\alpha_{max} < 0$.

To recap, in Case 2 we have a stable manifold at $(1, 0, 0)$ and an unstable manifold at $(0, 0, 1)$ and in Case 4 we have a stable manifold at $(1, 0, 0)$ and an unstable manifold at $(a^*, 0, f^*)$. In either case, we have the possibility of a trajectory lying entirely in the region $a \geq 0$, $f \geq 0$ connecting the steady state with an unstable manifold to the steady state with a stable manifold. These are sufficient conditions for a travelling wavefront solution.

Linearising about the leading edge of the wave, where we have, approximately, $(a, b, f) = (0, 0, 1)$, gives a minimum wave speed: we require a non-oscillatory approach to the steady state since otherwise a would become negative. The condition to ensure this is that all the eigenvalues are purely real or,

$$c_{min} = 2\sqrt{1 - \lambda_a}. \tag{8.38}$$

8.3.3 Numerical solution

As in previous chapters, we solved the system of equations given by (8.13) and (8.14) numerically using the NAG library routine D03PCF. We approximated the infinite domain by using zero flux boundary conditions on a finite domain and used initial conditions of the form

$$\text{Case 2:} \quad a(z,0) = \begin{cases} 1 & z \leq 0, \\ 0 & z > 0, \end{cases} \qquad f(z,0) = \begin{cases} 0 & z \leq 0, \\ 1 & z > 0, \end{cases} \tag{8.39}$$

and

$$\text{Case 4:} \quad a(z,0) = \begin{cases} a^* & z \leq 0, \\ 0 & z > 0, \end{cases} \qquad f(z,0) = \begin{cases} f^* & z \leq 0, \\ 1 & z > 0. \end{cases} \tag{8.40}$$

Figures 8.4 and 8.5 show the results of numerical solution of the 2-species competition model. Figure 8.4 shows simulation in a parameter regime consistent with Case 2 and Figure 8.5 shows simulation in a parameter regime consistent with Case 4. With the initial conditions given above, each case exhibits the travelling wave behaviour predicted by earlier analysis. We note that lineari-

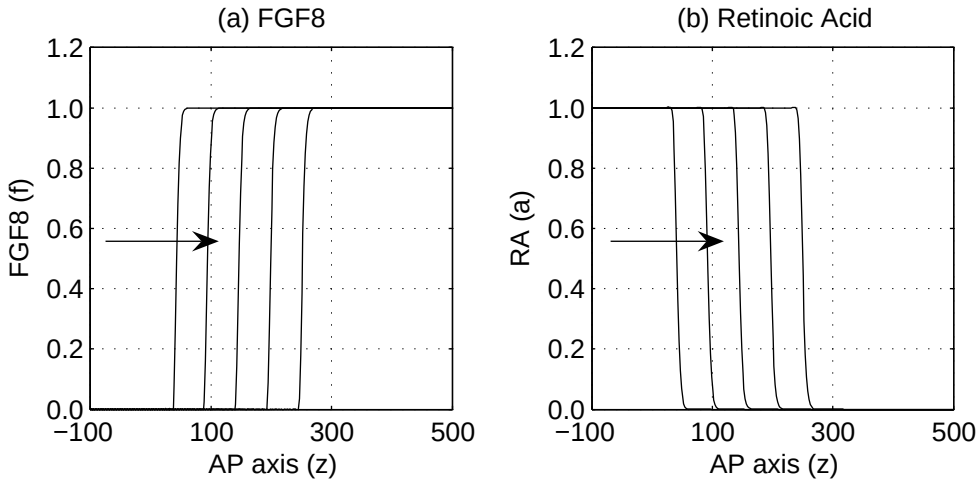


Figure 8.4: Case 2 - A plot of the numerical solution for the 2-species competition model over a series of time steps. We see progression of travelling waves of fgf8 and RA along the AP axis as predicted by previous analysis. The solutions are plotted for $t = 30, 60, 90, 120, 150$. Parameters are as follows: $\lambda_a = 0.6$, $\lambda_f = 1.5$, $r = 10.0$ and $D = 0.1$.

sation about the leading edge of the wave predicted a minimum wave speed of $c_{min} = 2\sqrt{1-\lambda_a}$ and this result is displayed in our models: with the initial conditions chosen, we expect the solution to evolve to a wave with minimum wave speed. In Case 2 we see that the wave progresses over a smaller distance (i.e. has smaller wave speed) than in Case 4 and this is consistent with the result that λ_a is larger in Case 2 than in Case 4.

8.4 The general model with $n_a = 1$ and $n_f = 1$

We now turn our attention to the original model with the assumption that $n_a = 1$ and $n_f = 1$. The governing equations become

$$\frac{\partial a}{\partial \tau} = \frac{a}{(\mu_a + f)(1+a)} - \lambda_a a + \frac{\partial^2 a}{\partial y^2}, \tag{8.41}$$

$$\frac{\partial f}{\partial \tau} = \frac{r}{(\mu_f + a)(1+f)} - \lambda_f f + D\frac{\partial^2 f}{\partial y^2}. \tag{8.42}$$

8.4.1 Phase plane analysis

The system given by equations (8.41) and (8.42) has spatially uniform steady states which satisfy

$$g(a, f) = \frac{a}{(\mu_a + f)(1+a)} - \lambda_a a = 0, \tag{8.43}$$

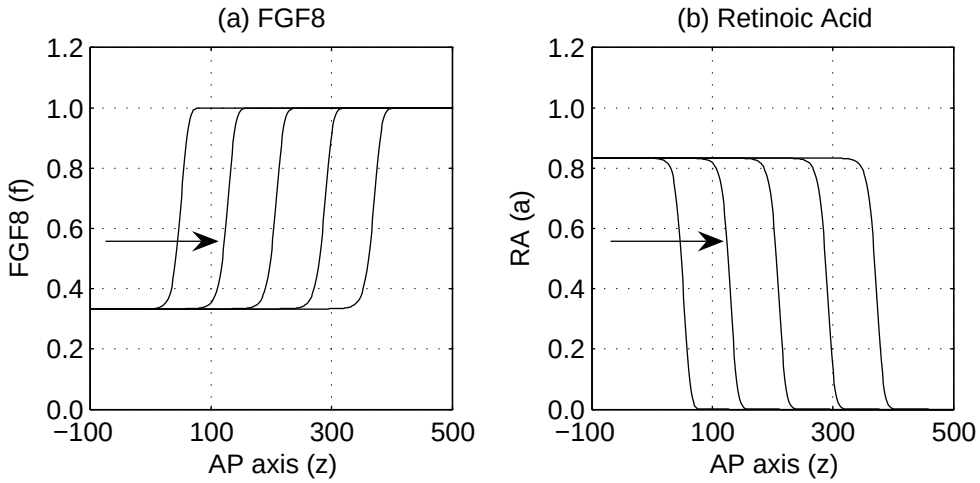


Figure 8.5: Case 4 - A plot of the numerical solution for the 2-species competition model over a series of time steps. We see progression of travelling waves of fgf8 and RA along the AP axis as predicted by previous analysis. The solutions are plotted for $t = 30, 60, 90, 120, 150$. Parameters are as follows: $\lambda_a = 0.5$, $\lambda_f = 0.8$, $r = 2.0$ and $D = 0.1$.

$$h(a, f) = \frac{r}{(\mu_f + a)(1 + f)} - \lambda_f f = 0. \tag{8.44}$$

The nullclines a and f nullclines, given by equations (8.43) and (8.44) respectively, are plotted in Figure 8.6. At this point, we can see the similarities between the nullclines of this model and the 2-species competition model: the a nullclines are either $a = 0$ or

$$f = \frac{1}{\lambda_a(1 + a)} - \mu_a, \tag{8.45}$$

and the f nullclines are either $f = 0$ or

$$f = \frac{r}{\lambda_f(\mu_f + a)} - 1. \tag{8.46}$$

The phase planes for this model look qualitatively similar to those for the 2-species competition model: in this model the nullclines are concave curves that intersect the a and f axes on the positive half lines whereas in the 2-species competition model, the nullclines are straight lines which intersect the a and f axes on the positive half lines. The manner of their intersection (and hence the behaviour of the nullclines at the steady states) is very similar. Accordingly, we expect that the resulting behaviour displayed by this more general model will bear many similarities to the competition model. This forms a helpful guide in the following analysis.

It is important to note that we must ensure that each of the non-zero parts of the nullclines intersect the a and f axes on the positive half lines so that the steady states are feasible (i.e. positive). The

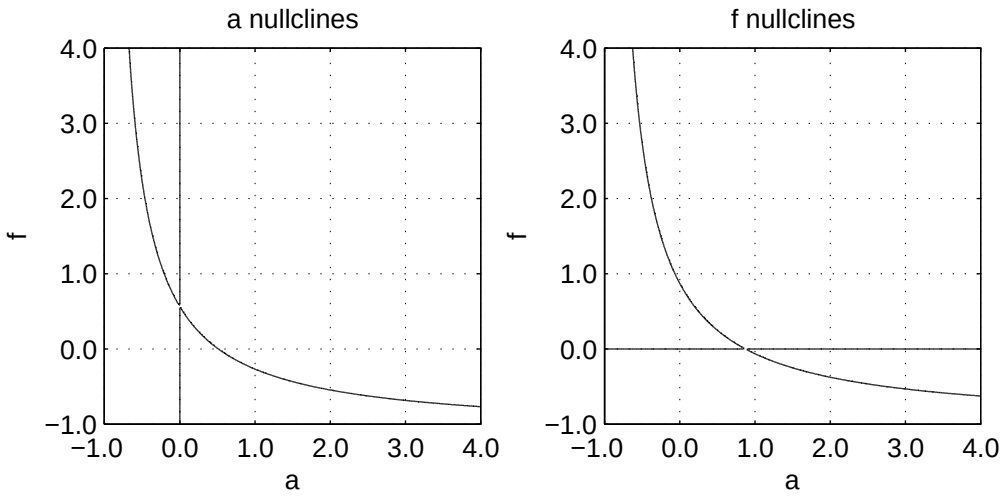


Figure 8.6: The nullclines for the general model with $n_a, n_f = 1$. The a and f nullclines are specified by equations (8.43) and (8.44) respectively. Parameters are as follows: $\lambda_a = 0.6$, $\lambda_f = 0.8$, $\mu_a = 1.0$, $\mu_f = 1.1$, $r = 1.5$ and $D = 0.1$.

conditions for this are that

$$\frac{1}{\lambda_a \mu_a} - 1 > 0 \quad \text{and} \quad \frac{r}{\lambda_f \mu_f} - 1 > 0. \tag{8.47}$$

These are the same conditions that we required for simplification of the model to the 2-species competition model format in Section 8.2 (see also equation (8.10)).

Depending on the values of λ_a, λ_f, μ_a, μ_f and r, there are three or four possible steady states:

$$(a, f) = \quad (0,0), \quad \left(\frac{1}{\lambda_a \mu_a} - 1, 0\right), \quad \left(0, \frac{r}{\lambda_f \mu_f} - 1\right), \quad \text{and} \quad (a^*, f^*), \tag{8.48}$$

where f^* satisfies the quadratic

$$\lambda_a \lambda_f (1 - \mu_f)(1 + f^*)(\mu_a + f^*) + r\lambda_a(\mu_a + f^*) - \lambda_f(1 + f^*) = 0, \tag{8.49}$$

and

$$a^* = \frac{1}{\lambda_a(\mu_a + f^*)} - 1. \tag{8.50}$$

8.4.1.1 Linear stability analysis

To analyse the linear stability of the system, we consider the eigenvalues of the matrix A evaluated at each of the steady states, where

$$A = \begin{pmatrix} 1/[(\mu_a + f)(1+a)^2] - \lambda_a & -a/[(\mu_a + f)^2(1+a)] \\ -rf/[(\mu_f + a)^2(1+f)] & r/[(\mu_f + a)(1+f)^2] - \lambda_f \end{pmatrix}. \tag{8.51}$$

The steady state $(0,0)$**:** The eigenvalues of A are given by

$$\alpha = \frac{1}{\mu_a} - \lambda_a > 0 \quad \text{and} \quad \alpha = \frac{r}{\mu_f} - \lambda_f > 0, \tag{8.52}$$

and the steady state is therefore an unstable node.

The steady state $\left(\frac{1}{\lambda_a \mu_a} - 1, 0\right)$**:** The eigenvalues of A are given by

$$\alpha = \lambda_a(\lambda_a \mu_a - 1) < 0 \quad \text{and} \quad \alpha = \frac{\lambda_f}{\mu_f + \frac{1}{\lambda_a \mu_a} - 1}\left(\frac{r}{\lambda_f} - \mu_f - \frac{1}{\lambda_a \mu_a} - 1\right). \tag{8.53}$$

The first two terms in the second eigenvalue give the intersection of the f nullcline with $f = 0$ and the second two terms give the intersection of the a nullcline with $f = 0$. Using Figure 8.7 we can see that in Case 2 and Case 3 this point is therefore a stable node and in Case 1 and Case 4 it is a saddle point.

The steady state $\left(0, \frac{r}{\lambda_f \mu_f} - 1\right)$**:** The eigenvalues of A are given by

$$\alpha = \lambda_f\left(\frac{\lambda_f \mu_f}{r} - 1\right) < 0 \quad \text{and} \quad \alpha = \frac{\lambda_a}{\mu_a + \frac{r}{\lambda_f \mu_f} - 1}\left(\frac{1}{\lambda_a} - \mu_a - \frac{r}{\lambda_f \mu_f} - 1\right). \tag{8.54}$$

The first two terms in the second eigenvalue give the intersection of the a nullcline with $a = 0$ and the second two terms give the intersection of the f nullcline with $a = 0$. Using Figure 8.7 we can therefore see that in Case 1 and Case 3 this point is a stable node and in Case 2 and Case 4 it is a saddle point.

The steady state (a^*, f^*)**:** We take a slightly different approach to find the eigenvalues at this steady state. We know that

$$A = \begin{pmatrix} \frac{\partial g}{\partial a} & \frac{\partial g}{\partial f} \\ \frac{\partial h}{\partial a} & \frac{\partial h}{\partial f} \end{pmatrix}\Bigg|_{(a^*, f^*),} \tag{8.55}$$

and therefore the eigenvalues of A are determined by solving the equation

$$\alpha^2 - (g_a + h_f)\alpha + (g_a h_f - h_a g_f) = 0, \tag{8.56}$$

where g, h represent the a and f nullclines and are given by equations (8.43) and (8.43) respectively, and the partial derivatives are evaluated at the steady state. We have

$$g_a + h_f = \lambda_a \left(\frac{1}{1+a^*} - 1 \right) + \lambda_f \left(\frac{1}{1+f^*} - 1 \right) < 0, \tag{8.57}$$

since both a^* and f^* are positive. We can determine the sign of the constant term in the eigenvalue equation by considering the manner in which the nullclines intersect each other at the steady state.

In Case 3 we have

$$\left| \frac{df}{da} \right|_{h=0} > \left| \frac{df}{da} \right|_{g=0} \Rightarrow \left| \frac{h_a}{h_f} \right|_{(a^*,f^*)} > \left| \frac{g_a}{g_f} \right|_{(a^*,f^*)} \Rightarrow [g_a h_f - h_a g_f]\Big|_{(a^*,f^*)} < 0. \tag{8.58}$$

The opposite holds in Case 4:

$$\left| \frac{df}{da} \right|_{h=0} < \left| \frac{df}{da} \right|_{g=0} \Rightarrow \left| \frac{h_a}{h_f} \right|_{(a^*,f^*)} < \left| \frac{g_a}{g_f} \right|_{(a^*,f^*)} \Rightarrow [g_a h_f - h_a g_f]\Big|_{(a^*,f^*)} > 0. \tag{8.59}$$

Hence using the method described in Theorem B.1.1 (see appendix for more details) we see that in Case 3, (a^*, f^*) is a saddle point whilst in Case 4 it is either a stable node or spiral. To ensure that (a^*, f^*) is a stable node and hence that we have monotonic convergence to the steady state we must have

$$(g_a + h_f)^2 - 4(g_a h_f - h_a g_f) > 0. \tag{8.60}$$

Figure 8.7 shows plots of the four possible phase planes with the nullclines, steady states and the trajectories clearly marked.

8.4.2 Travelling wave analysis

From the previous phase plane analysis, we see that in Case 2 there is the possibility of a trajectory connecting

$$\left(0, \frac{r}{\lambda_f \mu_f} - 1 \right) \to \left(\frac{1}{\lambda_a \mu_a} - 1, 0 \right), \tag{8.61}$$

and in Case 4 there is the possibility of a trajectory connecting

$$\left(0, \frac{r}{\lambda_f \mu_f} - 1 \right) \to (a^*, f^*). \tag{8.62}$$

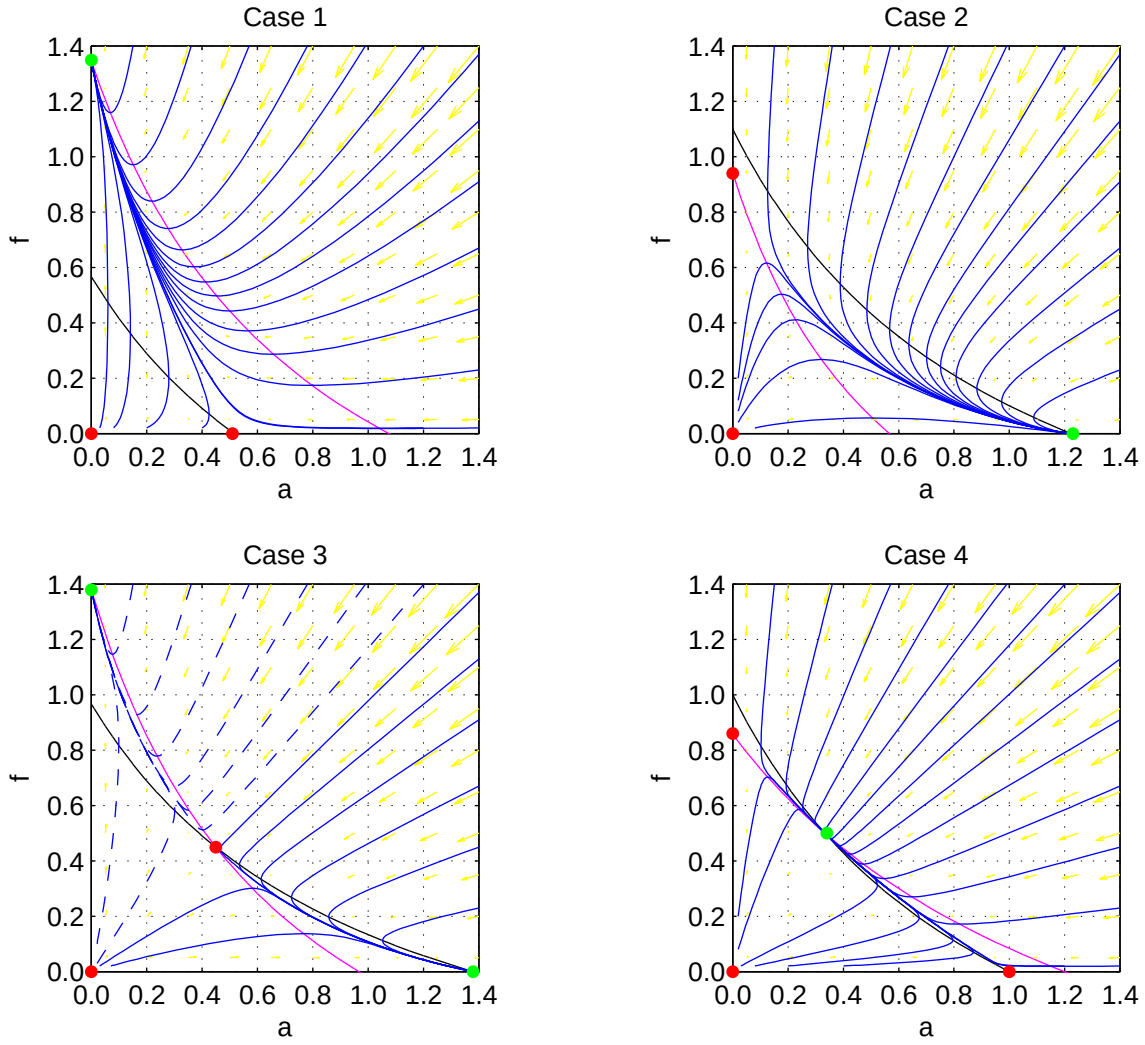


Figure 8.7: The phase planes for the general model with $n_a, n_f = 1$. Stable steady states are indicated by green dots, unstable steady states by red dots, the trajectories by blue lines and the velocity field by yellow arrows. The black line indicates the non-zero part of the a nullcline and the pink line indicates the non-zero part of the f nullcline. In Case 1 there is a stable node at $(0, r/\lambda_f\mu_f - 1)$ and a saddle at $(1/\lambda_a\mu_a - 1, 0)$. The reverse is true in Case 2. Cases 3 and 4 have an extra steady state in which both a and f are non-zero. In Case 3 this is a saddle and trajectories tend to one of the stable nodes at $(0, r/\lambda_f\mu_f - 1)$ and $(1/\lambda_a\mu_a - 1, 0)$. Trajectories tending to the first of these are indicated by dashed lines. In Case 4 the steady state (a^*, f^*) is stable and all trajectories tend to this point. Parameters are as follows: Case 1: $\lambda_a = 0.6$, $\lambda_f = 0.8$, $\mu_a = 0.8$, $\mu_f = 0.7$, $r = 1.5$; Case 2: $\lambda_a = 0.6$, $\lambda_f = 0.7$, $\mu_a = 0.4$, $\mu_f = 0.8$, $r = 1.2$; Case 3: $\lambda_a = 0.9$, $\lambda_f = 0.7$, $\mu_a = 0.4$, $\mu_f = 0.8$, $r = 1.2$; Case 4: $\lambda_a = 0.8$, $\lambda_f = 0.7$, $\mu_a = 0.7$, $\mu_f = 0.6$, $r = 0.6$.

We search for travelling wavefront solutions of the system given by equations (8.41) and (8.42) by transforming to travelling wave coordinates:

$$\boldsymbol{u}(y,\tau) = \boldsymbol{U}(\xi), \quad \text{where} \quad \xi = y - c\tau \quad \text{and} \quad \boldsymbol{u} = \begin{pmatrix} a \\ f \end{pmatrix}, \tag{8.63}$$

where c is the speed of the wavefront. We wish to find a solution such that either

$$\text{Case 2}: \quad a(-\infty) = \frac{1}{\lambda_a \mu_a} - 1, \quad a(\infty) = 0, \quad f(-\infty) = 0, \quad f(\infty) = \frac{r}{\lambda_f \mu_f} - 1, \tag{8.64}$$

or

$$\text{Case 4}: \quad a(-\infty) = a^*, \quad a(\infty) = 0, \quad f(-\infty) = f^*, \quad f(\infty) = \frac{r}{\lambda_f \mu_f} - 1. \tag{8.65}$$

Carrying out the above transformation gives (letting $'$ denote $d/d\xi$):

$$-ca' = \frac{a}{(\mu_a + f)(1+a)} - \lambda_a a + a'', \tag{8.66}$$

$$-cf' = \frac{rf}{(\mu_f + a)(1+f)} - \lambda_f f + Df''. \tag{8.67}$$

Assuming (as is consistent with previous analysis) that $D \ll 1$ and converting to a system of first order ODEs we have

$$a' = g(a,b,f) = b, \tag{8.68}$$

$$b' = h(a,b,f) = -cb - \frac{a}{(\mu_a + f)(1+a)} + \lambda_a a, \tag{8.69}$$

$$f' = k(a,b,f) = \frac{1}{c}\left[\frac{-rf}{(\mu_f + a)(1+f)} + \lambda_f f\right]. \tag{8.70}$$

Depending on the parameter regime, there are up to four steady states given by

$$(a,b,f) = \quad (0,0,0), \quad \left(\frac{1}{\lambda_a \mu_a} - 1, 0, 0\right), \quad \left(0, 0, \frac{r}{\lambda_f \mu_f} - 1\right) \quad \text{and} \quad (a^*, 0, f^*). \tag{8.71}$$

As before, we investigate the linear stability of the above system by considering the eigenvalues of the matrix A evaluated at the steady states, where

$$A = \begin{pmatrix} 0 & 1 & 0 \\ \lambda_a - \frac{1}{(\mu_a+f)(1+a)^2} & -c & \frac{a}{(\mu_a+f)^2(1+a)} \\ \frac{rf}{c(\mu_f+a)^2(1+f)} & 0 & \frac{1}{c}\left[\lambda_f - \frac{r}{(\mu_f+a)(1+f)^2}\right] \end{pmatrix}. \tag{8.72}$$

The steady state $(0,0,0)$**:** The eigenvalues of A are given by

$$\alpha = 0, \quad \alpha = -c \quad \text{and} \quad \alpha = \frac{1}{c}\left(\lambda_f - \frac{r}{\mu_f}\right) < 0, \tag{8.73}$$

which all have non-positive real parts. (c.f. the 2-species competition model for all these results).

The steady state $\left(\frac{1}{\lambda_a\mu_a} - 1, 0, 0\right)$**:** The eigenvalues of A are given by

$$\alpha = \frac{\lambda_f}{c(\mu_f + \frac{1}{\lambda_a\mu_a} - 1)}\left[\frac{1}{\lambda_a\mu_a} - 1 - \frac{r}{\lambda_f} + \mu_f\right], \tag{8.74}$$

and

$$\alpha = \frac{1}{2}\left[-c \pm \sqrt{c^2 + 4\lambda_a^2\left(\frac{1}{\lambda_a} - \mu_a\right)}\right]. \tag{8.75}$$

In Case 1 and Case 4 we have two eigenvalues with negative real part and one eigenvalue with positive real part. The reverse is true in Case 2 and Case 3.

The steady state $\left(0, 0, \frac{r}{\lambda_f\mu_f} - 1\right)$**:** The eigenvalues of A are given by

$$\alpha = \frac{r\lambda_f^2}{c}\left[\frac{r}{\lambda_f} - \mu_f\right], \tag{8.76}$$

and

$$\alpha = \frac{1}{2}\left[-c \pm \sqrt{c^2 + \sigma}\right], \tag{8.77}$$

where

$$\sigma = \frac{\lambda_a}{\mu_a + \frac{r}{\lambda_f\mu_f} + 1}\left(\frac{r}{\lambda_f\mu_f} - 1 - \frac{1}{\lambda_a} + \mu_a\right). \tag{8.78}$$

In Case 1 and Case 3 we have two eigenvalues with positive real part and one eigenvalue with negative real part. The reverse is true in Case 2 and Case 4.

The steady state $(a^*, 0, f^*)$**:** The eigenvalues for this steady state satisfy the equation

$$p(\alpha) = \alpha^3 + (c - k_f)\alpha^2 - (ck_f + h_a)\alpha + (k_f h_a - h_f k_a), \tag{8.79}$$

where h, k represent the b and f nullclines and are given by equations (8.69) and (8.70) respectively, and their partial derivatives are evaluated at the steady state and are given by

$$k_f = \frac{\lambda_f f^*}{c(1+f^*)}, \quad h_a = \frac{\lambda_a a^*}{c(1+a^*)}, \quad k_a = \frac{\lambda_f f^*}{c(\mu_f + a^*)}, \quad h_f = \frac{\lambda_a a^*}{(\mu_a + f^*)}. \tag{8.80}$$

Again, we consider the local minima and maxima of p:

$$\alpha = \alpha_{max,min} = \frac{1}{3}\left[(k_f - c) \mp \sqrt{(k_f - c)^2 + 3(ck_f + h_a)}\right]. \tag{8.81}$$

We have $\alpha_{max} < 0$ and $\alpha_{min} > 0$ so that once more, we have one eigenvalue with positive real part and one eigenvalue with negative real part. The sign of the real part of the remaining eigenvalue is found by considering the sign of $p(0)$: in Case 4, $p(0) > 0$ and we have two eigenvalues with positive real parts and one eigenvalue with negative real part. Conversely, in Case 3, $p(0) < 0$ and we have two eigenvalues with negative real parts and one eigenvalue with positive real part.

To summarise, in Case 2 and Case 4 we have a stable manifold associated with the steady state $(0, 0, r/\lambda_f\mu_f - 1)$, in Case 2 we have an unstable manifold associated with the steady state $(1/\lambda_a\mu_a - 1, 0, 0)$ and in Case 4 we have an unstable manifold associated with the steady state $(a^*, 0, f^*)$. These conditions are sufficient to allow the evolution of travelling wave solutions under certain initial conditions.

As before, to ensure non-oscillatory divergence from (a^*, f^*), we must have both

$$p(\alpha_{max}) \geq 0 \quad \text{and} \quad p(\alpha_{min}) \leq 0. \tag{8.82}$$

Linearising about the leading edge of the wave, where we have, approximately, $(a, b, f) = (0, 0, r/\lambda_f\mu_f - 1)$, gives a minimum wave speed: we require a non-oscillatory approach to the steady state which requires that all the eigenvalues at $(0, 0, r/\lambda_f\mu_f - 1)$ must be purely real. To ensure this, we must have

$$c_{min} = 2\sqrt{\frac{\lambda_a}{\left(\mu_a + \frac{r}{\lambda_f\mu_f} - 1\right)}\left[\frac{1}{\lambda_a} - \mu_a - \frac{r}{\lambda_f\mu_f} + 1\right]}. \tag{8.83}$$

In conclusion, we see that sufficient conditions hold for travelling waves solutions in Case 2 and Case 4.

8.4.3 Numerical solution

As in previous chapters, we solved the system of equations given by (8.41) and (8.42) numerically using the NAG library routine D03PCF. We approximated the infinite domains by zero flux boundary conditions on a finite domain and used initial conditions of the form

$$\text{Case 2:} \quad a(y,0) = \begin{cases} \frac{1}{\lambda_a\mu_a} - 1 & y \leq 0, \\ 0 & y > 0, \end{cases} \qquad f(y,0) = \begin{cases} 0 & y \leq 0, \\ \frac{r}{\lambda_f\mu_f} - 1 & y > 0, \end{cases} \tag{8.84}$$

and

$$\text{Case 4:} \quad a(y,0) = \begin{cases} a^* & y \leq 0, \\ 0 & y > 0, \end{cases} \qquad f(y,0) = \begin{cases} f^* & y \leq 0, \\ \frac{r}{\lambda_f\mu_f} - 1 & y > 0. \end{cases} \tag{8.85}$$

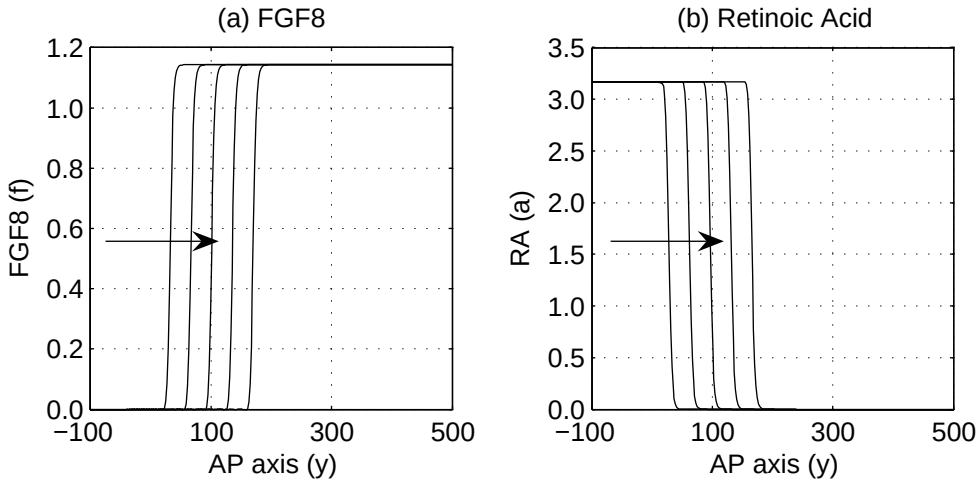


Figure 8.8: Case 2 - A plot of the numerical solution for the general model with $n_a = n_f = 1$ over a series of time steps. We see progression of travelling waves of fgf8 and RA along the AP axis as predicted by previous analysis. The solutions are plotted for $t = 60, 120, 180, 240, 300$. Parameters are as follows: $\lambda_a = 0.6$, $\lambda_f = 0.7$, $\mu_a = 0.4$, $\mu_f = 0.8$, $r = 1.2$ and $D = 0.1$.

Figures 8.8 and 8.9 show the results of numerical solution of the general model with $n_a = n_f = 1$. Case 2 is shown in Figure 8.8 and Case 4 in Figure 8.9. With the initial conditions given above, each case exhibits the travelling wave behaviour predicted by earlier analysis. Note that in Case 4 the wave speed is much lower than in Case 2.

8.5 The general model as n_a and n_f vary

Finally, we turn our attention to the most general case where n_a and n_f are allowed to vary from unity. The model is described by the system of equations:

$$\frac{\partial a}{\partial \tau} = \frac{a}{(\mu_a + f)(1 + a^{n_a})} - \lambda_a a + \frac{\partial^2 a}{\partial y^2}, \tag{8.86}$$

$$\frac{\partial f}{\partial \tau} = \frac{r}{(\mu_f + a)(1 + f^{n_f})} - \lambda_f f + D\frac{\partial^2 f}{\partial y^2}. \tag{8.87}$$

The spatially uniform steady states are given by the solutions of

$$g(a, f) = \frac{a}{(\mu_a + f)(1 + a^{n_a})} - \lambda_a a = 0, \tag{8.88}$$

$$h(a, f) = \frac{r}{(\mu_f + a)(1 + f^{n_f})} - \lambda_f f = 0. \tag{8.89}$$

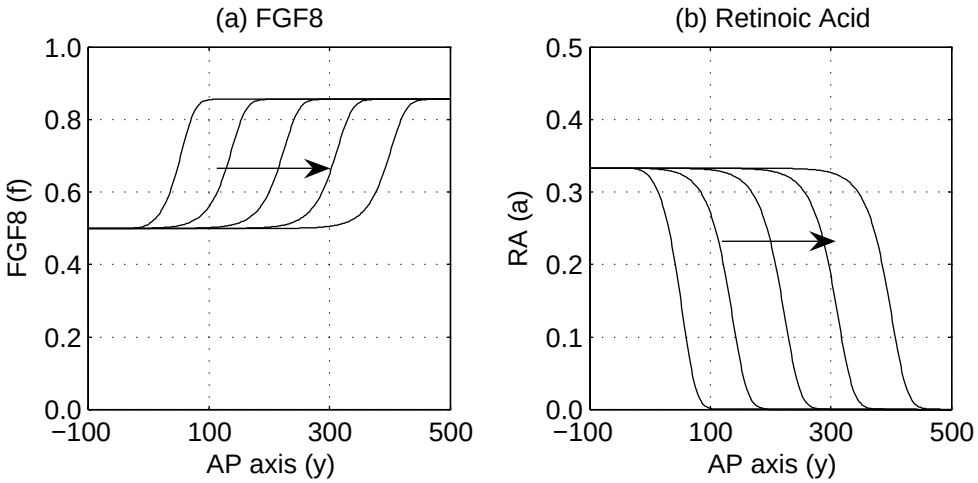


Figure 8.9: Case 4 - A plot of the numerical solution for the general model with $n_a = n_f = 1$ over a series of time steps. We see progression of travelling waves of fgf8 and RA along the AP axis as predicted by previous analysis. The solutions are plotted for $t = 200, 400, 600, 800, 1000$. Parameters are as follows: $\lambda_a = 0.5$, $\lambda_f = 0.5$, $\mu_a = 1.0$, $\mu_f = 1.4$, $r = 1.3$ and $D = 0.1$.

We can see immediately that there are at least three steady states (given the parameter conditions of equation (8.10)):

$$(a, f) = \quad (0, 0), \quad (A_0, 0) \quad \text{and} \quad (0, F_0), \tag{8.90}$$

where

$$A_0^{n_a} = \frac{1}{\lambda_a \mu_a} - 1 \quad \text{and} \quad F_0^{n_f} = \frac{r}{\lambda_f \mu_f} - 1. \tag{8.91}$$

The non-zero parts of the nullclines given by equations (8.88) and (8.89) are plotted for a range of values of n_a and n_f in Figure 8.10. As the exponents increase, the nullclines become increasingly convex but they retain the same general properties as those seen in sections 8.3 and 8.4. With variation of the parameters n_a and n_f from unity, the phase plane and travelling wave analysis rapidly becomes less tractable. However, we can investigate the behaviour of the model numerically and we do so using the previous models as a guide.

8.5.1 Cases 1 – 4

Figure 8.10 suggests that we can find parameter regimes in which cases corresponding to Case 1 to Case 4 in sections 8.3 and 8.4 occur and we found parameters within these regimes by methodical exploration of the parameter space.

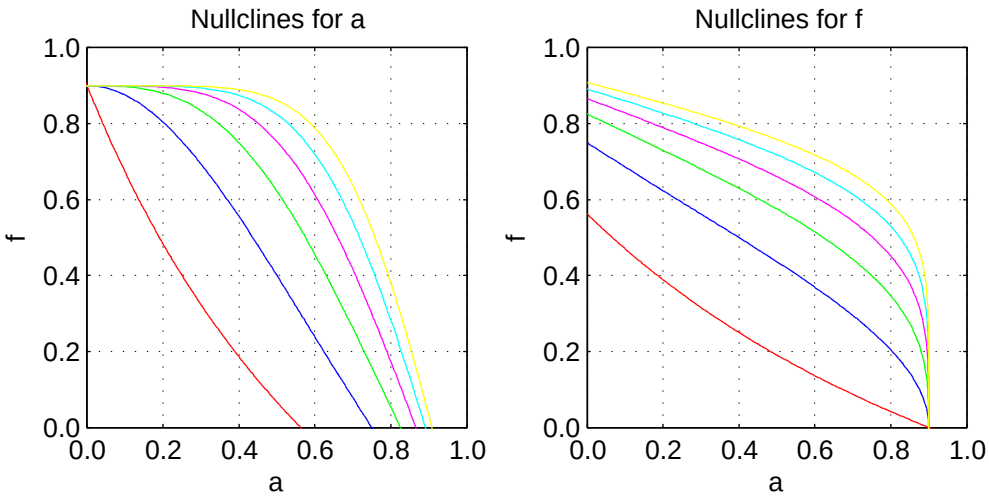


Figure 8.10: The a and f nullclines as n_a and n_f are increased. Parameters are as follows: $\lambda_a = 0.4$, $\lambda_f = 0.4$, $\mu_a = 1.6$, $\mu_f = 1.6$, $r = 1.0$. $n_a, n_f = 1$: red, $n_a, n_f = 2$: blue, $n_a, n_f = 3$: green, $n_a, n_f = 4$: light blue, $n_a, n_f = 5$: purple and $n_a, n_f = 6$: yellow.

Figure 8.11 shows plots of the phase planes for Cases 1 – 4. As with previous models, the nullclines are plotted along with the trajectories and the velocity field. We expect Case 2 and Case 4 to be able to exhibit travelling wavefront solutions of the required format: a wavefront solution from a region of high f/low a to a region of low f/high a.

8.5.1.1 Numerical solution of the general model with $n_a, n_f \neq 1$ - Cases 1 – 4

Figure 8.12 shows the result of numerical solution in a parameter regime corresponding to Case 2 and Figure 8.13 shows the result of numerical solution in a parameter regime corresponding to Case 4. With the initial conditions as specified, numerical solution in each regime results in travelling wavefront solutions.

8.5.2 Further cases

A new and very important aspect of the model introduced by variation of n_a and n_f comes from considering the nature of the nullclines: we see that it is now possible for there to be more than one steady state with both a and f non-zero. Figure 8.14 shows the nullclines in cases in which there are two steady states with both a and f non-zero. In Case 5 we see that there is the possibility of a trajectory connecting the unstable steady state with high f/low a to the stable steady state with low f/high a. In Case 6 there is the possibility of a trajectory connecting the unstable steady state with zero a/high f to the stable steady state with lower f/higher a. Either case provides a sufficient condition for a travelling wave from a region of high f/low a to a region of low f/high a: the case in which we are interested in this work.

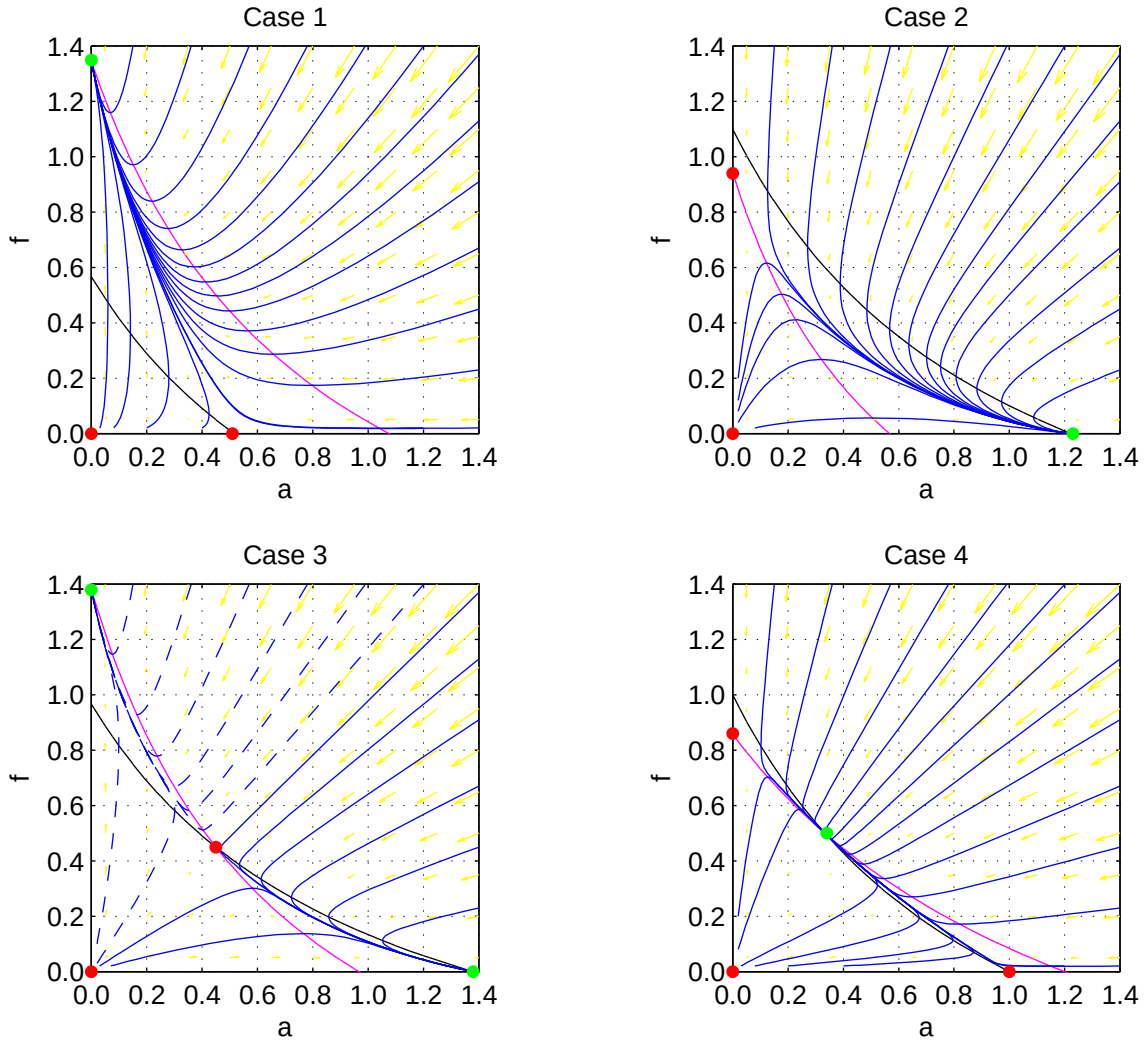


Figure 8.11: The phase planes for the general model with $n_a, n_f \neq 1$. Stable steady states are indicated by green dots, unstable steady states by red dots, the trajectories by blue lines and the velocity field by yellow arrows. The black line indicates the non-zero part of the a nullcline and the pink line indicates the non-zero part of the f nullcline. In Case 1 there is a stable node at $(0, F^0)$ and a saddle at $(A^0, 0)$. The reverse is true in Case 2. Cases 3 and 4 have an extra steady state in which both a and f are non-zero. In Case 3 this is a saddle and trajectories tend to one of the stable nodes at $(0, F^0)$ and $(A^0, 0)$. Trajectories tending to the first of these are indicated by dashed lines. In Case 4 the steady state (a^*, f^*) is stable and all trajectories tend to this point. Parameters are as follows: Case 1: $\lambda_a = 0.6$, $\lambda_f = 0.8$, $\mu_a = 0.8$, $\mu_f = 0.7$, $r = 1.5$, $n_a = 3.0$, $n_f = 3.0$; Case 2: $\lambda_a = 0.6$, $\lambda_f = 0.7$, $\mu_a = 0.4$, $\mu_f = 0.8$, $r = 1.2$, $n_a = 4.0$, $n_f = 3.0$; Case 3: $\lambda_a = 0.9$, $\lambda_f = 0.7$, $\mu_a = 0.4$, $\mu_f = 0.8$, $r = 1.2$, $n_a = 3.0$, $n_f = 3.0$; Case 4: $\lambda_a = 0.4$, $\lambda_f = 0.7$, $\mu_a = 0.9$, $\mu_f = 0.7$, $r = 1.5$, $n_a = 3.0$, $n_f = 3.0$.

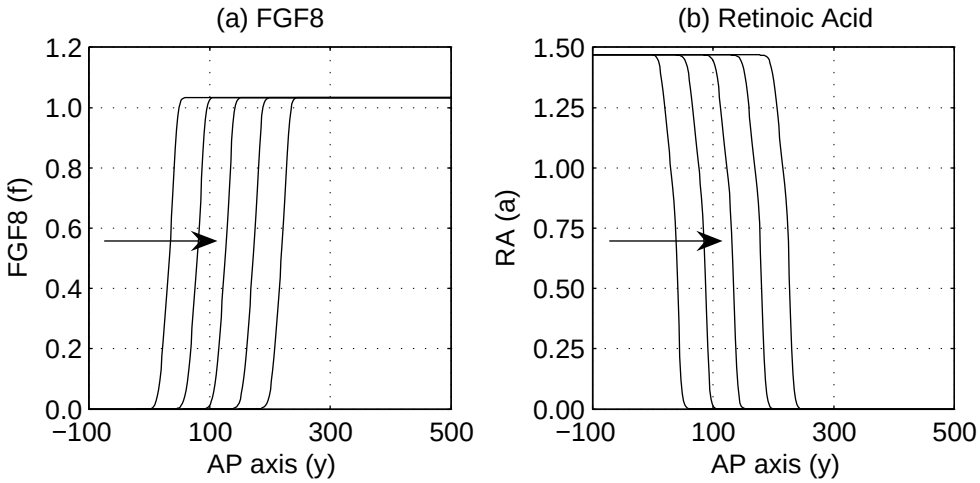


Figure 8.12: Case 2 - A plot of the numerical solution for the general model with $n_a, n_f \neq 1$ over a series of time steps. We see progression of travelling waves of fgf8 and RA along the AP axis as predicted by previous analysis. The solutions are plotted for $t = 200, 400, 600, 800, 1000$. Parameters are as follows: $\lambda_a = 0.6$, $\lambda_f = 0.7$, $\mu_a = 0.4$, $\mu_f = 0.8$, $r = 1.2$ and $D = 0.1$.

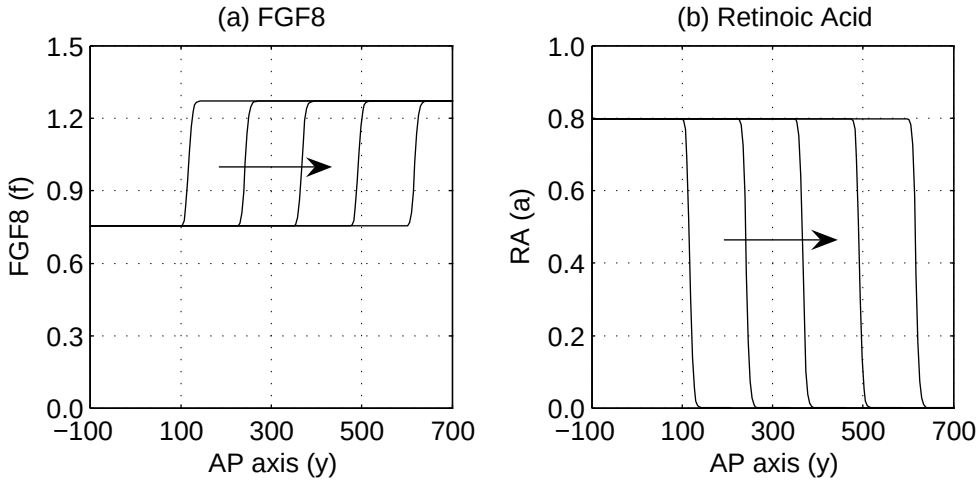


Figure 8.13: Case 4 - A plot of the numerical solution for the general model with $n_a, n_f \neq 1$ over a series of time steps. We see progression of travelling waves of fgf8 and RA along the AP axis as predicted by previous analysis. The solutions are plotted for $t = 200, 400, 600, 800, 1000$. Parameters are as follows: $\lambda_a = 0.5$, $\lambda_f = 0.7$, $\mu_a = 0.4$, $\mu_f = 0.8$, $r = 1.5$ and $D = 0.1$.

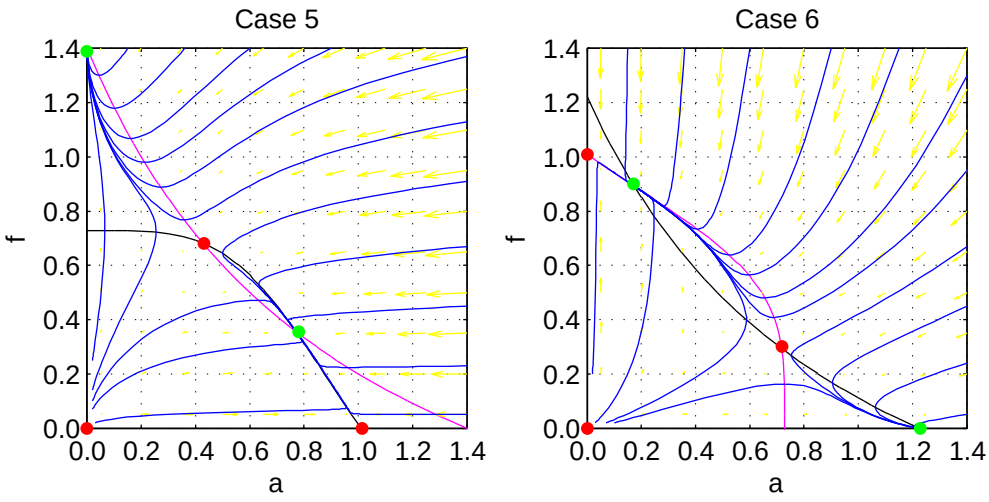


Figure 8.14: The Case 5 and Case 6 phase planes for the general model with $n_a, n_f \neq 1$. Stable steady states are indicated by green dots, unstable steady states by red dots, the trajectories by blue lines and the velocity field by yellow arrows. The black line indicates the non-zero part of the a nullcline and the pink line indicates the non-zero part of the f nullcline. In Case 5 there is a stable node at $(0, F^0)$ and a saddle at $(A^0, 0)$. There are two steady states with both a and f non-zero: the one with larger a being stable and the other unstable. The reverse is true in Case 6. Parameters are as follows: Case 5: $\lambda_a = 0.7$, $\lambda_f = 0.3$, $\mu_a = 0.7$, $\mu_f = 1.0$, $r = 0.6$, $n_a = 4.0$, $n_f = 1.0$; Case 6: $\lambda_a = 0.5$, $\lambda_f = 0.7$, $\mu_a = 1.0$, $\mu_f = 0.7$, $r = 1.0$, $n_a = 1.0$, $n_f = 4.0$.

8.6 Discussion

We began this chapter by introducing a new model for the opposing gradients of fgf8 and RA along the AP axis. Motivation for this new, simplified model came from the fact that the more detailed model for gradient formation provided little opportunity for insight into key mechanisms that could drive progression of these gradients.

We proceeded to analyse the new model from a number of different viewpoints: we considered the simplest case first in which the exponents controlling self-regulation of a and f (n_a and n_f) were unity. We broke this model down further by expanding the quotients and discarding terms of cubic order and higher. Further non-dimensionalisation of this model led to the standard 2-species competition model.

The 2-species competition model was analysed thoroughly for each of the four possible parameter regimes and we found sufficient conditions on the parameter space for the evolution of travelling wavefront solutions of the required form along the AP axis. Numerical simulations were used to confirm the analytical results.

We next used results from the 2 species competition model to guide analysis of the general model for $n_a = n_f = 1$. Once more, we found that the parameter space could be broken down into 4 regions, each having a corresponding regime in the competition model parameter space. Again, we

found parameter conditions to facilitate the evolution of travelling wavefronts of the required form and we validated these results numerically.

Finally, we moved to consider the case in which the exponents n_a and n_f were not necessarily equal to unity. Using numerical evaluation of the phase plane, we were again able to find regions of parameter space corresponding to the four cases shown to exist in each of the two previous models. As previously, we were able to solve the system numerically to confirm the existence of travelling wavefronts.

What was important to note in the final, more general model, was that the four regions of parameter space corresponding to the four cases we had found in previous models, did not cover the whole of parameter space. We were able to find two other parameter regimes which gave two spatially uniform steady states with both a and f non-zero - both of these were able to produce travelling wavefront solutions.

8.6.1 Travelling wave speed

In the 2-species competition model, the minimum wave speed in Cases 2 and 4 was determined solely by λ_a, the rate of decay of RA. In the general model with $n_a = n_f = 1$, the minimum wave speed in Cases 2 and 4 was found to be a more complex function of all the model parameters:

$$c_{min} = 2\sqrt{\frac{\lambda_a}{\left(\mu_a + \frac{r}{\lambda_f \mu_f} + 1\right)}\left[\frac{1}{\lambda_a} - \mu_a - \frac{r}{\lambda_f \mu_f} - 1\right]}. \tag{8.92}$$

At this stage we are particularly interested in the rate at which fgf8 decays and how this affects progression of the wavefront. We made some experimental predictions in Chapter 6 on the effect of somite size when the speed of the wavefront is perturbed. Our experimental collaborators [42] have suggested that the speed of the wavefront is closely linked to the rate of decay of *fgf8* (mRNA) and it seems likely that this may be the primary route of investigation in an experimental setting.

Figure 8.15 shows how the minimum wave speed c_{min} varies as λ_f, the rate of decay of FGF8 varies. For $\lambda_f \lessapprox 0.7$ the parameter regime travelling waves do not exist (c_{min} would contain imaginary parts). As $\lambda_f \to 2.5$, $c_{min} \to \infty$ (the denominator of the quotient under the square root tends to zero). *In vivo* we expect that increasing λ_f would result in faster progression of the determination front. Using our predictions in Chapter 6 we anticipate the result of this being the formation of larger somites. It would be interesting to see if this could be observed experimentally.

8.6.2 Conclusions and further work

The models used in this chapter have provided much useful insight into the possible mechanisms driving the progression of opposing fgf8/RA gradients along the AP axis. In particular, the general model with $n_a = n_f = 1$ was shown to possess the qualities needed for evolution of travelling wavefronts and provided a useful relationship between the parameters of the model and the minimum wave speed c_{min}, to which we expect the solutions to evolve.

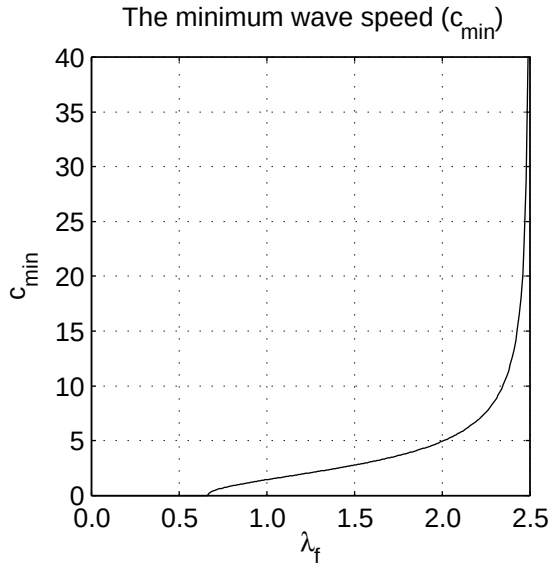


Figure 8.15: The minimum wave speed as λ_f, the rate of decay of FGF8, varies. Parameters are as follows: $\lambda_a = 0.6$, $\mu_a = 0.4$, $\mu_f = 0.8$, $r = 1.2$, $n_a = 1.0$, $n_f = 1.0$.

One particular gain from this model is that it should now be possible to dispense with the Heaviside functions controlling wavefront progression that have been used throughout previous models for the fgf8 gradient (see Chapter 4 and Chapter 5). The discovery of RA acting in a mutually inhibitory feedback loop with fgf8 [12] provides the required mechanism for down-regulation of fgf8 in the anterior PSM and the evolution of travelling wavefronts.

For future progression of this model, we now rely on experimentalists to provide data on the levels of fgf8/RA expressed in the PSM. Our analysis suggests that if fgf8 levels decrease to zero in the anterior PSM then we should focus attention on Case 2; if not, then we need to consider Case 4 (and others in the more general model). Confirmation of fgf8 levels decreasing to zero would allow consideration of only Case 2 in the most general model (n_a, n_f not necessarily equal to unity) and facilitate easier phase plane/travelling wave analysis.

The final step, once determination of the parameter values is complete, will be to integrate the models presented in this chapter with those presented in Chapters 4–6 in order to derive a more complete model for somitogenesis.

Chapter 9

Discussion and Conclusions

This study used mathematical modelling as a tool to investigate the mechanisms underlying certain aspects of somitogenesis. With recent experimental evidence, previous mathematical studies had become increasingly unable to explain the mechanisms involved in somitogenesis or to explain the patterns of somites seen when factors influential to these mechanisms are disturbed.

The principal aims of this study were to

- Develop mathematical models that use present experimental hypotheses of interaction of a segmentation clock and a wavefront to explain somite formation.
- Adapt these models to explain the somite anomalies seen *in vivo* when certain elements crucial to somitogenesis are perturbed.
- Use the models to make experimentally testable predictions that can further understanding of the mechanisms involved in somite formation.
- Develop a series of models with varying degrees of biological realism which accurately capture the mechanisms underlying the maintenance of AP gradients of morphogens in the embryo.

We began this study by considering some of the existing models for somitogenesis. By definition, a model is a partial representation of reality and cannot explain all aspects of a biological process: but with new experimental evidence on the presence of a segmentation clock (linked to oscillating gene expression [27, 37]) and a wavefront of determination (connected to expression of FGF8 [15]), each of the models became further redundant. However, the basis of the mathematical formulation of the cell cycle model for somitogenesis [4, 29] is that of a signalling process with regulation of the signal and its subsequent action being determined by external factors: hence with suitable modifications, it could still be applied to study somitogenesis. With this in mind, Chapter 2 and Chapter 3 concentrate on eliciting the critical components and driving forces of the model as tools for future reference.

In Chapter 4 we concentrated on building models to explain the FGF8 gradient along the AP axis of vertebrate embryos. We began with a simplistic model which considered fgf8 mRNA and protein,

the results of which indicated that transcriptional delay (i.e. a delay in producing protein from mRNA) was unimportant to the nature of the wavefront. If mRNA decay is very rapid, then our model showed that it is possible to consider solely levels of fgf8 protein along the AP axis (as the limiting case of the fgf8 mRNA/protein model).

We carried this approximation through into Chapter 5 where we used an interaction between the FGF8 gradient and the segmentation clock to control the processes involved in the signalling model. Analytical and numerical techniques showed that periodic pulses in the signal generated a series of coherent somites: in short, this new "clock and wavefront" model was able to reproduce somites in a manner that was tightly regulated both in space and in time. The model was also able (in a slightly adapted form) to predict the sequences of anomalies seen when the FGF8 gradient was perturbed through local application of FGF8: we reproduced all the cases seen *in vivo* both analytically and numerically.

Building on the adaptations of the new clock and wavefront model, in Chapter 6 we were able to make a series of experimentally testable predictions regarding perturbation of the regression rate of the FGF8 gradient and of the period of the segmentation clock. In order to validate the model further, it is hoped that some of these predictions can be tested *in vivo* by our experimental collaborators.

Chapter 7 considered a more biologically realistic model for the FGF8 gradient: experimental collaboration provided us with a network of biochemical pathways involving both FGF8 and RA from which we were able to build a more accurate model. The downside of improved biological accuracy was an increase in the size of the model system involved: from two to seven equations for the maintenance of the wavefront of FGF8. Although informative from a wider perspective, the model was too complex to allow any great understanding of the feedback mechanisms between FGF8 and RA. The subsequent chapter (Chapter 8) considered only the dynamics of generic fgf8 and RA substances, and as a result we were able to find a range of kinetics that displayed the following, critical behaviour: fgf8 is produced solely in the tail region of the embryo. This is something that we had to introduce artificially in the preceding models. What is also important to note, and corresponds to present experimental hypotheses, is that the speed of determination front regression was shown to be heavily linked to the rate of decay of fgf8.

9.1 Future work

There are many avenues open for further exploration, both from a theoretical and biological viewpoint and we consider some of these below.

9.1.1 Modelling directions

There are a range of ways in which this model can be improved. The first would be to integrate the model system of fgf8/RA used in Chapter 8 into the new clock and wavefront model to see if this can produce a coherent sequence of somites. If so, can it mimic the anomalies seen upon local application of fgf8, and would this model make the same predictions as the previous model does in

Chapter 6? In particular, how does changing the rate of fgf8 decay influence the size of somites?

Another avenue for exploration is directly related to these points - the reduced model for fgf8/RA allows easier exploration of the feedback network between fgf8 and RA, but can these reaction kinetics be used in the more biologically accurate system to produce travelling wavefronts of fgf8?

Other directions for this model involve more drastic alterations: the signalling molecule, as yet, has no biological basis, but it seems that dynamic, periodic expression of *c-hairy1* and *l-fng* are integral in determining the fate of a cell. It may be that one or more of these cycling genes activates production of the somitic factor (which itself could be linked to expression of genes such as mesp2).

Lastly, we remark that the models presented in this work provide a mechanism for a pre-pattern for somite formation. We have not, as yet, addressed the mechanisms via which cells undergo changes in their adhesive and locomotory properties and coalesce together to form somites.

9.1.2 Experimental directions

There are a number of ways in which further experimental research would be useful in improving the validity and accuracy of the mathematical models. Smaller scale projects lie in trying to measure parameter values: for example, diffusion coefficients and decay rates for FGF8 and RA, and the levels of FGF8 and RA in the anterior and posterior PSM. We also need to have a clearer understanding of the way in which components of the FGF/RA biochemical pathways interact with each other: for example, are allosteric effects important and how quickly do FGF8 and RA get transported across the cell membrane?

In order to validate the models of this study, it is important that the experimental predictions be tested. Some aspects of these predictions are easier to test than others, for example, what happens if FGF8 is inhibited over a time scale similar to that taken to form several somites? Others, for example, changing the period of the segmentation clock or the rate of regression of the determination front, will require the use of sophisticated experimental techniques to ensure that other factors influencing somitogenesis are not disturbed at the same time.

9.2 Final words

In conclusion, this study has looked at building a series of models which are able to explain different parts of the somitogenic process. As more experimental data becomes available and/or our experimental predictions are tested, we will be able to refine the models and continue to further understanding of the somitogenic process. Increasingly, mathematical models are becoming key to our understanding of the complex, non-linear interactions that underlie many biological processes and somitogenesis is an important paradigm model for investigating the interaction of processes such as biological oscillations, gene expression and cell signalling.

Appendix A

Numerical Methods

A.1 The NAG library solver D03PCF

Throughout this work we have solved systems of PDEs using the NAG (Numerical Algorithm Group) library routine D03PCF, which is designed for nonlinear parabolic (including some elliptic) PDEs in one space variable.

The general form of the system of equations to be solved is [36]:

$$\sum_{j=1}^{NPDE} P_{i,j}\frac{\partial \boldsymbol{U}_j}{\partial t} + Q_i = \frac{\partial R_i}{\partial x}, \quad i = 1, 2, \ldots, NPDE, \quad a \leq x \leq b, \quad t \geq t_0, \tag{A.1}$$

where $P_{i,j}$, Q_i and R_i depend on x, t, $\boldsymbol{U}$, $\boldsymbol{U}_x$ and

$$\boldsymbol{U} = [U_1(x,t), \ldots, U_{NPDE}(x,t)]. \tag{A.2}$$

Throughout this work, the system of equations is solved on the domain in (x,t) space specified by $[a,b]$ x $[0,T]$, which can be represented by a mesh described by the points (x_j, t_n). If $h, k > 0$ describe the spatial and temporal steps between the mesh points, then $x_j = jh$ and $t_n = nk$ where $j, n \in \mathbb{N}$. The aim of the solver is to be able to write the solution as a series of approximations at the points of the mesh, that is,

$$\boldsymbol{v}_j^n = \boldsymbol{v}(x_j, t_n) \approx \boldsymbol{U}(x_j, t_n). \tag{A.3}$$

Figure A.1 illustrates the construction of a regular finite difference mesh in the (x,t) plane.

The routine is based on the method of lines, using a finite difference approximation in the spatial variable to reduce the system of PDEs to a system of ODEs in the time variable. The resulting system is solved using an implementation of Gear's method and the Backward Differentiation Formulae (BDFs). Here we give an overview of the main techniques used in D03PCF (and also in some of the other numerical methods detailed in the appendix).

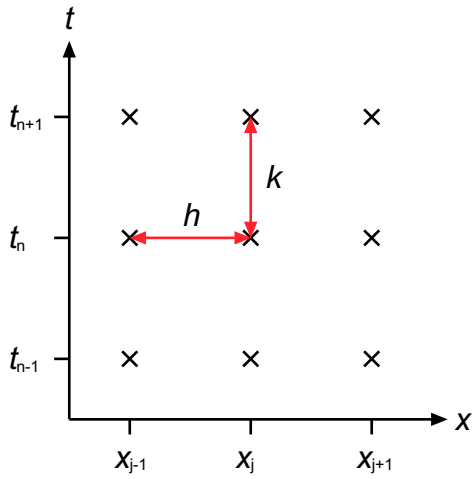


Figure A.1: An illustration of a regular finite difference grid in x and t. See text for more details.

Note We note here that for simplicity, the NAG (Numerical Algorithm Group) library routine D03PCF has been solved using a square mesh (i.e. an equal number of points in both space and time) throughout this work. This is not an optimal strategy in terms of efficiency of the routine and future work should be directed towards addressing this matter.

A.1.1 Method of lines

A general approach to the numerical solution of parabolic systems is the method of lines. It can be employed to reduce a system of PDEs to a (larger) system of ODEs in time, which can then be solved using one of the many ODE solvers available. Choice of an ODE solver depends on the form of the equation, its stiffness and other factors.

Given a simple parabolic equation of the form [10]

$$c\frac{\partial u}{\partial t} = \frac{\partial}{\partial x}\left[g\left(x,t,u,\frac{\partial u}{\partial x}\right)\frac{\partial u}{\partial x}\right] + f\left(x,t,u,\frac{\partial u}{\partial x}\right), \tag{A.4}$$

spatial difference operators are used to approximate the spatial differential operators of the RHS. Supposing that we wish to approximate u by a sequence of functions of the form $v = \{v_j(t)\}$ where $v_j(t) \approx u(x_j, t)$ for $j \in \mathbb{Z}$, then upon making such an approximation we would have a system of equations of the form

$$c\frac{\partial v}{\partial t} = g_0(x_j, t, v) + f_0(x_j, t, v). \tag{A.5}$$

That is, $v_j(t)$ describes the solution at a point x_j in terms of the solution at a prescribed number of other points x_i, for $i \in \mathbb{Z}$. We note that the spatial approximation must be taken so that the boundary conditions are still satisfied.

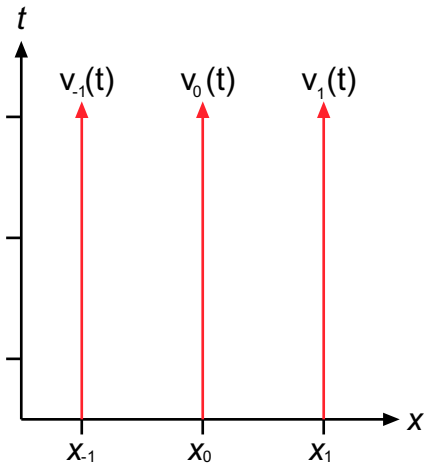


Figure A.2: The method of lines: a semi-discrete approximation is constructed on an array of parallel lines in the (x, t) plane.

Figure A.2 shows how the method of lines can be employed to find the numerical solution to a system of parabolic PDEs. A semi-discrete approximation is constructed on an array of parallel lines in the (x, t) plane to reduce the original PDE system to a system of ODEs in time.

A.1.2 Spatial discretisation

One method by which the system of PDEs can be reduced to a system of ODEs is by performing a spatial discretisation. The main procedure is to find an approximation for the n^{th} derivatives of a variable for $n = 1, 2, \ldots$ at the points of a spatial mesh x_j, in terms of a linear combination of the variable evaluated at other mesh points and the values of those mesh points.

In particular, the NAG routine D03PCF uses a centered finite difference method such that at each internal point of the mesh an approximation of the form [10]

$$\left[\frac{\partial u}{\partial x}\right]_{x_j} \approx \frac{u_{j+1} - u_j}{x_{j+1} - x_j}, \tag{A.6}$$

and

$$\begin{aligned}\left[\frac{\partial}{\partial x}\left\{g\left(x, t, u, \frac{\partial u}{\partial x}\right)\frac{\partial u}{\partial x}\right\}\right]_{x_j} = & \frac{1}{x_{j+\frac{1}{2}} - x_{j-\frac{1}{2}}}\left\{\left(\frac{g_{j+1} - g_j}{2}\right)\left(\frac{u_{j+1} - u_j}{x_{j+1} - x_j}\right)\right\} - \\ & \frac{1}{x_{j+\frac{1}{2}} - x_{j-\frac{1}{2}}}\left\{\left(\frac{g_j - g_{j-1}}{2}\right)\left(\frac{u_j - u_{j-1}}{x_j - x_{j-1}}\right)\right\},\end{aligned} \tag{A.7}$$

is made where

$$u_j = u(x_j, t), \quad g_j = g(u_j, t) \quad \text{and} \quad x_{j+\frac{1}{2}} = \frac{1}{2}(x_{j+1} + x_j). \tag{A.8}$$

The approximation is of 2^{nd} order if the step-size varies smoothly and g is continuous. Modifications are made at the boundaries where complete data is not available.

There is no spatial error control or estimate used in D03PCF so one reason for using a finite difference approximation is so that users are familiar with the technique used for the spatial discretization. It is also a very versatile method with comparable accuracy to the finite element method.

A.1.3 Backwards differentiation formula method

The BDFs are used to reduce the semi-discrete approximation to a set of algebraic equations which can be solved iteratively. Consider finding a discrete approximation to the equation

$$\frac{\partial u}{\partial t} = f(u(t), t). \tag{A.9}$$

The BDFs use Linear Multistep (LMS) methods to construct a sequence $\{v^j\}$ for $j = 0, 1, \ldots$ such that $v^n = v(t_n) \approx u(t_n)$. v^{n+1} is calculated from $v^{n-j}, v^{n-j+1}, \ldots$ and $f^{n-j}, f^{n-j+1}, \ldots$ where $f^n = f(v^n, t_n)$ [59]. The aim is to find a method for constructing the sequence defining v^{n+1} with the prescribed accuracy, whilst using as few (computationally expensive) function evaluations as possible.

A general S-step LMS formula is given by

$$\sum_{j=0}^{s} \alpha_j v^{n+j} = k \sum_{j=0}^{s} \beta_j f^{n+j}, \tag{A.10}$$

where $\alpha_s = 1$ and either α_0 or β_0 is zero. If $\beta_s = 0$ the method is explicit and otherwise it is implicit.

A.1.3.1 Accuracy and consistency of the LMS formulae

The characteristic polynomials are defined by

$$\rho(z) = \sum_{j=0}^{s} \alpha_j z^j \quad \text{and} \quad \sigma(z) = \sum_{j=0}^{s} \beta_j z^j. \tag{A.11}$$

Defining the time shift operator Z such that $Zv^n = v^{n+1}$ in the discrete case and $Zu(t) = u(t+k)$ in the continuous case, the S-step LMS formula can be written as

$$\rho(Z)v^n - k\sigma(Z)f^n = 0, \tag{A.12}$$

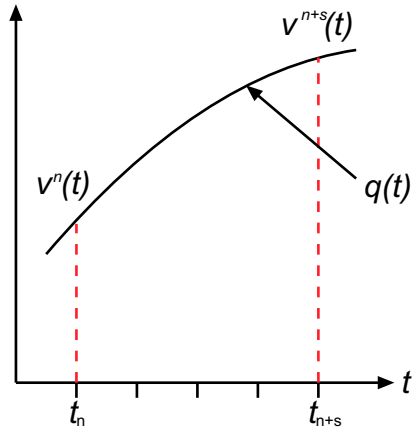


Figure A.3: Construction of a unique polynomial interpolating the points $v^n, \ldots, v^{n+s}$. See text for details.

which gives a definition to the approximations $\{v^n\}$. If the approximation is good then equation (A.12) should be nearly satisfied by the discretisation of u and u_t: defining the LMS difference operator $\mathcal{L} := \rho(Z) - k\mathcal{D}\sigma(Z)$ where $\mathcal{D}$ is the time differential operator so that

$$\mathcal{L}u(t_n) = \rho(Z)u(t_n) - k\sigma(Z)u_t(t_n) = \sum_{j=0}^{s} \alpha_j u(t_{n+j}) - k\sum_{j=0}^{s} \beta_j u_t(t_{n+j}), \tag{A.13}$$

then if the LMS formula is accurate $\mathcal{L}u(t_n)$ should be small. Expanding $u(t_{n+j})$ and $u_t(t_{n+j})$ using a Taylor series:

$$u(t_{n+j}) = u(t_n) + jku_t(t_n) + \frac{1}{2}(jk)^2 u_{tt}(t_n) + \ldots, \tag{A.14}$$

$$u_t(t_{n+j}) = u_t(t_n) + jku_{tt}(t_n) + \frac{1}{2}(jk)^2 u_{ttt}(t_n) + \ldots, \tag{A.15}$$

and substituting into the equation for $\mathcal{L}u(t_n)$ gives the formal local discretization error

$$\mathcal{L}u(t_n) = C_0 u(t_n) + kC_1 u_t(t_n) + k^2 C_2 u_{tt}(t_n) + \ldots, \tag{A.16}$$

with the C_i given as in [59].

The method is said to have order of accuracy p if $\mathcal{L}u(t_n) = \mathcal{O}(k^{p+1})$ as $k \to 0$ i.e. if $C_0 = C_1 = \ldots = C_p = 0$, $C_{p+1} \neq 0$. The error constant is equal to the coefficient C_{p+1}. The idea behind the definition is that if a LMS method is applied to a problem with a sufficiently smooth solution u, then an error of approximately

$$C_{p+1}k^{p+1}\frac{d^{p+1}u}{dt^{p+1}}(t_n) = \mathcal{O}(k^{p+1}), \tag{A.17}$$

Number of steps (S)	Order (p)	α_s	α_{s-1}	α_{s-2}	α_{s-3}	α_{s-4}	β_s
1	1	1	-1				1
2	2	1	$-\frac{4}{3}$	$\frac{1}{3}$			$\frac{2}{3}$
3	3	1	$-\frac{18}{11}$	$\frac{9}{11}$	$-\frac{2}{11}$		$\frac{6}{11}$
4	4	1	$-\frac{48}{25}$	$\frac{36}{25}$	$-\frac{16}{25}$	$\frac{3}{25}$	$\frac{12}{25}$

Table A.1: A table showing the values of the coefficients for the various BDFs.

is introduced locally at step n. The total number of steps is T/k (where T is the length of time over which the equations are to be solved) and therefore the local errors are expected to add up to a global error of $\mathcal{O}(k^p)$.

A.1.3.2 The s-step backwards differentiation formulae

The s-step BDFs are the optimally implicit LMS formulae and are defined such that $\beta_0 = \ldots = \beta_{s-1} = 0$ [59]. It is maximally implicit in the sense that f only appears at the level $n+s$. The coefficients ($\alpha_0, \ldots, \alpha_s$ and β_s) are derived using polynomial interpolation of v^{n+s}: given points $v^n, \ldots, v^{n+s}$ then a unique polynomial $q(t)$ of degree less than or equal to s can be found interpolating $v^n, \ldots, v^{n+s}$. Although v^{n+s} is not known, it can be defined implicitly by $q_t(t_{n+s}) = f^{n+s} = f(x_{n+s}, v^{n+s})$. The derivative in the last expression represents a linear function from which the coefficients can be computed. This method of construction is illustrated in Figure A.3. The general expression for an s-step BDF can be written as

$$\sum_{j=1}^{s} \frac{1}{j} \nabla^j v^{n+s} = k f^{n+s} \quad \text{where} \quad \nabla y^n = y^n - y^{n-1}. \tag{A.18}$$

Example - 2nd order BDF Newton's interpolation formula can be used to find the unique polynomial $q(t)$:

$$q(t) = \left(1 + \theta\nabla + \frac{\theta(\theta-1)\nabla^2}{2!}\right) v^n \quad \text{where} \quad \theta = \frac{t - t_n}{k}. \tag{A.19}$$

Expanding the above gives

$$q(t) = 1 + \frac{1}{k}(t - t_n)(v^{n+1} - v^n) + \frac{1}{2k^2}(t - t_n)(t - t_n - k)(v^{n+2} - 2v^{n+1} + v^n). \tag{A.20}$$

Differentiating and evaluating at $t = t_{n+2}$ gives the 2nd order BDF

$$v^{n+2} - \frac{4}{3}v^{n+1} + \frac{1}{3}v^n = \frac{2}{3}k f^{n+2}, \tag{A.21}$$

as seen in Table A.1.

A.2 The MATLAB ODE Solver ode15s

The MATLAB ODE solver ode15s solves systems of equations of the form

$$\boldsymbol{M}(t,\boldsymbol{y})\boldsymbol{y}' = \boldsymbol{f}(t,\boldsymbol{y}), \quad t_0 \le t \le t_f, \quad \boldsymbol{y}(t_0) = \boldsymbol{y}_0. \tag{A.22}$$

The method employed by ode15s is based on the Numerical Difference Formulas (NDFs) which were developed from the BDFs. In Appendix A.1 we noted that the general s-step BDF can be written in the form (dropping the bold font used for vectors)

$$\sum_{j=1}^{s} \frac{1}{j} \nabla^j v^{n+s} = k f^{n+s} \quad \text{where} \quad \nabla y^n = y^n - y^{n-1}, \tag{A.23}$$

which is solved by using Newton's interpolation formula. General purpose BDFs use a quasi-constant step size [53] i.e. they use a constant step size wherever possible and when it is desirable or necessary to change the step size, they do so by interpolating the solution at the old mesh points to the new mesh points.

The main problem with the BDFs is that they have very poor stability at higher order [53]. A BDF iteration is started with a value predicted by the formula

$$y_{n+1}^{(0)} = \sum_{j=0}^{s} \nabla^j y_n, \tag{A.24}$$

which involves one more term from the past than equation (A.23). The above term is used to improve the stability of the BDF method.

A general NDF can be written in the form

$$\sum_{j=1}^{s} \frac{1}{j} \nabla^j v^{n+s} - k f^{n+s} - \kappa\gamma_s (y_{n+1} - y_{n+1}^{(0)}) = 0, \tag{A.25}$$

where κ is a scalar parameter and $\gamma_k = \sum_{j=1}^{k} j^{-1}$. The role of the extra term can be understood by noting that

$$y_{n+1} - y_{n+1}^{(0)} = \nabla^{s+1} y_{n+1}, \tag{A.26}$$

and that the leading term in the truncation error of the corresponding BDF can be approximated by

$$\frac{1}{s+1} \nabla^{s+1} y_{n+1}. \tag{A.27}$$

Hence for any value of κ, the NDF method given by equation (A.25) is of order (at least) s and the leading term in the truncation error is [53]:

$$\left(\kappa\gamma_s + \frac{1}{s+1}\right) k^{s+1} y^{(s+1)}, \tag{A.28}$$

so the error can be reduced by choice of the parameter κ.

We consider this with regard to the efficiency of the numerical method: selection of the step size is governed by the largest value of k for which the leading term in the truncation error is no bigger than a given tolerance [53]. We have the following for the leading terms of the truncation errors of the s-step BDF and NDF:

$$T_{BDF} = \frac{1}{s+1} k^{s+1} y^{(s+1)} \quad \text{and} \quad T_{NDF} = \left(\kappa \gamma_s + \frac{1}{s+1} \right) k^{s+1} y^{(s+1)}, \tag{A.29}$$

which for both formulae is of the form $Ck^{s+1}y^{(s+1)}$.

A smaller coefficient C will result in the achievement of a given accuracy with a larger step size k and hence traversal of the interval of integration in fewer steps. Assuming that steps in the BDF and NDF both have the same computational cost [53], the NDF formula is therefore a more efficient way of finding an approximate solution, given a suitable choice of κ.

If the s-step BDF uses a step size k then the corresponding NDF can use a step of size rk where

$$r = \left[\frac{\frac{1}{s+1}}{\kappa \gamma_s + \frac{1}{s+1}} \right]^{\frac{1}{s+1}}. \tag{A.30}$$

It should be noted however, that the NDFs are rarely stable for orders greater than 2 and that the price of increased stability (i.e. less negative κ) is reduced efficiency [53].

A.2.1 odeset

The error tolerance of the `ode15s` can be controlled using the options RelTol and AbsTol, which control the size of the relative and absolute tolerances respectively. The default values are RelTol $\leq 10^{-3}$ and AbsTol $\leq 10^{-6}$. It is also possible to limit the maximum step size used in the computation of the solution and set the initial step size. `ode15s` has additional features that allow choice of the maximum order of the NDF used and also choice of the BDFs over the NDFs.

A.3 The MATLAB PDE Solver pdepe

The MATLAB PDE solver `pdepe` solves initial-boundary value problems for systems of parabolic and elliptic equations in a single space variable and time. The system of equations should be of the form:

$$\boldsymbol{c}(x,t,\boldsymbol{u},\boldsymbol{u}_x)\boldsymbol{u}_t = x^{-m}\left[x^m \boldsymbol{f}(x,t,\boldsymbol{u},\boldsymbol{u}_x)\right]_x + \boldsymbol{s}(x,t,\boldsymbol{u},\boldsymbol{u}_x), \tag{A.31}$$

where m can take the values $0, 1, 2$ and defines the geometry of the problem (slab, cylindrical and spherical, respectively).

Once the system has been defined, initial and boundary conditions, the x mesh ($\boldsymbol{x}_{mesh}$) and the t

span ($\boldsymbol{t}_{span}$) need to be input to produce a solution. The time integration of the spatially discretised system is performed with a MATLAB ODE solver (such as ode15s) that selects the time step and formula dynamically; the elements of $\boldsymbol{t}_{span}$ are merely the points at which the solution is output. Conversely, $\boldsymbol{x}_{mesh}$ is the mesh over which the 2^{nd} order spatial discretisation is carried out, and this needs to be taken into consideration when choosing $\boldsymbol{x}_{mesh}$.

There are optional control parameters that may be input and these are detailed further in Appendix A.2.

A.4 The MATLAB BVP Solver bvp4c

The MATLAB solver bvp4c can be used to solve two-point boundary value problems for ODEs. It solves two-point boundary value problems (BVPs) of systems of ODEs of the form

$$\boldsymbol{y'} = \boldsymbol{f}(x, \boldsymbol{y}, \boldsymbol{p}), \tag{A.32}$$

subject to boundary value conditions

$$\boldsymbol{g}(\boldsymbol{y}(a), \boldsymbol{y}(b), \boldsymbol{p}), \tag{A.33}$$

where $\boldsymbol{p}$ is a vector of unknown parameters. The solver must be given an initial guess solution, which includes a guess for the initial solver mesh and the unknown vector of parameters.

bvp4c uses a collocation method: it finds an approximate solution $\boldsymbol{S}(x)$ to the problem which is a cubic polynomial on each subinterval $[x_n, x_{n+1}]$ of the interval $a = x_0 < x_1 < \ldots < x_N = b$. $\boldsymbol{S}$(x) satisfies the boundary conditions $\boldsymbol{g}(\boldsymbol{S}(a), \boldsymbol{S}(b)) = \boldsymbol{0}$ along with the differential equations (collocates) at both ends and the midpoint of each interval:

$$\begin{aligned}
\boldsymbol{S'}(x_n) &= \boldsymbol{f}(x_n, \boldsymbol{S}(x_n)), && \text{(A.34)}\\
\boldsymbol{S'}\left(\tfrac{1}{2}(x_n + n_{n+1})\right) &= \boldsymbol{f}\left(\tfrac{1}{2}(x_n + n_{n+1}), \boldsymbol{S}\left(\tfrac{1}{2}(x_n + n_{n+1})\right)\right), && \text{(A.35)}\\
\boldsymbol{S'}(x_{n+1}) &= \boldsymbol{f}(x_{n+1}, \boldsymbol{S}(x_{n+1})). && \text{(A.36)}
\end{aligned}$$

The result is a system of nonlinear algebraic equations for the coefficients defining $\boldsymbol{S}(x)$ which is solved iteratively by linearisation. The basic method employed by bvp4c is Simpson's Method (see Section A.5.1) which produces a numerical approximation $\boldsymbol{S}(x)$ which is a 4^{th} order accurate approximation to the function $\boldsymbol{y}(x)$ [52], that is,

$$\|\boldsymbol{y}(x) - \boldsymbol{S}(x)\| \leq Ch^4, \tag{A.37}$$

where C is a constant and h is the maximum of the step sizes $h = \max_n[h_n] = \max_n[(x_{n+1} - x_n)]$.

The residual of the approximate solution is defined such that $\boldsymbol{r}(x) := \boldsymbol{S}(x) - \boldsymbol{f}(x, \boldsymbol{S}(x))$, therefore $\boldsymbol{S}(x)$ is the exact solution of the perturbed system of ODEs

$$\boldsymbol{S}'(x) = \boldsymbol{f}(x, \boldsymbol{S}(x)) - \boldsymbol{r}(x).$$

The residual in the boundary conditions is given by $\boldsymbol{r}(a,b) = \boldsymbol{g}(\boldsymbol{S}(a), \boldsymbol{S}(b))$.

The relative tolerance (RelTol) and absolute tolerance (AbsTol) control the size of the components of the residual vector, with $\boldsymbol{r}(x)$ satisfying

$$\left\| \left(\frac{\boldsymbol{r}(i)}{\max|\boldsymbol{f}(i)|}, \frac{\text{AbsTol}(i)}{\text{RelTol}} \right) \right\| \leq \text{RelTol}. \tag{A.38}$$

A.5 The MATLAB numerical integrators quad and quadl

quad and quadl can be used to evaluate numerically integrals of the form

$$I = \int_a^b f(x)\mathrm{d}x. \tag{A.39}$$

The general method used in approximating integrals numerically is to use two different methods for evaluating the integral to give the approximations I_1 and I_2 for I. If

$$|I_1 - I_2| < \text{tol}, \tag{A.40}$$

where tol is a prescribed tolerance, then I_1 is accepted as the value of the integral. However, if equation (A.40) does not hold then the range of integration is divided into two parts so that

$$I = \int_a^m f(x)\mathrm{d}x + \int_m^b f(x)\mathrm{d}x, \tag{A.41}$$

and each integral on the RHS is approximated individually using both methods. The same constraints that were imposed on the original approximations can now be imposed on the sum of the individual approximations. The method is repeated until the desired accuracy is reached.

Both quad and quadl use an adaptive quadrature method to approximate integrals of the form in equation (A.39): the points at which the function is evaluated are chosen carefully to ensure that evaluation is required at as few points as possible whilst maintaining the required accuracy of the solution. In general, this results in the function being evaluated often in regions where it changes rapidly and *vice versa*. quad uses Simpson's method and quadl uses a Lobatto method to compute the integrals.

A.5.1 Simpson's method

Simpson's method approximates the integral given by equation (A.39) by approximating the function f with a collection of arcs of quadratic functions and integrating across each one.

Figure A.4 demonstrates the method: the interval $[a,b]$ is divided into regular intervals of the form $[x_{i-2}, x_i]$ where $a = x_0 < x_1 < \ldots < x_n = b$ and n is even. The unique quadratic through the

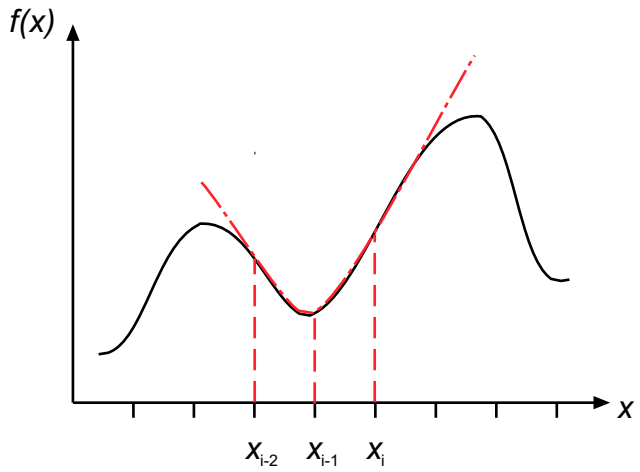


Figure A.4: A diagram illustrating Simpson's method. A unique polynomial (indicated by the dash-dotted red line) can be constructed through the points $f(x_{i-2})$, $f(x_{i-1})$ and $f(x_i)$ and used to approximate the integral of $f(x)$ over the interval $[x_{i-2}, x_i]$. See the text for more details.

points $f(x_{i-2})$, $f(x_{i-1})$ and $f(x_i)$ is given by

$$\begin{aligned} y_i(x) &= \frac{(x-x_{i-2})(x-x_{i-1})}{(x_i-x_{i-2})(x_i-x_{i-1})} f(x_i) \\ &+ \frac{(x-x_{i-1})(x-x_i)}{(x_{i-2}-x_{i-1})(x_{i-2}-x_i)} f(x_{i-2}) \\ &+ \frac{(x-x_i)(x-x_{i-2})}{(x_{i-1}-x_i)(x_{i-1}-x_{i-2})} f(x_{i-1}), \end{aligned} \tag{A.42}$$

and hence we can write

$$\int_{x_{i-2}}^{x_i} f(x)\mathrm{d}x \approx \frac{\Delta x}{3}[f(x_i) + 4f(x_{i-1}) + f(x_{i-2})], \tag{A.43}$$

where $\Delta x = x_i - x_{i-1}$. Over the whole interval we have

$$\int_a^b f(x)\mathrm{d}x \approx \frac{\Delta x}{3}[f(x_0) + 4f(x_1) + 2f(x_2) + \ldots + 2f(x_{n-2}) + 4f(x_{n-1}) + f(x_n)]. \tag{A.44}$$

The above is known as Simpson's 1/3 rule and there is an equivalent Simpson's 3/8 rule which uses cubic arcs and intervals of the form $[x_{i-3}, x_i]$. The degree of accuracy is equal to the degree of the lowest order polynomial that cannot be integrated exactly by the method [19]. Therefore Simpson's 1/3 rule is of order 3 and Simpson 's 3/8 rule of order 4.

A.5.2 Lobatto method

The Lobatto method is similar to Simpson's method except that it employs weighting functions when approximating the integral so that, for example,

$$\int_{-1}^{1} f(x)\mathrm{d}x \approx w_1 f(-1) + w_2 f(-x_1) + w_2 f(x_1) + w_1 f(1). \tag{A.45}$$

A.6 The MATLAB function fzero

The MATLAB function fzero uses a combination of traditional methods for finding the zeros of functions. An outline of the method for a function f is as follows [32]:

(i) Start with a, b such that $f(a)$ and $f(b)$ have opposite signs.

(ii) Use a secant step to find c between a and b.

(iii) Repeat the following until $|b - a| < \epsilon|b|$ or $f(b) = 0$ (where ϵ is a small parameter):

  (a) Arrange a, b, c, so that (i) $f(a)$ and $f(b)$ have opposite signs, (ii) $|f(b)| < |f(a)|$ and (iii) c is the previous value of b.

  (b) $c = a$ then consider a secant step.

  (c) $c \neq a$ then consider an inverse quadratic interpolation (IQI) step.

  (d) If the secant or IQI step is in $[a, b]$ then take it, otherwise use bisection.

Both the secant method and the IQI method are derived from Newton's method for finding roots of a function f. This method relies upon drawing a tangent to the graph of $f(x)$ at any point and determining where the tangent intersects the x-axis. The general formula is

$$x_{n+1} = x_n - \frac{f(x_n)}{f'(x_n)}, \tag{A.46}$$

where x_0 is specified.

The secant method replaces the derivative used in Newton's method with a finite difference approximation based on the two most recent iterates for x: instead of drawing a tangent through one point, a secant is drawn through two points and the next iteration is given by the intersection of the secant with the x-axis. The general formula is

$$x_{n+1} = x_n - \frac{f(x_n)}{s_n}, \quad \text{where} \quad s_n = \frac{f(x_n) - f(x_{n-1})}{x_n - x_{n-1}}. \tag{A.47}$$

This method has the added bonus that computation of the derivative of f is not required.

The IQI method is similar to the secant method except that it uses three points instead of two: if a, b and c are distinct points then a parabola P can be found such that $a = P(f(a))$, $b = P(f(b))$ and $c = P(f(c))$. The parabola always intersects the x-axis at the point $x = P(0)$ which gives the next iterate.

Appendix B

Linear stability criteria

Theorem B.1.1 *Given an eigenvalue equation of the form $\alpha^2 + b\alpha + c = 0$, we have the following stability conditions:*

Stable node or spiral *if $b < 0$ and $c > 0$.*

Unstable saddle *if $c < 0$.*

Unstable node or spiral *if $b > 0$ and $c < 0$.*

Proof of Theorem B.1.1 *We first consider $c < 0$: in this case*

$$\sqrt{b^2 - 4c} > b \Rightarrow \alpha_1 > 0,\ \alpha_2 < 0 \Rightarrow \textit{Unstable saddle.} \tag{B.1}$$

Now consider $b < 0$, $c > 0$: we have

$$\textit{Re}\left(\sqrt{b^2 - 4c}\right) < b \Rightarrow \textit{Re}(\alpha_1, \alpha_2) < 0 \Rightarrow \textit{Stable node or spiral.} \tag{B.2}$$

Finally we consider $b > 0$, $c > 0$: we have

$$\textit{Re}\left(\sqrt{b^2 - 4c}\right) < b \Rightarrow \textit{Re}(\alpha_1, \alpha_2) > 0 \Rightarrow \textit{Unstable node or spiral.} \tag{B.3}$$

Appendix C

Error function

Theorem C.1.1

$$\textit{erfc}(z) \sim \frac{2}{\sqrt{\pi}} \frac{e^{z^2}}{2z} \left[1 - \frac{1}{2z^2} + \frac{1.3}{(2z^2)^2} + \frac{1.3.5}{(2z^2)^3} \right] + \mathcal{O}(z^{-8}) \quad \textit{as} \quad z \to \infty \tag{C.1}$$

Proof of Theorem C.1.1

$$\begin{aligned} \frac{\sqrt{\pi}}{2}\textit{erfc}(z) &= \int_z^\infty e^{-u^2}\, du \\ &= \int_z^\infty \frac{-2ue^{-u^2}}{-2u}\, du \\ &= \left[\frac{-e^{-u^2}}{2u} \right]_z^\infty - \int_z^\infty \frac{e^{u^2}}{2u^2}\, du \\ &\vdots \\ &= \frac{2}{\sqrt{\pi}} \frac{e^{z^2}}{2z} \left[1 - \frac{1}{2z^2} + \frac{1.3}{(2z^2)^2} + \frac{1.3.5}{(2z^2)^3} \right] + R, \end{aligned} \tag{C.2}$$

where

$$|R| = \int_z^\infty \frac{105}{32u^9} \frac{d}{du}\left(e^{-u^2}\right) du < \frac{105}{32z^9} \int_z^\infty \frac{d}{du}\left(e^{-u^2}\right) du = \frac{105e^{-z^2}}{32z^9} \tag{C.3}$$

Letting $z \to \infty$ the above result is obtained.

Appendix D

Glossary

AP Antero-posterior

BDF Backwards differentiation formula

Dll1 Delta like 1

Fgf8 Fibroblast growth factor 8

L-fng Lunatic fringe

LHS Left hand side

LMS Linear multistep

NAG Numerical algorithms group

NDF Numerical difference formula

ODE Ordinary differential equation

PDE Partial differential equation

PSM Presomitic mesoderm

RA Retinoic acid

RHS Right hand side

Appendix E

Analytical results from Chapter 7

In this section of the appendix, we consider finding analytical approximations for the '*Outer system* - $\mathcal{O}(1)$'

$$\frac{\partial r_0}{\partial t} = \frac{k_1}{1+F_{e0}} - k_3 r_0, \tag{E.1}$$

$$\frac{\partial A_{e0}}{\partial t} = k_{18} r_0 - k_{10} A_{e0} + D\frac{\partial^2 A_{e_0}}{\partial x^2}, \tag{E.2}$$

$$\frac{\partial f_0}{\partial t} = \frac{k_{11}}{1+A_{e0}}\chi_f - k_{13} f_0, \tag{E.3}$$

$$\frac{\partial F_{e0}}{\partial t} = k_{19} f_0 - F_{e0} + \frac{\partial^2 F_{e_0}}{\partial x^2}, \tag{E.4}$$

where

$$k_{18} = \frac{1}{k_5(k_8+k_9)} \quad \text{and} \quad k_{19} = \frac{1}{k_{15}+k_{16}}.$$

E.1 Solution of the '*Outer system* - $\mathcal{O}(1)$' with $c_n = 0$

All variable subscripts within the '*Outer system* - $\mathcal{O}(1)$' will be dropped for the remainder of this section, and without loss of generality, it will be assumed that $x_n = 0$. Rescaling in x so that $y = \sqrt{D}x$ and assuming that $D \gg 1$ so that terms of $\mathcal{O}\left(D^{-1}\right)$ can be ignored, gives the '*Outer*

system - $\mathcal{O}(1)$, rescaled x, zero c_n':

$$\frac{\partial r}{\partial t} = \frac{k_1}{1+F} - k_3 r, \tag{E.5}$$

$$\frac{\partial A}{\partial t} = k_{18} r - k_{10} A + \frac{\partial^2 A}{\partial y^2}, \tag{E.6}$$

$$\frac{\partial f}{\partial t} = \frac{k_{11}}{1+A} H(x) - k_{13} f, \tag{E.7}$$

$$\frac{\partial F}{\partial t} = k_{19} f - F. \tag{E.8}$$

Justification for the above assumption for D can be found by considering the relative physical properties of the RA and FGF8 molecules. FGF8 protein molecules are relatively large in comparison to RA proteins and are also very "sticky"; they bind easily to cells of the extracellular matrix (ECM) [11]. We therefore expect $D_A \gg D_F$ and hence $D \gg 1$.

Due to the presence of the Heaviside function in the equation for *fgf8* (f), the y domain can be split into 2 regions; the positive and negative half axes. For $y < 0$, the steady state ($\partial/\partial t = 0$) equations can be solved to give

$$(r^*_-, A^*_-, f^*_-, F^*_-) = \left(\frac{k_1}{k_3}, B_1 e^{\sqrt{k_{10}} y} + \frac{k_1 k_{18}}{k_3 k_{10}}, 0, 0 \right), \tag{E.9}$$

where B_1 will be determined by continuity conditions of A^* and its derivative at $y = 0$. For $y > 0$, the equations can be rearranged to give a single equation for A:

$$\frac{\partial^2 A}{\partial y^2} - k_{10} A + \frac{k_1 k_{18} (1+A)}{k_3 \left[1 + \frac{k_{11} k_{19}}{k_{13}} + A \right]} = 0. \tag{E.10}$$

Multiplying through by A_y and integrating w.r.t. y gives

$$\frac{1}{2}(A_y)^2 + \frac{k_1 k_{18}}{k_3} A - \frac{k_1 k_{11} k_{18} k_{19}}{k_3 k_{13}} \log \left[1 + \frac{k_{11} k_{19}}{k_{13}} + A \right] - \frac{1}{2} k_{10} A^2 = B_2, \tag{E.11}$$

where B_2 is to be determined by matching conditions. Using continuity of the solution at $y = 0$ and noting that the negative root of the above must be taken to ensure that $A_y < 0$ (we wish RA levels to be high in the anterior region and decrease monotonically with y) gives an implicit solution for A^* in $y > 0$:

$$A^*_+(y) = -\int_0^y \sqrt{2B_2 + k_{10} A^{*2}_+ - 2\frac{k_1 k_{18}}{k_3} A^*_+ + 2\frac{k_1 k_{11} k_{18} k_{19}}{k_3 k_{13}} \log \left[1 + \frac{k_{11} k_{19}}{k_{13}} + A^*_+ \right]} \mathrm{d}y + B_1 + \frac{k_1 k_{18}}{k_3 k_{10}}. \tag{E.12}$$

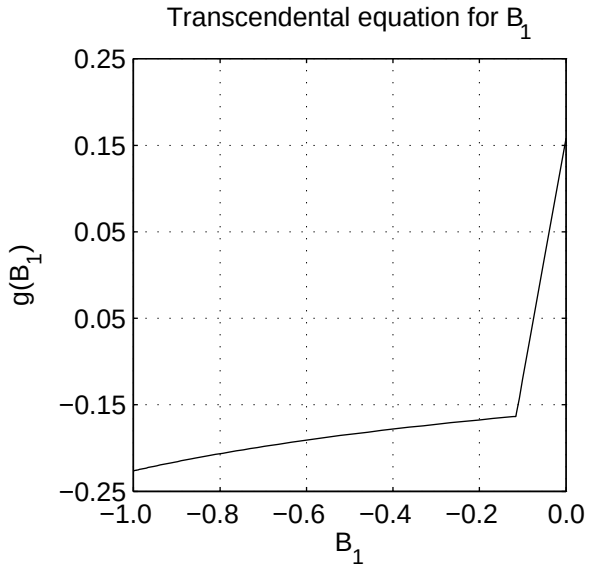


Figure E.1: A plot of the transcendental function $g(B_1)$ for the parameter B_1. The parameters are as follows: $k_1 = 1.0$, $k_3 = 1.5$, $k_{10} = 2.0$, $k_{11} = 1.3$, $k_{13} = 2.5$, $k_{18} = 1.5$ and $k_{19} = 0.8$. Using the MATLAB function fzero (see Appendix A.6 for more details), B_1 is found numerically to be -0.0568 (4 d.p.)

By using continuity of A and A_y and requiring $A_y \to 0$ as $y \to \infty$, B_2 can be found:

$$B_2 = -\frac{1}{2}\left\{k_{10}A_\infty^2 - 2\frac{k_1k_{18}}{k_3}A_\infty + 2\frac{k_1k_{11}k_{18}k_{19}}{k_3k_{13}}\log\left[1 + \frac{k_{11}k_{19}}{k_{13}} + A_\infty\right]\right\}, \tag{E.13}$$

where

$$A_\infty = \frac{1}{2}\left\{\frac{k_1k_{18}}{k_3k_{10}} - 1 - \frac{k_{11}k_{19}}{k_{13}} + \sqrt{\left[\frac{k_1k_{18}}{k_3k_{10}} - 1 - \frac{k_{11}k_{19}}{k_{13}}\right]^2 + \frac{4k_1k_{18}}{k_3k_{10}}}\right\}. \tag{E.14}$$

This gives a transcendental equation for B_1:

$$g(B_1) = B_1 + \frac{1}{\sqrt{k_{10}}}\sqrt{2B_2 + k_{10}C_1^2 - \frac{2k_1k_{18}}{k_3}C_1 + 2\frac{k_1k_{11}k_{18}k_{19}}{k_3k_{13}}\log\left[1 + \frac{k_{11}k_{19}}{k_{13}} + C_1\right]} = 0, \tag{E.15}$$

where $C_1 = B_1 + (k_1k_{18})/(k_3k_{10})$. Figure E.1 shows a plot of $g(B_1)$ for a set of parameter values which will be used throughout this Appendix. A solution to the equation can clearly be seen to exist around -0.01 and the MATLAB function fzero will be used to determine the value of B_1 in any further numerical solutions.

Variable	**Solution for** $y \leq 0$	**Solution for** $y > 0$
Raldh2	$\frac{k_1}{k_3}$	$\frac{k_1(1+A_+^*)}{k_3\left[1+\frac{k_{11}k_{19}}{k_{13}}+A_+^*\right]}$
Extracellular RA	$B_1 e^{\sqrt{k_{10}}y} + \frac{k_{18}}{k_3 k_{10}}$	A_+^*
fgf8	0	$\frac{k_{11}}{k_{13}(1+A_+^*)}$
Extracellular FGF8	0	$\frac{k_{11}k_{19}}{k_{13}(1+A_+^*)}$

Table E.1: A summary of the solutions for the '*Outer system - $\mathcal{O}(1)$, rescaled x, zero c_n*' for each dependent variable. B_1 and A_+^* are given by equations (E.12) and (E.15) respectively.

The remainder of the variables can be written in terms of A_+^* so that

$$(r_+^*, A_+^*, f_+^*, F_+^*) = \left(\frac{k_1\left(1+A_+^*\right)}{k_3\left[1+\frac{k_{11}k_{19}}{k_{13}}+A_+^*\right]}, A_+^*, \frac{k_{11}}{k_{13}(1+A_+^*)}, \frac{k_{11}k_{19}}{k_{13}(1+A_+^*)} \right). \quad \text{(E.16)}$$

Although it is not possible to solve equation (E.12) explicitly for A_+^*, it is possible to solve equation (E.11) numerically to gain insight into the shape of the concentration profiles of r^*, A^*, f^* and F^*. This can be done using the MATLAB function `ode15s`, a stiff solver of initial value problems for ODEs. For more information see Appendix A.2.

The steady state solutions of the '*Outer system - $\mathcal{O}(1)$, rescaled x, zero c_n*' are plotted in Figure E.2 and demonstrate opposing expression gradients of *Raldh2*/extracellular RA and *fgf8*/extracellular FGF8 as required.

E.1.1 Stability of the '*Outer system $\mathcal{O}(1)$, rescaled x, zero c_n*' steady states

Letting the steady states be denoted by r^*, A^*, f^* and F^*, the linear stability of these states can be explored by letting

$$r = r^* + \tilde{r}, \quad A = A^* + \tilde{A}, \quad f = f^* + \tilde{f}, \quad F = F^* + \tilde{F},$$

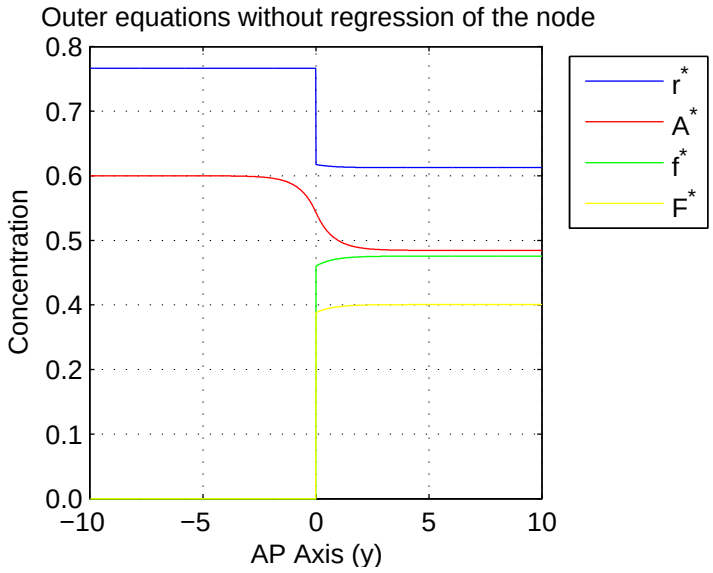


Figure E.2: Plots of the steady state profiles of *Raldh2*, external RA, *fgf8* and external FGF8 as given in Table E.1. The plot demonstrates the opposing gradients of *Raldh2*/extracellular RA and *fgf8*/extracellular FGF8 set up by the reduced model. The solution for RA on the positive half axis was found using the MATLAB ODE solver ode15s. Parameters are as follows: $k_1 = 1.0$, $k_3 = 1.5$, $k_{10} = 2.0$, $k_{11} = 1.3$, $k_{13} = 2.5$, $k_{18} = 1.5$ and $k_{19} = 0.8$.

where $|\tilde{r}|$, $|\tilde{A}|$, $|\tilde{f}|$, $|\tilde{F}| \ll 1$. Substituting the above into the '*Outer system* $\mathcal{O}(1)$, *rescaled* x, *zero* c_n' given by equations (E.5)-(E.8), gives the following equations for $\tilde{r}$, $\tilde{A}$, $\tilde{f}$, $\tilde{F}$ correct to first order:

$$\frac{\partial \tilde{r}}{\partial t} = -\frac{k_1 \tilde{F}}{(1+F^*)^2} - k_3 \tilde{r}, \tag{E.17}$$

$$\frac{\partial \tilde{A}}{\partial t} = k_{18}\tilde{r} - k_{10}\tilde{A} + \frac{\partial^2 \tilde{A}}{\partial y^2}, \tag{E.18}$$

$$\frac{\partial \tilde{f}}{\partial t} = -\frac{k_{11}\tilde{A}}{(1+A^*)^2} H(y) - k_{13}\tilde{f}, \tag{E.19}$$

$$\frac{\partial \tilde{F}}{\partial t} = k_{19}\tilde{f} - \tilde{F}. \tag{E.20}$$

Letting $\boldsymbol{w}(y) = (\tilde{r}, \tilde{A}, \tilde{f}, \tilde{F})'$ and defining $\boldsymbol{W}_k$, the time independent solution of the spatial eigenvalue problem

$$\frac{\partial^2 \boldsymbol{W}_k}{\partial y^2} + k^2 \boldsymbol{W}_k = 0, \tag{E.21}$$

with $\partial \boldsymbol{W}_k/\partial y \to 0$ as $y \to \pm\infty$, we consider a solution of the form

$$\boldsymbol{w} = \sum_k c_k e^{\lambda t} \boldsymbol{W}_k(y). \tag{E.22}$$

Substituting into equations (E.17)–(E.20) we have the following result for each k:

$$\begin{pmatrix} (\lambda + k_3) & 0 & 0 & \frac{k_1}{(1+F^*)^2} \\ -k_{18} & (\lambda + k_{10} + k^2) & 0 & 0 \\ 0 & \frac{k_{11}}{(1+A^*)^2} H(y) & (\lambda + k_{13}) & 0 \\ 0 & 0 & -k_{19} & (\lambda + 1) \end{pmatrix} \boldsymbol{W}_k = \boldsymbol{0}. \tag{E.23}$$

The above has a solution for each k if and only if

$$(\lambda+k_3)(\lambda+k_{10}+k^2)(\lambda+k_{13})(\lambda+1) - k_1 k_{11} k_{18} k_{19} \frac{1}{(1+F^*)^2} \frac{1}{(1+A^*)^2} H(y) = 0. \tag{E.24}$$

We now consider the range of possible values for k. Supposing that $k^2 > 0$, then the general solution of equation (E.21) is given by

$$\boldsymbol{W}_k = \boldsymbol{\alpha}_k \cos(|k|y) + \boldsymbol{\beta}_k \sin(|k|y). \tag{E.25}$$

Applying the zero flux boundary conditions as $y \to \pm\infty$ we see that $\boldsymbol{W}_k \equiv \boldsymbol{0}$. Similarly for $k^2 < 0$, the general solution of equation (E.21) is given by

$$\boldsymbol{W}_k = \boldsymbol{\alpha}_k e^{|k|y} + \boldsymbol{\beta}_k e^{|k|y}. \tag{E.26}$$

By requiring continuity of $\boldsymbol{W}$ and $\partial \boldsymbol{W}/\partial y$ at $y = 0$ we see that $\boldsymbol{W}_k \equiv 0$. For $k = 0$, the general solution is given by $\boldsymbol{W}_k \equiv \boldsymbol{\alpha}_k$ where $\boldsymbol{\alpha}_k$ is constant. So the only non-trivial solution for $\boldsymbol{W}_k$ occurs when $k \equiv 0$ and the equation for λ becomes

$$(\lambda + k_3)(\lambda + k_{10})(\lambda + k_{13})(\lambda + 1) - k_1 k_{11} k_{18} k_{19} \frac{1}{(1+F^*)^2} \frac{1}{(1+A^*)^2} H(y) = 0. \tag{E.27}$$

Substituting for F^* using Table E.1 we see that the solution is stable whenever

$$k_3 k_{10} k_{13} - \frac{k_1 k_{11} k_{18} k_{19}}{\left(1 + \frac{k_{11} k_{19}}{k_{13}} + A^*\right)^2} > 0. \tag{E.28}$$

Given that $A^* > 0$, then a sufficient condition for stability is

$$k_3 k_{10} k_{13} - \frac{k_1 k_{11} k_{18} k_{19}}{\left(1 + \frac{k_{11} k_{19}}{k_{13}}\right)^2} > 0. \tag{E.29}$$

E.2 Solution of the '*Outer system* - $\mathcal{O}(1)$' with $c_n \neq 0$

As in the previous section, all variable subscripts within the '*Outer system* - $\mathcal{O}(1)$' will be dropped for the remainder of this section, and without loss of generality, it will be assumed that $x_n = 0$. Rescaling the '*Outer system* - $\mathcal{O}(1)$' in x so that $y = \sqrt{D}x$ and assuming that $D \gg 1$ so that terms of $\mathcal{O}\left(D^{-1}\right)$ can be ignored, making a change to travelling wave coordinates of the form

$$\xi = \tilde{c}_n t - y, \qquad \tau = t, \tag{E.30}$$

and substituting into equations (E.5)-(E.8) gives

$$\begin{aligned}
\tilde{c}_n \frac{\partial r}{\partial \xi} + \frac{\partial r}{\partial \tau} &= \frac{1}{1+F} - k_3 r, && \text{(E.31)}\\
\tilde{c}_n \frac{\partial A}{\partial \xi} + \frac{\partial A}{\partial \tau} &= k_{18} r - k_{10} A + \frac{\partial^2 A}{\partial \xi^2}, && \text{(E.32)}\\
\tilde{c}_n \frac{\partial f}{\partial \xi} + \frac{\partial f}{\partial \tau} &= \frac{k_{11}}{1+A} H(-\xi) - k_{13} f, && \text{(E.33)}\\
\tilde{c}_n \frac{\partial F}{\partial \xi} + \frac{\partial F}{\partial \tau} &= k_{19} f - F, && \text{(E.34)}
\end{aligned}$$

where $\tilde{c}_n = \sqrt{D} c_n$. We term this system the '*Outer system* - $\mathcal{O}(1)$, *rescaled* x, *non-zero* $\tilde{c}_n$, *travelling wave*'.

Assuming that $\tilde{c}_n \ll 1$ (see Chapter 4 for justification) and expanding the steady state solution ($\partial/\partial\tau = 0$) in terms of $\tilde{c}_n$ so that

$$r = r_{c0} + \tilde{c}_n r_{c1} \ldots, \quad A = A_{c0} + \tilde{c}_n A_{c1} + \ldots, \quad f = f_{c0} + \tilde{c}_n f_{c1} + \ldots, \quad F = F_{c0} + \tilde{c}_n F_{c1} + \ldots,$$

gives the following correct to $\mathcal{O}(1)$:

$$\begin{aligned}
0 &= \frac{k_1}{1+F_{c0}} - k_3 r_{c0}, && \text{(E.35)}\\
0 &= k_{18} r_{c0} - k_{10} A_{c0} + \frac{\partial^2 A_{c0}}{\partial \xi^2}, && \text{(E.36)}\\
0 &= \frac{k_{11}}{1+A_{c0}} H(-\xi) - k_{13} f_{c0}, && \text{(E.37)}\\
0 &= k_{19} f_{c0} - F_{c0}, && \text{(E.38)}
\end{aligned}$$

We term this the '*Outer system* - $\mathcal{O}(1)$, *rescaled* x, *non-zero* $\tilde{c}_n$, *travelling wave* - $\mathcal{O}(1)$'. Correct to

first order in $\tilde{c}_n$ we have:

$$\frac{\partial r_{c0}}{\partial \xi} = -\frac{k_1 F_{c1}}{(1+F_{c0})^2} - k_3 r_{c1}. \tag{E.39}$$

$$\frac{\partial A_{c0}}{\partial \xi} = k_{18} r_{c1} - k_{10} A_{c1} + \frac{\partial^2 A_{c1}}{\partial \xi^2}, \tag{E.40}$$

$$\frac{\partial f_{c0}}{\partial \xi} = -\frac{k_{11} A_{c1}}{(1+A_{c0})^2} H(-\xi) - k_{13} f_{c1}, \tag{E.41}$$

$$\frac{\partial F_{c0}}{\partial \xi} = k_{19} f_{c1} - F_{c1}. \tag{E.42}$$

Similarly, we term this the '*Outer system - $\mathcal{O}(1)$, rescaled x, non-zero c_n, travelling wave - $\mathcal{O}(\tilde{c}_n)$*'.

E.2.1 *'Outer system - $\mathcal{O}(1)$, rescaled x, non-zero c_n, travelling wave - $\mathcal{O}(1)$'*

The above system, described by equations (E.31)-(E.34), can be solved in a similar manner to the previous section to give for $\xi > 0$:

$$r_{c0+}(\xi) = \frac{k_1}{k_3}, \quad f_{c0+}(\xi) = 0, \quad F_{c0+}(\xi) = 0, \quad A_{c0+}(\xi) = \alpha_1 e^{-\sqrt{k_{10}}\xi} + \frac{k_1 k_{18}}{k_3 k_{10}}. \tag{E.43}$$

For $\xi < 0$ we have

$$r_{c0-}(\xi) = \frac{k_1 \left(1 + A_{c0-}(\xi)\right)}{k_3[1 + \frac{k_{11}k_{19}}{k_{13}} + A_{c0-}(\xi)]}, \tag{E.44}$$

$$f_{c0-}(\xi) = \frac{k_{11}}{k_3[1 + A_{c0-}(\xi)]}, \tag{E.45}$$

$$F_{c0-}(\xi) = \frac{k_{11}k_{19}}{k_3[1 + A_{c0-}(\xi)]}, \tag{E.46}$$

where

$$A_{c0-}(\xi) = \int_0^\xi \sqrt{2\alpha_2 + k_{10}A_{c0-}^2 - 2\frac{k_1 k_{18}}{k_3}A_{c0-} + 2\frac{k_1 k_{11} k_{18} k_{19}}{k_3 k_{13}} \log\left[1 + \frac{k_{11}k_{19}}{k_{13}} + A_{c0-}\right]}\, \mathrm{d}\xi + \alpha_1 + \frac{k_1 k_{18}}{k_3 k_{10}}. \tag{E.47}$$

The constants α_1 and α_2 are given by

$$\alpha_1 = -\frac{1}{\sqrt{k_{10}}}\sqrt{2\alpha_2 + k_{10}D_1^2 - 2\frac{k_{18}}{k_3}D_1 + 2\frac{k_{11}k_{18}k_{19}}{k_3 k_{13}} \log\left[1 + \frac{k_{11}k_{19}}{k_{13}} + D_1\right]}, \tag{E.48}$$

$$\alpha_2 = -\frac{1}{2}\left\{k_{10}A_\infty^2 - 2\frac{k_1 k_{18}}{k_3}A_\infty + 2\frac{k_1 k_{11} k_{18} k_{19}}{k_3 k_{13}} \log\left[1 + \frac{k_{11}k_{19}}{k_{13}} + A_\infty\right]\right\}, \tag{E.49}$$

Variable	**Solution for $\xi \geq 0$**	**Solution for $\xi < 0$**
Raldh2	$\frac{k_1}{k_3}$	$\frac{k_1(1+A_{c0-}(\xi))}{k_3\left[1+\frac{k_{11}k_{19}}{k_{13}}+A_{c0-}(\xi)\right]}$
Extracellular RA	$\alpha_1 e^{\sqrt{-k_{10}}\xi} + \frac{k_1 k_{18}}{k_3 k_{10}}$	$A_{c0-}(\xi)$
fgf8	0	$\frac{k_{11}}{k_{13}[1+A_{c0-}(\xi)]}$
Extracellular FGF8	0	$\frac{k_{11}k_{19}}{k_{13}[1+A_{c0-}(\xi)]}$

Table E.2: A summary of the solutions for the '*Outer system* - $\mathcal{O}(1)$, *rescaled* x, *non-zero* c_n, *travelling wave* - $\mathcal{O}(1)$' for each dependent variable. α_1 and $A_{c0-}(\xi)$ are given by equations (E.48) and (E.47) respectively.

where A_∞ is as given in equation (E.14) and $D_1 = \alpha_1 + (k_1 k_{18})/(k_3 k_{10})$.

The solutions of the system '*Outer system* - $\mathcal{O}(1)$, *rescaled* x, *non-zero* c_n, *travelling wave* - $\mathcal{O}(1)$' found above are summarised in Table E.2.

Figure E.3 shows a plot of the $\mathcal{O}(1)$ steady state profiles of *Raldh2*, extracellular RA, *fgf8* and extracellular FGF8 with regression of the node as given in Table E.2. Equation (E.47) is solved as in the previous section using the MATLAB ODE solver ode15s.

E.2.2 '*Outer system* - $\mathcal{O}(1)$, *rescaled* x, *non-zero* $\tilde{c}_n$, *travelling wave* - $\mathcal{O}(\tilde{c}_n)$'

The above system of equations is

$$\frac{\partial r_{c0}}{\partial \xi} = -\frac{k_1 F_{c1}}{(1+F_{c0})^2} - k_3 r_{c1}. \tag{E.50}$$

$$\frac{\partial A_{c0}}{\partial \xi} = k_{18} r_{c1} - k_{10} A_{c1} + \frac{\partial^2 A_{c1}}{\partial \xi^2}, \tag{E.51}$$

$$\frac{\partial f_{c0}}{\partial \xi} = -\frac{k_{11} A_{c1}}{(1+A_{c0})^2} H(-\xi) - k_{13} f_{c1}, \tag{E.52}$$

$$\frac{\partial F_{c0}}{\partial \xi} = k_{19} f_{c1} - F_{c1}, \tag{E.53}$$

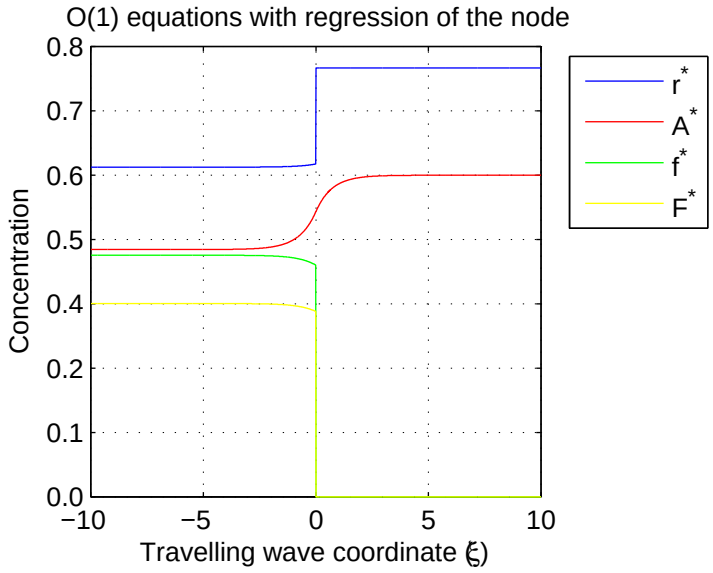


Figure E.3: Plots of the $\mathcal{O}(1)$ steady state profiles of *Raldh2*, extracellular RA, *fgf8* and extracellular FGF8 with regression of the node. As in the previous section, the plot demonstrates the opposing gradients of *Raldh2*/extracellular RA and *fgf8*/extracellular FGF8 set up by the reduced model. Notice that the solution has become reversed in the spatial coordinate; a consequence of the change of variables to travelling wave coordinates. The solution for RA on the negative half axis was found using the MATLAB ODE solver ode15s. Parameters are as follows: $k_1 = 1.0$, $k_3 = 1.5$, $k_{10} = 2.0$, $k_{11} = 1.3$, $k_{13} = 2.5$, $k_{18} = 1.5$ and $k_{19} = 0.8$.

and it can be solved for $\xi > 0$ to give

$$f_{c1+}(\xi) = 0, \quad F_{c1+}(\xi) = 0, \quad r_{c1+}(\xi) = 0, \quad A_{c1+}(\xi) = \alpha_3 e^{-\sqrt{k_{10}}\xi} + \frac{1}{2}\alpha_1 \xi e^{-\sqrt{k_{10}}\xi}, \tag{E.54}$$

where α_1 is fixed by the $\mathcal{O}(1)$ equation and α_3 will be determined by continuity of the solution and its derivative at $\xi = 0$.

For $\xi < 0$ the equations may be rearranged to give

$$r_{c1-}(\xi) = \frac{k_1 k_s \left[1 + \frac{1}{k_3} + \frac{1}{k_{13}}\right]}{k_3[1 + A_{c0-}(\xi) + k_s]^2} \frac{\partial A_{c0}}{\partial \xi} + \frac{k_1 k_s}{k_3[1 + A_{c0-}(\xi) + k_s]^2} A_{c1-}(\xi), \tag{E.55}$$

$$f_{c1-}(\xi) = \frac{k_{11}}{k_{13}^2[1 + A_{c0}(\xi)]^2} \frac{\partial A_{c0}}{\partial \xi} - \frac{k_{11}}{k_{13}[1 + A_{c0}(\xi)]^2} A_{c1-}(\xi), \tag{E.56}$$

$$F_{c1-}(\xi) = \frac{k_s \left[1 + \frac{1}{k_{13}}\right]}{[1 + A_{c0}(\xi)]^2} \frac{\partial A_{c0}}{\partial \xi} - \frac{k_s}{[1 + A_{c0}(\xi)]^2} A_{c1-}(\xi), \tag{E.57}$$

where $k_s = k_{11}k_{19}/k_{13}$, and A_{c1-} is given by

$$\frac{\partial^2 A_{c1-}}{\partial \xi^2} = (k_{10} - \bar{A}_0)A_{c1-} + \left[1 + \bar{A}_0\left(1 + \frac{1}{k_3} + \frac{1}{k_{13}}\right)\right]\frac{\partial A_{c0-}}{\partial \xi}, \tag{E.58}$$

with

$$\bar{A}_0(\xi) = \frac{k_1 k_s k_{18}}{k_3\left[1 + A_{c0-}(\xi) + k_s\right]^2}. \tag{E.59}$$

E.2.2.1 Matching conditions

The matching conditions ensure continuity of A_{c1-} and its derivative at $\xi = 0$. For this we require

$$A_{c1-}(0) = \alpha_3, \quad \frac{\partial A_{c1-}}{\partial \xi}(0) = -\sqrt{k_{10}}\alpha_3 + \frac{1}{2}\alpha_1. \tag{E.60}$$

We note that there is a free parameter, α_3, that can be chosen to ensure that $\partial A_{c1-}/\partial \xi \to 0$ as $\xi \to -\infty$, and hence that there is a bounded solution of (E.31)-(E.34) correct to first order in c_n.

E.2.2.2 Uniqueness of solution to equation (E.58)

Consider an equation of the form

$$A_{xx} = f(x)A + g(x), \tag{E.61}$$

where $f \geq 0$ and g are continuous functions on $(-\infty, 0]$, with boundary conditions

$$A(0) = \alpha, \quad A_x(0) = -\alpha\beta + \kappa, \quad A_x \to 0 \quad \text{as} \quad x \to -\infty, \tag{E.62}$$

where α is a free parameter. Making the transformation $\bar{A} = A - \kappa/\beta$, then $\bar{A}$ satisfies

$$\bar{A}_{xx} = f(x)\bar{A} + \left[g(x) + \frac{\kappa}{\beta}\right] = f(x)\bar{A} + \bar{g}(x), \tag{E.63}$$

with homogeneous boundary conditions

$$\beta\bar{A} + \bar{A}_x = 0 \quad \text{at} \quad x = 0 \quad \text{and} \quad \bar{A}_x \to 0 \quad \text{as} \quad x \to -\infty. \tag{E.64}$$

Suppose that there are two solutions u, v, of the above equation and consider $w = u - v$. Then w satisfies the homogeneous equation

$$w_{xx} = f(x)w, \tag{E.65}$$

with the same boundary conditions as $\bar{A}$. Whenever $f > 0$ for $x \in (-\infty, 0]$, the homogeneous

Variable	Solution for $\xi \geq 0$	Solution for $\xi < 0$
Raldh2	0	$\frac{k_1 k_s \left[1+\frac{1}{k_{13}}+\frac{1}{k_{13}}\right]}{k_3[1+A_{c0-}(\xi)+k_s]^2}\frac{\partial A_{c0}}{\partial \xi} + \frac{k_1 k_s}{k_3[1+A_{c0-}(\xi)+k_s]^2}A_{c1-}(\xi)$
Extracellular RA	$\alpha_3 e^{-\sqrt{k_{10}}\xi} + \frac{1}{2}\alpha_1 \xi e^{-\sqrt{k_{10}}\xi}$	$A_{c1-}(\xi)$
fgf8	0	$\frac{k_{11}}{k_{13}^2[1+A_{c0}(\xi)]^2}\frac{\partial A_{c0}}{\partial \xi} - \frac{k_{11}}{k_{13}[1+A_{c0}(\xi)]^2}A_{c1-}(\xi)$
Extracellular FGF8	0	$\frac{k_s\left[1+\frac{1}{k_{13}}\right]}{[1+A_{c0}(\xi)]^2}\frac{\partial A_{c0}}{\partial \xi} - \frac{k_s}{[1+A_{c0}(\xi)]^2}A_{c1-}(\xi)$

Table E.3: A summary of the solutions for the '*Outer system* - $\mathcal{O}(1)$, *rescaled* x, *non-zero* c_n, *travelling wave* - $\mathcal{O}(c_n)$' for each dependent variable. α_3 may be chosen to ensure a bounded solution for A_{c1-} and $k_s = k_{11}k_{19}/k_{13}$. A_{c1-} is specified by equation (E.58).

equation $w_{xx} = f(x)w$ has only the trivial solution since

$$\int_{-\infty}^{0} w_{xx} w \, \mathrm{d}x = \int_{-\infty}^{0} f(x) w^2 \, \mathrm{d}x \geq 0, \tag{E.66}$$

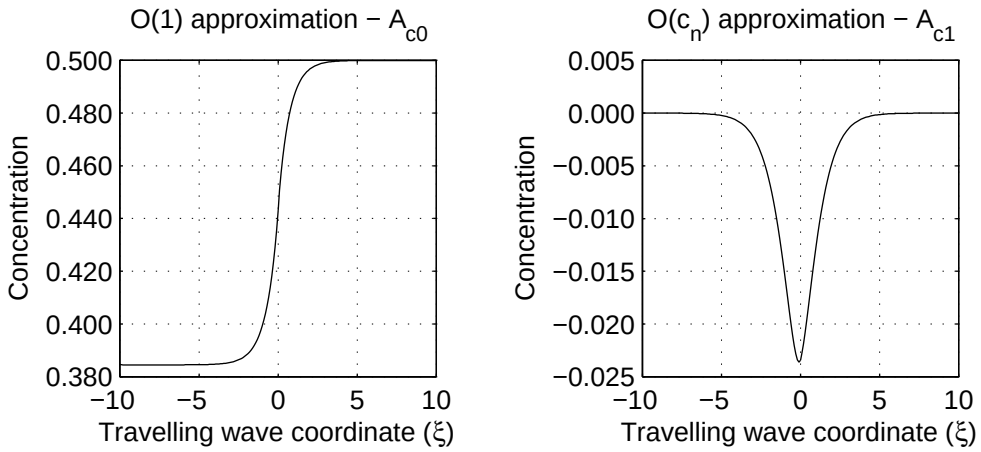


Figure E.4: Plots of the $\mathcal{O}(1)$ and $\mathcal{O}(c_n)$ steady state profiles of the extracellular RA concentrations along the AP axis. Equations (E.68) and (E.69) for the dynamics in $\xi < 0$ were solved using the MATLAB solver bvp4c (see Appendix A.4 for more details). Parameters are as follows: $k_1 = 1.5$, $k_3 = 1.5$, $k_{10} = 2.0$, $k_{11} = 1.3$, $k_{13} = 2.5$, $k_{18} = 1.5$ and $k_{19} = 0.8$.

implies (integrating LHS by parts)

$$[ww_x]_{-\infty}^{0} - \int_{-\infty}^{0} w^2 \,\mathrm{d}x = w(0)w_x(0) - w(\infty)w_x(-\infty) - \int_{-\infty}^{0} w^2 \,\mathrm{d}x = -\frac{w(0)^2}{\beta} - \int_{-\infty}^{0} w^2 \,\mathrm{d}x \leq 0.$$

We can therefore conclude that $u \equiv v$ and that the solution is unique.

Applying the above method to equation (E.58) with boundary conditions given by (E.60) it can be seen (using the transformation $\bar{A} = A - \alpha_1/(2\sqrt{k_{10}})$), that if a solution to the problem exists, then such a solution will be unique whenever

$$k_{10} - \frac{k_{11}k_{18}k_{19}}{k_3 k_{13}\left[1 + \frac{k_1 k_{11} k_{19}}{k_{13}}\right]^2} > 0. \tag{E.67}$$

Note that this is the same sufficient (but not necessary) condition to that required for stability of the steady state without regression of the node (equation (E.29)).

Having proved that there is a unique, bounded solution for A_{c1}, the $\mathcal{O}(c_n)$ component of the extracellular RA concentration, we see from Table E.3 that for each of r, A_e, f and F_e (*Raldh2*, extracellular RA, *fgf8* and extracellular FGF8) in the '*Outer system - $\mathcal{O}(1)$, rescaled x, non-zero c_n, travelling wave - $\mathcal{O}(c_n)$*' there is a unique, bounded solution.

Table E.3 summarises the results of solution of the '*Outer system - $\mathcal{O}(1)$, rescaled x, non-zero c_n, travelling wave - $\mathcal{O}(c_n)$*'. We solve the system numerically in Section E.2.3.

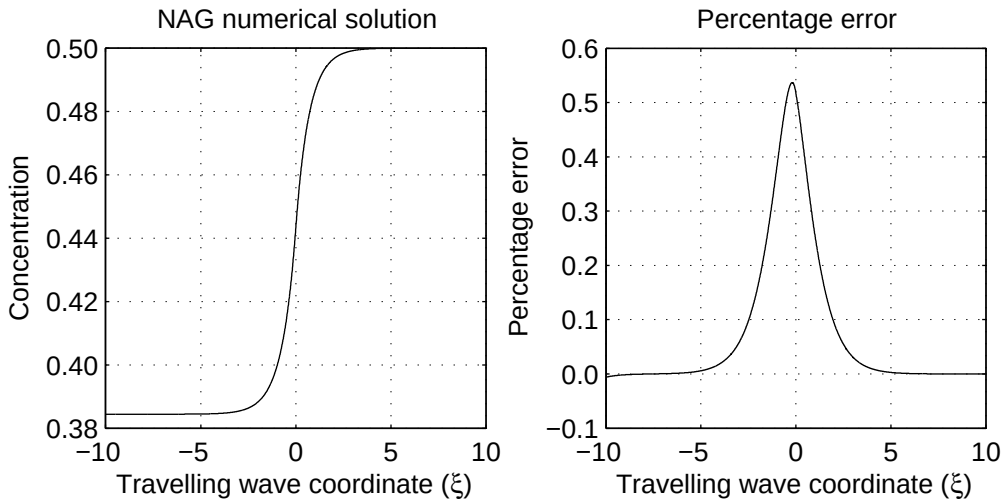


Figure E.5: Plots of the NAG numerical solution of equations (E.31)-(E.34) and the percentage error between the NAG numerical solution of the '*Outer system*' and the first order outer approximation given by $A_{c0} + c_n A_{c1}$ ('*Outer system - $\mathcal{O}(1)$, rescaled x, non-zero c_n, travelling wave*'). The numerical solution is plotted for $\tau = 20$ to allow the concentrations to reach their steady state profiles. The percentage error is also calculated using the numerical solution at $\tau = 20$. Parameters are as follows: $k_1 = 1.0$, $k_3 = 1.5$, $k_{10} = 2.0$, $k_{11} = 1.3$, $k_{13} = 2.5$, $k_{18} = 1.5$, $k_{19} = 0.8$ and $c_n = 0.1$.

E.2.3 Numerical Solution for '*Outer system - $\mathcal{O}(1)$, rescaled x, non-zero c_n, travelling wave*' correct to first order in c_n

The system of equations governing the behaviour of A_{c0-} and A_{c1-} (the $\mathcal{O}(1)$ and $\mathcal{O}(c_n)$ extracellular RA concentrations of the '*Outer system - $\mathcal{O}(1)$, rescaled x, non-zero c_n, travelling wave*') is

$$\frac{\partial^2 A_{c0}}{\partial \xi^2} = k_{10} A_{c0} - \frac{k_1 k_{11} k_{18} k_{19}}{k_3 k_{13} \left[1 + A_{c0} + \frac{k_{11} k_{19}}{k_{13}}\right]^2}, \tag{E.68}$$

$$\frac{\partial^2 A_{c1}}{\partial \xi^2} = \left[k_{10} - \bar{A}_0\right] A_{c1} + \left[1 + \bar{A}_0 \left(1 + \frac{1}{k_3} + \frac{1}{k_{13}}\right)\right] \frac{\partial A_{c0}}{\partial \xi}, \tag{E.69}$$

with initial/boundary conditions

$$A_{c0}(0) = \alpha_1 + \frac{k_1 k_{18}}{k_3 k_{10}}, \quad \frac{\partial A_{c0}}{\partial \xi}(0) = -\sqrt{k_{10}}\alpha_1, \quad A_{c1}(0) = \alpha_3, \quad \frac{\partial A_{c1}}{\partial \xi}(0) = -\sqrt{k_{10}}\alpha_3 + \frac{1}{2}\alpha_1.$$

The parameter α_3 can be chosen to ensure that $\partial A_{c1-}/\partial \xi \to 0$ as $\xi \to -\infty$ and hence that we have a bounded solution for A_{c1-}.

The MATLAB solver bvp4c can be used to solve the above system of equations and to compute

the value of α_3. More information about the numerical methods used in bvp4c can be found in Appendix A.4. Before solving, equations (E.68) and (E.69) must be converted to a system of four first order equations with five boundary value conditions (including an unknown parameter). The vector of initial conditions was chosen to be $\big(A_\infty, 0, -0.2\exp(\sqrt{k_{10}}\xi), 0\big)$. Figure E.4 shows a plot of the numerical solutions for the $\mathcal{O}(1)$ and $\mathcal{O}(c_n)$ approximations (A_{c0} and A_{c1}) defined by the system of equations (E.68) and (E.69).

E.2.3.1 Comparison with the NAG numerical solution

The '*Outer system - $\mathcal{O}(1)$, rescaled x, non-zero c_n, travelling wave*' (equations (E.31)-(E.34)) can also be solved using the NAG library routine DO3PCF. As in previous simulations, the infinite domain boundary conditions are approximated by using zero flux boundary conditions with the domain being large enough to ensure that conditions at the boundary do not have significant effects. The initial conditions are taken to be zero everywhere and as before, a $\tanh$ function was used to approximate the Heaviside function at $\xi = 0$.

Figure E.5 shows a plot of the solution generated by the NAG solver D03PCF along with a plot of the percentage error between the numerical solution and the $\mathcal{O}(c_n)$ approximation given by $A_{c0}+c_nA_{c1}$. We calculate the percentage error as

$$\text{Percentage error} = \frac{A_{num} - (A_{c0} + c_nA_{c1})}{A_{num}}\text{x}100. \tag{E.70}$$

The percentage error lies below 1% throughout the domain covered, corresponding to an absolute error of order 10^{-3} and indicating that the first order approximation is in very good agreement with the numerical solution.

Bibliography

[1] G. BEGEMANN AND A. MEYER, *Hindbrain patterning revisited: timing and effects of retinoic acid signalling*, BioEssays, 23 (2001), pp. 981–986.

[2] K. BERGGREN, P. MCCAFFERY, U. DRAGER, AND C. J. FOREHAND, *Differential distribution of retinoic acid synthesis in the chicken embryo as determined by the immunolocalization of the retinoic acid synthetic enzyme, RALDH-2*, Dev. Bio., 210 (1999), pp. 288–304.

[3] J. R. COLLIER, *Spatial and propagating patterns in embryology*, PhD thesis, Oxford University, 1997.

[4] J. R. COLLIER, D. MCINERNEY, S. SCHNELL, P. K. MAINI, D. J. GAVAGHAN, P. HOUSTON, AND C. D. STERN, *A cell cycle model for somitogenesis: mathematical formulation and numerical solution*, J. theor. Biol., 207 (2000), pp. 305–316.

[5] J. COOKE, *Control of somite number during morphogenesis of a vertebrate*, xenopus laevis, Nature, 254 (1975), pp. 196–199.

[6] J. COOKE AND E. C. ZEEMAN, *A clock and wavefront model for control of the number of repeated structures during animal morphogenesis*, J. theor. Biol., 58 (1976), pp. 455–476.

[7] J. K. DALE, M. MAROTO, M.-L. DEQUEANT, P. MALAPERT, M. MCGREW, AND POURQUIÉ, *Periodic notch inhibition by lunatic fringe underlies the chick segmentation clock*, Nature, 421 (2003), pp. 275–278.

[8] K. J. DALE AND O. POURQUIÉ, *A clock-work somite*, BioEssays, 22 (2000), pp. 72–83.

[9] I. DEL BARCO BARRANTES, A. J. ELIA, K. WÜNSCH, M. HRABĚ DE ANGELIS, T. W. MAK, J. ROSSANT, R. A. CONLON, A. GOSSLER, AND J. L. DE LA POMPA, *Interaction between Notch signalling and Lunatic fringe during somite boudary formation in the mouse*, Curr. Biol., 9 (1999), pp. 470–480.

[10] P. M. DEW AND J. E. WALSH, *A set of library routines for solving parabolic equations in one space variable*, ACM Trans. Math. Softw., 7 (1981), pp. 295–314.

[11] R. DIEZ DEL CORRAL, *Pers. comm.*, 2004.

[12] R. DIEZ DEL CORRAL, I. OLIVERA-MARTINEZ, A. GORIELY, E. GALE, M. MADEN, AND K. STOREY, *Opposing FGF and retinoid pathways control ventral neural pattern, neuronal differentiation and segmentation during body axis extension*, Neuron, 40 (2003), pp. 65–79.

[13] R. DIEZ DEL CORRAL AND K. STOREY, *Opposing FGF and retinoid pathways: a signalling switch that controls differentiation and patterning onset in the extending vertebrate body axis*, BioEssays, 26 (2004), pp. 957–869.

[14] B. DOBBS-MCAULIFFE, Q. ZHAO, AND E. LINNERY, *Feedback mechanisms regulate retinoic acid production and degradation in the zebrafish embryo*, Mech. Dev., 121 (2004), pp. 339–350.

[15] J. DUBRULLE, M. J. MCGREW, AND O. POURQUIÉ, *FGF signalling controls somite boundary position and regulates segmentation clock control of spatiotemporal* Hox *gene activation*, Cell, 106 (2001), pp. 219–232.

[16] J. DUBRULLE AND O. POURQUIÉ, *From head to tail: links between the segmentation clock and antero-posterior patterning of the embryo*, Curr. Op. Gen. Dev., 5 (2002), pp. 519–523.

[17] ——, fgf8 *mRNA decay establishes a gradient that couples axial elongation to pattering in the vertebrate embryo*, Nature, 427 (2004), pp. 419–422.

[18] B. EROL, K. KUSUMI, J. LOU, AND J. P. DORMANS, *Etiology of congenital scoliosis*, University of Pennsylvania Othopaedic Journal, 15 (2002), pp. 37–42.

[19] W. GANDER AND W. GAUTSCHI, *Adaptice quadrature - revisited*, BIT, (2000).

[20] S. F. GILBERT, *Developmental Biology*, Sunderland, Mass: Sinauer Associates, 3rd ed., 1991.

[21] A. GOSSLER AND M. HRABĚ DE ANGELIS, *Somitogenesis*, Curr. Top. Dev. Biol., 38 (1998), pp. 225–287.

[22] Y.-J. JIANG, B. L. AERNE, L. SMITHERS, C. HADDON, D. ISH-HOROWICZ, AND J. LEWIS, *Notch signalling and the synchronization of the segmentation clock*, Nature, 408 (2000), pp. 475–479.

[23] M. KAERN, M. MENZINGER, AND A. HUNDING, *Segmentation and somitogenesis derived from phase dynamics in growing oscillatory media*, J. theor. Biol., 207 (2000), pp. 473–493.

[24] R. J. KEYNES AND C. D. STERN, *Mechanisms of vertebrate segmentation*, Development, 103 (1988), pp. 413–429.

[25] A. LINVILLE, E. GUMUSANELI, R. A. S. CHANDRARATNA, AND T. F. SCHILLING, *Independent roles for retinoic acid in segmentation and neuronal differentiation in the zebrafish hindbrain*, Dev. Bio, 270 (2004), pp. 186–199.

[26] M. MADEN, A. GRAHAM, M. ZILE, AND E. GALE, *Abnormalities of somite development in the absence of retinoic acid*, Int. J. Dev. Biol., 44 (2000), pp. 151–159.

[27] M. J. MCGREW, J. K. DALE, S. FRABOULET, AND O. POURQUIÉ, *The* lunatic fringe *gene is a target of the molecular clock linked to somite segmentation in avian embryos*, Curr. Biol., 8 (1998), pp. 979–982.

[28] D. MCINERNEY, *Spatio-temporal patterning in biological systems: Numerical techniques and mathematical modelling*, PhD thesis, Oxford University, 2001.

[29] D. MCINERNEY, S. SCHNELL, R. E. BAKER, AND P. K. MAINI, *A mathematical formulation for the cell cycle model in somitogenesis: parameter constraints and numerical solutions*, IMA J. Math. Appl. Med. & Biol., 21 (2004), pp. 85–113.

[30] H. MEINHARDT, *Models of Biological Pattern Formation*, Academic Press, London, 1982.

[31] H. MEINHARDT, *Models of segmentation*, in Somites in Developing Embryos, R. Bellairs, D. A. Ede, and J. W. Lash, eds., Plenum Press, New York, 1986, pp. 179–189.

[32] C. MOLER, *Numerical computing with Matlab*, Online at http://www.mathworks.com/moler/, 2004.

[33] T. A. MORENO AND C. KINTER, *Regulation of segmental patterning by retinoic acid signalling during* Xenopus *somitogenesis*, Dev. Cell, 6 (2004), pp. 205–218.

[34] J. D. MURRAY, *Mathematical biology I: an introduction*, vol. I, Springer-Verlag, 3rd ed., 2003.

[35] ——, *Mathematical biology II: spatial models and biochemical applications*, vol. II, Springer-Verlag, 3rd ed., 2003.

[36] NUMERICAL ALGORITHMS GROUP, *D03PCF - NAG Fortran library routine document*, http://www.nag.co.uk/numeric/FL/manual/pdf/D03/d03pcf.pdf.

[37] I. PALMEIRIM, D. HENRIQUE, D. ISH-HOROWICZ, AND O. POURQUIÉ, *Avian* hairy *gene expression identifies a molecular clock linked to vertebrate segmentation and somitogenesis*, Cell, 91 (1997), pp. 639–648.

[38] A. A. POLEZHAEV, *A mathematical model of the mechanism of vertebrate somitic segmentation*, J. theor. Biol., 156 (1992), pp. 169–181.

[39] ——, *Mathematical model of segmentation in somitogenesis in vertebrates*, Biophysics, 40 (1995), pp. 583–589.

[40] ——, *Mathematical modelling of somite segmentation in vertebrates*, in Origin and Fate of Somites, E. J. Sanders, J. W. Lash, and C. P. Ordahl, eds., IOS Press, Amsterdam, 2001, pp. 107–115.

[41] O. POURQUIÉ, *The chick embryo: a leading model for model in somitogenesis studies*, Mech. Dev., 121 (2004), pp. 1069–1079.

[42] ——, *Pers. comm.*, 2004.

[43] O. POURQUIÉ AND K. KUSUMI, *When body segmentation goes wrong*, Clin. Genet., 60 (2001), pp. 409–416.

[44] D. R. N. PRIMMETT, W. E. NORRIS, G. J. CARLSON, R. J. KEYNES, AND C. D. STERN, *Periodic anomalies induced by heat shock in the chick embryo are associated with the cell cycle*, Development, 105 (1989), pp. 119–130.

[45] D. R. N. PRIMMETT, C. D. STERN, AND R. J. KEYNES, *Heat shock causes repeated segmental anomalies in the chick embryo*, Development, 104 (1988), pp. 331–339.

[46] Y. SAGA AND H. TAKEDA, *The making of the somite: molecular events in vertebrate segmentation*, Nat. Rev. Genet., 2 (2001), pp. 835–845.

[47] A. SAWADA, S. MINORI, Y.-J. JIANG, A. KAWAKAMI, AND A. KUROIWA, *FGF/MAPK signalling is a crucial positional cue in somite boundary formation*, Development, 128 (2001), pp. 4873–4880.

[48] A. F. SCHIER, *Tail of decay*, Nature, 427 (2004), pp. 403–404.

[49] S. SCHNELL AND P. K. MAINI, *Clock and induction model for somitogenesis*, Dev. Dyn., 217 (2000), pp. 415–420.

[50] S. SCHNELL, P. K. MAINI, D. MCINERNEY, D. J. GAVAGHAN, AND P. HOUSTON, *Models for pattern formation in somitogenesis: a marriage of cellular and molecular biology*, C.R. Biologies, 325 (2002), pp. 179–189.

[51] S. SCHNELL, K. J. PAINTER, P. K. MAINI, AND H. G. OTHMER, *Spatiotemporal pattern formation in early development: a review of primitive streak formation and somitogenesis*, in Mathematical Models for Biological Pattern Formation, P. K. Maini and H. G. Othmer, eds., vol. 121 of IMA Volumes in Mathematics and its Applications, Springer, New York, 2000, pp. 11–37.

[52] L. F. SHAMPINE, J. KIERZENKA, AND M. W. REICHELT, *Solving boundary value problems for ordinary differential equations in* MATLAB *with* bvp4c, tech. report, ftp://ftp.mathworks.com/pub/doc.papers/bvp/tutorial.pdf, 2000.

[53] L. F. SHAMPINE AND M. W. REICHELT, *The* MATLAB *ODE suite*, SIAM journal on scientific computing, 18 (1997), pp. 1–22.

[54] C. D. STERN AND R. BELLAIRS, *Mitotic activity during somite segmentation in the early chick embryo*, Anat. Embryol. (Berl.), 169 (1984), pp. 97–102.

[55] C. D. STERN, S. E. FRASER, R. J. KEYNES, AND D. R. N. PRIMMETT, *A cell lineage analysis of segmentation in the chick embryo*, Development, 104S (1988), pp. 231–244.

[56] M. S. J. STICKNEY, H. L. BARRESI AND S. H. DEVOTO, *Somite development in zebrafish*, Dev. Dyn., 219 (2000), pp. 287–303.

[57] F. E. STOCKDALE, W. J. NIKOVITS, AND B. CHRIST, *Molecular and cellular biology of avian somite development*, Dev. Dyn., 219 (2000), pp. 304–321.

[58] C. J. TABIN AND R. L. JOHNSON, *Clocks and hox*, Nature, 412 (2001), pp. 780–781.

[59] L. N. TREFETHEN, *Finite difference and spectral methods for ordinary and partial differential equations*. available at http://web.comlab.ox.ac.uk/oucl/work/nick.trefethen/pdetext.html, 1996.

[60] D. VASILIAUSKAS AND C. D. STERN, *Patterning the embryonic axis: FGF signalling and how vertebrate embryos measure time*, Cell, 106 (2001), pp. 133–136.

[61] M. VEINI AND R. BELLAIRS, *Heat shock effects in chick embryos*, in Somites in Developing Embryos, R. Bellairs, D. A. Ede, and J. W. Lash, eds., Plenum Press, New York, 1986, pp. 135–145.

[62] V. WALBOT AND N. HOLDER, *Developmental Biology*, Random House, New York, 1987.

[63] E. C. ZEEMAN, *Primary and secondary waves in developmental biology*, in Some mathematical questions in biology, VI (Proc. Eighth Sympos., Mathematical Biology, San Francisco, Calif., 1974), Amer. Math. Soc., Providence, R.I., 1974, pp. 69–161. Lectures on Math. in the Life Sciences, Vol. 7.